

Technische Universität München

Fakultät für Maschinenwesen
Institut für Energietechnik
Professur für Thermofluiddynamik

Acoustic and Thermal Characterization of Quarter-Wave Resonators

Simon Hendrik van Buren

Vollständiger Abdruck der von der Fakultät für Maschinenwesen der
Technischen Universität München zur Erlangung des akademischen Grades
eines

DOKTOR – INGENIEURS

genehmigten Dissertation.

Vorsitzender:

Prof. Dr.-Ing. Michael Zäh

Prüfer der Dissertation:

Prof. Wolfgang Polifke, Ph. D.

Assoc. Prof. Dr. Guillaume Penelet

Die Dissertation wurde am 23.03.2021 bei der Technischen Universität München eingereicht
und durch die Fakultät für Maschinenwesen am 02.06.2021 angenommen.

Abstract

The present thesis addresses the effect of temperature inhomogeneities on the damping characteristic of acoustic quarter-wave resonators. A comprehensive investigation of heat transfer in turbulent oscillating flows is given to derive the underlying temperature distributions. In particular, the work focuses on (i) analytical models to generate in-depth knowledge about the physical mechanisms involved and on (ii) high-fidelity fluid dynamic simulations as a numerical design tool and for the parametric quantification of turbulent effects.

Based on Rott's thermoacoustic theory, analytical correlations for the acoustic wave propagation in ducts and channels with non-uniform temperature are derived. The framework considers viscous and thermal losses attributed to wall-interaction. At constant temperatures, the equations closely resemble the formulation as characteristic waves, extended by a loss-induced spatial decay. Linear temperature gradients are studied under the assumption of temperature-independent viscosity. The analytical correlations transfer to a simple model that predicts the acoustic impedance of a quarter-wave resonator. As a more flexible tool for arbitrary temperature profiles, the thesis proposes a numerical framework. Compressible fluid dynamic simulations are conducted for the acoustic characterization. The numerical forcing is realized via the Navier-Stokes characteristics boundary condition. The simulations are successfully validated against semi-empirical correlations.

Longitudinal heat transfer inside the resonator tube is studied via Kurzweg's analysis of incompressible flows. An in-depth comparison to Rott's thermoacoustic theory reveals identical results at an acoustic pressure node location. Simplified versions of the two correlations allow a comprehensive discussion on the interplay between hydrodynamic and thermal boundary layers. The longitudinal thermal transport is maximum if the thermal boundary layer approximately exceeds the center of the channel. Subdivided into six characteristic regimes, the thesis derives qualitative statements for the heat transfer in each combination of hydrodynamic and thermal boundary layer thickness.

High-fidelity Large Eddy Simulations are used to study the effect of turbulence on heat transfer in pulsating flows. The study considers a fully developed turbulent incompressible flow within an cyclic domain. At large pulsation amplitudes with pronounced flow reversal, significant wall-normal enhancement shows between a hot and cold channel wall. The numerical results confirm qualitative experimental data and strengthen the significance of enhanced heat transfer as an important aspect of a comprehensive design process of technical applications. Moreover, significant turbulence-induced enhancement is found in the longitudinal direction.

Abstract

Kurzfassung

Die vorliegende Arbeit untersucht den Einfluss von lokalen Temperaturinhomogenitäten auf das Dämpfungsverhalten von akustischen $\lambda/4$ -Resonatoren. Dafür wird eine umfassende Untersuchung des Wärmeübergangs in turbulent oszillierenden Strömungen durchgeführt, um die zugrundeliegenden Temperaturverteilungen herzuleiten. Die Schwerpunkte der Arbeit liegen auf (i) analytischen Modellen zur Gewinnung fundierte Kenntnisse der vorliegenden physikalischen Mechanismen, sowie auf (ii) hochauflösenden Strömungssimulationen als numerisches Entwurfswerkzeug und zur parametrischen Quantifizierung von turbulenten Effekten.

Basierend auf der thermoakustischen Theorie von Rott werden analytische Korrelationen für die akustische Wellenausbreitung in Rohren und Kanälen mit konstanten und linearen Temperaturverteilungen abgeleitet. Die Modellierung berücksichtigt viskose und thermische Verluste, die auf die Wechselwirkung mit der Wand zurückzuführen sind. Bei konstanten Temperaturen ähneln die Gleichungen stark der Formulierung charakteristischer Wellen, erweitert um ein verlustbehaftetes, räumliches Abklingen. Lineare Temperaturgradienten werden unter der Annahme einer temperaturunabhängigen Viskosität untersucht. Die analytischen Zusammenhänge werden an einem einfachen Modell angewandt, das die akustische Impedanz eines $\lambda/4$ -Resonators vorhersagt. Als flexibleres Werkzeug für beliebige Temperaturprofile schlägt die Arbeit eine numerische Implementierung vor. Für die akustische Charakterisierung werden kompressible Strömungssimulationen durchgeführt. Die numerische Anregung wird über die Navier-Stokes charakteristische Randbedingung realisiert. Die Simulationen werden erfolgreich gegen semi-empirische Korrelationen validiert.

Der longitudinale Wärmeübergang innerhalb des Resonatorrohrs wird mit Hilfe der analytischen Modelle von Kurzweg für inkompressible Strömungen untersucht. Ein zusätzlicher Vergleich mit der thermoakustischen Theorie von Rott zeigt identische Ergebnisse an einem akustischen Druckknotenpunkt. Vereinfachungen der beiden Korrelationen erlauben eine umfassende Diskussion des Zusammenspiels zwischen hydrodynamischen und thermischen Grenzschichten. Der longitudinale thermische Transport ist maximal, wenn die thermische Grenzschicht annähernd die Mitte des Kanals erreicht. Unterteilt in sechs charakteristische Regime leitet die Arbeit qualitative Aussagen für den Wärmetransport in jeder Kombination von hydrodynamischer und thermischer Grenzschichtdicke ab.

Zur Untersuchung des Einflusses der Turbulenz auf den Wärmeübergang in pulsierenden Strömungen werden hochauflösende Large Eddy Simulationen eingesetzt. Die Arbeit betrachtet eine vollständig entwickelte turbulente inkompressible Strömung innerhalb eines periodischen Kanalbereiches. Bei großen Pulsationsamplituden mit ausgeprägter Strömungsumkehr zeigt sich ein signifikant erhöhter, wandnormaler Wärmetransport zwischen einer heißen und kalten Ka-

Kurzfassung

nalwand. Die numerischen Ergebnisse bestätigen experimentelle Untersuchungen und verdeutlichen die Bedeutung des erhöhten Wärmeübergangs als wichtigen Aspekt eines umfassenden Designprozesses technischer Anwendungen. Weitergehende numerische Untersuchungen zeigen, dass ebenso der longitudinale Wärmeübergang durch Turbulenz erhöht wird.

Vorwort

Die vorliegende Arbeit entstand an der Professur für Thermofluiddynamik der Technischen Universität München während meiner Tätigkeit als wissenschaftlicher Mitarbeiter. Diese wurde durch die Deutsche Forschungsgemeinschaft (DFG) im Rahmen des Sonderforschungsbereichs Transregio 40 (SFB TRR40) gefördert. Das Leibniz-Rechenzentrum (LRZ) gewährte Zugang zu seinen Rechenclustern.

Meinem Doktorvater, Professor Wolfgang Polifke, danke ich herzlichst für die spannende Zeit in seiner Forschungsgruppe und die damit verbundene Chance, diese Arbeit anfertigen zu dürfen. Neben seinem exzellenten fachlichen Rat und dem erfahrenen Blick fürs „Ganze“, genoss ich sein entgegengebrachtes Vertrauen und die vielen Freiräume auf dem Weg zur Promotion. Ich schätze sehr die unkomplizierte, pragmatische und offene Art der Zusammenarbeit, die insbesondere während meines letzten Jahres an der TFD, dem Corona-Jahr 2020, die herausfordernde Situation bestmöglichst gestaltete. Wenngleich die zuvor etablierten persönlichen Montagsmeetings, gemeinsamen Mittagsessen und Kaffeepausen mit dem Austausch von Alltäglichen, Zwischenmenschlichem und Privaten dennoch fehlten. Neben dem wertvollen fachlichen Feedback und den spannenden Diskussionen danke ich Professor Guillaume Penelet für die Übernahme des Koreferates sowie Herrn Prof. Dr.-Ing. Michael Zäh für seine Tätigkeit als Prüfungsvorsitzender.

Bei allen Kolleginnen und Kollegen der Professur für Thermofluiddynamik und des Lehrstuhls für Thermodynamik bedanke ich mich für die gute (Arbeits-)Atmosphäre. Camilo stand mir als Büro-Kollege stets als erster Ansprechpartner mit seiner langjährigen fachlichen Erfahrung beiseite. Für die geduldige und fachlich hervorragende Einarbeitung danke ich meinem TRR40-Vorgänger Kilian. Ebenso danke ich Alejandro für die Diskussion wichtiger Grundsteine, die bereits in der ersten Förderperiode des TRR40 gelegt wurden. Stellvertreten für alle Kolleginnen und Kollegen, mit denen sich über die spannenden und konstruktiven Gespräche hinaus auch gute Freundschaften entwickelt haben, nenne ich hier Felix, Johannes und Moritz. Neben der Forschung hat mir die Gestaltung und Durchführung der Lehre sowie das Arbeiten mit unzähligen Studenten immer viel Freude bereitet: Max, danke für die gemeinsame Zeit als „WTP-Affen“. Stellvertreten für das Sekretärinnen-Team danke ich Helga für die reibungslose organisatorische Unterstützung. Das Lehrstuhlleben mit den Mensarunden, Betriebsausflügen, Kneipentouren, Einstands- und Doktorfeiern fehlt mir schon jetzt. Danke für diese etwas verlängerte „Studentenzeit“.

Ich danke selbstverständlich meinen Eltern, Anna und Johan, für die Unterstützung auf dem gesamten, langen Ausbildungsweg, sowie meiner Schwester Lea für die vielen, schönen Besuche in München. Und ja Bruder Jona, Du warst schneller fertig!

Vorwort

Zu guter Letzt danke ich meiner wunderbaren Frau Kerstin für ihre Unterstützung und das Verständnis während unserem gemeinsamen Abenteuer „München“. Ich freue mich auf unseren kommenden Weg, wohin er uns auch führen mag. Danke!

Contents

1	Introduction	1
2	Duct Acoustics with Viscous and Thermal Dissipation	5
2.1	Revisiting the Literature	5
2.1.1	From the Navier-Stokes Equations to Isentropic Acoustic Characteristic Waves	5
2.1.2	Overview on Dissipative Acoustic Formulations	7
2.1.3	Rott's Thermoacoustic Theory	10
2.2	Characteristic Waves with Losses at Homogeneous Temperature	12
2.2.1	The General Derivation	13
2.2.2	Application to a Quarter-Wave Channel	16
2.3	Extending to Linear Temperature Profiles at Constant Kinematic Viscosity	18
2.3.1	The General Derivation	18
2.3.2	Application to a quarter-wave channel	21
2.4	Results	22
2.4.1	Parametric Set-Up	22
2.4.2	Evaluation of Eigenfrequencies	23
2.4.3	Evaluation of Pressure and Velocity Profiles	26
2.4.4	Validation	29
2.5	Summary and Conclusions on Duct Acoustics with Viscous and Thermal Dissipation	30
2.6	Outlook: Considerations on Exponential Temperature Profiles	31
2.7	Outlook: Pressure and Velocity Profiles for Higher Mode Orders	31
3	Modeling of an Acoustic Quarter-Wave Resonator	37
3.1	The Acoustic Resonator	37
3.1.1	Analytical Model by Laudien et al.	39
3.2	Novel and Spatially Resolved Model	40
3.3	Validation	41
3.4	Results	43
3.4.1	Parametric Set-Up	43
3.4.2	Evaluation of Reflection Coefficient and Impedance	43
3.4.3	Evaluation of Spatial Pressure and Velocity Profiles	47
3.5	Summary and Conclusions on the Novel Model of a Quarter-Wave Resonator .	57
4	Heat Transfer in Resonators	59
4.1	Summary of the Analytical Approaches	59

Contents

4.1.1	Effective Thermal Diffusivity by Kurzweg	60
4.1.2	Simplification to the Derivation of Kurzweg	62
4.1.3	Total Energy Flux by Rott	63
4.2	Analytical Transformation: Kurzweg vs. Rott	63
4.3	Discussion of the Formulations by Kurzweg and Rott	65
5	Contextualization and Discussion of Publications	69
5.1	Numerical Assessment of a Resonator with Temperature Inhomogeneities	69
5.2	Theoretical Considerations on Boundary Layer Interplay	70
5.3	The Effect of Turbulence on Heat Transfer	71
5.3.1	Enhancement of Wall-Normal Heat Transfer	72
5.3.2	Enhancement of Longitudinal Heat Transfer	72
6	Summary and Conclusions	75
6.1	Heat Transfer in Pulsating Flow and Its Impact on Temperature Distribution and Damping Performance of Acoustic Resonators	77
6.2	Acoustic Impedance of a Quarter-Wave Resonator with Non-Uniform Temperature	78
6.3	Enhanced Longitudinal Heat Transfer in Oscillatory Channel Flow – a Theoretical Perspective	79
6.4	Large Eddy Simulation of Enhanced Heat Transfer in Pulsatile Turbulent Channel Flow	80
6.5	Turbulence-Induced Enhancement of Longitudinal Heat Transfer in Oscillatory Channel Flow	81
Bibliography		81
List of Figures		89
Supervised Students		95
Appendix A Reproduction of Papers		97
A.1	Heat Transfer in Pulsating Flow and Its Impact on Temperature Distribution and Damping Performance of Acoustic Resonators	98
A.2	Acoustic Impedance of a Quarter-Wave Resonator with Non-Uniform Temperature	113
A.3	Enhanced Longitudinal Heat Transfer in Oscillatory Channel Flow – a Theoretical Perspective	121
A.4	Large Eddy Simulation of Enhanced Heat Transfer in Pulsatile Turbulent Channel Flow	140
A.5	Turbulence-Induced Enhancement of Longitudinal Heat Transfer in Oscillatory Channel Flow	155

1 Introduction

Thermoacoustic instabilities present a relevant challenge in designing diverse combustion applications as domestic heaters, gas turbines, or rocket engines (e.g., [1–3]). The fluctuating heat release of the combustion causes an unsteady thermal expansion of the gaseous working fluid and leads to spatial and temporal pressure and velocity variations: a state of disturbances that we – more intuitively – know as acoustic sound. The sound waves propagate inside the combustion chamber and are eventually reflected by the chamber walls or exit. When returning to the flame, the reflected waves themselves now influence the combustion process. Thereby, the thermoacoustic feedback loop may lead to very large pressure and velocity fluctuations. The resulting structural and thermal loads may exceed the safety margins and lead to the breaking or melting of liners or face plates (see Fig. 1.1). Prevention of such catastrophic failures requires a thoughtful design process of many combustion applications.

One measure to ensure safe operating conditions is installing resonators to increase acoustic dissipation and suppress the thermoacoustic feedback [4, 5]. Figure 1.2 exemplarily shows the L-shaped quarter-wave resonator of a Vulcain 2 engine (main stage of the Ariane 5 rocket). For efficient performance, the eigenfrequency of the resonator needs to be tuned to the potentially unstable modes. However, a change in temperature leads to a change in the speed of sound and thus may detune the resonator. In general, the resonator design according to the undamped system is not sufficient. Instead, the coupled system of the chamber and the resonators has to be taken into account [6]. The detuning is particularly critical because a coupled analysis of combustion chamber and resonator elements shows a high sensitivity of the global stability with regard to the damping characteristics of the resonator [7]. This underlines the importance of precise acoustic characterization for a safe design of the engine. Numerous corresponding studies are of analytical (e.g., [8, 9]), experimental (e.g., [8, 10]), or numerical (e.g., [11, 12]) nature.

In a rocket engine combustion chamber, the resonator may not be treated as a decoupled element: On one hand, the damping performance of a quarter-wave resonator depends on the underlying temperature distribution of the gaseous working fluid (e.g., [9, 12]). On the other hand, the amplitude of the acoustic fluctuations influences the local heat transfer. The heat transfer – in turn – affects the local temperature distribution and illustrates the necessity of a more sophisticated and coupled analysis. Therefore, the present thesis focuses on two conceptual problems:

First, the thesis investigates the acoustic characterization of quarter-wave resonators via analytical considerations and via the development of a numerical tool. The analytical study is based on Rott's thermoacoustic approximation [13], a framework that accounts for viscous and thermal dissipation in one-dimensional duct acoustics. It offers a compact expression for the acoustic reflection. Furthermore, it provides valuable insight into the physical interplay of the hydrodynamic and thermal boundary layer that drives convective heat transfer. However, Rott's analytical framework is restricted to specific temperature profiles at constant viscosity. To over-



Figure 1.1: Damages of a combustor face plate due to thermoacoustic instability.¹



Figure 1.2: L-shaped quarter-wave resonator in a Vulcain 2 engine.²

come these limitations, the use of a numerical framework offers a more flexible approach at the disadvantage of computational cost. To avoid the excessive parametric investigation of each frequency, the use of System Identification (SI) techniques allows a broadband evaluation during one single simulation run.

Second, the present thesis focuses on the more fundamental investigation of heat transfer in turbulent, pulsating flows. Conditions typical for the flow inside rocket engine combustion chambers are commonly reported to provoke significant heat transfer enhancement (e.g., [4, 14–26]). However, the literature offers contradictory findings for the problem at hand, and high fidelity numerical investigations on the topic are rare. The present thesis classifies two relevant heat transfer mechanisms inside a combustion chamber: wall-normal heat transfer (e.g., between the hot combustion gas and the cooled chamber wall) and heat transfer longitudinal to the acoustic oscillation (e.g., in axial direction of a resonator tube). For both mechanisms, high-fidelity numerical studies reveal for the first time significant turbulence-induced enhancement of more than 100% based on Large Eddy Simulation (LES). These results are in line with previous studies of thermoacoustic instabilities that may lead to the fatal thermal destruction of rocket engine combustion chambers.

Parts of the results reported in this thesis have already been presented at conferences or in journals, book chapters, and reports. Appendix A reproduces the major publications. The present publication-based dissertation guides through these publications by summarizing the most important results, embedding them in the literature context, and – most importantly – showing the interconnections between them (see Chapter 5). Furthermore, the methodology of the thesis elucidates fundamental consideration of acoustic dissipation in duct and channels, the derivation of an analytical model for a quarter-wave resonator, and more general findings regarding heat transfer in duct acoustics (see Chapter 2 - 4).

The first part of the thesis provides the methodology based on the existing literature and con-

¹Reproduced with kind permission of Dr. Tim Lieuwen

²Reproduced with kind permission of Dr. Kilian Förner

tributes the following novelties: Chapter 2 presents the theoretical background on fluid mechanics of acoustics. Based on Rott's thermoacoustic theory [13], a dissipative duct acoustic formulation at constant and linear temperature profiles is derived and discussed. Chapter 3 uses the previous derivations to model an acoustic quarter-wave resonator analytically. Chapter 4 focuses on heat transfer in laminar, oscillating channel flows that mimic a quarter-wave resonator: Two analytical approaches by Rott [13] (thermoacoustic) and Kurzweg [27] (incompressible channel flow) are compared.

The second part of the thesis guides through the major publications connected to this dissertation (Chapter 5). Thereby, the individual publications stand for themselves and can also be approached outside the framework of this dissertation. In addition, the thesis shows their interconnections and their relevance within the present Ph. D. project: Section 5.1 discusses a numerical investigation on the effect of temperature inhomogeneities inside a resonator tube. It follows a comprehensive interpretation of the interplay between hydrodynamic and thermal boundary layers follows (Sec. 5.2). Section 5.3 focuses on the impact of turbulence on heat transfer. First, wall-normal heat transfer enhancement in a pulsating channel flow is investigated via Large Eddy Simulation. In a second step, the numerical framework is adopted to study the longitudinal enhancement in an oscillating flow.

Chapter 6 summarizes the thesis and gives the conclusions of the investigations. Furthermore, it lists the attached papers and clearly states the authors' contributions. Appendix A reproduces the papers.

Introduction

2 Duct Acoustics with Viscous and Thermal Dissipation

This chapter begins with the introduction of the compressible Navier-Stokes equations. The set of conservation equations that uncontroversially states the fundamentals of fluid mechanics. Most of the subsequent work is based on these equations: In Sec. 2.1.1, the assumption of an isentropic flow in a one-dimension channel or duct (e.g., a quarter-wave tube) leads to the description via two characteristic acoustic waves, known as the Riemann invariants. Likewise, all numerical simulations (e.g., Direct Numerical Simulation (DNS) for a compressible, laminar flow (Sec. 5.1) and Large Eddy Simulation (LES) for an incompressible, turbulent flow (Sec. 5.3.1 and 5.3.2) are based on the Navier-Stokes equations. Existing frameworks that account for dissipative viscous and thermal wall interaction are outlined in Sec. 2.1.2. In the course of this thesis, the subsequent Chapter 3 will focus in more detail on the crucial importance of boundary layers and their dissipative effects on the overall acoustic damping performance of a resonator tube. Rott's thermoacoustic theory (Sec. 2.1.3) serves as the basis for the further analytical examinations: Section 2.2 derives a characteristic solution for spatially constant temperatures; Section 2.3 extends to linear temperature gradients. As an important limitation, the presented approach is only valid if the kinematic viscosity of the fluid does not change with temperature. Both formulations – for constant and linear temperature profiles, respectively – are applied to a quarter-wave channel with one open and one closed end. Section 2.4 discusses the resulting eigenfrequencies as well as the pressure and velocity profiles inside the channel. The conclusions (Sec. 2.5) directly link to applying the presented method to the modeling approach of a quarter-wave resonator in the following Chapter 3. For completeness, Secs. 2.6 and 2.7 outline a solution method for exponential temperature profiles and display pressure and velocity profiles for higher mode orders.

2.1 Revisiting the Literature

2.1.1 From the Navier-Stokes Equations to Isentropic Acoustic Characteristic Waves

The *Navier-Stokes equations* present the fundamental framework of conservation equations that model the motion of viscous Newtonian fluids. The general formulation considers compressible fluids with no external forces and is well described in the literature (see e.g., [28–30]).

The Navier-Stokes equations contain the conservation of mass and momentum via the *continuity* and the *momentum equation*. Formulated in the Einstein notation for the Cartesian coordinates with space direction x_i , the differential equations that couple density ρ , velocity u_i , and pressure

p read:

$$\frac{d\rho}{dt} + \rho \frac{\partial u_i}{\partial x_i} = 0 \quad (2.1)$$

and

$$\rho \frac{du_i}{dt} = -\frac{\partial p}{\partial x_i} + \frac{\partial p}{\partial x_j} \left(2\mu S_{ij} - \frac{2}{3}\mu \frac{\partial u_k}{\partial x_k} \delta_{ij} \right), \quad (2.2)$$

where t is the time and μ is the (dynamic) viscosity of the fluid. The material derivative $d \cdot / dt$ is defined as $d \cdot / dt = \partial \cdot / \partial t + u_i \partial \cdot / \partial x_i$, and the strain rate tensor S_{ij} reads $S_{ij} = 1/2(\partial u_i / \partial x_j + \partial u_j / \partial x_i)$.

The *energy equation* completes the above set of differential equations (Eqs. (2.1) and (2.2)):

$$\rho \frac{de}{dt} = -p \frac{\partial u_i}{\partial x_i} + 2\mu S_{ij} S_{ij} - \frac{2}{3}\mu S_{kk} S_{ii} + \frac{\partial}{\partial x_i} \left(k \frac{\partial T}{\partial x_i} \right), \quad (2.3)$$

where e denotes the internal energy, T the temperature, and k the thermal conductivity of the fluid. This additional equation is typically required to incorporate compressibility and heat transfer, two key effects of the present study.

The closure of the Navier-Stokes equations requires two additional equations of state: The ideal gas relation yields:

$$p = \rho RT, \quad (2.4)$$

where R denotes the specific gas constant. The relation between the internal energy e and the temperature reads:

$$e = \int c_v dT = \int c_p dT - \frac{p}{\rho}, \quad (2.5)$$

where c_v and c_p denote the specific heat capacity at constant specific volume and constant pressure, respectively.

The following considerations will develop the above and more general derivations towards the acoustic characteristics. A detailed introduction to acoustics may, for example, be found in the textbook by Rienstra and Hirschberg [31]. The assumption of isentropic acoustic perturbations simplifies the momentum equation (2.2) to the inviscid *Euler equation*

$$\rho \frac{du_i}{dt} + \frac{\partial p}{\partial x_i} = 0. \quad (2.6)$$

Many acoustical applications are characterized by small disturbances q' compared to the temporal mean q_m , decomposing a varying quantity q as $q = q_m + q'$. Considering only the fluctuating parts of the continuity and the inviscid momentum equation ((2.1) and (2.6), respectively) and neglecting higher order terms yields:

$$\frac{d_m \rho'}{dt} + \rho_m \frac{\partial u'_i}{\partial x_i} = 0 \quad (2.7)$$

and

$$\rho_m \frac{d_m u'_i}{dt} + \frac{\partial p'}{\partial x_i} = 0, \quad (2.8)$$

where $d_m \cdot / dt$ denotes the material derivative with respect to the mean flow $u_{m,i}$.

In the case of isentropic compression, which is given in lossless acoustics flows, the fluctuation in pressure p' and density ρ' correlate linearly via

$$p' = \left. \frac{\partial p}{\partial \rho} \right|_s \rho' = c^2 \rho' , \quad (2.9)$$

where $c = \sqrt{\gamma RT_m}$ is the *speed of sound* and $\gamma = c_p/c_v$ denotes the heat capacity ratio.

Finally, the *wave equation* results from Eqs. (2.7), (2.8), and (2.9) and only obtains the unknown pressure fluctuation:

$$\frac{d_m^2 p'}{dt^2} - c^2 \frac{\partial^2 p'}{\partial x_i \partial x_i} . \quad (2.10)$$

For one-dimensional plane acoustic waves, the wave equation can be factorized:

$$\left(\frac{d_m}{dt} + c \frac{\partial}{\partial x_i} \right) \left(\frac{d_m}{dt} - c \frac{\partial}{\partial x_i} \right) p' = 0 . \quad (2.11)$$

The resulting equation reveals two independent convection equations: One wave travels downstream and the other upstream with a velocity of $c \pm u_m$, respectively. The Riemann invariants describe the corresponding characteristic waves (f and g -wave):

$$f = \frac{p'}{\rho_m c} + u' \quad (2.12)$$

and

$$g = \frac{p'}{\rho_m c} - u' . \quad (2.13)$$

The reverse relation for the fluctuation in pressure p' and velocity u' directly follows:

$$\frac{p'}{\rho_m c} = \frac{1}{2} (f + g) \quad (2.14)$$

and

$$u' = \frac{1}{2} (f - g) . \quad (2.15)$$

2.1.2 Overview on Dissipative Acoustic Formulations

In 1868, Kirchhoff [32] formulated an exact solution to the propagation of sound in a uniform circular tube. He considered an ideal gas and accounted for both effects of viscosity and thermal conductivity. Stinson [33] gave a valuable overview of the method by Kirchhoff. However, the analytical correlations are complex, and solving for the specific acoustic profiles requires the use of numerical methods. Although the approach by Kirchhoff is generally valid, numerous researchers introduced simplifications.

Many of these methods are based on a separate treatment of viscous and thermal effects, which are subsequently superimposed (e.g., Zwicker and Kosten [34] or Kinsler and Frey [35]). Others suggest mathematical simplifications for different limiting cases (e.g., for narrow or wide

channels, Stinson [33]). Therefore, the geometrical restriction of Kirchhoff's original solution may be relaxed (i.e., the circular shape of the tube).

In their textbook “Fundamentals of Acoustics”, Kinsler and Frey [35] dedicated one chapter to the “Absorption and Attenuation of Sound”. They divided the dissipation sources into two general categories: “(i) those intrinsic to the medium and (ii) those associated with the boundaries of the medium”. Losses in the medium specify viscous losses, heat conduction losses, and further internal molecular processes that are all independent of an external influence (e.g., a wall). For this literature review and the scope of the thesis (i.e., viscous losses generated at the resonator walls), the focus lies on the latter category. It particularly lies on losses attributed to the fluid-wall interaction and the associated viscous and thermal boundary layers.

For either category, Kinsler and Frey [35] formulated a *spatial absorption coefficient* and a *complex-valued wavenumber*.¹ In general, the spatial absorption coefficient depends on frequency (e.g., frequency changes the boundary layer thickness). The *phase speed* c_p describes the velocity of a perturbation at a certain frequency. In this context, Kinsler and Frey [35] discussed the concept of a *complex-valued speed of sound* for mono-frequent acoustic waves. As part of this thesis, the subsequent derivations of characteristic waves will also lead to a complex-valued wavenumber and a complex-valued speed of sound (see Sec. 2.2).

Kinsler and Frey [35] analyzed losses at rigid walls for dissipative duct and channel flows via boundary layer theory. As a specific example, they discussed losses in wide pipes where boundary layers are much smaller than the tube diameter. Fluid disks with boundary layers were used to describe the local flow properties. Viscous and thermal losses were considered separately and recombined by superposition of the individual absorption coefficient.

Kinsler and Frey's remarkable conclusions included that “the presence of the viscous boundary layer also modifies the phase speed of the acoustic wave” [35]. This leads to a distortion of a broadband signal or a (complex-valued) speed of sound for mono-frequent excitation. Furthermore, the *reactance* (a comprehensive definition and application follows in Chapter 3) is affected by the viscosity, such that “the apparent mass of the fluid disk is slightly larger. This is equivalent to the fluid having a slightly greater density.”

Numerous authors presented very similar or even identical approaches and formulations to Kinsler and Frey [35] (compare, e.g., the textbook “Acoustics - An Introduction to Its Physical Principles and Applications” by Pierce [36]).

Keefe [37] considered a smooth cylindrical duct and emphasized the exact nature of Kirchhoff's derivation [32]. As a novelty, his work offered approximations that also hold with good accuracy in the critical transition zones (boundary layers in the order of magnitude of the tube diameter). If the acoustic frequency is sufficiently low, there is only a single plane mode that travels over axial distances that are large compared to the tube diameter. Considering isothermal walls, Keefe [37] related the pressure and volume flow rate oscillations via the acoustic *series impedance* and the *shunt admittance*. In their combination, they yield the complex-valued *characteristic impedance* and the *propagation wavenumber*. Again, there is a close similarity to nu-

¹Both definitions will reappear during the derivations of Sec. 2.2 and are therefore not closer specified in the present section. Also, further characteristics (e.g., of the acoustic impedance, reactance, etc.) that are only briefly introduced in the present literature review, will be presented in more detail alongside their mathematical definitions throughout the later course of this work.

merous previous definitions where the losses drive a spatial decay (mathematically described by a complex-valued wavenumber or (alternatively) by a complex-valued phase velocity or speed of sound, e.g., Kinsler and Frey [35]).

As a final remark on the work by Keefe [37], it is worth to mention the physical interpretation of the real- and imaginary-valued part of the series impedance and the shunt admittance: He interpreted these four parameters in the same way as Rott and Swift [38] (introduced in Sec. 2.1.3) as the *inertance*, *resistance*, *compliance*, and *conductance*. Thus, the selected conservation equations of this thesis based on Rott's framework will also be identical to those by Keefe [37].

The studies of Hynninen and Abom [39, 40] built on Keefe's formulations [37] and connected the framework of acoustic losses with transfer/scattering matrices and the idea of traveling waves. Viscous friction and heat exchange with a solid substrate generated the losses. The substrate was modeled as an aggregation of capillary tubes via a specific impedance. Similar to Kinsler and Frey's work [35], Hynninen and Abom [39, 40] derived a complex-valued speed of sound and a complex-valued density.

Until today, the research on boundary layer losses in the characteristic wave framework (see Sec. 2.1.3) is limited. Indeed, Hynninen and Abom [39, 40] only implicitly pointed in this direction: They formulated a *transfer matrix* and formally gave instructions to derive the *scattering matrix*. The scattering matrix related the upstream and downstream traveling pressure waves, which closely compare to the characteristic *f* and *g*-waves. However, there was neither a clear statement of how these relations were used nor a physical discussion of the spatial perturbations.

Gobin [41] gave a first review and formulation that centrally focused on characteristic waves with losses. In line with all the previous authors, the problem at hand was tackled via the mathematical use of a complex-valued wavenumber. In contrast to the following derivations of the present thesis (see Sec. 2.2), the study by Gobin allowed for a non-zero mean flow that led to propagation velocities at $c_p \pm u_m$. In agreement with Kinsler and Frey [35], the speed of sound was interpreted as a decreased (complex-valued) phase velocity.

Gobin referenced Kinsler and Frey's formulations [35] to determine the loss-related (imaginary-valued) component of the wavenumber. The characteristic *f* and *g*-waves corresponded to the respective traveling pressure perturbations (compare Hynninen and Abom [39, 40]). In a final step, Gobin formulated a transfer matrix to couple the pressure and velocity perturbations (p' and u' , respectively) at the in- and outlet of a duct.

However, Gobin stated a constant factor of ρc between pressure p' and velocity u' . This contradicts prior conclusions by Kinsler and Frey [35], who found that viscous and thermal dissipation will increase local density. Alternatively, in a more intuitive interpretation, pressure gradients need to increase to compensate for the friction and to maintain constant velocity amplitudes. This missing correction in the study by Gobin [41] will show in the subsequent derivation of the present thesis (see Sec. 2.2).

2.1.3 Rott's Thermoacoustic Theory

In 1980, Rott introduced a (thermo-)acoustic approximation for channel flows [13, 38]. As a first and important difference to the inviscid and isentropic derivations presented in Sec. 2.1.1, Rott's theory includes the viscous and thermal impact of the surrounding walls on the fluid, a crucial aspect for the dissipating characteristics of an acoustic resonator (see Chapter 3). The second difference lies in the more general perspective that allows axial temperature gradients, a crucial aspect for the occurrence of heat transfer (see Chapter 4). This section outlines the fundamentals of Rott's approximation that are of relevance throughout the course of this thesis.

The work by Rott included the following assumption:

- an ideal gas is assumed (consistent with the isentropic derivations in Sec. 2.1.1),
- the flow is laminar and without mean-flow (i.e., in comparison to the more general formulation of Sec. 2.1.1, $u_m = 0$ is assumed as an addition constraint),
- the wall temperature is spatially non-uniform but temporally constant (i.e., its heat capacity is very large compared to the gaseous working fluid), and
- the acoustic wavelength is (much) larger than the displacement amplitude and the boundary layer thickness.

The last assumption allows to consider the diffusive effects imposed by the geometry via two integrated parameters f_v and f_κ (for hydrodynamic and thermal wall-effects, respectively). Thereby, the longitudinal velocity oscillations are described by the cross-sectional volume flow rate since the velocity profile varies in wall-normal direction.

Periodical and sinusoidal oscillations of a (in the acoustic framework small) quantity q are classically defined as

$$q(t) = q_a \cos(\omega t + \varphi), \quad (2.16)$$

where $\omega = 2\pi f$ denotes the angular frequency and f the (ordinary) frequency. The amplitude of the oscillation q_a and the temporal phase of the oscillation φ are arbitrary constants that depend on the initial conditions of the problem at hand. Oftentimes, it is more convenient to rewrite Eq. (2.16) in the complex notation

$$q(t) = \operatorname{Re} \left[q_1 e^{i\omega t} \right], \quad (2.17)$$

where the complex-valued amplitude q_1 combines the two prior parameters q_a and φ such that the absolute of q_1 is $|q_1| = q_a$ and its respective phase is $\angle q_1 = \varphi$. The subscript 1 denotes the first-order characteristic of the small parameter q_1 itself (whereas e.g., “small squared” terms are called second-order). The identity $e^{i\alpha} = \cos \alpha + i \sin \alpha$ exploits the definition of the exponential function with imaginary-valued input arguments (i.e., $i = \sqrt{-1}$).

Rott introduced the complex-valued pressure and velocity amplitudes p_1 and u_1 as the respectively primary acoustic variables. Furthermore, the volume flow rate U_1 calculates the integral

of the velocity u_1 over the cross-sectional area A of the channel. Rott summarized all relevant variables and parameters as follows:

$$\begin{aligned}
 p &= p_m + \operatorname{Re} [p_1(x) e^{i\omega t}] \\
 U &= \operatorname{Re} [U_1(x) e^{i\omega t}] \\
 u &= \operatorname{Re} [u_1(x, y, z) e^{i\omega t}] \\
 T &= T_m(x) + \operatorname{Re} [T_1(x, y, z) e^{i\omega t}] \\
 \rho &= \text{similar to } T \\
 \nu &= \nu(x) \\
 c, \kappa, \text{ etc.} &= \text{similar to } \nu,
 \end{aligned} \tag{2.18}$$

where $\nu = \mu/\rho$ denotes the kinematic viscosity and $\kappa = k/(\rho c_p)$ the thermal diffusivity.

Note the spatially uniform mean temperature T_m throughout the first derivations in Sec. 2.2. Thus, for an ideal gas, the density ρ_m is also constant in space. In the later course of the thesis, this restriction is relaxed to linear and exponential temperature profiles $T_m(x)$ (Sec. 2.3 and 2.6, respectively). However, these derivations are only valid for (theoretical) fluids with constant kinematic viscosity $\nu \neq \nu(T)$.

Considering the boundary conditions at the wall surfaces and integrating the velocity u_1 over the channel cross-section to obtain the volume flow rate U_1 yields the momentum equation of Rott's acoustic approximation:

$$dp_1 = -\frac{i\omega\rho_m dx/A}{1-f_\nu} U_1, \tag{2.19}$$

with the alternative formulation:

$$\frac{\partial(U'/A)}{\partial t} \frac{\rho_m}{a^*} + \frac{\partial p'}{\partial x} = 0, \tag{2.20}$$

where the parameter $a^* = 1 - f_\nu$ is introduced for a more compact notation. The mean temperature gradient dT_m/dx does not affect the momentum equation.

The derivation of the continuity equation follows a similar (though slightly more complicated) procedure and requires the mean cross-sectional temperature. For arbitrary cross sections, it reads:

$$dU_1 = -\frac{i\omega A dx}{\gamma\rho_m} [1 + (\gamma - 1)f_\kappa] p_1 + \frac{(f_\kappa - f_\nu)}{(1 - f_\nu)(1 - \operatorname{Pr})} \frac{dT_m}{T_m} U_1, \tag{2.21}$$

with the alternative formulation:

$$\frac{\partial p'}{\partial t} \frac{b^*}{\gamma p_m} + \frac{\partial(U'/A)}{\partial x} - \frac{d^*}{T_m} \frac{dT_m}{dx} (U'/A) = 0, \tag{2.22}$$

where the parameters $b^* = [1 + (\gamma - 1)f_\kappa]$ and $d^* = [(f_\kappa - f_\nu)] / [(1 - f_\nu)(1 - \operatorname{Pr})]$ are introduced for a more compact notation.

The functions f_v and f_κ are known for different geometries [38]. For a channel flow (channel width of $2r_h$), they read:

$$f_{v/\kappa} = \frac{\tanh[(1+i)r_h/\delta_{v/\kappa}]}{(1+i)r_h/\delta_{v/\kappa}}. \quad (2.23)$$

For a circular duct, $f_{v/\kappa}$ are defined as

$$f_{v/\kappa} = \frac{2J_1\left[(i-1)\frac{2r_h}{\delta_{v/\kappa}}\right]}{J_0\left[(i-1)\frac{2r_h}{\delta_{v/\kappa}}\right](i-1)\frac{2r_h}{\delta_{v/\kappa}}}, \quad (2.24)$$

where J_0 and J_1 are Bessel functions (first kind) of the zeroth and first order, respectively. The hydraulic radius is denoted by

$$r_h \equiv \frac{A}{\Pi}, \quad (2.25)$$

where A denotes the cross-sectional area of the channel and Π its perimeter.

The hydrodynamic boundary layer thickness δ_v (also known as “Stokes boundary layer”) is

$$\delta_v = \sqrt{2\nu/\omega} \quad (2.26)$$

and its thermal analog δ_κ is

$$\delta_\kappa = \sqrt{2\kappa/\omega}. \quad (2.27)$$

They describe the respective hydrodynamic and thermal penetration depth of wall-effects on oscillatory flows.

The *Prandtl number* Pr defines the ratio of momentum diffusivity to thermal diffusivity:

$$\text{Pr} \equiv \frac{\nu}{\kappa}. \quad (2.28)$$

Thereby it also relates the hydrodynamic and thermal boundary layer thickness of Eqs. (2.26) and (2.27).

All further derivations in the subsequent course of this chapter will be based on the conservation equations of Rott’s thermoacoustic theory as presented above.

2.2 Characteristic Waves with Losses at Homogeneous Temperature

This section applies the derivation of the Riemann invariants (as presented by Polifke et al. [42]) to the conservation equations of Rott’s thermoacoustic theory [38]. In agreement with the work by Rott, the velocity profile has no mean flow. This first instance of derivation considers a spatially uniform temperature profile for a channel with a constant cross-sectional area. The extension to linear temperature profiles follows in Sec. 2.3.

The derivation in Sec. 2.2.1 yields a general solution independent from the additional boundary and initial conditions. Section 2.2.2 elaborates on the specific solution for a quarter-wave channel. Results for the uniform temperature are presented alongside those for linear temperature profiles in Sec. 2.4.

2.2.1 The General Derivation

Polifke et al. [42] presented linear partial differential equations with two variables

$$\mathbf{A}\mathbf{u}_x + \mathbf{B}\mathbf{u}_t = 0 , \quad (2.29)$$

where the subscripts $_x$ and $_t$ denote the derivatives in space and time, respectively.

Using the perfect gas law $p_m = \rho_m RT_m$ and the speed of sound $c = \sqrt{\gamma RT_m}$, Rott's conservation equation (Eqs. (2.20) and (2.22), [38]) are rewritten and rearranged:

$$\frac{d\left(\frac{p'}{\rho_m c}\right)}{dx} + \frac{1}{a^* c} \frac{d\left(\frac{U'}{A}\right)}{dt} = 0 \quad (2.30)$$

and

$$\frac{d\left(\frac{U'}{A}\right)}{dx} + \frac{b^*}{c} \frac{d\left(\frac{p'}{\rho_m c}\right)}{dt} = 0 , \quad (2.31)$$

where the constants a^* and b^* incorporate the effects of viscous and thermal boundary layers (compare to the definition in Sec. 2.1.3). Note the omission of the term that includes the local temperature gradient in the continuity equation. This significantly simplifies the problem at hand. Thereby, the mathematical form of Rott's conservation equations is identical to those of numerous researchers (e.g., Keefe [37], compare Sec. 2.1.2).

The corresponding matrices \mathbf{A} and \mathbf{B} and the vector \mathbf{u} read:

$$\mathbf{A} = \begin{bmatrix} 1 & 0 \\ 0 & 1 \end{bmatrix} , \quad (2.32)$$

$$\mathbf{B} = \begin{bmatrix} 0 & \frac{1}{a^* c} \\ \frac{b^*}{c} & 0 \end{bmatrix} , \quad (2.33)$$

and

$$\mathbf{u} = \begin{bmatrix} \frac{p'}{\rho_m c} \\ \frac{U'}{A} \end{bmatrix} . \quad (2.34)$$

In particular, the vector \mathbf{u} strongly resembles the definition in the derivation by Polifke et al. [42]: Merely the velocity u' is replaced by the spatially averaged velocity over the cross-sectional area U'/A . (Since u' locally varies in wall-normal due to boundary effects.)

The eigenvalues λ and eigenvectors \mathbf{s} of this problem ($\mathbf{A}^T \mathbf{s} = \lambda \mathbf{B}^T \mathbf{s}$) are:

$$\lambda_{\pm} = \pm c \sqrt{\frac{a^*}{b^*}} \quad (2.35)$$

and

$$\mathbf{s}_{\pm} = \begin{bmatrix} 1 \\ \pm \sqrt{\frac{1}{a^* b^*}} \end{bmatrix} . \quad (2.36)$$

According to Polifke et al. [42], the problem is of *hyperbolic type* if the eigenvalues λ_{\pm} are real-valued. This is required to reduce the system to the *characteristic normal form*. Although the eigenvalues λ_{\pm} are not real-valued in the present work², the corresponding reduction yields:

$$\frac{d}{dt} \frac{p'}{\rho_m c} \pm \sqrt{\frac{1}{a^* b^*}} \frac{d}{dt} \frac{U'}{A} = 0 \quad (2.37)$$

and is valid along the characteristics propagating at

$$\frac{dx}{dt} = \pm c \sqrt{\frac{a^*}{b^*}}. \quad (2.38)$$

Note at this point: Without dissipation (f_v and $f_k \rightarrow 0$), the acoustic disturbances would propagate into the positive and negative direction at the speed of sound c . With dissipation, a complex-valued speed of sound (e.g., c_p , compare Sec. 2.1.2) reappears and it is smaller (in the absolute and real part) than the lossless speed of sound c . The characteristic wave amplitudes (that now vary in space) read:

$$f = \frac{p'}{\rho_m c} + \sqrt{\frac{1}{a^* b^*}} \frac{U'}{A} \quad (2.39)$$

and

$$g = \frac{p'}{\rho_m c} - \sqrt{\frac{1}{a^* b^*}} \frac{U'}{A}. \quad (2.40)$$

From the present state of understanding and the mathematical perspective, the independence of f and g is maintained. In particular, for uniform temperature distributions, an upstream traveling f -wave does not scatter to a downstream traveling g -wave, and vice versa.

In alignment with the procedure described in Polifke et al. [42], the Riemann invariants are interpreted as harmonic (and now spatially decaying) waves and introduce

$$\frac{p'}{\rho_m c} = \hat{P} e^{(i\omega t - ik_x x)} \quad (2.41)$$

and

$$\frac{U'}{A} = \hat{U} e^{(i\omega t - ik_x x)}. \quad (2.42)$$

Note that the wavenumber k_x may be complex-valued to model a spatially decaying behavior attributed to viscous and thermal losses. Introducing the definition of the wavenumber $k = \omega/c$ to describe the harmonic oscillation of an inviscid and non-heat-conducting reference, Eqs. (2.30) and (2.31) reduce to matrix notation

$$\begin{bmatrix} kb^* & -k_x \\ -k_x & k/a^* \end{bmatrix} \begin{bmatrix} \hat{P} \\ \hat{U} \end{bmatrix} = \begin{bmatrix} 0 \\ 0 \end{bmatrix}, \quad (2.43)$$

where \hat{P} and \hat{U} are constant amplitudes at a reference position $x = 0$.

²Despite the complex-valued eigenvalues the characteristic waves are independent. However, as it will become apparent in the course of the present section, they exhibit a spatial decay.

The determinant of the above matrix is zero if

$$k_{x\pm} = \pm k \sqrt{\frac{b^*}{a^*}} . \quad (2.44)$$

Reinserting the expression of the complex-valued wavenumber $k_{x\pm}$ into the matrix equation above yields the ratio of the amplitudes \hat{P} and \hat{U} :

$$\hat{U} = \pm \sqrt{a^* b^*} \hat{P} . \quad (2.45)$$

Note: At this point, the increased density (or equivalently pressure) that was predicted by Kinsler and Frey [35] shows in the presence of losses: Without any viscous or thermal dissipation (f_v and $f_k \rightarrow 0$), the factor between velocity u' and pressure p' is $\rho_m c$. With losses, the square-root expression is smaller than 1, indicating the increase in the pressure-to-velocity ratio (an increased pressure is required to compensate the losses). Gobin [41] did not consider this factor in his thesis (compare Sec. 2.1.2).

The amplitudes of the upstream and downstream traveling waves are defined as $\hat{P}_+ \equiv \hat{F}/2$ and $\hat{P}_- \equiv \hat{G}/2$ to obtain the solutions

$$\begin{aligned} \frac{p'}{\rho_m c} &= \frac{f}{2} + \frac{g}{2} \\ &= \frac{\hat{F}}{2} e^{(i\omega t - ik_{x+}x)} + \frac{\hat{G}}{2} e^{(i\omega t - ik_{x-}x)} \end{aligned} \quad (2.46)$$

and

$$\begin{aligned} \frac{U'}{A} &= \sqrt{a^* b^*} \left(\frac{f}{2} - \frac{g}{2} \right) \\ &= \sqrt{a^* b^*} \left(\frac{\hat{F}}{2} e^{(i\omega t - ik_{x+}x)} - \frac{\hat{G}}{2} e^{(i\omega t - ik_{x-}x)} \right) . \end{aligned} \quad (2.47)$$

Along the characteristic $\frac{dx}{dt} = \pm c \sqrt{a^*/b^*}$, the term $\omega t - k_{x\pm}x$ (argument to the exponential function) is constant. Integration of the characteristic yields:

$$x(t) = \pm c \sqrt{\frac{a^*}{b^*}} t + C_\pm , \quad (2.48)$$

where C_\pm is a constant. Rewriting the (temporal and spatial dependent) exponent yields:

$$\omega t - k_{x\pm}x = k \sqrt{\frac{b^*}{a^*}} C_\pm = \text{const.} , \quad (2.49)$$

and shows that the latter expression neither depends on the time t nor the axial location x .

The final expression for the Riemann invariants f and g for the one-dimensional system with viscous and thermal dissipation (no mean flow, no temperature gradient, isothermal walls) for

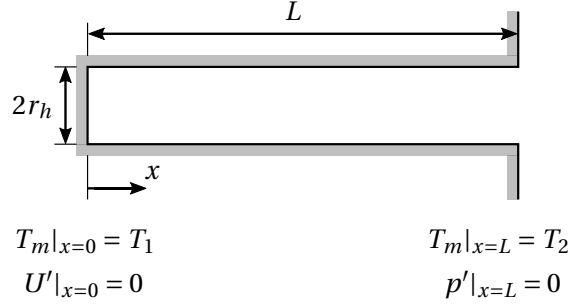


Figure 2.1: Geometry and boundary conditions of a quarter-wave channel.

the acoustic pressure and velocity (averaged over the cross-sectional area) read:

$$\begin{aligned}
f &= \hat{F} \exp(i\omega t - ik_{x+}x) \\
&= \hat{F} \exp\left(k \sqrt{\frac{b^*}{a^*}} C_+\right) \\
&= \hat{F} \exp\left(i\omega \left[t - \sqrt{\frac{b^*}{a^*}} \frac{x}{c}\right]\right).
\end{aligned} \tag{2.50}$$

and

$$\begin{aligned}
g &= \hat{G} \exp(i\omega t - ik_{x-}x) \\
&= \hat{G} \exp\left(k \sqrt{\frac{b^*}{a^*}} C_-\right) \\
&= \hat{G} \exp\left(i\omega \left[t + \sqrt{\frac{b^*}{a^*}} \frac{x}{c}\right]\right).
\end{aligned} \tag{2.51}$$

Finally, note the perfect consistency between the “conventional” characteristic formulation in [42] and the present equations for the inviscid and non-heat-conducting limiting case when neither hydrodynamic nor thermal boundary layers exist and the parameters a^* and b^* approach unity: $a^* \rightarrow 1$ and $b^* \rightarrow 1$. This implies that:

1. the complex-valued wavenumber $k_{x\pm}$ reduces to the real-valued wavenumber $k = \omega/c$,
2. the complex-valued phase speed that defines the characteristic dx/dt reduces to the real-valued speed of sound $c = \sqrt{\gamma RT_m}$, and that
3. the friction-induced increase in pressure vanishes ($\hat{U} = \pm \hat{P}$).

2.2.2 Application to a Quarter-Wave Channel

In this section, the equations derived in Sec. 2.2.1 (characteristic waves with losses) are applied to a quarter-wave channel, depicted in Fig. 2.1. The channel of length L has a closed end at

the location $x = 0$, suppressing the axial volume flow at this node ($U'|_{x=0} = 0$). At the channel mouth ($x = L$), the large area jump to the surrounding implies a pressure node ($p'|_{x=L} = 0$). The mean temperature along the channel axis is constant with $T_1 = T_2 = T_m$. Linear temperature profiles follow in Sec. 2.3. The parameters f_v and f_k consider the cross-sectional geometry of the channel. Thus, the following derivation is independent of further specifications in this respect.

Equations (2.46) and (2.47) state the local pressure and volume flow fluctuation, respectively. The boundary conditions at either side of the channel (at $x = 0$ and $x = L$, as stated above) define the complex-valued amplitudes \hat{F} and \hat{G} . At the closed end ($x = 0$, velocity node), Eq. (2.47) reads:

$$\frac{U'}{A} = \sqrt{a^* b^*} \left[\frac{\hat{F}}{2} \exp\left(i\omega t - i\omega \sqrt{\frac{b^*}{a^*}} \frac{x|_0}{c}\right) - \frac{\hat{G}}{2} \exp\left(i\omega t + i\omega \sqrt{\frac{b^*}{a^*}} \frac{x|_0}{c}\right) \right] = 0. \quad (2.52)$$

At the open end ($x = L$, pressure node), Eq. (2.46) reads:

$$\frac{p'}{\rho_m c} = \frac{\hat{F}}{2} \exp\left(i\omega t - i\omega \sqrt{\frac{b^*}{a^*}} \frac{x|_L}{c}\right) + \frac{\hat{G}}{2} \exp\left(i\omega t + i\omega \sqrt{\frac{b^*}{a^*}} \frac{x|_L}{c}\right) = 0. \quad (2.53)$$

Note that the solution of both, Eqs. (2.52) and (2.53) respectively, is independent of the time t (the expression $\exp(i\omega t)$ cancels out for the non-trivial solution at $t < \infty$). The linear system of equations is solvable when its determinant vanishes, which yields the following relationship for the eigenfrequency ω :

$$\exp\left(i\frac{\omega}{c} \sqrt{\frac{b^*}{a^*}} 2L\right) + 1 = 0. \quad (2.54)$$

For the inviscid and non-heat-conducting case ($a^* \rightarrow 1$ and $b^* \rightarrow 1$), the solution for the eigenfrequencies is real-valued and spatially repeats at multiples of the wavelength traveling at the speed of sound c . For the case of hydrodynamic and thermal wall interaction, the expression $\sqrt{b^*/a^*}$ is complex-valued. This directly indicates complex-valued eigenfrequencies with exponential decay of the oscillation amplitude in time.

Solving for the oscillation amplitudes \hat{F} and \hat{G} , Eq. (2.52) directly implies for $x = 0$:

$$\hat{F} = \hat{G}. \quad (2.55)$$

The definition of boundary conditions fully specifies the problem at hand. For later comparability with the work by Sujith et al. [43], the pressure p' is specified at the closed end of the channel ($x = 0$) and at time $t = 0$:

$$p'|_{x=0, t=0} \equiv P_1. \quad (2.56)$$

Evaluating Eq. (2.46) for the initial condition finally yields the solution for the parameters \hat{F} and \hat{G} :

$$\hat{F} = \hat{G} = \frac{P_1}{\rho_m c}. \quad (2.57)$$

The derivation above defines acoustic eigenvalues in a quarter-wave channel with a homogeneous temperature distribution in the presence of hydrodynamic and thermal boundary layers.

A boundary condition fully defines the flow rate and pressure profiles. The following Sec. 2.3 extends the homogeneous temperature distribution to a linear profile. Numerical results of the present, more restrictive formulation are not shown in this section, but alongside the results of the more general derivations of the subsequent section.

2.3 Extending to Linear Temperature Profiles at Constant Kinematic Viscosity

This section extends the derivations in the previous section to a more general set-up of linear temperature profiles. As indicated in Fig. 2.1, the temperature varies linearly between T_1 at the closed end and T_2 at the mouth of the channel. As in the previous set-up with uniform temperature, a general solution independent of boundary and initial conditions is derived first (Sec. 2.3.1). The subsequent Sec. 2.3.2 presents the specific solution for a quarter-wave channel. Numerical results and discussion follow in Sec. 2.4. Section 2.6 outlines a solution strategy for exponential temperature distributions. Solutions to other temperature profiles (quadratic, polynomial, etc.) may exist and can be considered in future work.

Compared to the previous analysis, the linear temperature profile significantly complicates the problem at hand. Note the additional non-zero term in the continuity equation (2.22). Furthermore, the mean local density ρ_m and the speed of sound c vary in space. In consequence, the previous approach for homogeneous temperature is not applicable.

The present work assumes a temperature-independent Prandtl number Pr . Furthermore, the solution is restricted to fluids with a kinematic viscosity ν that does not change with temperature. However, for general gaseous fluids (e.g., air), empirical correlations show such temperature dependence. E.g., Sutherland's law suggests

$$\nu(T) = \nu_\infty \left(\frac{T}{T_\infty} \right)^{1+\beta}, \quad (2.58)$$

where $\beta \approx 0.7$ and ν_∞ and T_∞ are a reference viscosity and temperate, respectively. Therefore, the following derivations should be regarded from a more mathematical and theoretical perspective. They are not expected to give quantitatively accurate results if temperature gradients and the influence of viscosity are significant.

2.3.1 The General Derivation

The general derivations of this section are again based on the conservation equations of Rott's thermoacoustic theory (Eqs. (2.20) and (2.22)) and closely follow an approach suggested by Sujith et al. [43]. Sujith et al. derived exact solutions for one-dimensional acoustic fields in ducts with an axial temperature gradient: Since the wave equation has variable coefficients, exact solutions for an arbitrary temperature profile cannot be obtained. Instead, the differential equation is transformed from the physical x -space to the local temperature space of a specific presumed temperature distribution. Sujith et al. [43] successfully provided a solution for linear and exponential temperature profiles. Subsequent studies added solutions for quadratic and polynomial

distributions [44, 45]. However, the work by Sujith and coworkers is limited to inviscid and non-heat-conducting gases. The present approach considers to the impact of hydrodynamic and thermal boundary layers considered by Rott's thermoacoustic theory [38].

The analysis begins with the one-dimensional first-order momentum and continuity equations by Rott (see Eqs. (2.20) and (2.22), rearranged):

$$\frac{\partial(U'/A)}{\partial t} + \frac{a^*}{\rho_m} \frac{\partial p'}{\partial x} = 0 \quad (2.59)$$

and

$$\frac{b^*}{\gamma p_m} \frac{\partial p'}{\partial t} + \frac{\partial(U'/A)}{\partial x} - \frac{d^*}{T_m} \frac{dT_m}{dx} (U'/A) = 0. \quad (2.60)$$

Differentiating the momentum equation with respect to the axial location x and the continuity equation with respect to the time t and eliminating the cross-derivative term yields a differential equation with variable coefficients:

$$\frac{b^*}{\gamma p_m} \frac{\partial^2 p'}{\partial t^2} - \frac{a^*}{\rho_m} \frac{\partial^2 p'}{\partial x^2} + \frac{a^*}{\rho_m^2} \frac{\partial \rho_m}{\partial x} \frac{\partial p'}{\partial x} - \frac{d^*}{T_m} \frac{dT_m}{dx} \frac{\partial(U'/A)}{\partial t} = 0. \quad (2.61)$$

Note that this step requires the assumption of a constant kinematic viscosity ν : In general, the parameter a^* of the momentum equation (2.59) depends on the position x (via the local temperature T_m , which affects the viscosity). Thus, differentiating with respect to the axial location x would lead to an additional term that cannot be handled in the further derivation. This term drops under the assumption of a constant viscosity ν .

Differentiating the steady equation of state ($p_m = \rho_m RT_m$) and recalling that the steady channel pressure p_m is constant along the direction x (no mean flow) yields a relation between the steady temperature and density:

$$\frac{1}{\rho_m} \frac{d\rho_m}{dx} + \frac{1}{T_m} \frac{dT_m}{dx} = 0. \quad (2.62)$$

Simplifying Eq. (2.61) with Eq. (2.62) and substituting the derivative of the volume flow rate via the momentum equation (Eq. (2.59)) gives:

$$\frac{b^*}{\gamma p_m} \frac{\partial^2 p'}{\partial t^2} - \frac{a^*}{\rho_m} \frac{\partial^2 p'}{\partial x^2} - \frac{a^*}{\rho_m T_m} \frac{1}{dx} \frac{dT_m}{dx} \frac{\partial p'}{\partial x} + \frac{d^*}{T_m} \frac{dT_m}{dx} \frac{a^*}{\rho_m} \frac{\partial p'}{\partial x} = 0, \quad (2.63)$$

where only the pressure p' remains as a first-order acoustic property. Replacing the mean density via the equation of state and further rearrangements yields:

$$\frac{\partial^2 p'}{\partial x^2} + \frac{(1-d^*)}{T_m} \frac{dT_m}{dx} \frac{\partial p'}{\partial x} - \frac{b^*}{a^*} \frac{1}{\gamma R T_m} \frac{\partial^2 p'}{\partial t^2} = 0. \quad (2.64)$$

Assuming that the solution has a periodic time dependence (i.e., $p'(x, t) = p_1(x)e^{i\omega t}$), Eq. (2.64) reduces to the following second order differential equation for the complex-valued amplitude $p_1(x)$:

$$\frac{d^2 p_1}{dx^2} + \frac{(1-d^*)}{T_m} \frac{dT_m}{dx} \frac{dp_1}{dx} + \frac{b^*}{a^*} \frac{\omega^2}{\gamma R T_m} p_1 = 0. \quad (2.65)$$

Equation (2.65) has variable coefficients. Therefore, general analytical solutions for an arbitrary mean temperate profile $T_m(x)$ cannot be obtained. Instead, a temperature profile is presumed and two transformations will lead to a Sturm-Liouville equation (see Eq. 2.74). The first transformation of Eq. (2.65) from the physical x -space to the temperature space $T_m(x)$ yields:

$$\left(\frac{dT_m}{dx}\right)^2 \frac{d^2 p_1}{dT_m^2} + \frac{d^2 T_m}{dx^2} \frac{dp_1}{dT_m} + \frac{(1-d^\star)}{T_m} \left(\frac{dT_m}{dx}\right)^2 \frac{dp_1}{dT_m} + \frac{b^\star}{a^\star} \frac{\omega^2}{\gamma R T_m} p_1 = 0 . \quad (2.66)$$

No assumptions on the mean temperate profile $T_m(x)$ were made up to this point of the derivation. In the following, a linear temperature profile is assumed:

$$T_m(x) = T_0 + mx , \quad (2.67)$$

and thus

$$\frac{dT_m}{dx} = m \quad \text{and} \quad \frac{d^2 T_m}{dx^2} = 0 . \quad (2.68)$$

Section 2.6 outlines a solution strategy for an exponential temperature profile.

Using the linear properties from Eqs. (2.67) and (2.68) to simplify the transformed second order differential equation (Eq. (2.66)) yields:

$$\frac{d^2 p_1}{dT_m^2} + \frac{(1-d^\star)}{T_m} \frac{dp_1}{dT_m} + \frac{b^\star \omega^2 / m^2}{a^\star \gamma R T_m} p_1 = 0 . \quad (2.69)$$

For further simplification of Eq. (2.69), a new independent variable s is introduced:

$$s = 2 \sqrt{\frac{\omega^2 c^\star}{m^2 \gamma R}} \sqrt{T_m} , \quad (2.70)$$

where

$$c^\star = \frac{b^\star}{a^\star} \quad (2.71)$$

and the first and second derivative of s with respect to the temperature T_m read:

$$\frac{ds}{dT_m} = \sqrt{\frac{\omega^2 c^\star}{m^2 \gamma R}} \frac{1}{\sqrt{T_m}} \quad (2.72)$$

and

$$\frac{d^2 s}{dT_m^2} = -\frac{1}{2} \sqrt{\frac{\omega^2 c^\star}{m^2 \gamma R}} \frac{1}{\sqrt{T_m^3}} . \quad (2.73)$$

Again, note the underlying assumption of a temperature-independent kinematic viscosity ν and constant Prandtl number Pr , which implies that the parameter c^\star does not change with respect to the temperature T_m .

Transforming Eq. (2.69) from the T_m to the s -space yields:

$$\frac{d^2 p_1}{ds^2} + \frac{(1-2d^\star)}{s} \frac{dp_1}{ds} + p_1 = 0 , \quad (2.74)$$

which is a Sturm-Liouville equation [46]. The solution of this equation is known:

$$\begin{aligned} p_1 &= s^{d^*} [c_1 J_{d^*}(s) + c_2 Y_{d^*}(s)] \\ &= \left(\frac{\omega}{a}\sqrt{T_m}\right)^{d^*} \left[c_1 J_{d^*} \left(\frac{\omega}{a}\sqrt{T_m}\right) + c_2 Y_{d^*} \left(\frac{\omega}{a}\sqrt{T_m}\right) \right], \end{aligned} \quad (2.75)$$

where c_1 and c_2 are complex-valued constants. J_{d^*} and Y_{d^*} are the Bessel functions of first and second kind, respectively. Note that both functions are of complex-valued order d^* . The constant a is defined as

$$a = \frac{|m|}{2} \sqrt{\frac{\gamma R}{c^*}}. \quad (2.76)$$

Finally, the momentum equation (Eq. (2.59)) yields the acoustic volume flow U_1 , based on the derived pressure distribution p_1 (Eq. (2.75)):

$$\begin{aligned} \frac{U_1}{A} &= -\frac{a^*}{i\omega\rho_m} \frac{dp_1}{dx} = \frac{i a^*}{\omega\rho_m} \frac{dT}{dx} \frac{dp_1}{dT} \\ &= \frac{m}{|m|} \frac{i\sqrt{a^*b^*}}{\rho_m\sqrt{\gamma RT_m}} s^{d^*} [c_1 J_{d^*-1}(s) + c_2 Y_{d^*-1}(s)] \\ &= \frac{m}{|m|} \frac{i\sqrt{a^*b^*}}{\rho_m\sqrt{\gamma RT_m}} \left(\frac{\omega}{a}\sqrt{T_m}\right)^{d^*} \left[c_1 J_{d^*-1} \left(\frac{\omega}{a}\sqrt{T_m}\right) + c_2 Y_{d^*-1} \left(\frac{\omega}{a}\sqrt{T_m}\right) \right]. \end{aligned} \quad (2.77)$$

For an inviscid and non-heat-conducting gas ($a^* \rightarrow 1$, $b^* \rightarrow 1$, $c^* \rightarrow 1$, and $d^* \rightarrow 0$), the present analysis for the acoustic pressure and volume flow rate perfectly resembles the results obtained by Sujith et al. [43]. In this particular case, Eq. (2.74) is a zeroth order Bessel's differential equation. Consequently, the Bessel functions in the solution for pressure and velocity (Eq. (2.75) and (2.77)) are of zeroth and first order, respectively.

2.3.2 Application to a quarter-wave channel

In this section, the equations for a linear temperature gradient derived in Sec. 2.3.1 are applied to the quarter-wave channel depicted in Fig. 2.1. The general set-up corresponds to the description given in Sec. 2.2.2, except that the temperature profile under investigation describes a linear characteristic between T_1 at the closed end and T_2 at the mouth of the channel.

The pressure and velocity amplitudes need to satisfy the respective boundary conditions at either end of the channel (i.e. $U_1 = 0$ at $x = 0$ where $T_m = T_1$ and $p_1 = 0$ at $x = L$ where $T_m = T_2$, respectively):

$$c_1 J_{d^*-1} \left(\frac{\omega}{a}\sqrt{T_1}\right) + c_2 Y_{d^*-1} \left(\frac{\omega}{a}\sqrt{T_1}\right) = 0 \quad (2.78)$$

and

$$c_1 J_{d^*} \left(\frac{\omega}{a}\sqrt{T_2}\right) + c_2 Y_{d^*} \left(\frac{\omega}{a}\sqrt{T_2}\right) = 0. \quad (2.79)$$

This system of homogeneous equations is only solvable, when its determinant vanishes. Thus, all eigenfrequencies of the channel fulfill the mathematical relation

$$J_{d^*} \left(\frac{\omega}{a}\sqrt{T_2}\right) Y_{d^*-1} \left(\frac{\omega}{a}\sqrt{T_1}\right) - J_{d^*-1} \left(\frac{\omega}{a}\sqrt{T_1}\right) Y_{d^*} \left(\frac{\omega}{a}\sqrt{T_2}\right) = 0. \quad (2.80)$$

Finally, the acoustic pressure amplitude $p'|_{x=0, t=0} = p_1|_{x=0} \equiv P_1$ is defined as the initial condition. The unknown constants c_1 and c_2 from Eqs. (2.78) and (2.79) follow:

$$c_1 = \frac{\pi\omega\sqrt{T_1}}{2a\left(\frac{\omega}{a}\sqrt{T_1}\right)^{d^*}} P_1 Y_{d^*-1}\left(\frac{\omega}{a}\sqrt{T_1}\right) \quad (2.81)$$

and

$$c_2 = \frac{\pi\omega\sqrt{T_1}}{2a\left(\frac{\omega}{a}\sqrt{T_1}\right)^{d^*}} P_1 J_{d^*-1}\left(\frac{\omega}{a}\sqrt{T_1}\right). \quad (2.82)$$

Again, for the inviscid and non-heat-conducting limiting case ($c^* \rightarrow 1$, and $d^* \rightarrow 0$), the equations of this section perfectly match those derived by Sujith et al. [43].

The equations above clearly show that the present problem at hand (including the temperature gradient) does not allow a decoupled treatment via two independent characteristic waves that travel in the downstream and upstream direction with their respective propagation velocities. Instead, the acoustic perturbations are described by a (far more complicated) superposition of Bessel functions (compare Eqns. (2.75) and (2.77)).

2.4 Results

This section presents numerical results based on the previous derivations on uniform (Sec. 2.2) and linear (Sec. 2.3) temperature profiles. Over a wide parametric range of temperatures (Sec. 2.4.1), this Section reports the respective eigenfrequencies (Sec. 2.4.2) as well as pressure and velocity profiles (Sec. 2.4.3).

2.4.1 Parametric Set-Up

To facilitate a comparison, values selected for the channel length $L = 4\text{ m}$, the temperature at channel mouth $T_2 = 300\text{ K}$, and the pressure magnitude at the closed end $P_1 = 2000\text{ Pa}$ agree with the work by Sujith et al. [43]. The temperature range T_1 also follows the study by Sujith from 300 K to 1100 K at the closed end of the channel. Furthermore, the present study extends the parameter range to temperatures below the mouth temperature of $T_2 = 300\text{ K}$, yielding the range $T_1 = [100, 150, 200, 300, 500, 700, 900, 1100]\text{ K}$. Sujith and coworkers do not elaborate on the product of heat capacity ratio γ and the specific gas constant R . However, the evaluation of eigenfrequencies yields $\gamma R = 402.5 \frac{\text{m}^2}{\text{s}^2\text{K}}$. This motivates the selection of air-specific values $\gamma = 1.4$ and $R = 287.5 \frac{\text{m}^2}{\text{s}^2\text{K}}$ in the present study. The mean pressure along the channel is reconstructed by the ratio of acoustic pressure and velocity amplitude to $p_m = 101325\text{ Pa}$.

Expanding the scope to the effect of viscous and thermal boundary layers, this work investigates acoustics in the geometry of a (two-dimensional) channel flow between two confining parallel plates at the (hydraulic) distance of $2r_h$. The geometric parameter r_h controls the magnitude of impact that the boundary layers exert on the fluid. In contrast, the kinematic viscosity $\nu = 1.516 \times 10^{-5} \frac{\text{m}^2}{\text{s}}$ and the Prandtl number $Pr = 0.711$ are constant.

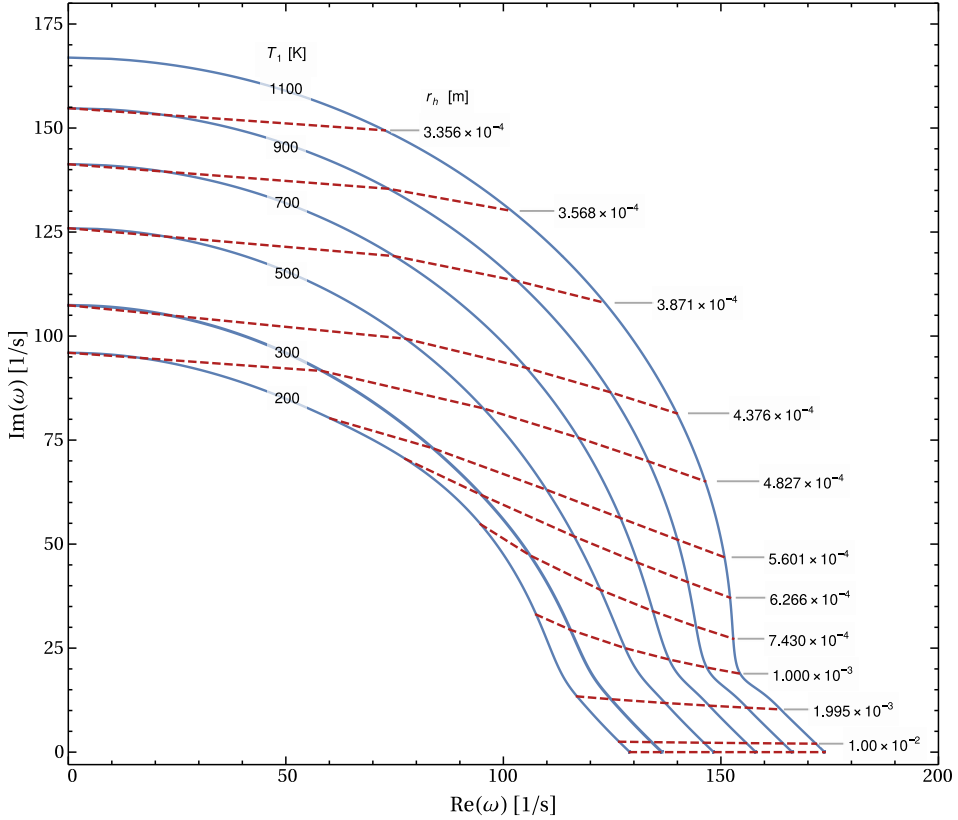


Figure 2.2: First eigenfrequency ω for different temperatures T_1 and channel widths r_h .

The parameters f_v and f_κ from Eq. (2.23) specify the geometric shape of the channel flow. Note that other geometries (circular/rectangular ducts, etc.) can easily be investigated by their corresponding geometric functions [38].

2.4.2 Evaluation of Eigenfrequencies

This section presents the numerical evaluation of the first three acoustic eigenfrequencies ω_0 in a quarter-wave channel. Equation (2.54) (uniform temperature distribution, $T_1 = T_2$) and Eq. (2.80) (linear temperature distribution, $T_1 \neq T_2$) are minimized with respect to the real- and imaginary-valued part of the frequency ω . The necessity to evaluate complex-ordered Bessel functions suggested using the software “Mathematica” [47]. The parametric set-up follows the description of the previous Sec. 2.4.1.

Figures 2.2 to 2.4 display the development of the first three complex-valued acoustic eigenfrequencies ω_0 (the real and imaginary values are depicted on the two axis of each plot). The solid blue isolines (—) represent instances of equal temperature distribution. The dashed red isolines (---) indicate the channel width r_h .

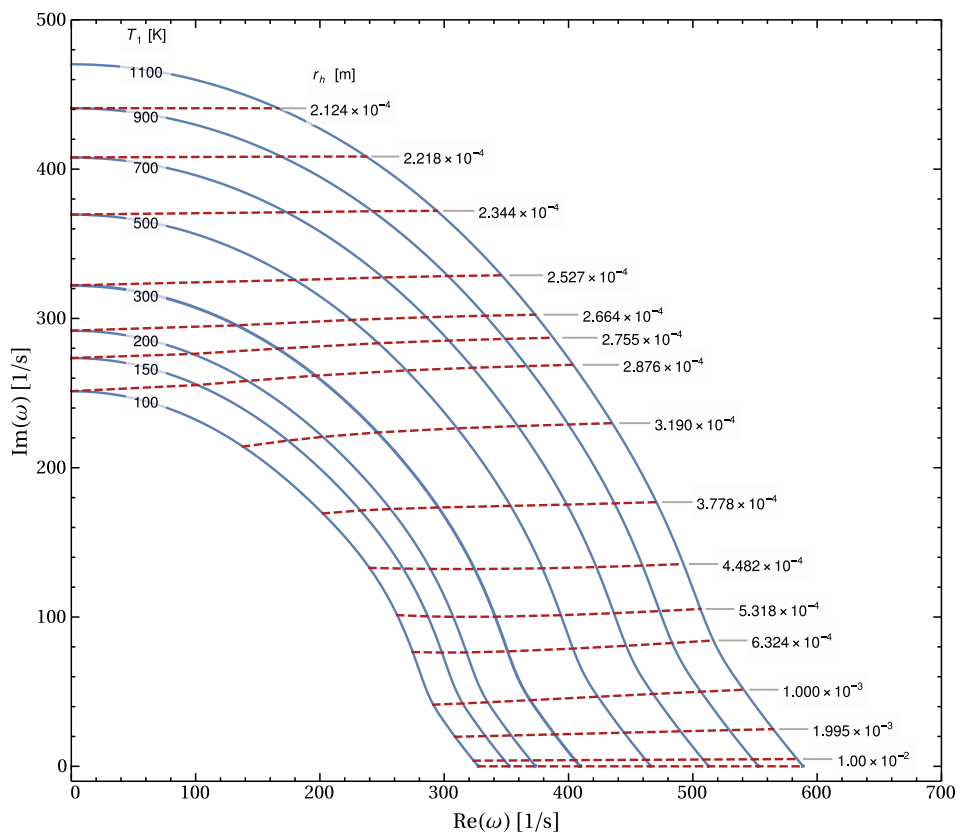


Figure 2.3: Second eigenfrequency ω for different temperatures T_1 and channel widths r_h .

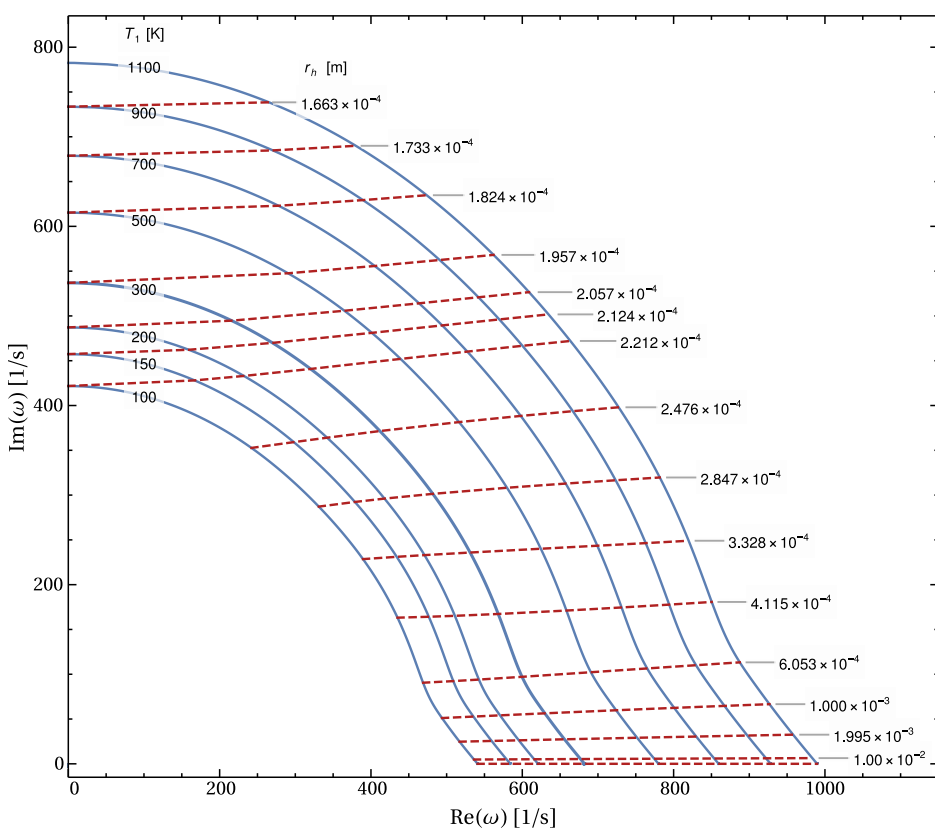


Figure 2.4: Third eigenfrequency ω for different temperatures T_1 and channel widths r_h .

First, investigating the limiting case of very wide channels ($r_h \rightarrow \infty$, here $r_h = 10\text{ m}$), the complex-valued part of the eigenfrequency ω_0 vanishes (see the bottom-most and unlabeled dashed line (---) of each plot). For this consideration, the effect of the hydrodynamic and thermal wall-to-fluid impact is negligible, yielding the inviscid and non-heat-conducting limiting case investigated by Sujith et al. [43]. Indeed, these real-valued eigenfrequencies perfectly agree between the present study and the results reported by Sujith et al. [43]. Furthermore, the qualitative impact of the temperature distribution on the eigenfrequency is self-evident: Increasing mean-temperatures increase the speed of sound and thus the eigenfrequency of the quarter-wave channel.

Turning to narrower channel widths r_h , the impact of hydrodynamic and thermal losses becomes apparent. Down to $r_h = 0.01\text{ m}$ (second dashed line (---) from the bottom in each plot), the moderate gain in losses only triggers small shifts in eigenfrequency (real- and imaginary-valued component). Narrowing the channel down to approximately $r_h = 0.001\text{ m}$ (depending on the order of the eigenfrequency), the relationship between the real- and imaginary-valued part of the eigenfrequency ω_0 continues to describe linear characteristics. A bend follows where the increase in the imaginary-valued part of the eigenfrequency accelerates compared to the decrease in the real-valued counter-part. After this bend, a circular characteristic of the complex-valued eigenfrequency ω_0 follows. The vanishing of its real part terminates the oscillatory behavior of the system.

Before closing this section on eigenfrequencies, one unexpected observation is mentioned: For the two lowest temperatures $T_1 = 100\text{ K}$ and 150 K , the first eigenfrequencies ω_0 develop differently compared to the higher temperature range. For clarity of the remaining content, these two temperatures are excluded from Fig. 2.2. At large channel widths r_h , the eigenfrequencies at lower temperatures follow an expected path. However, particularly for $T_1 = 100\text{ K}$ at medium channel widths (and thus medium real parts of ω_0), the imaginary part of ω_0 strongly increases. Finally, the real part of the eigenfrequency ω_0 vanishes at a significantly raised imaginary part of $\omega_0 \approx 600i\frac{1}{s}$. This phenomenon requires further clarification, including whether boundary conditions (physically/mathematically) are always satisfied.

2.4.3 Evaluation of Pressure and Velocity Profiles

In this section, pressure and velocity profiles (p_1 (—) and U_1/A (---), respectively) are presented for the first eigenfrequency of the quarter-wave channel. Equations (2.46) and (2.47) describe the cases with homogeneous temperatures, Eqs. (2.75) and (2.77) the cases of linear temperature distributions.

Figure 2.5 provides the local distribution of the absolute pressure $|p_1|$ and velocity $|U_1/A|$ for six distinct temperatures T_1 and six channel widths r_h (compare the consistency of parameters with Fig. 2.2). For presentation, the velocity $|U_1/A|$ is displayed as a normalized pressure $|U_1/A|\rho_2c_2$, where ρ_2 and c_2 are the density and speed of sound at $x = L$ where $T_m = T_2$. Note that boundary conditions are satisfied for each instance ($p'|_{x=0, t=0} = p_1|_{x=0} \equiv P_1 = 2000\text{ Pa}$, $U_1|_{x=0} = 0$ and $p_1|_{x=L} = 0$). The colored instances without data lie outside the parameter range of an acoustically oscillating flow: The channel width r_h falls below the threshold for which the real-valued part of the eigenfrequency ω_0 is larger zero (again, compare to Fig. 2.2).

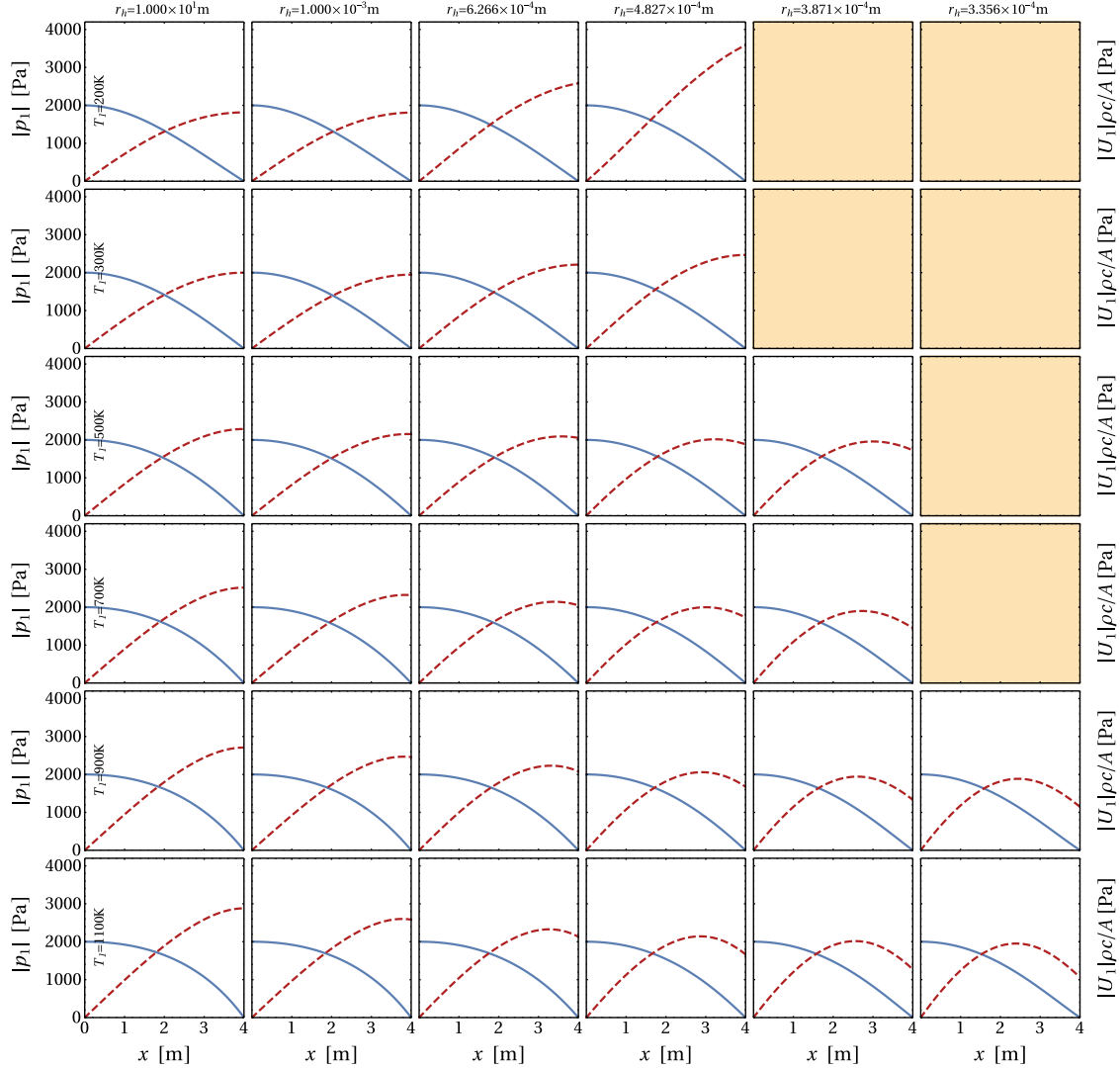


Figure 2.5: Absolute pressure amplitude $|p_1|$ (—) and velocity amplitude $|U_1/A|$ (---, factor $\rho_2 c_2$) for the first eigenfrequency at different temperatures T_1 and channel widths r_h .

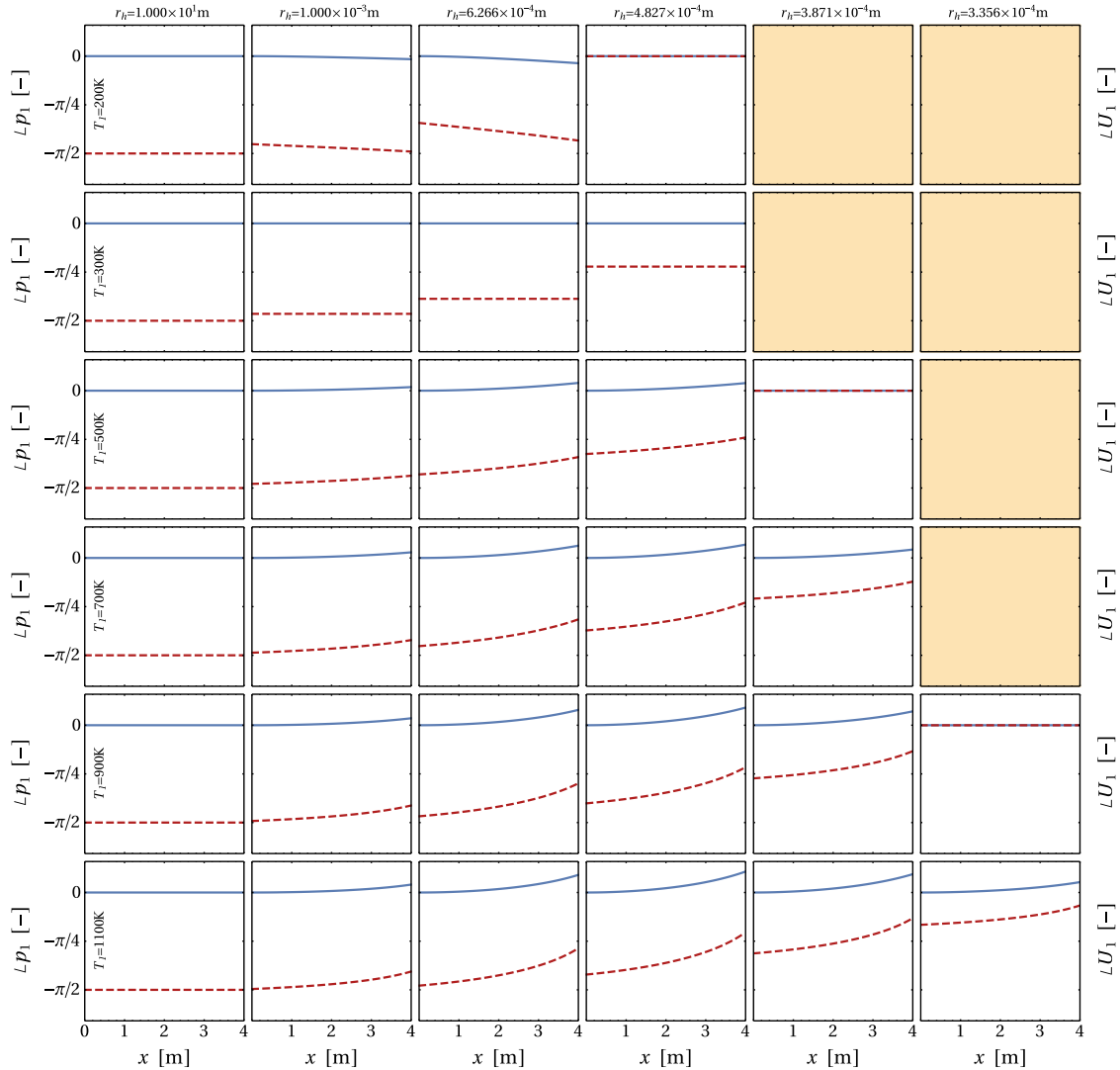


Figure 2.6: Phase of pressure p_1 (—) and velocity U_1/A (---) for the first eigenfrequency at different temperatures T_1 and channel widths r_h .

A qualitative comparison reveals the clear influence of the temperature T_1 on the velocity profile. In the case of negligible viscous and heat-conductive effects (left column, $r_h = 10\text{m}$), the maximum velocity amplitude at $x = L$ significantly increases from $|U_1/A| \approx 4.5 \frac{\text{m}}{\text{s}}$ at temperature $T_1 = 300\text{K}$ to $|U_1/A| \approx 7 \frac{\text{m}}{\text{s}}$ at temperature $T_1 = 1100\text{K}$ (moving down in Fig. 2.5). Turning to smaller channel widths r_h (moving right in Fig. 2.5), two temperature-dependent effects reveal: (i) A change in velocity amplitude: for low temperatures T_1 , the (low) amplitude increases, whereas for large temperatures T_1 , the (large) amplitude decreases. (ii) A shift of the location of maximum velocity: for low temperatures T_1 , the location of maximum velocity moves to larger positions x (beyond the channel length L). For large temperatures T_1 , the maximum velocity moves to smaller positions x , yielding the maximum velocity within the channel at $0 < x < L$.

Temperature T_1 and channel width r_h also impact the curvature of the pressure profile $|p_1|$. However, for a qualitative evaluation, the differences are far less significant and not further outlined at this point.

Figure 2.6 shows the corresponding phase profiles of the pressure p_1 (—) and velocity U_1/A (---). Again, the initial condition is fulfilled for each instance: $\angle p'|_{x=0, t=0} = \angle p_1|_{x=0} \equiv 0$. Next, for the inviscid and non-heat-conducting limit (left column, $r_h = 10\text{m}$), the temperature distribution does neither affect the pressure nor the velocity phase: Both phases are constant along the x -axis, with the pressure leading the velocity by an angle of $\Delta\phi = \pi/2$. Turning to smaller channel widths r_h (moving right in Fig. 2.6), two effects are revealed: (i) A temperature-independent decrease of the phase difference $\Delta\phi$: starting at $\Delta\phi = \pi/2$, the phase difference decreases to $\Delta\phi = 0$ when the real-part of the eigenfrequency vanishes (moving right in Fig. 2.6). Comparison to Fig. 2.2 reveals that the three rows for $T_1 = 200\text{K}, 500\text{K},$ and 900K perfectly capture this threshold of vanishing oscillation. (ii) A temperature-dependent curvature and incline of each phase profile: the curvature/incline initially increases before it decreases and vanishes as $\Delta\phi$ approaches zero. The characteristic of the curvature (left/right, incline/decline) depends on the temperature distribution. The homogeneous temperature profile at $T_1 = 300\text{K}$ yields the threshold with no curvature at constant phases.

This discussion only provides pressure and velocity profiles for the first eigenfrequency ω_0 . This particular eigenfrequency is consciously chosen for its primary relevance regarding the design of quarter-wave resonators. The evaluation of profiles with higher eigenfrequencies exhibits similar characteristics (see Sec. 2.7). The inviscid and non-heat-conducting limiting case of the third eigenfrequency perfectly resembles the absolute pressure and velocity profiles displayed in the work by Sujith et al. [43].

2.4.4 Validation

The inviscid and non-heat-conducting limit of the present work has been validated against the results obtained by Sujith et al. [43]. This includes the analytical validation, the numerical validation of the first three eigenfrequencies ω_0 ($T_1 = 300\text{K}$ to 1100K), and the numerical validation of the absolute pressure and velocity profiles ($T_1 = 500\text{K}$ and 1100K).

Furthermore, all results displayed in Figs. 2.2 to 2.4 (first three eigenfrequencies, various temperatures T_1 , and channel widths r_h) were numerically validated against the underlying momentum and continuity equations (Eqns. (2.20) and (2.22)): The derived equations were used

to calculate the pressure and velocity profiles (p' and U' , respectively) and their derivatives in respect to space and time along the finely discretized x -axis for various instances of time with $t = 2\pi\phi/\text{Re}(\omega_0)$ with $\phi = (i/8)\pi$ and $i = 0$ to 7. Inserting these profiles into the conservation equations, showed deviations of the order of machine precision and numerous orders of magnitude below the actual amplitudes and their derivatives. Thus, the author is confident that the derived equations satisfy Rott's differential equations [38].

2.5 Summary and Conclusions on Duct Acoustics with Viscous and Thermal Dissipation

This chapter presents two novel approaches for the analytical solution of acoustic equations in channel flows. The underlying framework of Rott's thermoacoustic approximation accounts for hydrodynamic and thermal losses induced by the boundary layers at the channel walls. In the case of spatially uniform temperature profiles, the solution is obtained in terms of characteristic waves. Linear temperature profiles (at constant viscosity) require a transformation into the temperature space to eliminate unknown coefficients. The general solution is applied to a quarter-wave channel with an open and closed end. For this specific application, the thesis presents quantitative results for the first three complex-valued eigenfrequencies that describe the decaying characteristic of the acoustic oscillation. Selected examples of pressure and velocity amplitudes and phases are presented and discussed. The calculated profiles are validated against the underlying conservation equations. Existing literature serves as validation and discussion of the inviscid and non-heat-conducting limit.

The present work provides insight into the impact of boundary layers on acoustic eigenfrequencies and the consequent temporal decay of amplitudes: Increasing boundary effects (generated by a decreasing channel width) lower the (real part of the) eigenfrequency subject to the decrease in the phase velocity. Besides, the temporal decay of the amplitudes increases. At a certain threshold, the oscillating characteristic vanishes. The analytical nature of the derivations allows the quick calculation of the velocity and temperature profiles. Boundary related effects generate significant changes in oscillation amplitudes and phase shifts.

To model a process of more technical relevance (i.e., a combustion chamber operating at its design point), the following Chapter 3 describes the adaption of the present framework to the steady state oscillation of an acoustic quarter-wave resonator (i.e., the imaginary part of the angular frequency is zero). Thereby, this thesis presents a novel modeling approach that spatially resolves the resonator tube to predict its acoustic performance. The particular importance and technical relevance of the hydrodynamic and thermal boundary layer will be highlighted and discussed in more detail.

In future research, the present analytical and thus computationally efficient calculation method of velocity and pressure profiles may serve to determine the axial heat flux (compare Chapter 4).

2.6 Outlook: Considerations on Exponential Temperature Profiles

This appendix outlines a solution strategy for exponential temperature profiles, reading:

$$T_m(x) = T_0 e^{-kx}, \quad (2.83)$$

and thus

$$\frac{dT_m}{dx} = -k T_0 e^{-kx} = -k T_m \quad \text{and} \quad \frac{d^2 T_m}{dx^2} = k^2 T_0 e^{-kx} = k^2 T_m. \quad (2.84)$$

Using the linear properties from Eqs. (2.83) and (2.84) to simplify the transformed second order differential equation (Eq. (2.66)) yields:

$$T_m^2 \frac{d^2 p_1}{dT_m^2} + (2 - d^*) T_m \frac{dp_1}{dT_m} + \frac{b^* \omega^2 / k^2}{a^* \gamma R T_m} p_1 = 0, \quad (2.85)$$

which, analogous to the set-up with the linear temperature profile, is a Sturm-Liouville equation [46]. The solution of this function is known:

$$p_1 = c_1 b^{(1-d^*)/2} \left(\frac{1}{T_m} \right)^{(1-d^*)/2} \Gamma(d^*) J_{d^*-1} \left(\frac{\omega}{a_{\exp}} \sqrt{\frac{1}{T_m}} \right) \\ + c_2 b^{(1-d^*)/2} \left(\frac{1}{T_m} \right)^{(1-d^*)/2} \Gamma(2-d^*) J_{1-d^*} \left(\frac{\omega}{a_{\exp}} \sqrt{\frac{1}{T_m}} \right), \quad (2.86)$$

where c_1 and c_2 are complex-valued constants, J is the Bessel functions of first kind, and Γ the gamma function. The constant a_{\exp} is defined as

$$a_{\exp} = \frac{|k|}{2} \sqrt{\frac{\gamma R}{c^*}}. \quad (2.87)$$

Subsequent derivations applied to linear temperature gradient (the analysis toward the volume flow U_1 , the calculation of eigenfrequencies ω , and the final determination of the unknown constants c_1 and c_2 , see Secs. 2.3.1 and 2.3.2) also hold for the exponential case. However, the corresponding formulas become significantly longer and are not further presented in this work.

2.7 Outlook: Pressure and Velocity Profiles for Higher Mode Orders

For completeness, this appendix presents the additional pressure and velocity profiles for the second and third eigenfrequency, respectively.

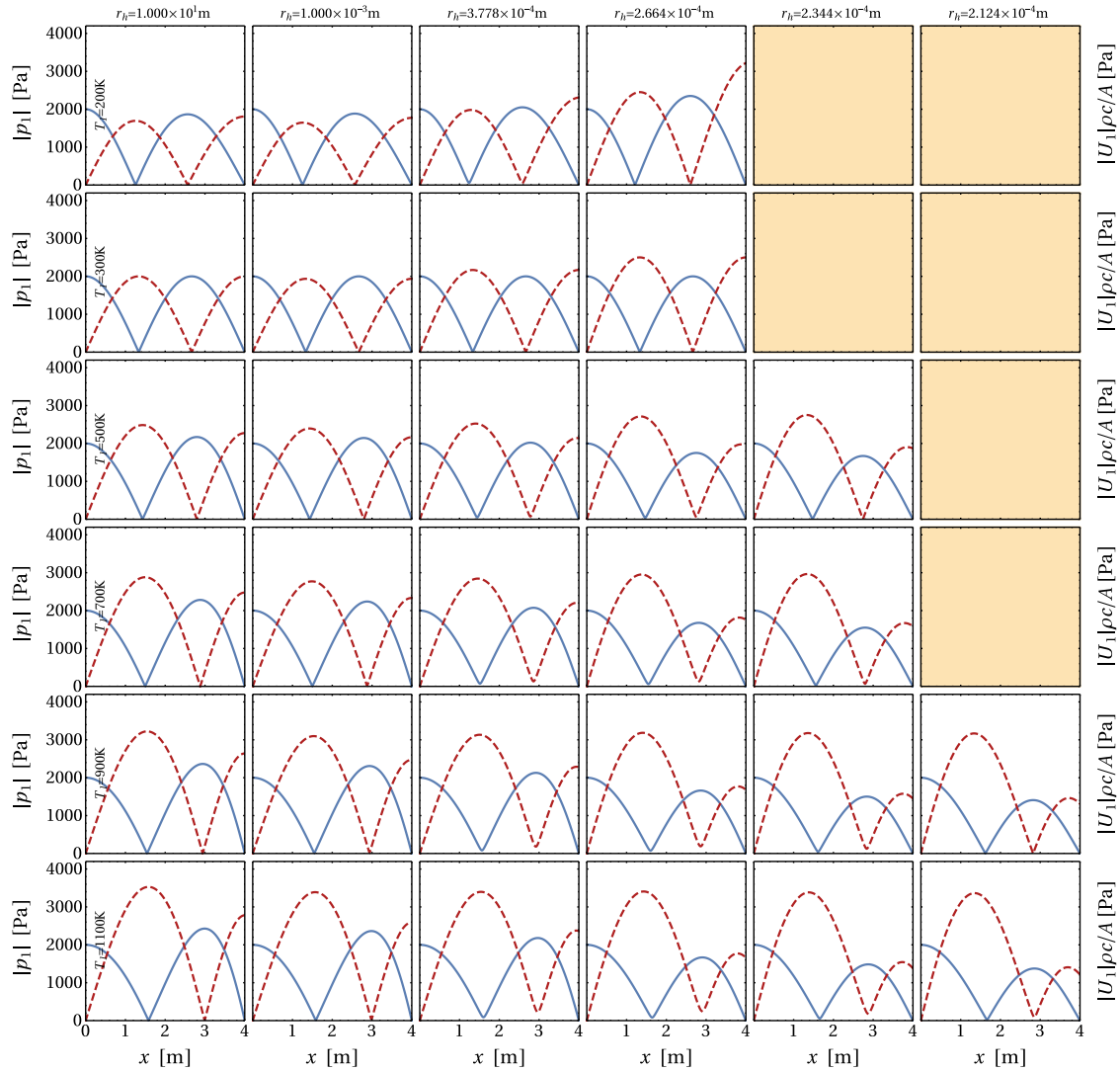


Figure 2.7: Absolute pressure amplitude $|p_1|$ (—) and velocity amplitude $|U_1/A|$ (---, factor $\rho_2 c_2$) for the second eigenfrequency at different temperatures T_1 and channel widths r_h .

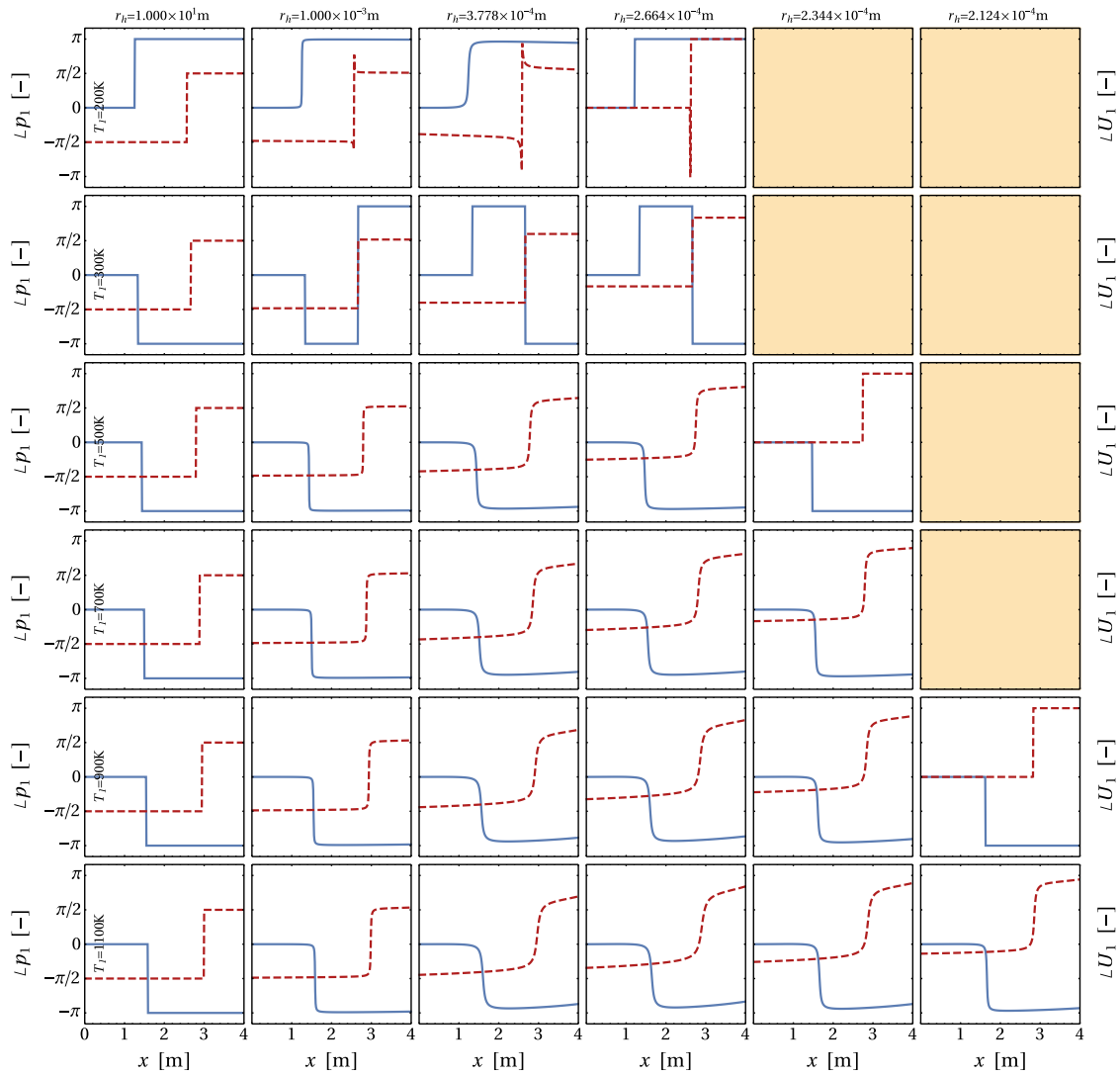


Figure 2.8: Phase of pressure p_1 (—) and velocity U_1/A (---) for the second eigenfrequency at different temperatures T_1 and channel widths r_h .

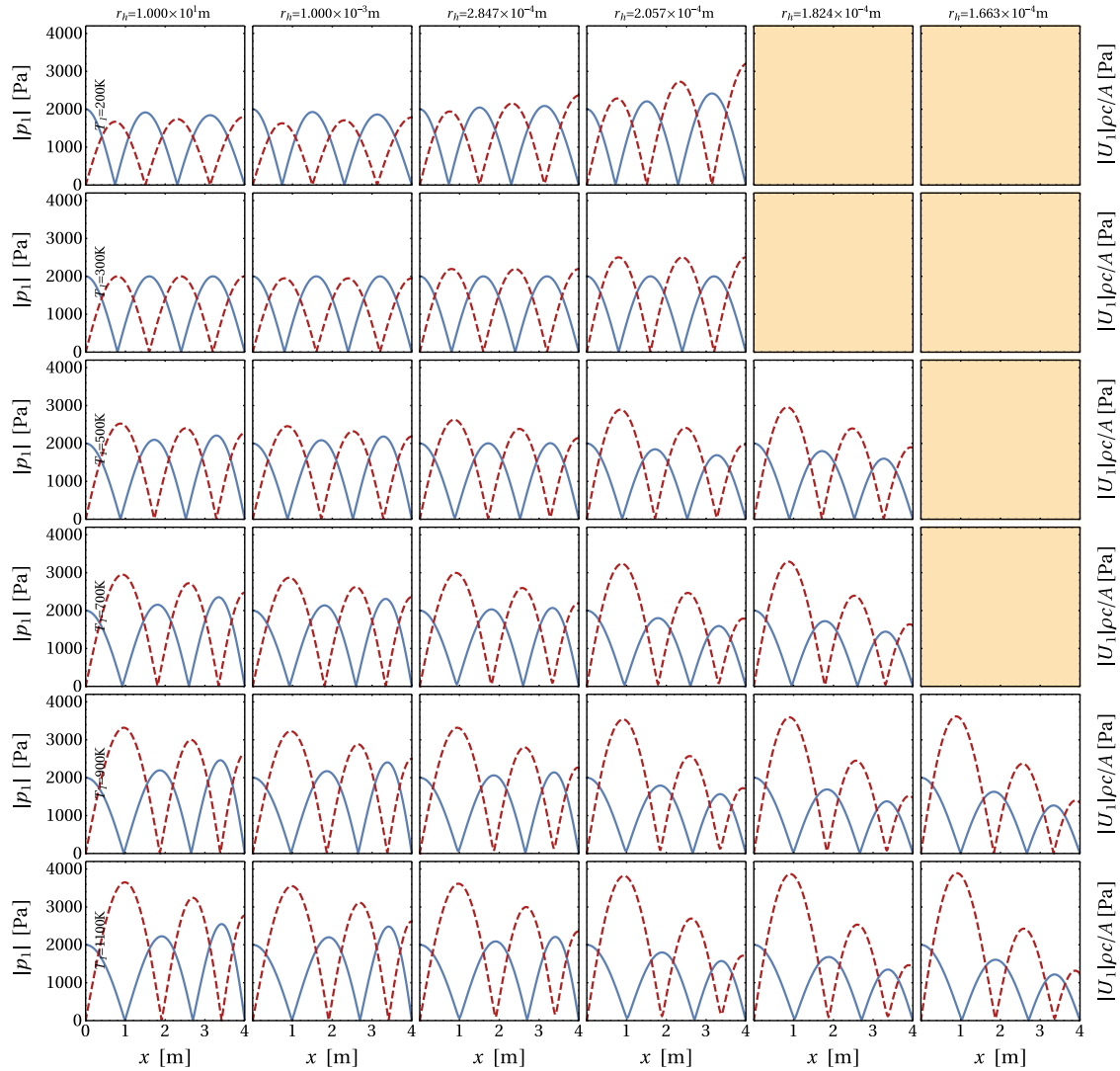


Figure 2.9: Absolute pressure amplitude $|p_1|$ (—) and velocity amplitude $|U_1/A|$ (---, factor $\rho_2 c_2$) for the third eigenfrequency at different temperatures T_1 and channel widths r_h .

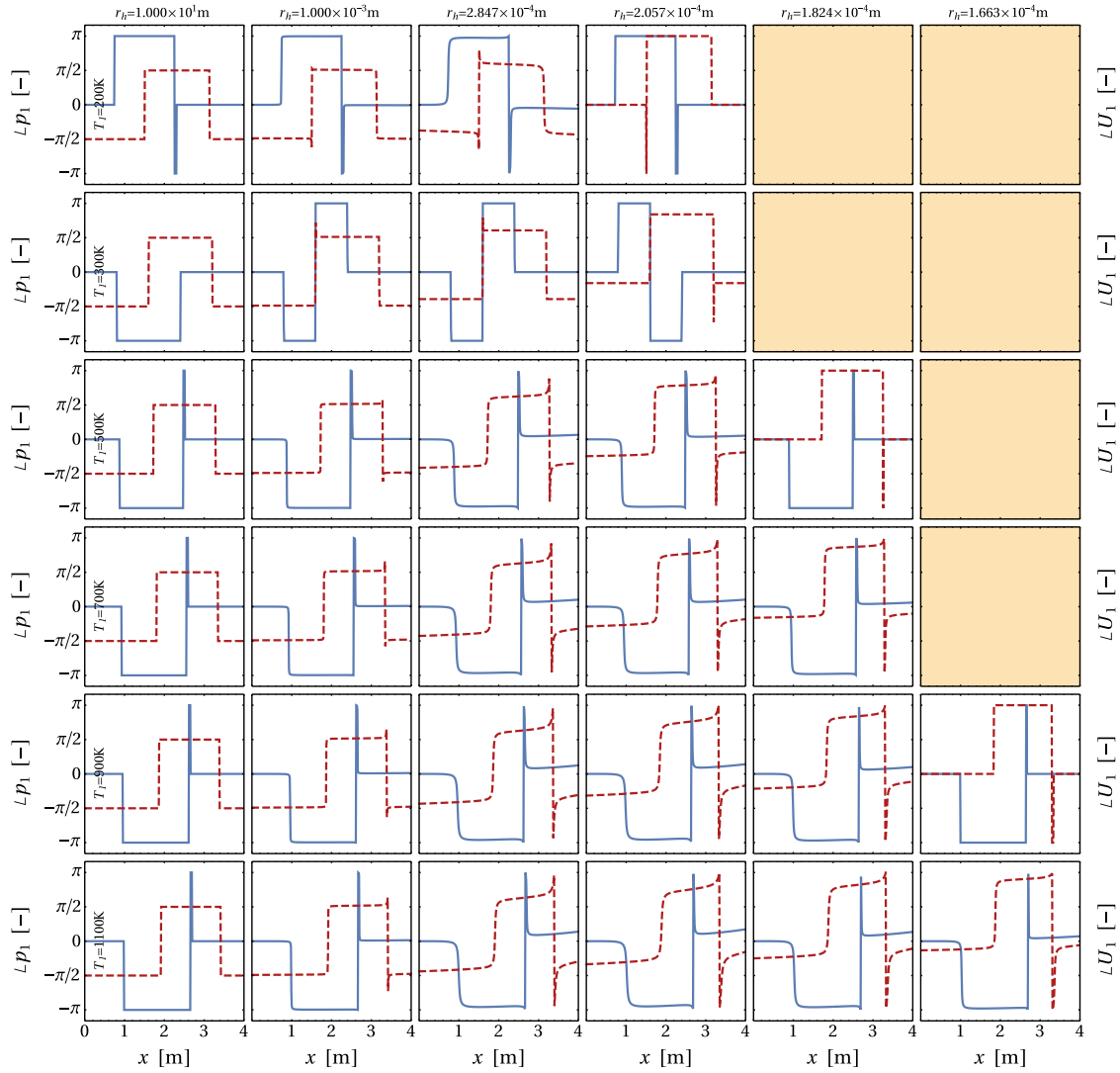


Figure 2.10: Phase of pressure p_1 (—) and velocity U_1/A (---) for the third eigenfrequency at different temperatures T_1 and channel widths r_h .

3 Modeling of an Acoustic Quarter-Wave Resonator

The previous Chapter 2 studied acoustically oscillating channel flows at constant and linear axial mean temperature profiles. The described model focused on the eigenfrequencies of a decaying oscillation in a quarter-wave channel. Building on the previous work, the present chapter introduces an analytical model to predict the acoustic damping characteristics (e.g., the acoustic impedance) of quarter-wave resonators. The model focuses on the linear damping regime and accounts for viscous and thermal losses formulated in Rott's thermoacoustic theory. The novelty of the present framework compared to existing models from the literature lies in the spatially resolved evaluation of the acoustic properties along the resonator tube. Consequently, the model does not require a fictive length parameter (i.e., for the modeling of an acoustically compact, oscillating mass). The present approach is valid over an extended range of parameters and accounts for thick hydrodynamic boundary layers. Furthermore, it examines more complex configurations including thermal heat exchange with the surrounding walls. Thereby, the separate treatment of hydrodynamic and thermal boundary layers allows modeling adiabatic or isothermal resonator walls. Besides determining the overall acoustic characteristics at the resonator mouth, the validated framework calculates the local pressure and velocity fluctuations along the resonator tube. The present work focuses on uniform temperature within the resonator. However, an extension to linear temperature profiles (see Sec. 2.3) shall be straight forward.

Section 3.1 outlines the fundamental background of acoustic resonators. In the following the reference model for quarter-wave resonators by Laudien et al. [8] is presented (Sec. 3.1.1). Section 3.2 develops the novel approach of the present study. Results of the new framework are validated (Sec. 3.3) and discussed via the reflection coefficient and the acoustic impedance (Sec. 3.4.2). Section 3.4.3 displays local profiles of acoustic velocity, pressure, and characteristic waves along the resonator tube. Section 3.5 concludes the modeling method of a quarter-wave resonator.

In rocket engine combustion chambers, strong temperature gradients affect the damping performance of acoustic quarter-wave resonators. Therefore, an accurate prediction of the damping characteristics is crucial for the safe operation of the engine. Section 5.1 presents a publication [12] and provides an overview of such a predictive numerical framework that quantifies the temperature-dependent performance.

3.1 The Acoustic Resonator

Hard walls perfectly reflect an incident acoustic wave without losses. Thus, a confining wall structure (e.g., a rocket engine combustion chamber) cannot absorb acoustic energy but only

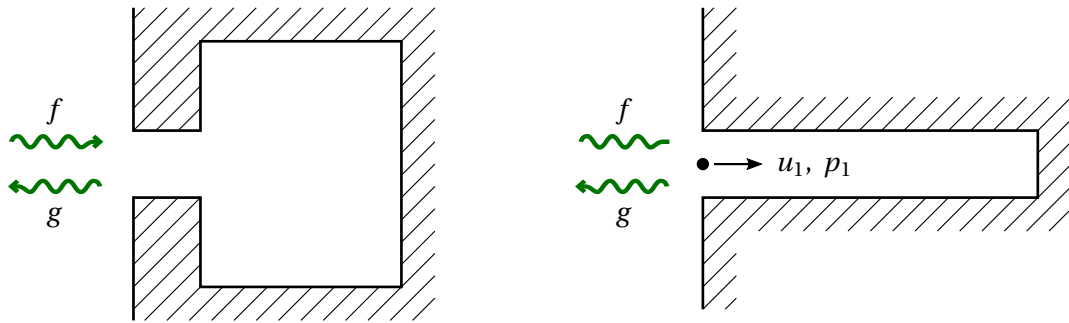


Figure 3.1: Sketch of a Helmholtz resonator (left) and a quarter-wave resonator (right).

diverts it. To prevent such potential feedback, acoustic resonators are commonly used to dissipate energy at the walls. Consequently, the reflected acoustic wave returns less energy than the incident wave.

Two widely applied types of resonators are the Helmholtz and the quarter-wave resonator (see Fig. 3.1). The *Helmholtz resonator* consists of a cavity that connects to the surrounding by an (acoustically compact) neck. In analogy to a mass-spring-damper system, the fluid within the neck corresponds to the mass. The compressible gas in the backing cavity acts as the restoring spring, and viscous dissipation (e.g., friction inside the neck) damps the system. This analogy indicates the eigenfrequency as one important characteristic of acoustic resonators. It depends on geometric properties (e.g., the neck length and the backing volume) and thermophysical properties (e.g., via the speed of sound).

The *quarter-wave resonator* consists of a single tube. At its mouth, one side of the tube connects to the wall surface, whereas the other end of the tube is closed. As the name of this resonator suggests, the tube length corresponds to a quarter of the acoustic wavelength of its eigenfrequency.

The dissipative properties of acoustic resonators result from two types of losses: First, viscous friction along the walls generates *linear losses*. Second, for increased oscillation amplitudes, the fluid flow may no longer follow the sharp, edge-shaped contours at the resonator mouth and vortex shedding generates *non-linear losses*. Förner provides a comprehensive study on the quantification of non-linear losses [30]. The present thesis focuses on linear losses at low oscillation amplitudes.

The *specific acoustic impedance* describes the normalized ratio of the pressure and velocity amplitudes (p_1 and u_1 , respectively) at the resonator mouth:

$$z_{\text{res}} = \frac{1}{\rho_m c} \frac{p_1}{u_1}. \quad (3.1)$$

Note that the velocity u_1 directs in wall-normal direction (compare Fig. 3.1).

The *reflection coefficient* R_{res} relates the reflected acoustic g -wave to the incident f -wave:

$$R_{\text{res}} = \frac{g}{f} = \frac{z-1}{z+1}. \quad (3.2)$$

Both the acoustic impedance and the reflection coefficient contain equivalent information. However, the reflection coefficient may appear as the more intuitive parameter: $|R_{\text{res}}| = 1$ indicates

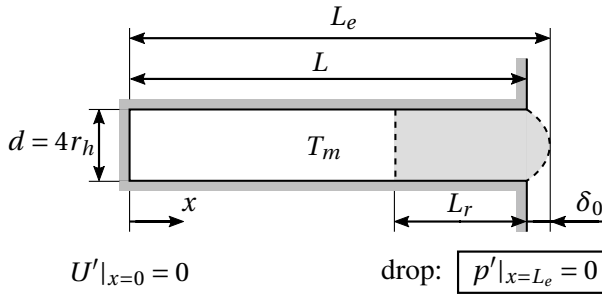


Figure 3.2: Geometry and boundary conditions of a quarter-wave resonator with geometrical length L , end correction δ_0 , and effective length L_e . Laudien et al. [8] proposed the fictive neck length L_r as a fitting parameter.

a fully reflecting boundary without losses, while $|R_{\text{res}}| = 0$ corresponds to a perfectly absorbing interface. In the range $0 < |R_{\text{res}}| < 1$, a reduced reflection occurs. Due to energy conservation, the reflection coefficient $|R_{\text{res}}|$ cannot exceed unity for a passively damped system.

3.1.1 Analytical Model by Laudien et al.

In 1896, Rayleigh [48] modeled the Helmholtz resonator as a mass-spring-damper system. Since then, many authors (see e.g., [49, 50]) have applied this analogy to describe the behavior of acoustic resonators in a semi-analytical way. This section outlines the work by Laudien et al. [8], who extended the former model to calculate the acoustic impedance of a quarter-wave resonator. Consecutive analytical and numerical studies expanded on temperature inhomogeneity along the resonator axis [9, 12].

Laudien et al. [8] devolved an acoustic model for a quarter-wave resonator. They extended a mass-spring-damper system, initially applied to the acoustically compact Helmholtz resonator [48–50], to the geometry of a quarter acoustic wavelength. The imaginary part of the specific impedance, the *reactance*, reads:

$$\text{Im}(z_{\text{res,Laud}}) = -\cot\left(\frac{\omega L_e}{c}\right), \quad (3.3)$$

and describes the ratio of pressure and velocity fluctuations in the absence of losses. The effective length L_e adjusts the geometric tube length L by an end correction δ_0 , a well-known correlation for a piston radiating into half-space [51]:

$$L_e = L + \delta_0 \approx L + \frac{4}{3\pi}d, \quad (3.4)$$

where $d = 4r_h$ is the tube diameter.¹

The real part of the specific impedance, the *resistance*, follows from the assumption of equal eigenfrequencies of the quarter-wave tube and the analogy to a Helmholtz resonator modeled

¹This – admittedly contra-intuitive – correlation follows from the definition of the hydraulic radius (compare Eq. (2.25)).

as a mass-spring-damper system:

$$\text{Re}(z_{\text{res}, \text{Laud}}) = 2 \left(1 + \epsilon_{nl} + \frac{L_r}{d} \right) \frac{\sqrt{2v\omega}}{c}, \quad (3.5)$$

where ϵ_{nl} includes non-linear effects (see e.g., [49, 52]) and L_r is the fictive neck length used as a fitting parameter [9] (compare Fig. 3.2).

$$\frac{L_r}{d} \approx 0.405 \frac{L}{d} - 0.08. \quad (3.6)$$

The model by Laudien et al. [8] includes several limitations: It (i) only holds for cylindrical ducts with small boundary layers δ_v , (ii) thermal exchange with the walls of the tube is not incorporated, and (iii) the resistance is calculated via a fictive neck-length based on an acoustically compact analogy, tuned to match eigenfrequencies. Thus, there is no continuous spatial evaluation over the resonator length. Despite its limitations, the model by Laudien et al. [8] serves for validation (Sec. 3.3) and discussion (Sec. 3.4) of the proposed novel model (Sec. 3.2).

3.2 Novel and Spatially Resolved Model

The previous Chapter 2 suggests a framework to calculate the eigenfrequencies of a quarter-wave channel depicted in Fig. 3.2: The resonator of effective length L_e (geometric length $L = L_e - \delta_0$) and diameter $d = 4r_h$ (the hydraulic radius of a tube is half the actual radius) is closed at $x = 0$ (implying $U_1|_{x=0} = 0$) and open at $x = L_e$ (implying $p_1|_{x=L_e} = 0$). Results show an exponential decay of acoustic amplitudes in time. However, this set-up is of little practical relevance. In technical applications operating at (time-averaged) steady state, resonators dissipate acoustic energy at constant (periodic) amplitudes. Obviously, the boundary conditions outlined above cannot hold: The presence of a pressure node at the resonator mouth contradicts a continuous flow rate of energy (which corresponds to the product of velocity and pressure). Thus, this assumption is dropped in the present study to allow operating conditions such that energy is conserved: The dissipated energy by the resonator equals the flow rate from the outside. The present thesis proposes a novel method to calculate the specific acoustic impedance z_{res} based on this idea. The following considerations are applied to the previous derivations with homogeneous mean temperature $dT_m/dx = 0$ (compare Sec. 2.2). However, an extension to linear mean temperature (Sec. 2.3) should be straight forward.

The boundary condition $U'|_{x=0} = 0$ at the closed end of the resonator $x = 0$ (compare e.g., Eq. 2.52) directly yields the ratio of the characteristic amplitudes \hat{F} and \hat{G} :

$$\hat{F} = \hat{G}. \quad (3.7)$$

Inserting the pressure p_1 (Eq. (2.46)) and velocity u_1 (Eq. (2.47)) into the specific impedance z_{res} (Eq. (3.1)) yields at the resonator mouth $x = L_e$:

$$z_{\text{res}} = \frac{e^{-ik_x L_e} + e^{ik_x L_e}}{-\sqrt{a^* b^*} (e^{-ik_x L_e} - e^{ik_x L_e})}. \quad (3.8)$$

Note that the direction of velocity u_1 within the resonator (according to Eq. (2.47)) opposes the wall-normal direction pointing into the resonator (compare Fig. 3.2). Therefore, the velocity u_1 is considered with the opposite sign in Eq. (3.1).

Considering the cross-sectional area jump between the resonator and the surrounding environment terminated by a hard wall ($R_{\text{wall}} = 1$, area ratio $\beta = (A_{\text{wall}} + A_{\text{res}})/A_{\text{res}}$, and $A_{\text{res}} = 4\pi r_h^2$) yields the overall reflection coefficient R [8]:

$$R = \frac{\beta z_{\text{res}} - 1}{\beta z_{\text{res}} + 1}. \quad (3.9)$$

This transformation incorporates the corresponding velocity jump across the area change.

The incident acoustic wave (index $+$) reaches the wall-resonator interface at $x = L_e^+$ with the amplitude \hat{G}^+ . The previous characteristic derivations for the pressure p' (Eq. (2.46)), velocity u' (Eq. (2.47)), and wavenumber k_x (Eq. (2.44)) are also valid outside of the resonator tube and significantly simplify within this inviscid and non-heat-conductive environment: $a^* = b^* = 1$. It directly follows that at $x = L_e$:

$$\hat{F}^+ = R\hat{G}^+ \quad (3.10)$$

and

$$\left. \frac{p'}{\rho c} \right|_{x=L_e} = (1 + R) \frac{\hat{G}^+}{2}. \quad (3.11)$$

Note: For the modeling of the end correction δ_0 , an equivalent (slightly longer) resonator of length L_e – that does not require an end correction – is considered. Thus, the front wall (resonator-to-environment interface) lies at position $x = L_e$. The end correction is required to include multi-dimensional effects at the resonator mouth, whereas the underlying framework of an (zero-dimensional) area jump neglects these effects.

The acoustic pressure p' does not change across the area jump at the resonator mouth. Thus, the specific values for $\hat{F} = \hat{G}$ follow from the pressure coupling condition at the mouth of the resonator ($x = L_e$):

$$\hat{F} = \hat{G} = \frac{(1 + R)\hat{G}^+}{\exp\left(-i\omega\sqrt{\frac{b^*}{a^*}}\frac{L}{c}\right) + \exp\left(i\omega\sqrt{\frac{b^*}{a^*}}\frac{L}{c}\right)}. \quad (3.12)$$

The two loss mechanisms of the present model are attributed to hydrodynamic and thermal wall interaction along the complete resonator axis: (i) within the hydrodynamic boundary layer, energy is reduced via viscous dissipation, and (ii) within the thermal boundary layer, energy is reduced via a heat flux between the fluid and wall. The model does not account for non-linear losses (i.e., generated by vortex shedding at the edges of the resonator mouth). The incorporation of such effects (e.g., via the coefficient ϵ_{nl} , compare Eq. (3.5)) would require modifications of the “jump condition” at the discrete location of the resonator mouth ($x = L_e$) and is not further examined in the present thesis.

3.3 Validation

In this section, the present model is validated against the analytical framework by Laudien et al. [8] (which is validated against experimental results) and against numerical results by van

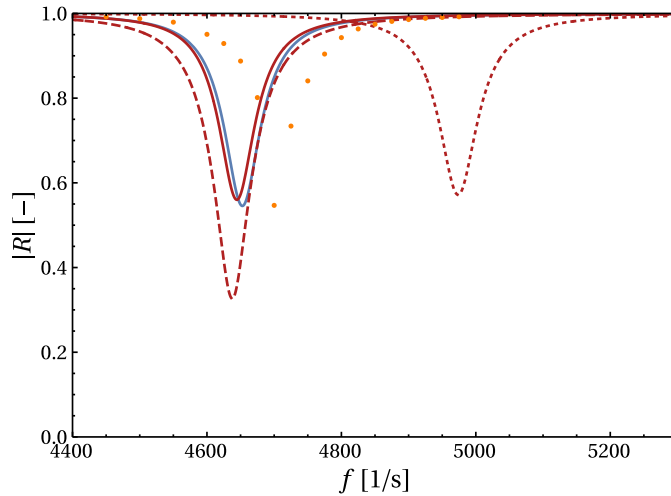


Figure 3.3: Validation of the magnitude of the reflection coefficient R vs. the frequency f . Analytical results (—) by Laudien et al. [8], numerical results (●) by van Buren et al. [12], and the present model: end correction and adiabatic walls (—), end correction and isothermal walls (---), and no end correction and adiabatic walls (.....).

Buren et al. [12] (see Sec. 5.1, reproduced in the Appendix on p. 113 ff.). The validation is restricted to thin hydrodynamic boundary layers compared to the tube diameter: $\delta_v \ll d$, a restriction that applies to the model by Laudien et al. [8]. Nevertheless, the underlying framework of characteristic acoustic waves with losses (Sec. 3.1) is validated against the conservation equations of Rott's thermoacoustic theorem (see Sec. 2.4.4).

The validation set-up corresponds to the study by van Buren et al. [12] (see Sec. 5.1, reproduced in the Appendix on p. 113 ff.) at the spatially constant temperature $T_m = 647\text{ K}$. Figure 3.3 depicts the magnitude of the reflection coefficient R vs. the frequency f . Applying the end correction to the present model (---), the results show very good agreement with existing analytical results (—, Laudien et al. [8]) and good agreement with numerical results (●, van Buren et al. [12]). The dotted red line (.....) illustrates the influence of the small fluid portion in front of the resonator mouth: not accounting for the end correction leads to a shift in eigenfrequency. Note that the end correction has a predominant effect at large tube diameters d compared to the geometric length L . For the latter results where $d \ll L$, this effect is (close to) negligible.

Also, note the influence of fluid-wall heat exchange (---) that significantly affects the reflection amplitude. Laudien et al. [8] and van Buren et al. [12] assume adiabatic walls, which implies $\delta_\kappa \rightarrow 0$ ($f_\kappa \rightarrow 0$ and $a^* \rightarrow 1$). The present model allows to drop this restriction and, thus to consider thermal boundary layer effects.

3.4 Results

3.4.1 Parametric Set-Up

The effective resonator length is $L_e = 4\text{ m}$ at a mean temperature of $T_m = 300\text{ K}$. The mean pressure along the resonator is $p_m = 101325\text{ Pa}$. Following the study of the previous Chapter 2, air-specific values for the heat capacity ratio $\gamma = 1.4$ and the gas constant $R = 287.5 \frac{\text{m}^2}{\text{s}^2\text{K}}$ are selected.

Evaluating the effect of viscous and thermal boundary layers, this work investigates acoustics in a circular tube geometry with a hydraulic radius r_h . The hydraulic radius r_h controls the impact that the boundary layers exerts on the fluid, whereas the kinematic viscosity $\nu = 1.516 \times 10^{-5} \frac{\text{m}^2}{\text{s}}$ and the Prandtl number $Pr = \nu/\kappa = 0.711$ are constant. The initial condition of the incident acoustic wave is $\hat{G}^+ = 1 \frac{\text{m}}{\text{s}}$. The present study covers three different area jumps to the environment with $\beta = 1, 10$, and 100 . The limit of $\beta = 1$ describes a transition from the tube (wall-effects) to the surrounding region (no wall-effects) without an area jump (e.g., a thermoacoustic stack). For the application of resonator rings in combustion chambers, $\beta = 10$ is selected. Finally, $\beta = 100$ characterizes a large area jump as it may be found in acoustic liners and as it was applied in numerical studies by van Buren et al. [12] (see Validation in Sec. 3.3).

3.4.2 Evaluation of Reflection Coefficient and Impedance

First, results that include hydrodynamic and thermal boundary layers are presented. Figure 3.4 shows the magnitude of the reflection coefficient R (first row), resistance $\text{Re}(z)$ (second row), and reactance $\text{Im}(z)$ (third row) vs. the angular frequency ω and the hydraulic radius r_h . From left to right, three different area ratios $\beta = 1, 10$, and 100 are selected. Minimum reflection occurs when the specific resistance $\text{Re}(z) = 1$ and the specific reactance $\text{Im}(z) = 0$ (— in the corresponding plots). The optimal resistance shifts to larger radii r_h with an increasing area ratio β . Furthermore, the gradient in reactance increases. Overall, these two dominant changes in resistance and reactance impact the reflection coefficient as follows: (i) a shift of minimum reflection towards larger radii r_h (i.e., due to the reduced impact of viscosity) while the frequency ω is almost unaffected and (ii) a narrowing bandwidth in frequency ω while the bandwidth in the hydraulic radius r_h is almost unaffected. The blue dots (•) indicate the parametric set-ups of the latter discussion of the acoustic profiles (see Sec. 3.4.3). Furthermore, the central blue dot (•) indicates the parametric set-up of minimum reflection in each plot (also compare Table 3.1).

Second, Figure 3.5 excludes the effects of thermal boundary layers, making the results more comparable to the model by Laudien et al. [8]. The specific reactance is almost unaffected by the lack of thermal exchange. However, the resistance changes, particularly at low frequencies ω and large area ratios β . Consequently, the parametric set-up of minimum reflection shifts to smaller hydraulic radii r_h for $\beta = 10$ and 100 . This observation agrees well with the validation section, where the thermal boundary layers affects the amplitude of the reflection coefficient R , but not the frequency ω .

For completeness, Fig. 3.6 shows the corresponding contour maps calculated with the model by

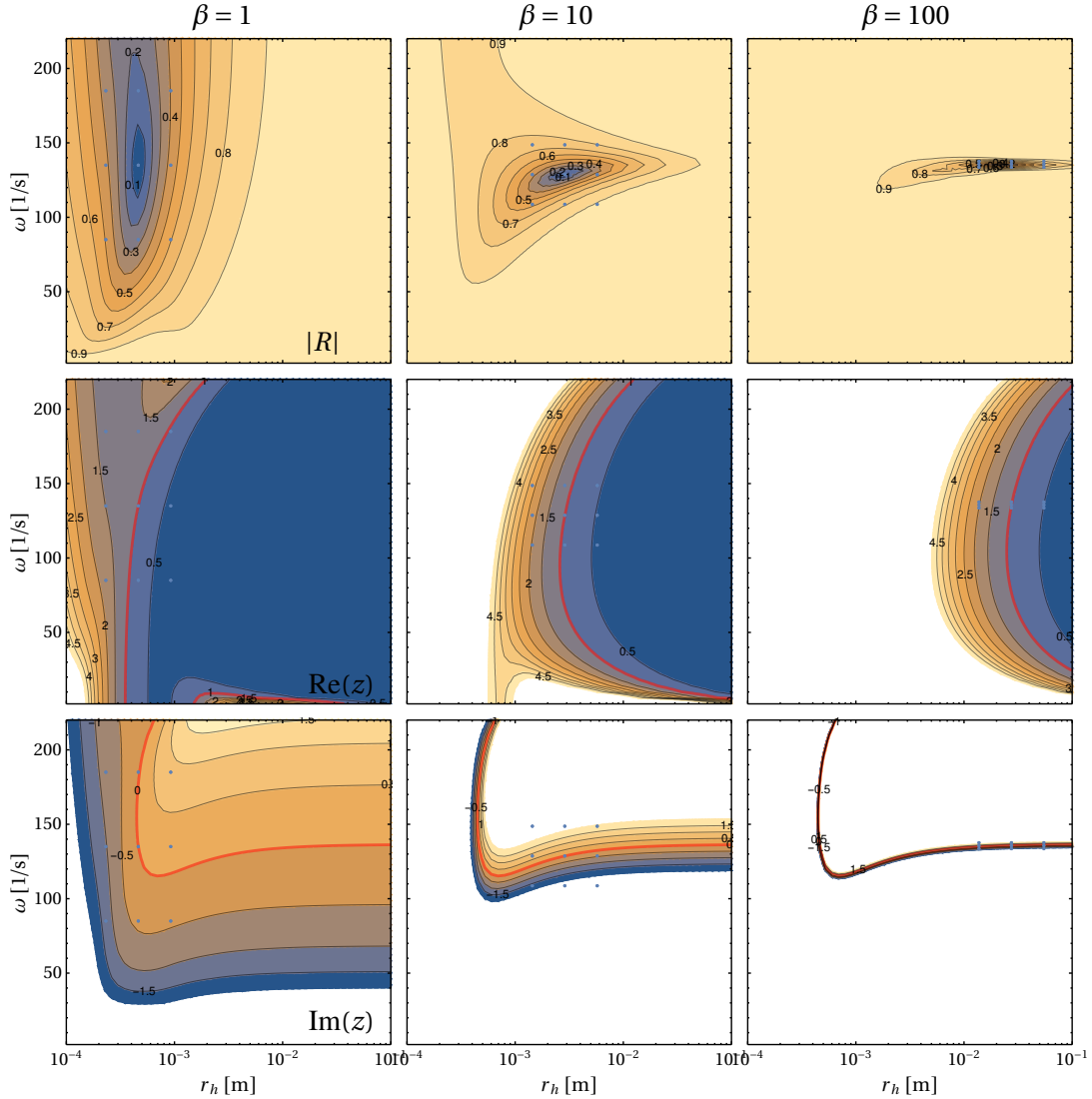


Figure 3.4: Model of the present study: Reflection coefficient $|R|$ (first row), specific resistance $\text{Re}(z)$ (second row), and specific reactance $\text{Im}(z)$ (third row) vs. the frequency ω and hydraulic radius r_h . From left to right, three different area ratios $\beta = 1, 10$, and 100 are shown. The blue dots (\bullet) indicate the parametric set-ups of the latter discussion of the acoustic profiles (see Sec. 3.4.3). Furthermore, the central blue dots indicate the parametric set-ups of optimal damping ($|R| = 0$).

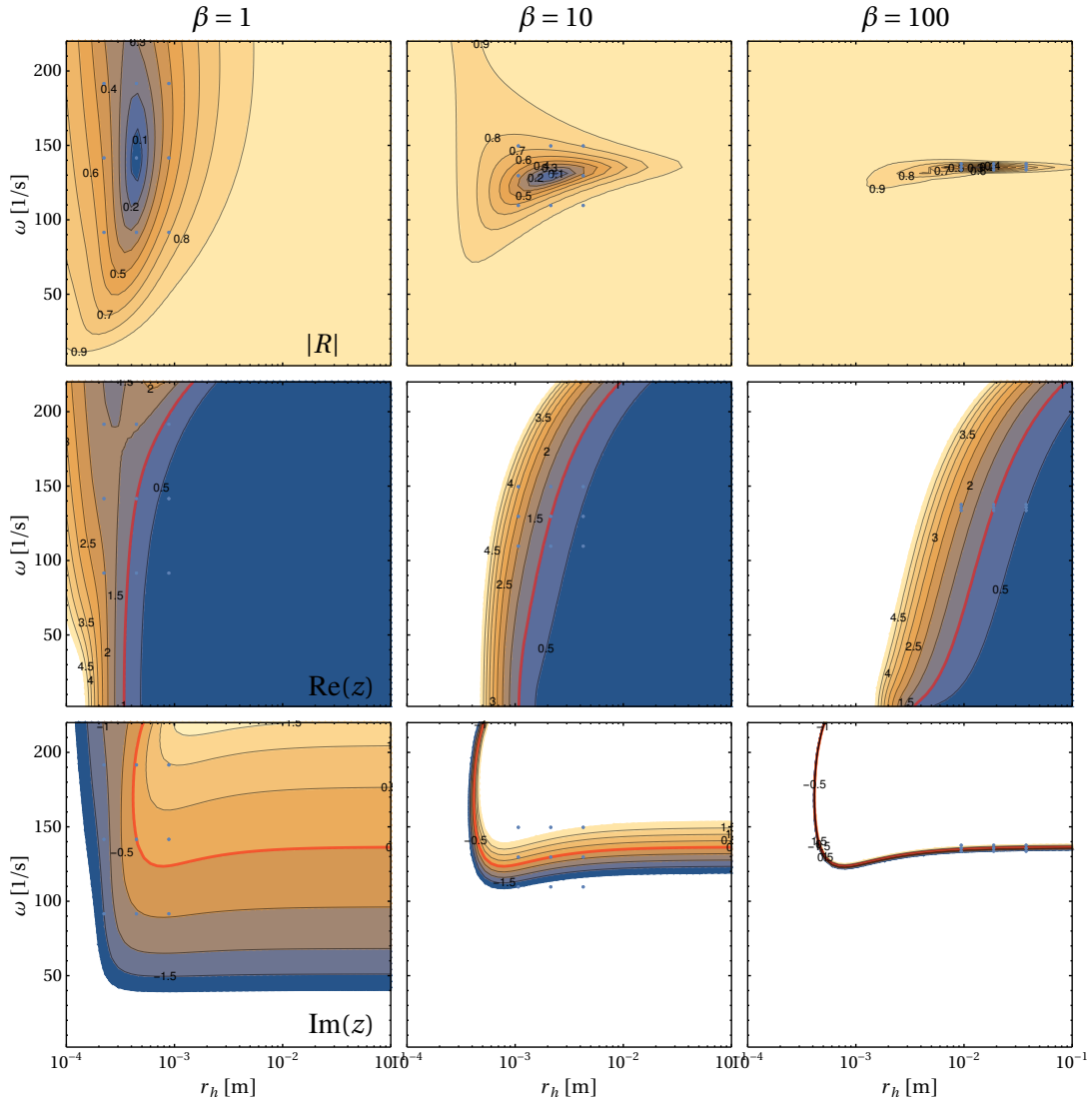


Figure 3.5: Model of the present study without thermal boundary layer: Reflection coefficient $|R|$ (first row), specific resistance $\text{Re}(z)$ (second row) and specific reactance $\text{Im}(z)$ (third row) vs. the frequency ω and hydraulic radius r_h . From left to right, three different area ratios $\beta = 1, 10$, and 100 are shown.

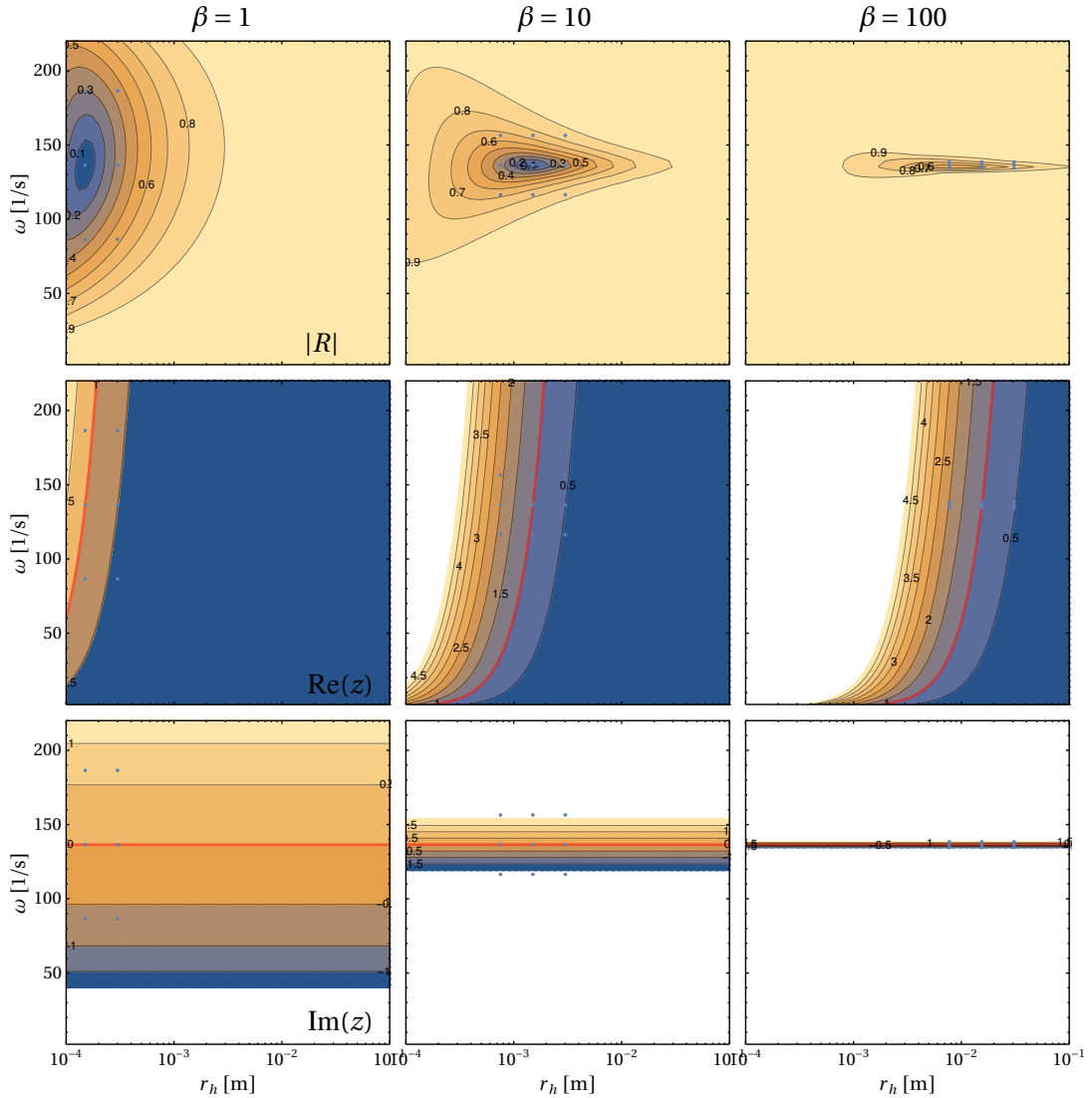


Figure 3.6: Model by Laudien et al. [8]: Reflection coefficient $|R|$ (first row), specific resistance $\text{Re}(z)$ (second row) and specific reactance $\text{Im}(z)$ (third row) vs. the frequency ω and hydraulic radius r_h . From left to right, three different area ratios $\beta = 1, 10$, and 100 are shown.

β	$\omega \left[\frac{1}{\text{s}} \right]$			$r_h [\text{m}]$		
	complete	no thermal	Laudien	complete	no thermal	Laudien
1	135.00	141.58	136.46	4.629e-4	4.448e-4	1.501e-4
10	128.70	129.65	136.46	2.876e-3	2.134e-3	1.505e-3
100	135.60	135.61	136.46	2.744e-2	1.880e-2	1.543e-2

Table 3.1: Parametric set-up of minimum acoustic reflection for the (i) complete model (Fig. 3.4), the (ii) adjusted model with no thermal boundary layers (Fig. 3.5), and the (iii) model by Laudien et al. [8] (Fig. 3.6).

Laudien et al. [8]. Clear deviations exist at low radii r_h , which result from the assumption of thin hydrodynamic boundary layers ($\delta_v \ll r_h$) implied by Laudien et al.: Close to eigenfrequency $\omega_0 = 136.46 \frac{1}{\text{s}}$, the hydrodynamic boundary layer is $\delta_v \approx 0.015 \text{ m}$. In the vicinity of minimum reflection, this obviously contradicts the assumption of relatively small boundary layers for the two instances with area ratios of $\beta = 1$ and $\beta = 10$ where the tube diameter is $d \approx 0.0006 \text{ m}$ and $d \approx 0.006 \text{ m}$, respectively. Only results for $\beta = 100$ with $d \approx 0.06 \text{ m}$ approach the assumption. Thus only for $\beta = 100$ the model by Laudien and coworkers yields potentially accurate results.

Table 3.1 summarizes the parametric set-up of minimum acoustic reflection for the three models presented above.

3.4.3 Evaluation of Spatial Pressure and Velocity Profiles

The present section focuses on the novel model with viscous and thermal losses (i.e., compare to the results of Fig. 3.4). Figures 3.7 to 3.14 show spatially resolved profiles for the pressure p_1 and velocity U_1/A and for the characteristic acoustic f and g -waves. Each complex-valued profile is presented via its magnitude and phase. Figures 3.7 to 3.10 correspond to the geometry without an area jump (i.e., $\beta = 1$) and Figs. 3.11 to 3.14 to $\beta = 10$. The central plot of each figure presents the parametric set-up of minimum acoustic reflection (i.e., $|R| \approx 0$). To the left and right, the hydraulic channel width r_h varies by the factors $10^{-0.3}$ and $10^{0.3}$, respectively. To the top and bottom, the angular frequency varies by $\pm 50 \frac{1}{\text{s}}$ ($\beta = 1$) and $\pm 20 \frac{1}{\text{s}}$ ($\beta = 10$). The blue dots (•) in Fig. 3.4 mark the nine selected parametric set-ups from Fig. 3.7 through 3.14.

The physical quantities of pressure p_1 and velocity U_1/A ($\beta = 1$, magnitude: Fig. 3.7 and phase: Fig. 3.8) show a few characteristics worth mentioning: First, note that the pressure (—) and the velocity (---) are contentiously resolved in space. Neither the magnitude nor the phase shows discontinuities, particularly not at the front interface at $x = 4 \text{ m}$. Second, the acoustic velocity diminishes at the backing wall of the resonator ($x = 0 \text{ m}$).

In front of the resonator ($x > 4 \text{ m}$) and for the non-reflecting interface ($|R| = 0$, central plot in Fig. 3.7), the magnitude of the normalized pressure and velocity is spatially constant and equals $|p_1|/(\rho c) = |U_1|/A = \hat{G}^+/2 = 0.5 \frac{\text{m}}{\text{s}}$ (there is no reflected f -wave). This corresponds to a purely traveling acoustic g -wave. For the remaining instances with $0 < |R| < 1$, pressure and velocity show wavy characteristics without pressure and velocity nodes. The reflected f -wave is of lower magnitude than the incident g -wave. The product of pressure p_1 and velocity u_1 scales with the rate of dissipated energy within the resonator and is larger than zero at the resonator mouth.

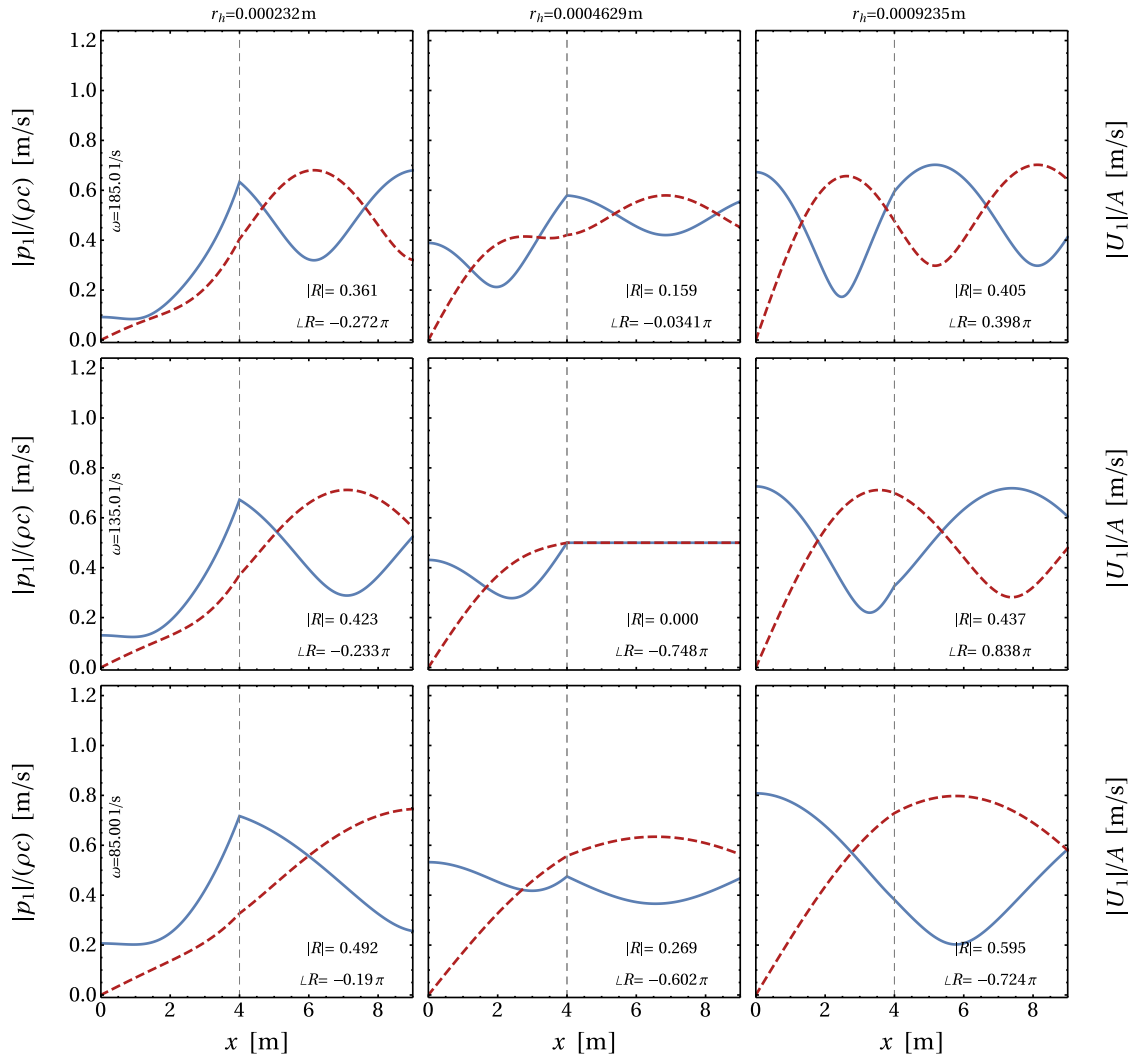


Figure 3.7: Magnitude of normalized pressure $|p_1|/(\rho c)$ (—) and velocity $|U_1|/A$ (- - -) for $\beta = 1$.

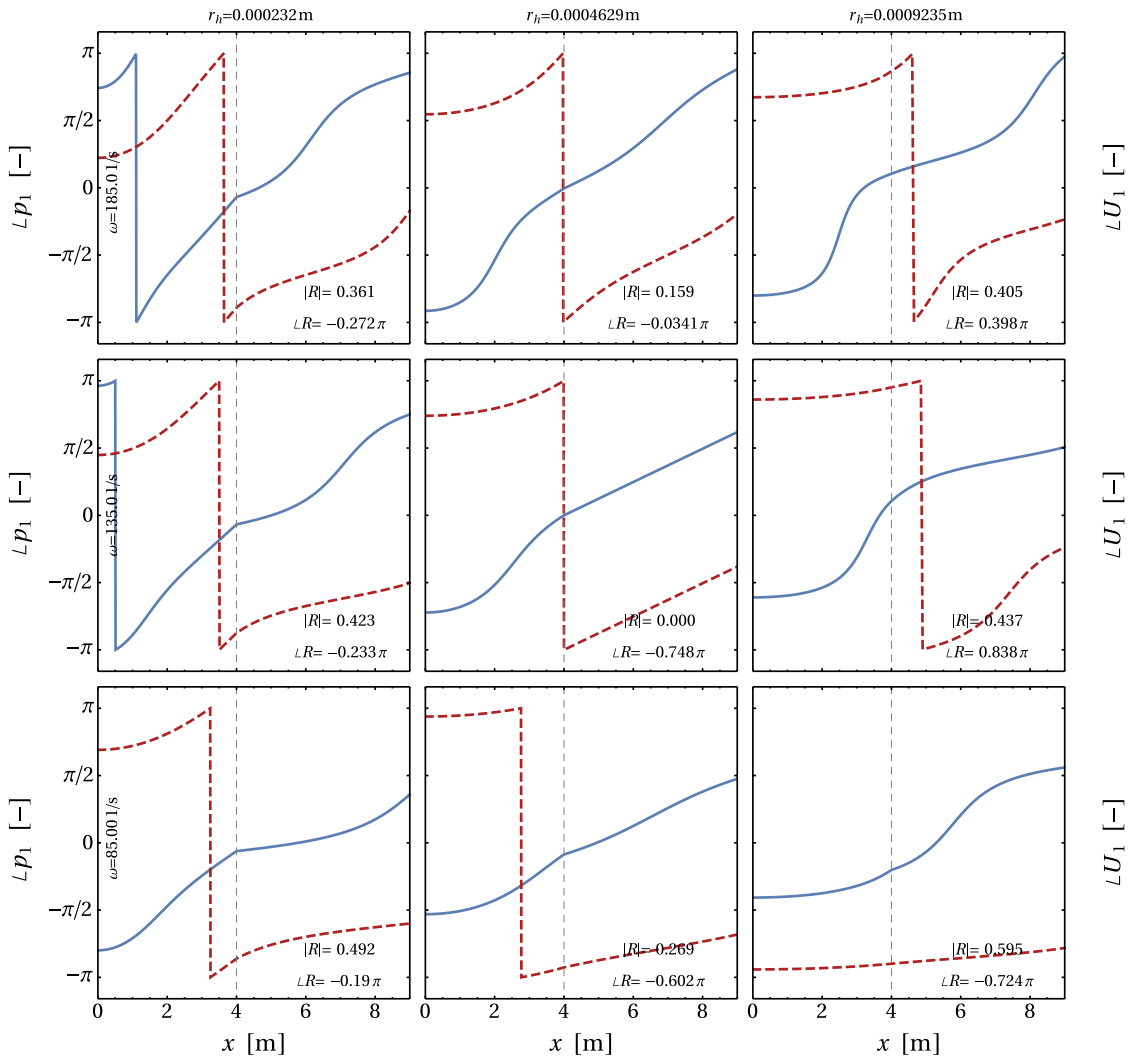


Figure 3.8: Phase of pressure $\angle p_1$ (—) and velocity $\angle U_1$ (- - -) for $\beta = 1$.

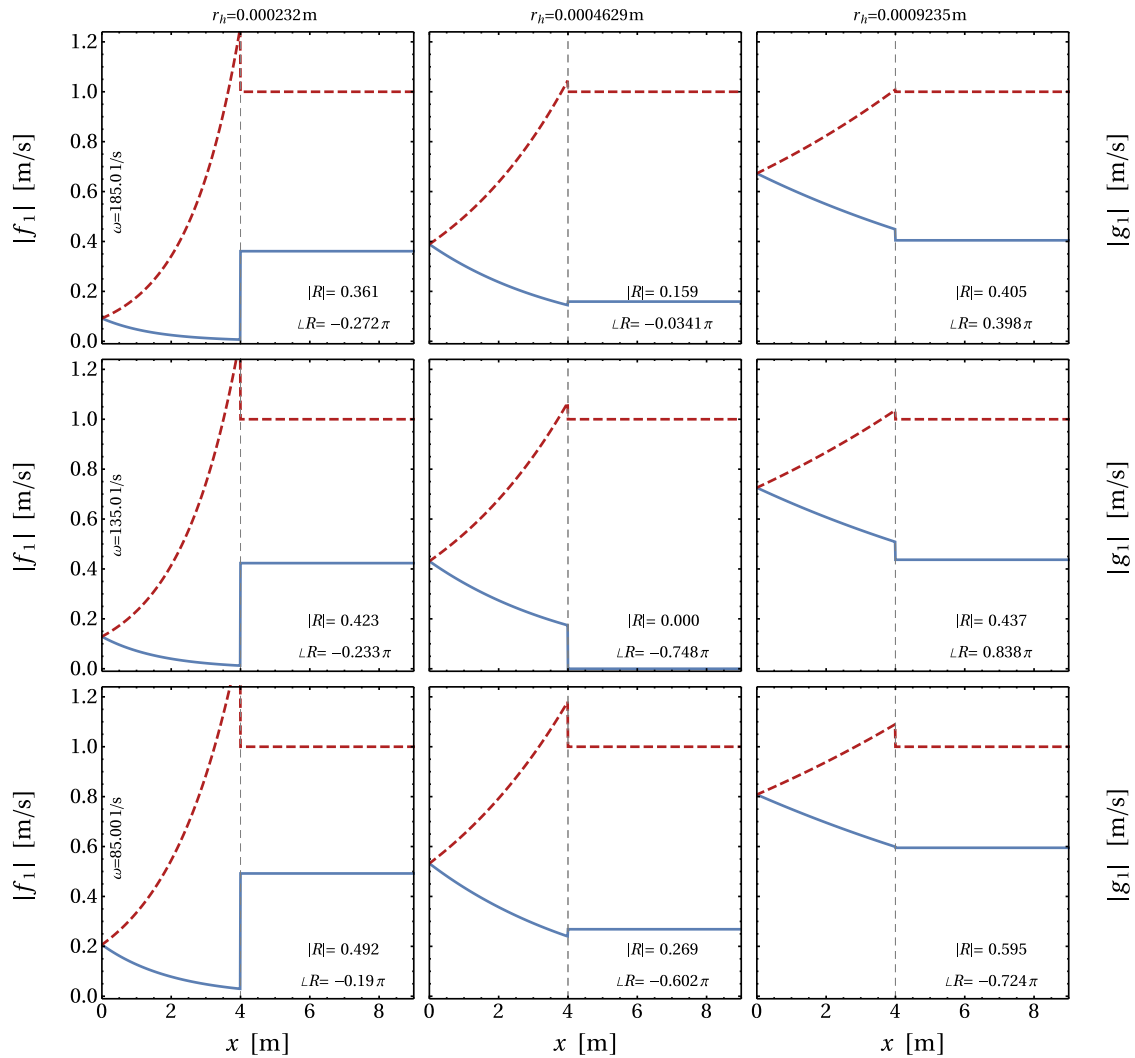


Figure 3.9: Magnitude of the characteristic waves $|f|$ (—) and $|g|$ (- - -) for $\beta = 1$.

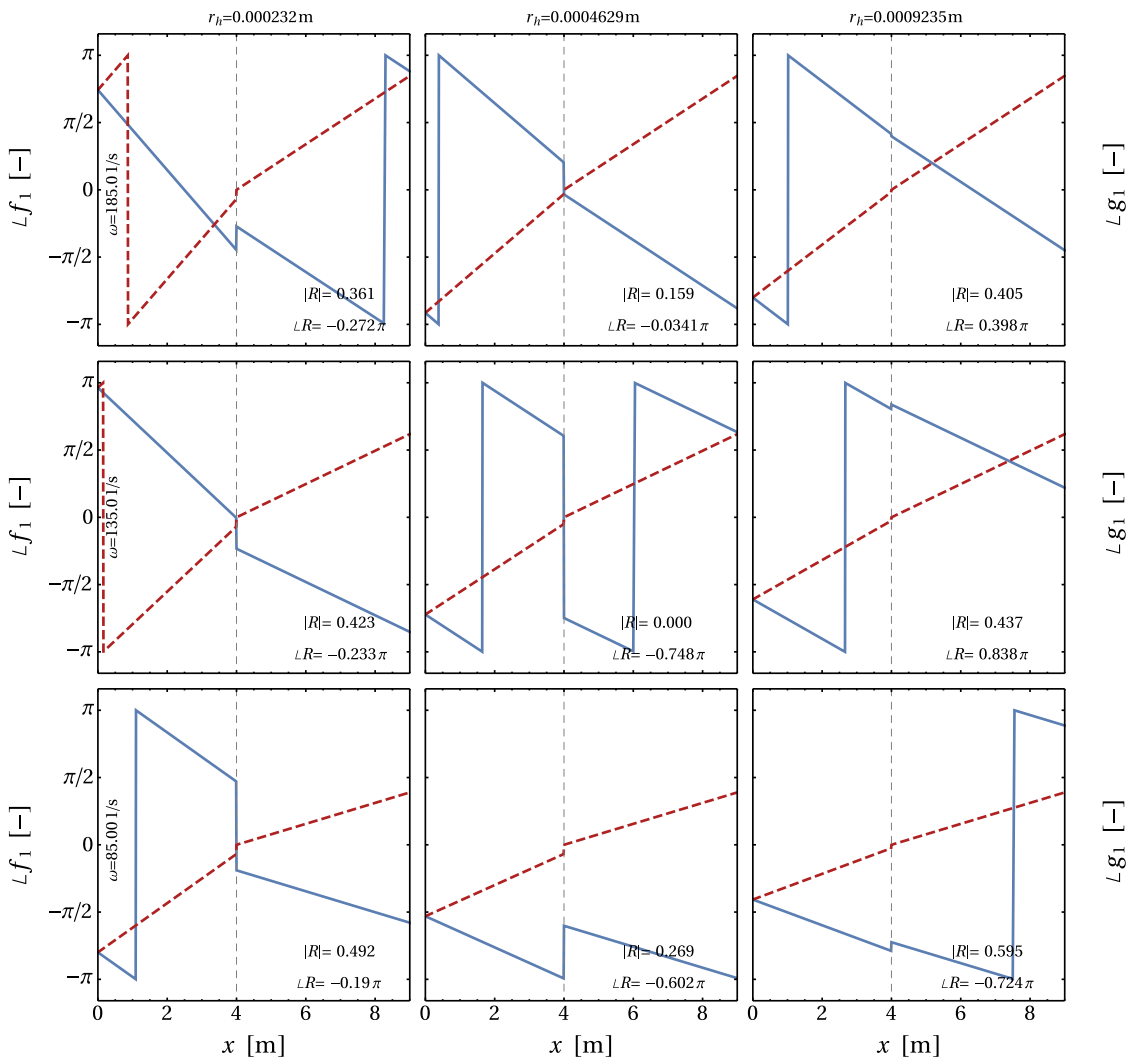


Figure 3.10: Phase of the characteristic waves $\angle f$ (—) and $\angle g$ (---) for $\beta = 1$.

Turning to the phase diagrams (Fig. 3.8), the central case on a non-reflecting boundary yields a constant spatial change in the phase of pressure p_1 and velocity u_1 in front of the resonator. Again, this indicates a purely traveling acoustic wave, where pressure and velocity maxima travel with the speed of sound c .

Figures 3.9 and 3.10 show the corresponding characteristic f and g -waves. The incident g -wave (---) travels from right-to-left and the reflected f -wave (—) from left-to-right. Outside of the resonator ($x > 4\text{ m}$), the flow is isentropic. Thus the magnitude of the two characteristic waves is spatially constant. Its ratio yields the reflection the magnitude of the reflection coefficient R . Inside the resonator tube ($x < 4\text{ m}$), the viscous and thermal dissipation yields an exponential spatial decay in magnitude. Moving to the left plots of Fig. 3.9, smaller hydraulic radii r_i induce higher losses and thus a stronger decay. At the hard backing wall of the resonator ($x < 0\text{ m}$) with $R_{\text{wall}} = 1$, a continuous transition from g to f -wave shows.

Within each domain (resonator tube and isentropic environment) the characteristic waves travel with constant speed (compare constant slopes in Fig. 3.10). They correspond to the phase speed and the speed of sound, respectively. For narrow resonator tubes with small hydraulic radii r_h , note the more significant change towards a steeper slope, indicating a more decreased phase velocity.

Figures 3.11 to 3.14 extend to the area jump corresponding to $\beta = 10$. Most discussions agree with those of the previous set-up ($\beta = 1$). Thus, this section highlights the relevant differences.

Inside the resonator, the area jump $\beta = 10$ leads to a strong increase of the magnitude in pressure $|p_1|$ and velocity $|U_1|/A$ (Fig. 3.11, note the normalization by the area ratio $\beta = 10$ inside the resonator). This increases the dissipation rate and balances the increased incident acoustic energy due to the increased area of the environment. The area jump leads to a discontinuity in the magnitude of the velocity profile. The magnitude of the pressure, as well as the phase of pressure and velocity (Fig. 3.12), show continuous transitions over the resonator-environment interface.

At the area ratio $\beta = 10$, the magnitude of the characteristic f and g -waves (Fig. 3.13) clearly deviates from the results obtained at $\beta = 1$: Figure 3.4 reveals that the area jump significantly increases the optimum hydraulic radii h_r for minimum acoustic reflection. Thus, the spatial decay of the in-traveling g -wave to the out-traveling f -wave clearly decreases. The characteristics within the resonator tube approach those of a standing acoustic wave. This conclusion also shows in Fig. 3.11, where the pressure amplitude p_1 converges to a pressure node. The slopes in the characteristic phase (Fig. 3.14) reveal the (close to) accordance between phase velocity and the speed of sound.

The finding of overall (close to) standing wave characteristics generates important insight for future work. E.g., the derivation of longitudinal heat transfer within the resonator may build on the underlying pressure and velocity oscillations of a standing wave.

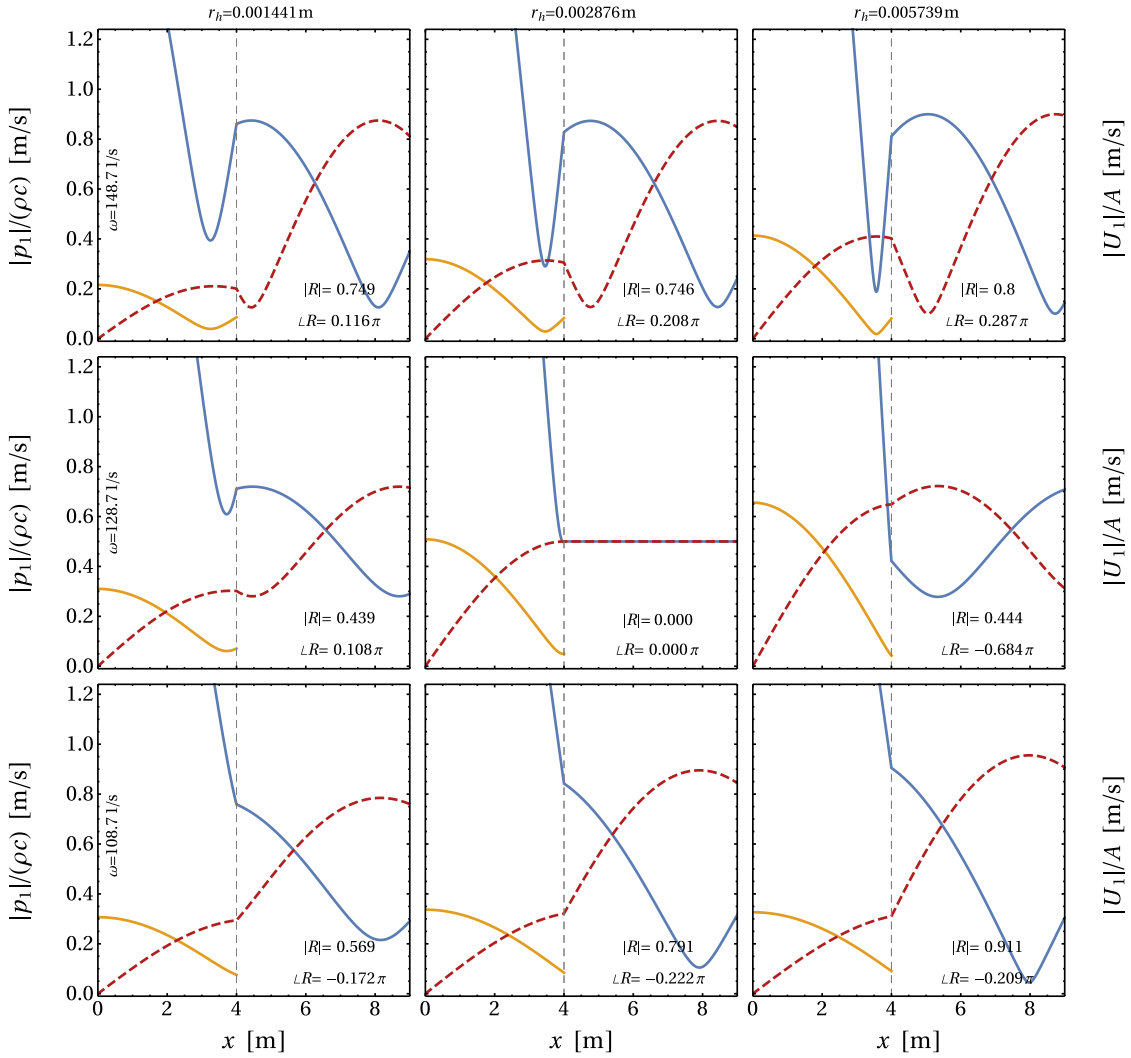


Figure 3.11: Magnitude of normalized pressure $|p_1|/(\rho c)$ (— and —) and velocity $|U_1|/A$ (---) for $\beta = 10$. The velocity (---) and pressure (—) are normalized by the area ratio $\beta = 10$ within the resonator ($x < 4 \text{ m}$).

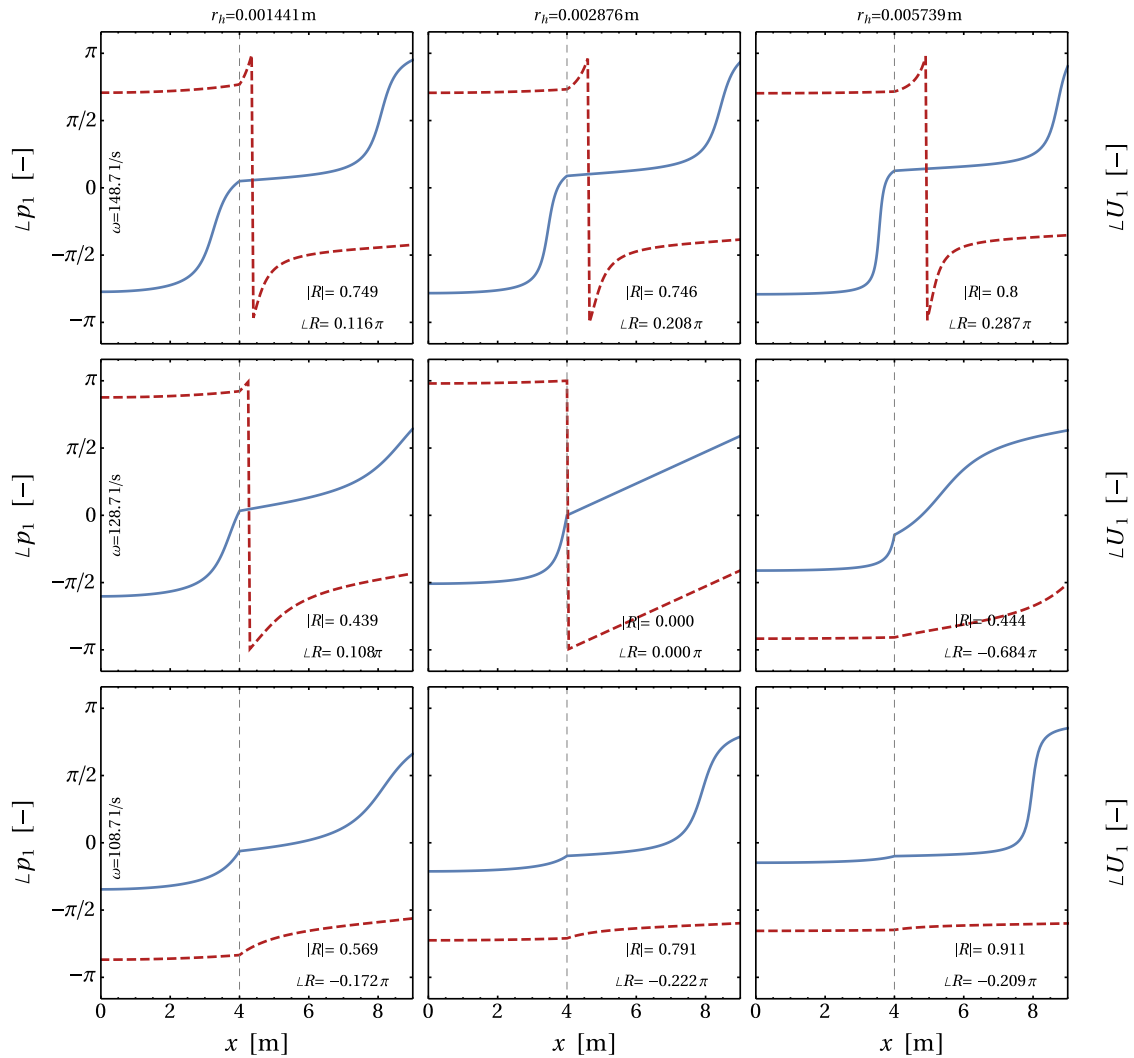


Figure 3.12: Phase of pressure $\angle p_1$ (—) and velocity $\angle U_1$ (- - -) for $\beta = 10$.

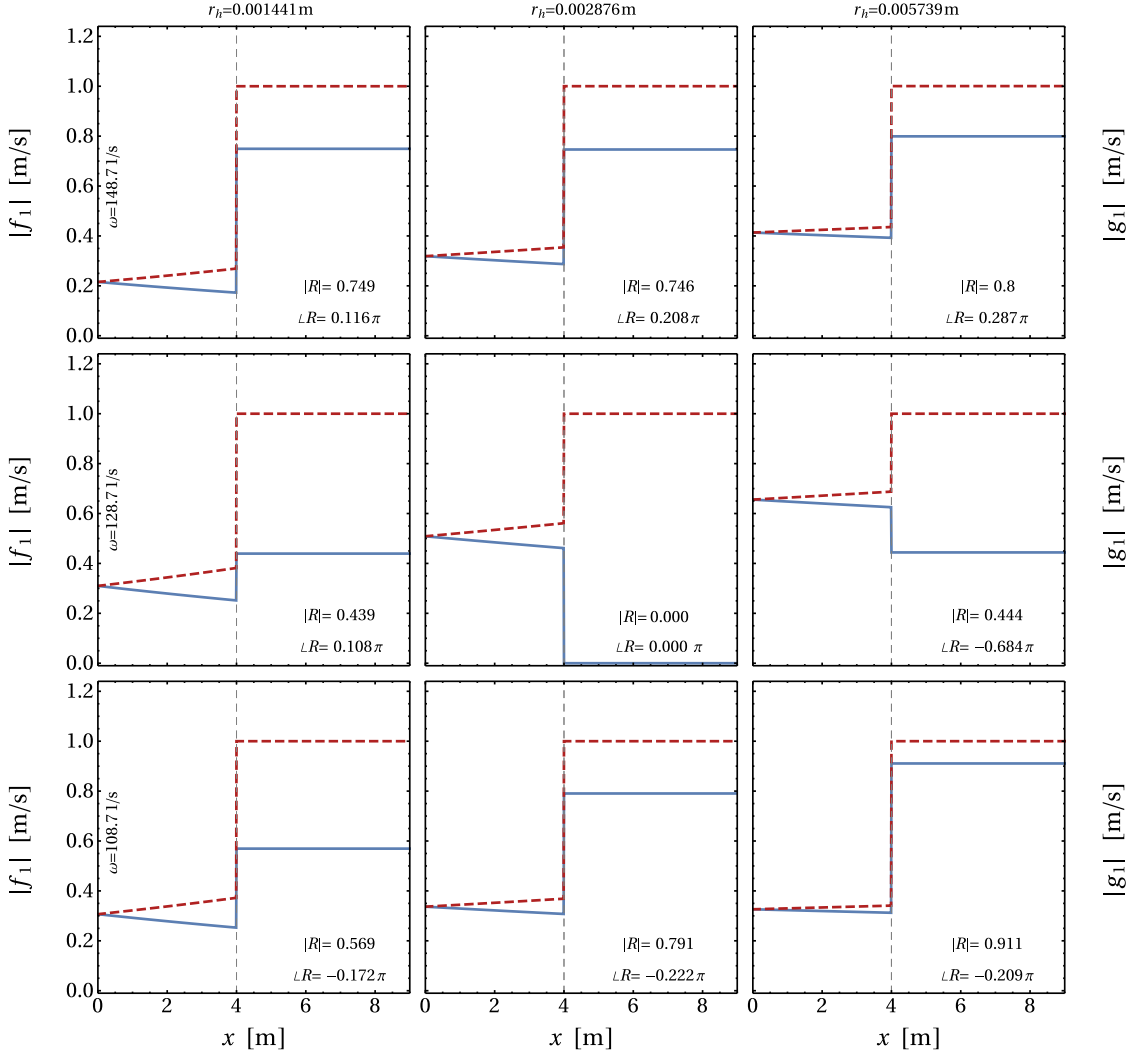


Figure 3.13: Magnitude of the characteristic waves $|f|$ (—) and $|g|$ (---) for $\beta = 10$. Within the resonator ($x < 4\text{ m}$) the characteristic waves are normalized by the area ratio $\beta = 10$.

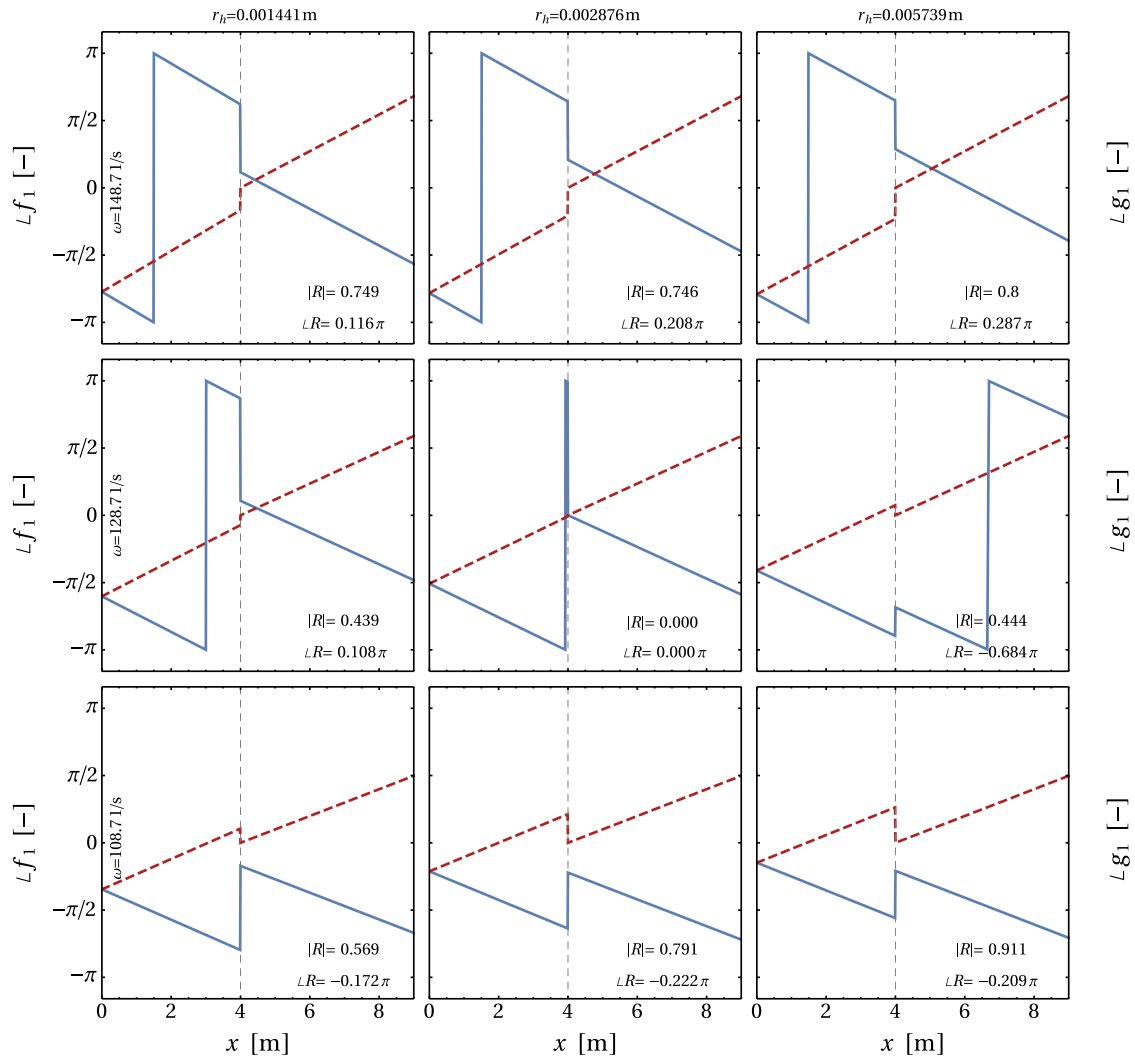


Figure 3.14: Phase of the characteristic waves $\angle f$ (—) and $\angle g$ (- - -) for $\beta = 10$.

3.5 Summary and Conclusions on the Novel Model of a Quarter-Wave Resonator

The present work develops a novel analytical model for acoustic quarter-wave resonators. The study accounts for viscous and thermal losses formulated in Rott's thermoacoustic theory. Unlike existing models from the literature, the present framework continuously evaluates the spatial acoustic properties along the resonator tube. The separate treatment of hydrodynamic and thermal boundary layers allows modeling adiabatic as well as isothermal resonator walls.

The present model is validated against the analytical model by Laudien et al. [8] and numerical results by van Buren et al. [12]. Thereby, the significant impact of wall-to-fluid heat transfer is revealed. Furthermore, the importance of an end correction shows.

The study reports overall acoustic characteristics of the resonator (acoustic impedance z and reflection coefficient R) over a wide parametric range. Local pressure and velocity fluctuations are carefully discussed. The presentation as characteristic waves reveals an important insight for future studies: At larger area jumps (e.g., $\beta \geq 10$, typical in many technical applications), the dissipation within the resonator is primarily generated by high oscillation amplitudes rather than a strong spatial decay. Thus, consecutive studies may also use inviscid approaches to estimate the acoustic profiles of a standing wave.

The present model considers spatially constant temperature profiles within the resonator. Based on previous derivations in Sec. 2.3, future work may extend the framework to linear temperature profiles. Such temperature inhomogeneities are of particular interest in rocket engine combustion chambers, where extreme temperature gradients exist between the hot combustion products and the regeneratively cooled chamber walls. Section 5.1 presents the numerical framework of a publication [12] that quantifies the influence of the local temperature distribution on the acoustic damping performance of a quarter-wave resonator.

4 Heat Transfer in Resonators

The present chapter focuses on longitudinal heat transfer inside a quarter-wave resonator. A comprehensive understanding of the thermal mechanisms in oscillating flows is of particular relevance for the derivation of accurate temperature distributions required for the subsequent calculation of the acoustic performance (compare Chapter 3).

The first part of the present chapter compares analytical work by Kurzweg [27] with the thermoacoustic theory by Rott [38]. Kurzweg studied longitudinal heat transfer in incompressible oscillating channel flows between parallel plates via the effective longitudinal thermal diffusivity (Sec. 4.1.1). Subsequent simplifications are proposed in Sec. 4.1.2. Rott quantified the so-called total power as an important measure for thermoacoustics (Sec. 4.1.3). This power is not acoustic power, not heat and not mechanical power, but a more subtle quantity: Imagine a control volume around an adiabatic stack. In a steady state and time-averaged over an integral number of acoustic cycles, the energy inside the system needs to be preserved. Thus the rate of total power inflow must be equal to the outflow rate. In direct comparison, the formulation by Kurzweg benefits from a more general wall-temperature setting that evaluates conjugate heat transfer in the fluid and the wall. On the other hand, Rott's theory considers pressure fluctuations. The comparison of the two approaches gives insight into the individual strengths of each approach. In particular, the respective field of application (incompressible/compressible, transient wall temperatures, etc.) becomes apparent.

In Sec. 4.2, the present thesis shows that both studies (Kurzweg and Rott, respectively) analytically yield the same results for the total power flow rate within a shared range of applicability (location of a pressure node and a temporally constant wall temperature). A numerical examination over a wide range of parameters reveals that both velocity- or pressure-related energy transfer may dominate in a standing wave (e.g., in a quarter-wave resonator, Sec. 4.3).

Section 5.2 presents a publication [53] and concludes with a theoretical investigation of the prevailing heat transfer mechanisms that define the problem at hand. The interplay of the hydrodynamic and thermal boundary layers is analyzed in more detail in this context.

4.1 Summary of the Analytical Approaches

The first part of the present chapter provides an overview of Kurzweg's work (Sec. 4.1.1) and proposes simplifications (Sec. 4.1.2). An introduction of Rott's total power follows in Sec. 4.1.3.

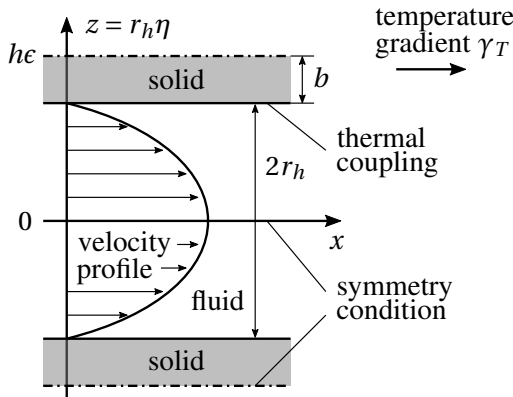


Figure 4.1: Heat transfer in oscillating channel flow as studied by Kurzweg [27].

4.1.1 Effective Thermal Diffusivity by Kurzweg

In 1985, Kurzweg analytically investigated the longitudinal heat transfer in oscillating channel flows [27]. His motivation derived from numerous studies that reported enhanced axial dispersion of passive scalars – such as contaminations – induced by oscillations [54–57]. Theoretical [58] and experimental studies [59] support Kurzweg’s work. In subsequent studies, researchers elaborated on analyzing the so-called *dream pipe*, a bundle of capillary heat transfer tubes [60–63]. The technical relevance for the industrial field is shown, e.g., by the topical work of Bothien and Wassmer [64] (influence of the temperature on the damping characteristics of a Helmholtz resonator) or Ćosić et al. [65] (concentration gradients in resonator tubes).

For the analytical derivation of the *effective thermal diffusivity* κ_e , Kurzweg considered oscillating channel flow under the following assumption [27]:

- the oscillating channel flow is laminar and incompressible,
- the set-up is two-dimensional,
- the heat transfer in the wall and channel flow is coupled (conjugate heat transfer),
- the velocity oscillation follows the exact solution of the “Stokes problem”,
- the heat transfer mechanisms are heat conduction (axial and radial) in the wall, and
- heat conduction (axial and radial) as well as convective (axial) heat transfer in the fluid.

Figure 4.1 depicts the set-up under investigation: Two parallel solid walls confine a fluid channel of width $2r_h$ in the z -direction. The non-dimensional position normal to the wall reads $\eta = z/r_h$ with the symmetry-line of the channel located at $z = \eta = 0$. Both walls are of thickness $2b$ and periodically adjoin neighboring fluid channels, yielding the indicated symmetry condition. The *wall-to-channel ratio* ϵ is an important geometrical parameter of the configuration:

$$\epsilon \equiv \frac{b + r_h}{r_h} . \quad (4.1)$$

Assuming harmonically oscillating laminar flow driven by the *non-dimensional pressure gradient*

$$\lambda \equiv \frac{|\partial p / \partial x| r_h^2}{\rho u_0 v}, \quad (4.2)$$

the axial velocity u is given by the real part of the harmonic oscillation

$$u(\eta, t) = u_0 f(\eta) e^{i\omega t} = u_0 \frac{i\lambda}{\alpha^2} \left[1 - \frac{\cosh(\sqrt{i}\alpha\eta)}{\cosh(\sqrt{i}\alpha)} \right] e^{i\omega t}, \quad (4.3)$$

where u_0 is a *representative velocity* and α the *Womersley number*:

$$\alpha \equiv r_h \sqrt{\frac{\omega}{v}}. \quad (4.4)$$

For further non-dimensional interpretation, the tidal displacement averaged over the channel width reads [27]:

$$\Delta x = \frac{2u_0\lambda}{\omega\alpha^2} \left| 1 - \frac{\tanh(\sqrt{i}\alpha)}{\sqrt{i}\alpha} \right|. \quad (4.5)$$

To determine the local, time-dependent temperature $T(x, \eta, t)$, differential equations for the solid and the fluid domain are formulated. Within the solid wall, heat conduction is the only transfer mechanism, whereas the fluid domain also accounts for convective transport induced by the oscillating flow. The ratio of the respective thermal conductivities k_f in the fluid and k_s in the solid is denoted by

$$\mu \equiv \frac{k_f}{k_s}. \quad (4.6)$$

Having found closed expressions for velocity $u(\eta, t)$ and temperature $T(x, \eta, t)$, the effective thermal diffusivity κ_e is formulated as the convective transport integrated across the channel width over one oscillation period:

$$\kappa_e \gamma_T = \frac{\omega}{2\pi} \int_0^{2\pi/\omega} \int_0^1 \operatorname{Re} [T(x, \eta, t)] \operatorname{Re} [u_0 f(\eta) e^{i\omega t}] d\eta dt, \quad (4.7)$$

where γ_T is the constant temperature gradient.

In non-dimensional presentation, Kurzweg [27] formulates the solution of Eq. (4.7) as

$$\frac{\kappa_e}{\omega \Delta x^2} = \frac{\operatorname{Pr} [(1-H)\bar{h} + (1-\bar{H})h] + (\bar{h} - \bar{j}\bar{H}) + (h - jH)}{16\alpha^2(\operatorname{Pr}^2 - 1) \left| 1 - \frac{\tanh(\sqrt{i}\alpha)}{\sqrt{i}\alpha} \right|^2}, \quad (4.8)$$

where

$$h(\alpha) = \sqrt{i}\alpha \tanh(\sqrt{i}\alpha), \quad (4.9)$$

$$j(\operatorname{Pr}, \alpha) = \sqrt{i\operatorname{Pr}}\alpha \tanh(\sqrt{i\operatorname{Pr}}\alpha), \quad (4.10)$$

and

$$H(\operatorname{Pr}, \mu, \sigma, \alpha, \epsilon) = \frac{1}{\operatorname{Pr}} \frac{\mu \sqrt{\operatorname{Pr}} \tanh(\sqrt{i}\alpha) + \sqrt{\sigma} \tanh(\sqrt{i\sigma\operatorname{Pr}}\alpha(\epsilon - 1))}{\mu \tanh(\sqrt{i\operatorname{Pr}}\alpha) + \sqrt{\sigma} \tanh(\sqrt{i\sigma\operatorname{Pr}}\alpha(\epsilon - 1))}, \quad (4.11)$$

where

$$\sigma \equiv \frac{\kappa_f}{\kappa_s} \quad (4.12)$$

is the ratio of the thermal diffusivities κ in the fluid and the wall, respectively.

The bar-operator $\bar{\cdot}$ denotes the complex conjugate of the functions h , j , and H . Kurzweg's final correlation reveals that the non-dimensional presentation in Eq. (4.8) is solely a function of material properties (Pr, μ , and σ), geometry (ϵ), and Womersley number α .

4.1.2 Simplification to the Derivation of Kurzweg

To facilitate the comparison of Kurzweg's results with Rott's acoustic theory, the wall-temperature is adjusted. Instead of a coupled system where conjugate heat transfer leads to temporal temperature oscillations within the wall, van Buren and Polifke [66] (see Sec. 5.3.2, reproduced in the Appendix on p. 155 ff.) suggested the following assumption for temporally constant, but spatially linear wall temperatures (temperature gradient $\gamma_T = dT/dx$). They studied a set-up characterized by a solid of high specific heat capacity c_p , density ρ , and thermal conductivity k compared to the fluid. In particular, this holds for metallic walls, confining a channel filled with air and allows the following assumptions:

$$k_f \ll k_s \rightarrow \mu \approx 0 \quad (4.13)$$

and

$$\rho_f c_f \ll \rho_s c_s . \quad (4.14)$$

For the ratio of thermal diffusivities σ , no definite limit exists due to the opposing effects of thermal conductivity and heat capacity.

Regarding the geometry, a small channel width r_h much smaller than the wall thickness b yields:

$$r_h \ll b \rightarrow \epsilon \approx \infty . \quad (4.15)$$

This set-up is typical for quarter-wave resonators in rocket engine combustion chambers.

The physical interpretation of the proposed assumptions yields a Dirichlet boundary condition at the fluid-solid interface ($z = r_h$). A simplified version (denoted by the star *) of Kurzweg's solution (4.8) reads [66]:

$$\frac{\kappa_e^*}{\omega \Delta x^2} = \frac{\text{Pr} \operatorname{Re}(h) - \frac{1}{\text{Pr}} \operatorname{Re}(j)}{8\alpha^2(\text{Pr}^2 - 1) \left| 1 - \frac{\tanh(\sqrt{i}\alpha)}{\sqrt{i}\alpha} \right|^2} . \quad (4.16)$$

This derivation exploits that $H^* = 1/\text{Pr}$ is purely real-valued. Consequently, the expansion of the complex conjugate terms in the numerator of Eq. (4.8) simplifies such that all imaginary-valued parts cancel out.

4.1.3 Total Energy Flux by Rott

The assumptions of Rott's fundamental thermoacoustic theory, the underlying conservation equations for mass and momentum conservation, and the resulting differential equations for the pressure p_1 and volume flow rate U_1 were previously presented in Sec. 2.1.3. Based on this framework, Rott defines the total power flux \dot{H} by the local energy flux density (whose divergence would cause a transient change in energy per unit volume). It combines convective transfer of specific enthalpy and kinetic energy, heat conduction, and effects attributed to viscous stress. Rott approximates the total power flux \dot{H}_2 in the x -direction as the time average over the cross-sectional area of the channel. The final formula for the total power \dot{H}_2 reads:

$$\begin{aligned}\dot{H}_2 = & \frac{1}{2} \operatorname{Re} \left[p_1 \bar{U}_1 \left(1 - \frac{f_\kappa - \bar{f}_\nu}{(1 + \operatorname{Pr})(1 - \bar{f}_\nu)} \right) \right] \\ & + \frac{\rho_m c_p |U_1|^2}{2 A \omega (1 - \operatorname{Pr}^2) |1 - f_\nu|^2} \operatorname{Im} (f_\kappa + \operatorname{Pr} \bar{f}_\nu) \frac{dT_m}{dx} \\ & - (A_f k_f + A_s k_s) \frac{dT_m}{dx},\end{aligned}\quad (4.17)$$

where the subscript $_2$ denotes that the term is of second-order. The expression consists of three terms: the first describes an interplay of pressure and velocity oscillations, the second term solely considers convective heat transfer via the velocity oscillations, and the third term accounts for the underlying thermal diffusivity of the fluid and the solid. The following Sec. 4.2 focuses on the second term and compare the convective transport to the formulation by Kurzweg. Section 4.3 also discusses the influence of the two remaining first and third terms in more detail.

4.2 Analytical Transformation: Kurzweg vs. Rott

This section shows that the formulations of Kurzweg and Rott are identical at positions where the assumptions of both derivations match. This position presents the pressure node of a standing wave, as Kurzweg does not account for any effects of compressibility. In this case, the first term of Eq. (4.17) in Rott's correlation equals zero. Furthermore, the formulation for the effective thermal diffusivity κ_e by Kurzweg does not include longitudinal heat transfer by pure heat conduction, but only convective transport (compare Eq. (4.7)). Thus, also the third term of Eq. (4.17) should be ignored. According to Fourier's law, the heat flux \dot{H}_2 should be proportional to the cross-sectional area A_f and to the negative temperature gradient dT_m/dx :

$$\begin{aligned}\dot{H}_2 &= -k_e^+ A_f \frac{dT_m}{dx} \\ &= -\kappa_e^+ \rho_m c_p A_f \frac{dT_m}{dx},\end{aligned}\quad (4.18)$$

where k_e^+ denotes the effective longitudinal thermal conductivity (derived from the set of equations by Rott). Combining Eq. (4.18) and the second term of Eq. (4.17) yields:

$$\begin{aligned}\kappa_e^+ &= -\frac{\dot{H}_2}{\rho_m c_p A_f \frac{dT_m}{dx}} \\ &= -\frac{|U_1|^2}{2A_f^2 \omega (1 - \text{Pr}^2) |1 - f_v|^2} \text{Im}(f_\kappa + \text{Pr} \bar{f}_v) .\end{aligned}\quad (4.19)$$

The tidal displacement Δx results directly from the volume flow rate U_1 of a harmonic oscillation over a half period $T_p/2$:

$$\begin{aligned}\Delta x &= \int_0^{T_p/2} \frac{\text{Re}(U_1 e^{i\omega t})}{A_f} dt \\ &= \frac{1}{A_f} \int_0^{T_p/2} |U_1| \sin(\omega t) dt \\ &= \frac{2|U_1|}{A_f \omega} .\end{aligned}\quad (4.20)$$

Introducing Kurzweg's non-dimensional notation for the effective thermal diffusivity $\kappa_e^*/(\Delta x^2 \omega)$, Eq. (4.19) converts to:

$$\frac{\kappa_e^+}{\Delta x^2 \omega} = -\frac{\text{Im}(f_\kappa + \text{Pr} \bar{f}_v)}{8(1 - \text{Pr}^2) |1 - f_v|^2} .\quad (4.21)$$

The parameter f_v and f_κ are reformulated to express their dependence on the Womersley and Prandtl numbers (α and Pr , respectively). Recall the boundary layer thicknesses δ_v and δ_κ (Eqs. (2.26) and (2.27), respectively), the definition of the Womersley number $\alpha = r_h \sqrt{\omega/\nu}$, and the Prandtl number $\text{Pr} = \nu/\kappa_f$ to express r_h/δ_v and r_h/δ_κ :

$$\frac{r_h}{\delta_v} = \frac{\alpha}{\sqrt{2}} \quad (4.22)$$

and

$$\frac{r_h}{\delta_\kappa} = \frac{\alpha \sqrt{\text{Pr}}}{\sqrt{2}} .\quad (4.23)$$

Substituting these ratios in the expressions for f_v and f_κ (Eq. (2.23)) allows the expression of Rott's parameters f_v and f_κ in terms of the functions $h(\alpha)$ and $j(\text{Pr}, \alpha)$ introduced by Kurzweg (Eqs. (4.9) and (4.10)):

$$f_v = \frac{\tanh \left[(1+i) \frac{\alpha}{\sqrt{2}} \right]}{(1+i) \frac{\alpha}{\sqrt{2}}} = \frac{\tanh(\sqrt{i} \alpha)}{\sqrt{i} \alpha} = -\frac{i h(\alpha)}{\alpha^2} \quad (4.24)$$

and

$$f_\kappa = \frac{\tanh \left[(1+i) \frac{\alpha \sqrt{\text{Pr}}}{\sqrt{2}} \right]}{(1+i) \frac{\alpha \sqrt{\text{Pr}}}{\sqrt{2}}} = \frac{\tanh(\sqrt{i} \text{Pr} \alpha)}{\sqrt{i} \text{Pr} \alpha} = -\frac{i j(\text{Pr}, \alpha)}{\text{Pr} \alpha^2} .\quad (4.25)$$

Next, the simplified version of Kurzweg's results is considered (including temporally constant wall temperature, Eq. (4.16)). Using Eq. (4.24), the expression reads (after some rearrangements):

$$\frac{\kappa_e^*}{\omega \Delta x^2} = -\frac{\frac{1}{\alpha^2 \Pr} \operatorname{Re}(j) + \frac{\Pr}{\alpha^2} \operatorname{Re}(h)}{8(1 - \Pr^2) |1 - f_v|^2}. \quad (4.26)$$

Finally, the real parts of the functions $h(\alpha)$ and $j(\Pr, \alpha)$ are rewritten:

$$\frac{\Pr}{\alpha^2} \operatorname{Re}(h) = \Pr \operatorname{Re}(if_v) = \Pr \operatorname{Im}(-f_v) = \Pr \operatorname{Im}(\bar{f}_v) \quad (4.27)$$

and

$$\frac{1}{\alpha^2 \Pr} \operatorname{Re}(j) = \operatorname{Re}(if_\kappa) = \operatorname{Im}(-f_\kappa) = -\operatorname{Im}(f_\kappa). \quad (4.28)$$

Inserting Eqs. (4.27) and (4.28) into Eq. (4.26) gives:

$$\frac{\kappa_e^*}{\omega \Delta x^2} = -\frac{\operatorname{Im}(f_\kappa + \Pr \bar{f}_v)}{8(1 - \Pr^2) |1 - f_v|^2}. \quad (4.29)$$

Both starting points, Rott and Kurzweg, respectively, result in identical expressions for the non-dimensional effective thermal diffusivity $\kappa_e/(\Delta x^2 \omega)$ (Eq. (4.21) and Eq. (4.29), respectively) for conditions where both approaches are applicable.

A side note on the pressure gradient by Kurzweg: Kurzweg introduces the amplitude of the oscillation via the non-dimensional pressure gradient λ (independent of any acoustic considerations):

$$\lambda = \left| \frac{\partial p}{\partial x} \right| \frac{r_h^2}{\rho u_0 \nu}. \quad (4.30)$$

In the acoustic framework and at the location of a pressure node without hydrodynamic or thermal losses ($p = \rho c u_0$), the spatial pressure gradient $\partial p / \partial x$ is proportional to the velocity amplitude u_0 :

$$\frac{\partial p}{\partial x} = \frac{p \omega}{c} = \rho \omega u_0. \quad (4.31)$$

Thus, if the pressure gradient results from a standing acoustic wave, the non-dimensional pressure gradient λ equals the square of the Womersley number:

$$\lambda = \frac{\omega r_h^2}{\nu} = \alpha^2. \quad (4.32)$$

4.3 Discussion of the Formulations by Kurzweg and Rott

This section first provides a quick summary of the effective normalized thermal diffusivity $\kappa_e/(\omega \Delta x)$ used by Kurzweg (see Fig. 4.2). Van Buren and Polifke give a comprehensive discussion of this three-dimensional plot [53] (see Sec. 5.2, reproduced in the Appendix on p. 121 ff.).

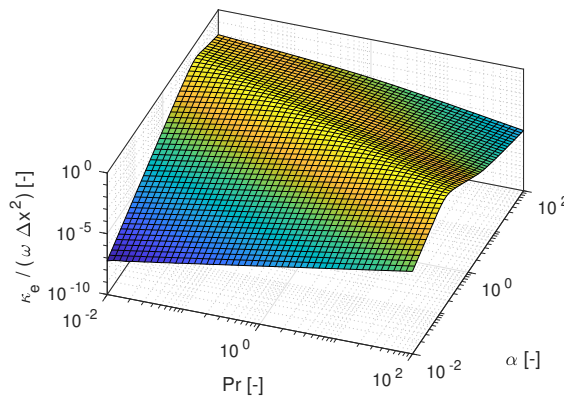


Figure 4.2: Effective normalized thermal diffusivity vs. Womersley and Prandtl numbers.

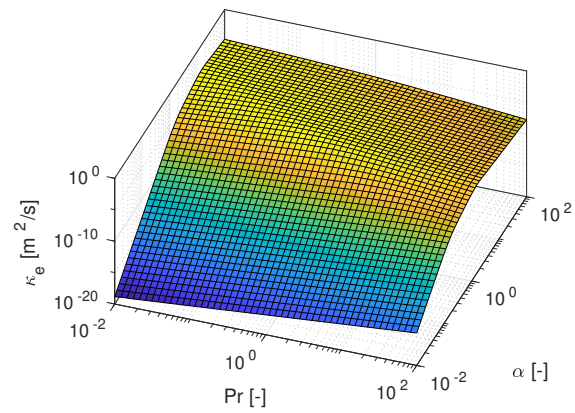


Figure 4.3: Effective (absolute) thermal diffusivity vs. Womersley and Prandtl numbers.

The main advantage of the non-dimensional representation is its independence of the tidal displacement/velocity and amplitude/forcing pressure gradient. To clarify this idea, Fig. 4.3 shows the non-normalized effective thermal diffusivity κ_e . The difference between low and high Womersley numbers α becomes apparent at first sight, where correspondingly low or high thermal diffusivity shows. The reason for this is the applied forcing. Kurzweg defines the oscillating velocity profile via the representative velocity u_0 and/or by the pressure gradient $\partial p / \partial x$, which causes the tidal displacement Δx . For large Womersley numbers α , hydrodynamic boundary layers are thin. Consequently, the maximum velocity of u_0 is reached in most parts of the cross-sectional area of the channel. On the other limit, low Womersley numbers α characterize a flow dominated by viscous friction. In this limit, the velocity remains well below the representative velocity u_0 . Figure 4.7 illustrates this behavior directly by the tidal displacement Δx (see the location of a pressure node in a quarter-wave resonator at $x = L$). This conclusion explains the opposite slopes for high/low Womersley numbers α in the respective normalized and absolute representation of the effective thermal diffusivity κ_e (Figs. 4.2 and 4.3).

As derived in the previous analytical transformation (Sec. 4.2), perfectly identical plots show for the formulation by Rott at the location of a pressure node.

What happens when moving away from the pressure node to an arbitrary position of a (standing wave) in a quarter-wave resonator? Obviously, this is the more exciting set-up, as also the first (pressure and velocity related) term of Rott's formulation (Eq. (4.17)) becomes non-zero. Here, the following problem appears: For hydraulic and thermal lossless acoustic waves, the Riemann invariant f and g hold. Thereby, the velocity and pressure profiles of a standing wave are quickly determined. However, this acoustic wave (in conformity with its isentropic definition) would not interact with the boundary walls in any way. Accordingly no oscillation-induced thermal net-energy is transferred along the resonator tube (i.e., $\alpha \rightarrow \infty$ and $Pr \approx 1$). Hence, the flow needs to show some boundary layer interaction and thus it deviates from a perfectly standing acoustic wave. This makes the problem at hand significantly more complex.

Returning to the location of a (perfect) pressure node, Fig. 4.4 exemplarily shows two of the three terms of Rott's total energy flux (Eq. (4.17)), expressed in terms of thermal diffusivity

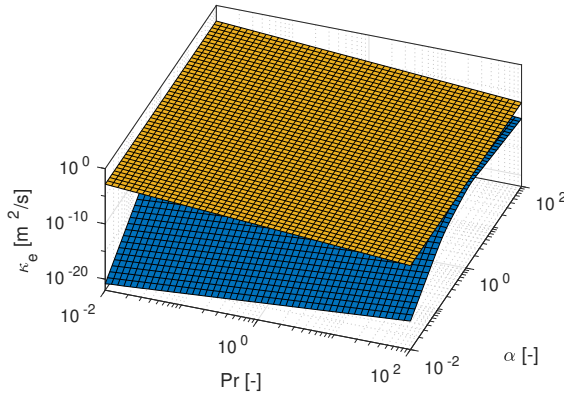


Figure 4.4: Individual components (term 2 (■) and term 3 (■)) of thermal diffusivity according to Rott at the pressure node ($x = L$).

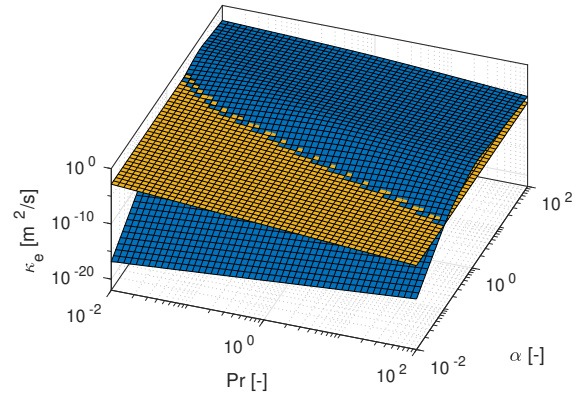


Figure 4.5: Individual components (term 2 (■) and term 3 (■)) of thermal diffusivity according to Rott for increased oscillation amplitudes at the pressure node ($x = L$).

	Set-up 1 Fig. 4.4	Set-up 2 Fig. 4.5	Set-up 3 Fig. 4.6
u_0	$0.1 \frac{\text{m}}{\text{s}}$	$10 \frac{\text{m}}{\text{s}}$	$10 \frac{\text{m}}{\text{s}}$
x	L	L	$L/2$
ω		$2\pi 300 \frac{1}{\text{s}}$	
γ_T		$0.01 \frac{\text{K}}{\text{m}}$	
T		293 K	
p		101300 Pa	
ν		$1.516 \times 10^{-5} \frac{\text{m}^2}{\text{s}}$	
c_p		$1007 \frac{\text{m}^2}{\text{s}^2 \text{K}}$	
R		$296.9 \frac{\text{m}^2}{\text{s}^2 \text{K}}$	
γ		1.4	
k_s		$0 \frac{\text{W}}{\text{mK}}$	

Table 4.1: Parametric set-up for the investigation of the three terms that drive longitudinal heat transfer.

κ_e). Table 4.1 summarizes the chosen parameters of the air-filled channel flow. The top-leveled plane (■) gives the pure thermal diffusivity of the underlying fluid (regardless of oscillations, term 3). It decreases with increasing Prandtl numbers Pr (due to lower thermal conductivity). The Womersley number α does not affect this term. The blue surface (■) presents the convection related thermal transport (term 2) also described by Kurzweg. Due to the absence of pressure oscillations, the (pressure and velocity related) term 1 of Eq. (4.17) is zero at the depicted location of a pressure node.

The magnitude of the three terms (and thus the question of which term dominates the problem

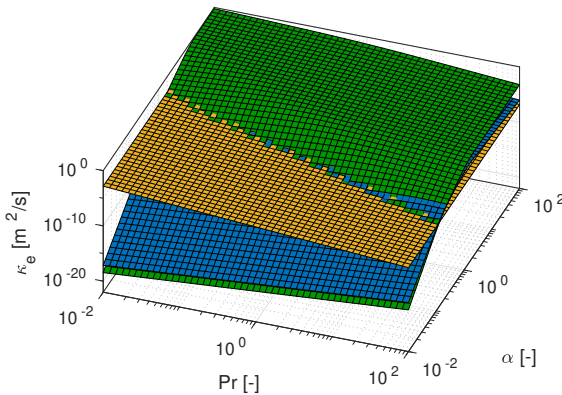


Figure 4.6: Individual components (term 1 (■), term 2 (□), and term 3 (■)) of thermal diffusivity according to Rott for increased oscillation amplitudes with pressure oscillations ($x = L/2$).

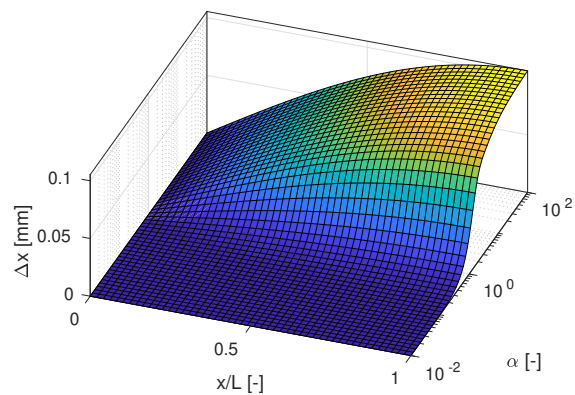


Figure 4.7: Tidal displacement vs. Womersley number and duct length.

at hand) can quickly change by the parametric set-up under investigation. Figure 4.5 shows the effect of an increase in the representative velocity amplitude u_0 from $0.1 \frac{\text{m}}{\text{s}}$ to $10 \frac{\text{m}}{\text{s}}$. The increase in velocity and thus in the tidal displacement clearly enhances the impact of the convective term 1. Thereby, its contribution to the longitudinal heat transfer exceeds the thermal diffusivity in the parameter range $\alpha^2 \text{Pr} \approx \pi$. An physical explanation of this regime follows in Sec. 5.2 based on a study by van Buren and Polifke [53] (reproduced in the Appendix on p. 121 ff.).

In a final step, consider moving to a position of a perfect standing wave, where pressure oscillations are existent, with velocity amplitudes smaller than at the pressure node. In this example, the center between the pressure and velocity nodes of an isentropic quarter-wave channel (i.e., $x = L/2$, compare to Fig. 2.5 is selected for $T_1 = 300 \text{ K}$ and $r_h = 10 \text{ m}$). Figure 4.7 additionally illustrates the tidal displacement Δx over the Womersley number α along the channel length. Figure 4.6 displays the three terms of Eq. (4.17) at an unchanged representative velocity $u_0 = 10 \frac{\text{m}}{\text{s}}$: Now, the pressure-related term 1 (■, opposite sign to the other two terms) shows. Again, it becomes apparent that this term can also dominate the problem at hand for a certain range of parameters.

5 Contextualization and Discussion of Publications

The project that led to the present Ph. D. thesis was funded by the *German Research Foundation* (DFG) in the framework of a *Collaborative Research Centres* (SFB-TRR40, 2008-2020). In the respective *Final Report*, van Buren and Polifke [67] (reproduced in the Appendix on p. 98 ff.) provide an overview of their results. On the whole, five universities, industrial partners, numerous professors, and even more Ph. D. students contributed to the multidisciplinary research program in different research areas on fundamental space-transportation-systems with a close focus on dominating phenomena in the propulsion systems of liquid propellant rocket engines. The final report [68] collects the joined results on *Structural Cooling* (research area of the present author), *Aft-Body Flows*, *Combustion Chamber*, *Thrust Nozzle*, and *Thrust-Chamber Assembly*.

The present chapter discusses and contextualizes the publications connected to the present thesis. The *Numerical Assessment of a Resonator with Temperature Inhomogeneities* (Sec. 5.1) is thematically closely related to the analytical modeling of quarter-wave resonators (compare Chapter 3). The *Theoretical Considerations on Boundary Layer Interplay* (Sec. 5.2) provides further interpretation on longitudinal heat transfer in oscillation channel flows (compare Chapter 4). Finally, the selected publications address the effect of turbulence on heat transfer: First, the *Enhancement of Wall-Normal Heat Transfer* (Sec. 5.3.1) and second, the *Enhancement of Longitudinal Heat Transfer* (Sec. 5.3.2).

5.1 Numerical Assessment of a Resonator with Temperature Inhomogeneities

Chapter 3 reviewed an existing and presented a novel analytical approach for the acoustic characterization of a quarter-wave resonator. However, they are restricted to constant temperature profiles along the resonator tube. Although there are certain methods and ideas to extend the frameworks to temperature inhomogeneities (e.g., the work by Cárdenas Miranda [9] or the derivations of the present thesis (see Sec. 2.3)), the resulting analytical correlations are restricted to selected temperature profiles (e.g., linear, exponential, polynomial, etc.). They are subject to several modeling assumptions (e.g., compare Sec. 3.1.1).

To overcome these restrictions, van Buren and coworkers [12] (reproduced in the Appendix on p. 113 ff.) developed a numerical framework to quantify the acoustic impedance of quarter-wave resonators with arbitrary temperature distributions. They use a compressible CFD simulation that is excited via inwards traveling acoustic waves via the Navier-Stokes Characteristic

Boundary Condition (NSCBC) [69] of either mono-frequent or broadband characteristic. The evaluation of the results excited by a broadband input-signal is realized by System-Identification (CFD/SI). The identification process utilizes the output-error model and is based on the studies by Förner and Polifke [70].

For the parameter range under investigation, the numerical results of the study by van Buren and coworkers [12] agree well with the analytical predictions by Cárdenas Miranda [9]. The study clearly underlines the crucial impact of the underlining temperature profile on the acoustic damping characteristics (e.g., a shift in eigenfrequency). In a coupled analysis of combustion chamber and resonator elements, Förner et al. [6] as well as Chemnitz et al. [7] showed a high sensitivity of global stability in regard to the damping characteristics of the resonator. Thus, a shift in the eigenfrequency of the resonator may result in insufficient damping of the acoustically unstable modes. This, in turn, may lead to catastrophic structural failure of the combustion chamber.

The previous findings illustrate the crucial importance of the temperature profile inside the resonator. However, the precise derivation of such temperate profiles requires a further understanding of the governing heat transfer mechanisms. Therefore, the focus of the following chapters will turn to two central challenges in this respect: Chapter 4 investigates heat transfer in oscillating channel flows. Chapter 5.3 extends to the impact of turbulence.

5.2 Theoretical Considerations on Boundary Layer Interplay

Chapter 4 offered an overview of longitudinal heat transfer in oscillating flows and a comparison of analytical models (Kurzweg [27] vs. Rott [38]). However, these considerations are – foremost – of mathematical nature and provide only limited insight and explanation of the physical mechanisms that define the problem at hand. Besides, particular relevance may be expected from its limiting cases and the interplay of the hydrodynamic and thermal boundary layers.

Therefore, van Buren and Polifke [53] (reproduced in the Appendix on p. 121 ff.) provide a more in-depth discussion of the physical mechanisms of longitudinal heat transfer in oscillatory channel flows. The focus lies on six limiting regimes that result from the hydrodynamic and thermal boundary layer characteristics with either parabolic or bulk profiles, respectively. The corresponding interplay of the boundary layers qualitatively explains the longitudinal heat transfer. For a non-dimensionalized analysis of the problem at hand, van Buren and Polifke introduce the non-dimensional *Kurzweg number* Ku to characterize the thermal penetration depth. Thereby, the extend of hydrodynamic and thermal boundary layers are presented as decoupled influence factors. Maximum effective thermal diffusivity reveals when the thermal penetration reaches the center of the channel, or $Ku^2 \approx \pi$.

All previous considerations of the present thesis are limited to laminar flows. However, the flows in rocket engine combustion chambers are highly turbulent. The literature commonly connects turbulent effects with a significant increase in heat transfer that may lead to fatal destruction of the structure. Therefore, the following Chapter 5.3 extends to the impact of turbulence in pulsating flows: First, the effect on wall-normal heat transfer is considered and, second, the

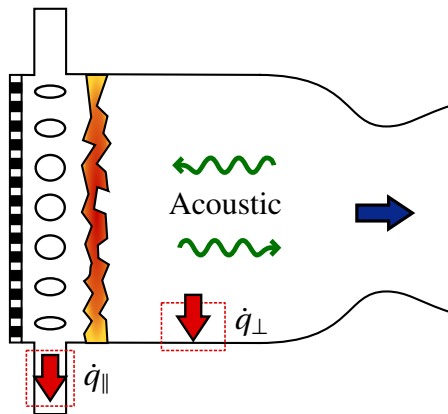


Figure 5.1: Sketch of a combustion chamber with wall-normal (\dot{q}_{\perp} , see Sec. 5.3.1) and longitudinal (\dot{q}_{\parallel} , see Sec. 5.3.2) heat transfer.

effect on longitudinal heat transfer.

5.3 The Effect of Turbulence on Heat Transfer

Chapter 4 and the previous publication of Sec. 5.2 focused on the oscillation-induced enhancement of convective heat transfer in laminar channel flows (e.g., in the tube of a quarter-wave resonator). However, the literature foremost associates a strong heat transfer enhancement of pulsating flows combined with turbulent effects. In extreme cases, the reported enhancement reached levels that compromise the thermal integrity of devices suffering from thermoacoustic instabilities. Numerous rocket engine combustion chambers suffered from this fatal mechanism: Exceeding the designed wall heat flux obviously endangers a secure operation with possibly catastrophic consequences. Therefore, the reliable prediction of heat transfer in turbulent pulsating flows is crucial for a comprehensive design process of combustion chambers.

Although numerous researchers experimentally studied the enhancement of heat transfer (e.g., [4, 14–22]), the results are of a rather qualitative nature. The reported enhancement ranges from only a few percent [21] up to 300% (e.g., [17–20]). Numerical investigations are limited and also contradictory: Wang and Zhang [26] tackled the problem at hand via a RANS simulation. However, Scotti and Piomelli [71, 72] found the RANS to be insufficient and confirmed that it requires a Large Eddy Simulation (LES) to capture relevant fluid-mechanical effects.

To close these gaps, the present chapter considers two different mechanisms of turbulence-induced enhanced heat transfer: Section 5.3.1 numerically studies wall-normal heat transfer. This mechanism mimics the thermal exchange between the cooled chamber walls and the hot combustion gas (compare the heat flux \dot{q}_{\perp} in Fig. 5.1). Section 5.3.1 turns to the effect of turbulence on the longitudinal heat transfer (the laminar case was discussed in Chapter 4). This modeling corresponds to the prevailing mechanisms inside a resonator tube, subject to a temperature gradient between the hot gases at the resonator mouth and the cooled backing of the cavity (compare \dot{q}_{\parallel} in Fig. 5.1).

5.3.1 Enhancement of Wall-Normal Heat Transfer

To establish a more comprehensive picture of the wall-normal enhancement of heat transfer, van Buren and coworkers [73] (reproduced in the Appendix on p. 140 ff.) performed a parametric LES study. The incompressible simulation within a periodic computational domain mimics the characteristics of a pressure node of a standing acoustic wave. Many researchers report the most significant enhancement at this location of maximum velocity fluctuations (e.g., [9, 15, 74]). A much wider range of oscillation parameters is studied compared to the existing literature. In particular, forcing frequencies correspond to Womersley numbers from $\alpha = 14$ to 70, while forcing amplitudes reach values that result in pronounced flow reversal, i.e., reverse flow velocities up to five times larger than the mean flow velocity.

As a first result, van Buren et al. [73] report strong deviations of instantaneous heat transfer rates from the temporal mean at moderate pulsation amplitudes (i.e., in the range of emerging flow reversal). Particularly at times of flow reversal, an increase in heat transfer up to 60% over the non-pulsatile reference is observed. However, when averaging over a complete cycle, the overall enhancement in mean heat transfer is only marginal. Thereby, it falls far below the enhancement up to 300% that Dec and coworkers reported in their experimental results [17–20]. It may also not explain the severe hardware damage of rocket motors attested by Harrje and coworkers [4, 14]. In conclusion, a rather contradictory picture of the magnitude of the enhancement in heat transfer exists in the literature.

In a subsequent part of the study, van Buren et al. [73] expand the numerical investigation to larger pulsations amplitudes resulting in strongly pronounced flow reversal. For the adjusted set-up, an enhancement of mean heat transfer above of 100% well compares to the findings of numerous experimental investigations. It also presents an increase that explains the fatal destruction of combustion chambers due to exceedingly aggressive thermal conditions. The study offers a physical interpretation of the results and concludes that an overall increase in turbulent transport is responsible for the observed significant enhancement of convective heat transfer.

5.3.2 Enhancement of Longitudinal Heat Transfer

The previous Section 5.3.1 shed insight on the turbulence-induced enhancement of wall-normal heat transfer in combustion chambers. The significant increase may explain the structural failure of the chamber walls or face-plate due to exceeded thermal loads. On the contrary, the transient heat-up of a resonator underlies a different heat transfer mechanism: As already discussed in Sec. 4, the axial temperature gradient along the resonator tube causes a heat flux in the direction of the acoustic fluid oscillation. However, these analytical derivations were limited to laminar flows. In his study from 1985, Kurzweg himself suggested further investigations for the turbulent regime [27]. Overall, precise knowledge of the temperature distribution inside the resonator is crucial for an accurate design of the resonator and thus for a safe design and operation of the combustion chamber and the entire engine (compare Sec. 5.1).

To fill this gap and to establish a more comprehensive picture of the effect of turbulence on longitudinal heat transfer, van Buren and Polifke [66] (reproduced in the Appendix on p. 155

ff.) present a parametric investigation. The basic structure of the Large Eddy Simulation was adapted from the previous work on wall-normal heat transfer [73] (solver, turbulence model, mesh, etc.). Adjustments of boundary conditions and evaluation methods allowed for investigating the present problem at hand.

The numerical results of laminar flows show excellent agreement with the analytical solution by Kurzweg [27] (see Sec. 4.1.1). In the turbulent case, enhanced longitudinal heat transfer emerges for flows characterized by the product of squared Womersley number α and Prandtl number Pr fulfilling $\alpha^2 \text{Pr} > \pi$. Transferring these characteristics to the application of rocket engine combustion chambers, the highlighted regime is of technical relevance since hydrodynamic and thermal boundary layers are typically small compared to the resonator diameter ($\delta_v \approx \delta_\kappa \ll d$, and thus $\alpha \gg 1$ and $\text{Pr} \approx 1$). Thus, future design processes should account for the effect under investigation. Furthermore, the study provides a physical explanation for the enhancement: Turbulence increases the wall-normal heat transfer (compare Sec. 5.3.1) and thus increases the thermal penetration depth. Consequently, a wider cross-sectional area of the channel contributes to the convective longitudinal heat transfer.

6 Summary and Conclusions

The present thesis addresses the effect of temperature inhomogeneities on the damping characteristic of acoustic quarter-wave resonators. A comprehensive investigation of heat transfer in turbulent oscillating flows is given to derive the underlying temperature distributions. In particular, the work focuses on (i) analytical models to gather in-depth knowledge about the physical mechanisms involved and on (ii) high-fidelity fluid dynamic simulations as a numerical design tool and for the parametric quantification of turbulent effects.

Starting from Rott's thermoacoustic approximation, the thesis formulates characteristic acoustic waves (f and g -wave) accounting for the viscous and thermal losses of a channel flow at homogeneous temperature. In the next step, the previous derivations are used to model the acoustic damping properties of a quarter-wave resonator, namely its impedance or reflection coefficient, respectively. The results compare well to an analytical analog of a mass-spring-damper system and numerical investigations.

The thesis generalizes the correlations of lossy duct acoustics to linear temperature profiles under the assumption of temperature-independent viscosity. The results reveal a significant effect of the temperature on the acoustic eigenfrequency of a quarter-wave channel. For the more applied example of a temperature gradient within a quarter-wave resonator (e.g., in a rocket engine combustion chamber), the thesis presents a predictive numerical framework. It applies System-Identification methods to calculate the acoustic impedance for arbitrary temperature distributions. Again, the underlying temperature significantly influences the acoustic characteristic of the resonator (e.g., the eigenfrequency and the magnitude of acoustic reflection). The thesis clearly shows that the spatial mean temperature is insufficient to describe the problem at hand. Instead, the accurate acoustic characterization of the resonator requires a more sophisticated knowledge of the local temperature distribution.

After the first part of the present thesis highlights the importance of the temperature distribution inside quarter-wave resonators, its second part focuses on two heat transfer mechanisms prevailing inside a rocket engine combustion chamber. The central challenges of this task are the highly turbulent flow characteristics and the acoustical pulsations. This combination of conditions often connects to significant heat transfer enhancement in the literature. Particularly during combustion instabilities that cause strong velocity and pressure oscillations, the increased thermal load may lead to severe damages or the destruction of the combustion chamber. However, related studies are of a rather qualitative nature. The author of the present thesis provides the first numerical evidence for significant enhancement of wall-normal heat transfer in a parametric LES campaign. The reported enhancement of more than 100% clearly states the relevance of this phenomenon in a comprehensive design process.

Longitudinal heat transfer in oscillating channel flows (e.g., inside the tube of a quarter-wave resonator) presents the second challenging heat transfer mechanism. The thesis comprehen-

sively discusses the interplay of hydrodynamics and thermal boundary layers that generates an effective enhancement over the molecular thermal conductivity. The introduced Kurzweg number accounts for the key factor of the thermal penetration depth as a non-dimensional parameter. Subsequently, the work on analytical considerations of laminar flows is extended to turbulent flows via high-fidelity numerical simulations. A significant turbulence-induced enhancement also shows for the case of longitudinal heat transfer. This is well explained by the wall-normal enhancement that increases the thermal penetration depth and thus the cross-sectional area contributing to the convective transport in the longitudinal direction.

The author (separately) studied the impact of temperature on the acoustic damping characteristic of a quarter-wave resonator and the effect of oscillations on the heat transfer. However, when considering technical combustion applications (e.g., rocket engine combustion chambers), the two elements mentioned above are closely interrelated: Large acoustic oscillation amplitudes during combustion instabilities affect the heat transfer and thus the local temperature distribution (e.g., inside a resonator tube). In direct consequence, the resulting change in temperature alters the damping performance of the resonator, which – in turn – changes the acoustics of the entire chamber. At this point, the loop closes as the acoustic amplitude directly impacts the heat transfer. One sees that a decoupled investigation of acoustic damping performance and heat transfer may not be feasible. Instead, a comprehensive design process requires a holistic treatment that simultaneously incorporates both effects.

However, a classical numerical investigation easily exceeds the computational resources of the present project: On the one hand, large spatial and temporal scales are required to model the complete combustion chamber (including the resonator elements) over the extensive, transient heat-up period. On the other hand, very finely resolved scales are indispensable for the accurate modeling of the enhanced heat transfer via LES. More sophisticated numerical approaches may reduce the computational cost to a feasible amount.

Regarding the large scales, network models can reduce the complexity of the combustion chamber. Linear state space systems account for parts of the geometry (e.g., the injector, flame, and nozzle) – corresponding boundary conditions couple the CFD simulation of the resonator with the surrounding state space systems. For the small scales, wall models may incorporate the effect of enhanced heat transfer. This approach significantly decreases the fine mesh resolution required for an LES. The present thesis provides a parametric data basis for designing such wall models.

The results of the author's work have been published in several papers. The key papers with the original abstracts and the respective contributions of the author are listed in the following sections.

6.1 Heat Transfer in Pulsating Flow and Its Impact on Temperature Distribution and Damping Performance of Acoustic Resonators

The final report of the Collaborative Research Centres SFB-TRR40 summarizes, interconnects and concludes the individual research topics of the third funding period, see Sec. 6. The book reflects the work of the author (representing research project A3) within the context of the multidisciplinary research program.

Original Abstract: A numerical framework for the prediction of acoustic damping characteristics is developed and applied to a quarter-wave resonator with non-uniform temperature. The results demonstrate a significant impact of the temperature profile on the damping characteristics and hence the necessity of accurate modeling of heat transfer in oscillating flow. Large Eddy Simulations are applied to demonstrate and quantify enhancement in heat transfer induced by pulsations. The study covers wall-normal heat transfer in pulsating flow as well as longitudinal convective effects in oscillating flow. A discussion of hydrodynamic and thermal boundary layers provides insight into the flow physics of oscillatory convective heat transfer.

Contribution: The original research topic was jointly defined by Prof. Wolfgang Polifke, Dr. Kilian Förner, and the lead author. Throughout the development of the third funding period of the Collaborative Research Centres SFB-TRR40, some aspects were redefined by Prof. Wolfgang Polifke and the lead author. Dr. Alejandro Cárdenas Miranda and Dr. Kilian Förner provided their research work from the first and second funding periods. The lead author contributed the further numerical implementation and evaluation of the results. Furthermore, the lead author prepared the manuscript. Prof. Wolfgang Polifke gave proofreading and suggestions for improvement.

Status: Published as a book chapter in Notes on Numerical Fluid Mechanics and Multidisciplinary Design (NNFM). Scopus listed.

Reference: BurenPolif20b [67], reproduced on p. 98ff.

6.2 Acoustic Impedance of a Quarter-Wave Resonator with Non-Uniform Temperature

A numerical tool for the aeroacoustic characterization of a quarter-wave resonator with arbitrary temperature profiles is developed, see Sec. 5.1. This approach allows a flexible investigation of the effect of temperature inhomogeneities (e.g. compare linear profiles in Sec. 2.3).

Original Abstract: This study proposes a semi-analytical approach to predict the acoustic impedance of a quarter-wave resonator with non-uniform temperature. In analogy to well-known models for Helmholtz resonators, the quarter-wave resonator is represented as a mass-spring-damper system. The treatment is limited to polynomial temperature profiles, but does take into account that the resonator cavity is not acoustically compact.

In order to assess the validity and accuracy of the semi-analytical results, computational fluid dynamics (CFD) simulations are carried out for a variety of temperature profiles in a quarter-wave resonator cavity. The acoustic reflection offered by the resonator opening to imposed incoming acoustic waves is evaluated, either by spectral analysis of time series generated by repeated, monofrequent excitation, or by system identification of acoustic signals generated with broad-band excitation. System identification – a variant of supervised machine learning – requires only a single simulation run to characterize the resonator over the frequency range of interest. The validation study shows good quantitative agreement between the mono-frequent and broadband excitation cases, as well as qualitative consistency with the analytical predictions.

The present study demonstrates that resonator eigenfrequencies as well as maximum effectiveness and bandwidth of acoustic damping are quite sensitive to temperature inhomogeneities. In the context of thermo-acoustic combustion instability, where resonators are frequently employed as a means of passive control. The results suggest that the acoustic characteristics of a resonator with hot combustion products at the inlet and a cooled backing cannot be computed simply with a representative average of the temperature distribution. These findings underline the necessity of a comprehensive design process, which includes thermal analysis in order to assure optimum resonator effectiveness.

Contribution: The research topic was jointly defined by Prof. Wolfgang Polifke, Dr. Kilian Förner, and the lead author. Dr. Kilian Förner implemented the numerical framework for the simulation of resonators at constant temperatures (e.g., [10, 70, 75]). The lead author contributed the extension to arbitrary temperature profiles conducted the parametric simulation campaign and its evaluation. Furthermore, the lead author prepared the manuscript. All co-authors gave proofreading and suggestions for improvement.

Status: This paper was submitted to and accepted for the 27th International Congress on Sound and Vibration (ICSV27). Due to the outbreak of the corona pandemic, the conference was postponed by one year to the dates from 11 to 15 July 2021. The paper will be presented in Prague on these dates and published in the ICSV Proceedings afterward. Scopus listed.

Reference: BurenForne20 [12], reproduced on p. 113ff.

6.3 Enhanced Longitudinal Heat Transfer in Oscillatory Channel Flow – a Theoretical Perspective

A comprehensive, theoretical discussion on the interplay of hydrodynamic and thermal boundary layers in oscillating channel flow, which is based on the analytical work by Kurzweg [27] (see Sec.5.2).

Original Abstract: Enhanced longitudinal heat transfer (ELHT) is a fascinating phenomenon in oscillatory channel flow. Kurzweg (J. Heat Transf. 107, 1985) formulated a theoretical analysis of conjugate heat transfer for the case of laminar, single-phase, oscillatory flow, which yields a correlation for ELHT in terms of Prandtl and Womersley numbers. The present investigation contributes physical interpretation to the results of Kurzweg. A simplified model with isothermal walls is proposed, applicable if gaseous fluid and metallic confinement exhibit sufficiently large differences in thermal inertia. Examined over a wide range of Womersley numbers, this model reveals six distinct regimes characterized by the Prandtl number of the fluid. The thickness of hydrodynamic and thermal boundary layers relative to the channel width is relevant in this context. Maximum ELHT is attained when the thermal boundary layer expands over the full channel width. The trend of ELHT vs. Womersley number is discussed and explained in terms of flow physics by the interplay of hydrodynamic and thermal flow characteristics. These patterns reveal either quasi-steady parabolic or oscillating bulk characteristics, respectively. The importance of the thermal boundary layer thickness motivates the introduction of a new non-dimensional group, which makes it easier to classify the various regimes of ELHT.

Contribution: The research topic was jointly defined by Prof. Wolfgang Polifke and the lead author. The lead author drew up the theoretical investigation and the manuscript. Prof. Wolfgang Polifke gave proofreading and suggestions for improvement.

Status: This paper was submitted to and presented at the 18th International Symposium on Transport Phenomena and Dynamics of Rotating Machinery (ISROMAC18). Due to the outbreak of the corona pandemic, the conference was held online from 23 to 26 November 2020. The paper was invited to and published in the ASME Journal of Fluids Engineering (JFE). Scopus listed.

Reference: BurenPolif20 [53], reproduced on p. 121ff.

6.4 Large Eddy Simulation of Enhanced Heat Transfer in Pulsatile Turbulent Channel Flow

Numerical evidence for significant enhancement of wall-normal heat transfer in pulsatile turbulent channel flow is given, see Sec. 5.3.1. The parametric study of Large Eddy Simulations is performed on an intrinsically generated turbulent flow in a periodic simulation domain.

Original Abstract: Heat transfer in pulsatile turbulent channel flow is investigated by means of Large Eddy Simulation. Incompressible flow within a periodic computational domain is driven by a pulsating axial pressure gradient at a turbulent Reynolds number of $Re_\tau = 350$. A localized dynamic sub-grid scale approach is chosen to model unclosed stress terms. A layer-averaged sub-grid model determines turbulent Prandtl numbers that depend on wall distance. Compared to the existing literature, a much wider range of oscillation parameters is studied. In particular, forcing frequencies correspond to Womersley numbers from $Wo = 14$ to 70 , while forcing amplitudes reach values that result in strongly pronounced flow reversal, i.e. reverse flow velocities up to five times larger than the mean flow velocity.

At moderate pulsation amplitudes, i.e. in the range of emerging flow reversal, strong deviations of instantaneous heat transfer rates from the temporal mean are observed. Particularly at times of flow reversal, an increase in heat transfer up to 60% above non-pulsatile values is observed. However, when averaging over a complete cycle, any enhancement in mean heat transfer is only minor.

On the other hand, simulations at larger pulsations amplitudes that result in strongly pronounced flow reversal, show a enhancement of mean heat transfer in excess of 100%. Note that such significant enhancement of heat transfer has not been reported previously in Large Eddy Simulation of turbulent pulsatile flow. The paper offers a physical interpretation of the results and concludes that an overall increase in turbulent transport is responsible for the observed significant enhancement of convective heat transfer.

Contribution: The original research topic was jointly defined by Prof. Wolfgang Polifke and Dr. Alejandro Cárdenas Miranda. Dr. Alejandro Cárdenas Miranda developed a framework for a numerical experiment. However, his simulation campaign did not reproduce the expected results of enhanced heat transfer (see [9]). Therefore, Prof. Wolfgang Polifke and the lead author jointly readdressed and redefined the research topic. The lead author contributed the complete redesign of the solver and the turbulence models. After the lead author recognized the significance of increased pulsation amplitudes, he conducted the parametric simulation campaign and prepared the manuscript. All co-authors gave proofreading and suggestions for improvement.

Status: Published in the International Journal of Heat and Mass Transfer (IJHMT). Scopus listed.

Reference: BurenCarde19 [73], reproduced on p. 140ff.

6.5 Turbulence-Induced Enhancement of Longitudinal Heat Transfer in Oscillatory Channel Flow

The effect of turbulence on the longitudinal heat transfer in oscillatory channel flow is investigated, see Sec. 5.3.2. The numerical set-up is based on the previous work of wall-normal heat transfer [73], see Sec. 5.3.1. Results are compared to the laminar reference by Kurzweg [27], see Sec. 4.1.1.

Original Abstract: An analytical correlation for longitudinal heat transfer in oscillatory flow was proposed by Kurzweg (1985). However, the treatment was limited to laminar flows, which motivates the extension of the analysis to the turbulent regime. In the present paper, turbulence-induced enhancement of longitudinal heat transfer in oscillatory channel flow is investigated by means of Large Eddy Simulation (LES) and supplemented with analytical considerations. Incompressible flow within a periodic computational domain is driven by an oscillating longitudinal pressure gradient, generating both laminar and turbulent flow characteristics. A wide range of oscillation amplitudes is considered, while a constant axial temperature gradient is maintained at the upper and lower channel walls. Kurzweg's analytical correlation for effective longitudinal thermal diffusivity is simplified to match the numerical setup.

The numerical results of laminar flows show excellent agreement with the analytical solution. In the turbulent case, enhanced longitudinal heat transfer emerges for flows characterized by the product of squared Womersley number α and Prandtl number Pr fulfilling $\alpha^2 \text{Pr} = \pi$. In order to explain this observation, the interaction of wall-confined thermal and hydrodynamics Stokes boundary layers is scrutinized, a simple correlation for the effective thermal diffusivity in laminar oscillatory flow is deduced from the analysis. This model consolidates the two phenomena of wall-normal heat transfer and the longitudinal convective transport. Finally, the correlation is expanded to account for the impact of turbulence intensity on heat transfer. This quantification compares favorably against the wall-normal heat transfer, which reveals similar characteristic features.

Contribution: The research topic was jointly defined by Prof. Wolfgang Polifke and the lead author. First numerical set-ups of a laminar reference case were collaboratively established with Joachim Ottinger in his bachelor thesis [76], which the lead author closely supervised. The lead author extended the numerical implementation to turbulent flows and conducted the parametric investigation and its evaluation. Furthermore, the lead author prepared the manuscript. Prof. Wolfgang Polifke gave proofreading and suggestions for improvement.

Status: To be submitted to the International Journal of Heat and Fluid Flow (IJHFF).

Reference: BurenPolif21 [66], reproduced on p. 155ff.

Summary and Conclusions

Bibliography

- [1] J. W. S. Rayleigh. The Explanation of Certain Acoustical Phenomena. *Nature*, 18:319–321, 1878. doi: 10.1038/018319a0.
- [2] T. Lieuwen and V. Yang, editors. *Combustion Instabilities in Gas Turbine Engines: Operational Experience, Fundamental Mechanisms and Modeling*. Number v. 210 in Progress in Astronautics and Aeronautics. American Institute of Aeronautics and Astronautics, Reston, VA, 2005. ISBN 978-1-56347-669-3.
- [3] F. E. Culick and V. Yang. Overview of Combustion Instabilities in Liquid-Propellant Rocket Engines. *Liquid Rocket Engine Combustion Instability*, 169:3–37, 1995.
- [4] D. T. Harrje and F. H. Reardon. Liquid Propellant Rocket Combustion Instability. Technical Report NASA-SP-194, Scientific and Technical Information Office, National Aeronautics and Space Administration, Washington, DC, U.S.A., 1972.
- [5] *The Jet Engine*. Rolls-Royce Ltd., Derby, U.K., fifth edition, 1996. ISBN 0902121 235.
- [6] K. Förner, A. Cárdenas Miranda, and W. Polifke. Mapping the Influence of Acoustic Resonators on Rocket Engine Combustion Stability. *Journal of Propulsion and Power*, 31(4):1159–1166, 2015. doi: 10.2514/1.B35660.
- [7] A. Chemnitz, N. Kings, and T. Sattelmayer. Modification of Eigenmodes in a Cold-Flow Rocket Combustion Chamber by Acoustic Resonators. *Journal of Propulsion and Power*, 35(4):765–779, 2019. doi: 10.2514/1.B37405.
- [8] E. Laudien, R. Pongratz, R. Piero, and D. Preclik. Fundamental Mechanisms of Combustion Instabilities: Experimental Procedures Aiding the Design of Acoustic Cavities. *Liquid Rocket Engine Combustion Instability*, pages 377–399, 1995. doi: 10.2514/5.9781600866371.0377.0399.
- [9] A. Cárdenas Miranda. *Influence of Enhanced Heat Transfer in Pulsating Flow on the Damping Characteristics of Resonator Rings*. PhD Thesis, TU Munich, Munich, Germany, 2014.
- [10] K. Förner, M. A. Temiz, W. Polifke, I. Lopez Arteaga, and A. Hirschberg. On the Non-Linear Influence of the Edge Geometry on Vortex Shedding in Helmholtz Resonators. In *22nd International Congress on Sound and Vibration (ICSV22)*, Florence, Italy, 2015.
- [11] J. Tournadre, K. Förner, W. Polifke, P. Martínez-Lera, and W. Desmet. Determination of Acoustic Impedance for Helmholtz Resonators Through Incompressible Unsteady Flow Simulations. *AIAA Journal*, 55(3):790–798, 2017. doi: 10.2514/1.J055337.

Bibliography

- [12] S. van Buren, K. Förner, and W. Polifke. Acoustic Impedance of a Quarter-Wave Resonator with Non-Uniform Temperature. In *27th International Congress on Sound and Vibration Sound Vibration (ICSV27)*, Prague, CZ, 2021.
- [13] N. Rott. Thermoacoustics. *Advances in Applied Mechanics*, bf20:135–175, 1980. doi: 10.1016/S0065-2156(08)70233-3.
- [14] P. K. Tang, D. T. Harrje, and W. A. Sirignano. Experimental Verification of the Energy Dissipation Mechanism in Acoustic Dampers. *Journal of Sound and Vibration*, 26(2): 263–276, 1973.
- [15] D. T. Harrje. Heat Transfer In Oscillating Flow. 3-g, Department of Aerospace and Mechanical Science, Princeton University, 1967.
- [16] E. H. Perry and F. E. C. Culick. Measurements of Wall Heat Transfer in the Presence of Large-Amplitude Combustion-Driven Oscillations. *Combustion Science and Technology*, 9(1-2):49–53, 1974. doi: 10.1080/00102207408960336.
- [17] J. E. Dec and J. O. Keller. Pulse Combustor Tail-Pipe Heat-Transfer Dependence on Frequency, Amplitude, and Mean Flow Rate. *Combustion and Flame*, 77(3-4):359–374, 1989. doi: 10.1016/0010-2180(89)90141-7.
- [18] J. E. Dec and J. O. Keller. Time-Resolved Gas Temperatures in the Oscillating Turbulent Flow of a Pulse Combustor Tail Pipe. *Combustion and Flame*, 80:358–370, 1990. doi: 10.1016/0010-2180(90)90112-5.
- [19] J. E. Dec, J. O. Keller, and V. S. Arpacı. Heat Transfer Enhancement in the Oscillating Turbulent Flow of a Pulse Combustor Tail Pipe. *Int. J. of Heat and Mass Transfer*, 35(9): 2311–2325, 1992. doi: 10.1016/0017-9310(92)90074-3.
- [20] V. S. Arpacı, J. E. Dec, and J. O. Keller. Heat Transfer in Pulse Combustor Tailpipes. *Combustion Science and Technology*, 94:131–146, 1993. doi: 10.1080/00102209308935307.
- [21] M. A. Habib, A. M. Attya, A. I. Eid, and A. Z. Aly. Convective Heat Transfer Characteristics of Laminar Pulsating Pipe Air Flow. *Heat and Mass Transfer*, 38(3):221–232, 2002. doi: 10.1007/s002310100206.
- [22] M. A. Habib, A. M. Attya, S. A. M. Said, A. I. Eid, and A. Z. Aly. Heat Transfer Characteristics and Nusselt Number Correlation of Turbulent Pulsating Pipe Air Flows. *Heat and Mass Transfer*, 40(3-4):307–318, 2004. doi: 10.1007/s00231-003-0456-6.
- [23] H. N. Hemida, M. N. Sabry, A. Abdel-Rahim, and H. Mansour. Theoretical Analysis of Heat Transfer in Laminar Pulsating Flow. *Int. J. of Heat and Mass Transfer*, 45(8): 1767–1780, 2002. doi: 10.1016/S0017-9310(01)00274-5.
- [24] E. Lundgren, U. Markstein, and A. Holst. Enhanced Heat Transfer in an Oscillating Pipe Flow. *6th ASME-JSME Thermal Engineering Joint Conference*, TED-AJO3-1, 2003.
- [25] S. Thyageswaran. Numerical Modeling of Pulse Combustor Tail Pipe Heat Transfer. *Int. J. of Heat and Mass Transfer*, 47(12 -13):2637–2651, 2004. doi: 10.1016/j.ijheatmasstransfer.2003.12.020.

- [26] X. Wang and N. Zhang. Numerical Analysis of Heat Transfer in Pulsating Turbulent Flow in a Pipe. *Int. J. of Heat and Mass Transfer*, 48(19-20):3957–3970, 2005. doi: 10.1016/j.ijheatmasstransfer.2005.04.011.
- [27] U. H. Kurzweg. Enhanced Heat Conduction in Oscillating Viscous Flows within Parallel-Plate Channels. *J. of Fluid Mechanics*, 156:291–300, 1985. doi: 10.1017/S0022112085002105.
- [28] G. K. Batchelor. *An Introduction to Fluid Dynamics*. Cambridge Mathematical Library. Cambridge Univ. Press, Cambridge, 1st cambridge mathematical ed., 14th print edition, 2010. ISBN 978-0-521-66396-0.
- [29] L. Davidson. Fluid Mechanics, Turbulent Flow and Turbulence Modeling. 2015.
- [30] K. Förner. *Nonlinear Aeroacoustic Characterization of Resonators*. Ph.D. Thesis, TU Munich, Munich, Germany, 2017. URL <https://mediatum.ub.tum.de/doc/1360567/1360567.pdf>.
- [31] S. W. Rienstra and A. Hirschberg. An Introduction to Acoustics. Technical Report IWDE 92-06, Eindhoven University of Technology, 2018.
- [32] G. Kirchhoff. über den Einfluss der Wärmeleitung in einem Gase auf die Schallbewegung. *Annalen der Physik*, 210(6):177–193, 1868.
- [33] M. R. Stinson. The Propagation of Plane Sound Waves in Narrow and Wide Circular Tubes, and Generalization to Uniform Tubes of Arbitrary Cross-Sectional Shape. *The Journal of the Acoustical Society of America*, 89(2):550–558, 1991. doi: 10.1121/1.400379.
- [34] C. Zwicker and C. Kosten. *Sound Absorbing Materials*. Elsevier Science Ltd, 1949. ISBN 978-0-444-40661-3.
- [35] L. E. Kinsler, A. R. Frey, A. B. Coppens, and J. V. Sanders. *Fundamentals of Acoustics*. John Wiley & Sons, New York, fourth edition, 2000. ISBN 978-0-471-84789-2.
- [36] A. D. Pierce. *Acoustics: An Introduction to Its Physical Principles and Applications*. Springer International Publishing, Cham, 2019. doi: 10.1007/978-3-030-11214-1.
- [37] D. H. Keefe. Acoustical Wave Propagation in Cylindrical Ducts: Transmission Line Parameter Approximations for Isothermal and Nonisothermal Boundary Conditions. *The Journal of the Acoustical Society of America*, 75(1):58–62, 1984. doi: 10.1121/1.390300.
- [38] G. W. Swift. *Thermoacoustics: A Unifying Perspective for Some Engines and Refrigerators*. Acoustical Society of America, 2002. ISBN 0-7354-0065-2.
- [39] A. Hynninen. *Acoustic In-Duct Characterization of Fluid Machines with Applications to Medium Speed IC-Engines*. PhD thesis, KTH Royal Institute of Technology, Stockholm, 2015.

Bibliography

- [40] A. Hynninen and M. Abom. Acoustic Simulation of Medium Speed IC-Engine Exhaust Gas After Treatment Devices with Substrate. In *8th International Styrian Noise, Vibration & Harshness Congress: The European Automotive Noise Conference*, pages 2014–01–2057, 2014. doi: 10.4271/2014-01-2057.
- [41] O. Gobin. *Entwicklung und Test eines Low-Order Modells zur Beschreibung von $\lambda/4$ -Resonatoren im Absorberring einer Raketenschubkammer*. Semester Thesis, TU Munich, 2005.
- [42] W. Polifke, J. van der Hoek, and B. Verhaar. Everything You always Wanted to Know about f and g. Technical report, Technical Report of ABB Corporate Research, Baden, Switzerland, 1997.
- [43] R. I. Sujith, G. A. Waldherr, and B. Zinn. An Exact Solution for One-Dimensional Acoustic Fields in Duct with an Axial Temperature Gradient. *Journal of Sound and Vibration*, 184(3):389–402, 1995. doi: 10.1006/jsvi.1995.0323.
- [44] B. M. Kumar and R. I. Sujith. Exact Solution for One-Dimensional Acoustic Fields in Ducts with a Quadratic Mean Temperature Profile. *The Journal of the Acoustical Society of America*, 101(6):3798–3799, 1997. doi: 10.1121/1.418385.
- [45] M. B. Kumar and R. I. Sujith. Exact Solution for One-Dimensional Acoustic Fields in Ducts With Polynomial Mean Temperature Profiles. *Journal of Vibration and Acoustics*, 120(4):965–969, 1998. doi: 10.1115/1.2893927.
- [46] G. B. Arfken and H.-J. Weber. *Mathematical Methods for Physicists*. Elsevier, Boston, sixth edition, 2005. ISBN 978-0-12-059876-2 978-0-12-088584-8.
- [47] Wolfram Research, Inc. Mathematica (Version 12.2) [software]. Champaign, Illinois, 2020.
- [48] L. Rayleigh. *The Theory of Sound*. Macmillan, London, 1896. ISBN 0-486-60292-3.
- [49] U. Ingard. On the Theory and Design of Acoustic Resonators. *Journal of Acoustical Society of America*, 25(6), 1953. doi: 10.1121/1.1907235.
- [50] J. J. Keller and E. Zauner. On the Use of Helmholtz Resonators as Sound Attenuators. *Zeitschrift für angewandte Mathematik und Physik*, 46:297–327, 1995. doi: 10.1007/BF01003552.
- [51] M. L. Munjal. *Acoustics of Ducts and Mufflers*. John Wiley & Sons, 1987.
- [52] G. D. Garrison, A. C. Schnell, C. D. Baldwin, and P. R. Russel. Suppression of Combustion Oscillations with Mechanical Damping Devices, Interim Report. Technical Report NAS8-21310, Pratt and Whitney Aircraft, West Palm Beach, Fla. Florida Research and Development Center, 1969.
- [53] S. van Buren and W. Polifke. Enhanced Longitudinal Heat Transfer in Oscillatory Channel Flow – a Theoretical Perspective. *Journal of Fluids Engineering*, 2021. doi: 10.1115/1.4052067.

- [54] P. C. Chatwin. On the Longitudinal Dispersion of a Passive Contaminant in Oscillatory Flows in Tubes. *J. of Fluid Mechanics*, 71:513–527, 1975. doi: 10.1017/S0022112075002716.
- [55] M. J. Jaeger and U. H. Kurzweg. Determination of the Longitudinal Dispersion Coefficient in Flows Subjected to High-Frequency Oscillations. *Physics of Fluids*, 26(6):1380, 1983. doi: 10.1063/1.864323.
- [56] E. J. Watson. Diffusion in Oscillatory Pipe Flow. *J. of Fluid Mechanics*, 133:233–244, 1983. doi: 10.1017/S0022112083001883.
- [57] C. H. Joshi, R. D. Kamm, J. M. Drazen, and A. S. Slutsky. An Experimental Study of Gas Exchange in Laminar Oscillatory Flow. *J. of Fluid Mechanics*, 133:245–254, 1983. doi: 10.1017/S0022112083001895.
- [58] U. H. Kurzweg. Enhanced Heat Conduction in Fluids Subjected to Sinusoidal Oscillations. *Int. J. of Heat Transfer*, 107(2):459, 1985. doi: 10.1115/1.3247437.
- [59] U. Kurzweg and L. de Zhao. Heat Transfer by High-Frequency Oscillations: A New Hydrodynamic Technique for Achieving Large Effective Thermal Conductivities. *Physics of Fluids*, 27(11):2624–2627, 1984. doi: 10.1063/1.864563.
- [60] M. Kaviany. Some Aspects of Enhanced Heat Diffusion in Fluids by Oscillation. *Int. J. of Heat and Mass Transfer*, 29(12):2002–2006, 1986. doi: 10.1016/0017-9310(86)90022-0.
- [61] M. Kaviany. Performance of a Heat Exchanger Based on Enhanced Heat Diffusion in Fluids by Oscillation: Analysis. *J. of Heat Transfer*, 112(1):49–55, 1990. doi: 10.1115/1.2910363.
- [62] M. Kaviany and M. Reckker. Performance of a Heat Exchanger Based on Enhanced Heat Diffusion in Fluids by Oscillation: Experiment. *J. of Heat Transfer*, 112(1):56–63, 1990. doi: 10.1115/1.2910364.
- [63] S. Nishio, X.-H. Shi, and W.-M. Zhang. Oscillation-Induced Heat Transport: Heat Transport Characteristics Along Liquid-Columns of Oscillation-Controlled Heat Transport Tubes. *Int. J. of Heat and Mass Transfer*, 38(13):2457–2470, 1995. doi: 10.1016/0017-9310(94)00372-3.
- [64] M. R. Bothien and D. Wassmer. Impact of Density Discontinuities on the Resonance Frequency of Helmholtz Resonators. *AIAA Journal*, 53(4):877–887, 2015. doi: 10.2514/1.J053227.
- [65] B. Ćosić, D. Wassmer, S. Terhaar, and C. O. Paschereit. Acoustic Response of Helmholtz Dampers in the Presence of Hot Grazing Flow. *J. of Sound and Vibration*, 335:1–18, 2015. doi: 10.1016/j.jsv.2014.08.025.
- [66] S. van Buren and W. Polifke. Turbulence-Induced Enhancement of Longitudinal Heat Transfer in Oscillatory Channel Flow. *to be submitted to Int. J. Heat Fluid Flow*, 2021.

Bibliography

- [67] S. van Buren and W. Polifke. Heat Transfer in Pulsating Flow and its Impact on Temperature Distribution and Damping Performance of Resonators. In W. Schröder, N. A. Adams, O. J. Haidn, R. Radespiel, T. Sattelmayer, W. Schröder, and B. Weigand, editors, *Future Space-Transport-System Components under High Thermal and Mechanical Loads*, number 146 in Notes on Numerical Fluid Mechanics and Multidisciplinary Design, pages 97–111. Springer International Publishing, 2021. doi: 10.1007/978-3-030-53847-7.
- [68] N. A. Adams, W. Schröder, R. Radespiel, O. J. Haidn, T. Sattelmayer, C. Stemmer, and B. Weigand, editors. *Future Space-Transport-System Components under High Thermal and Mechanical Loads: Results from the DFG Collaborative Research Center TRR40*, volume 146 of *Notes on Numerical Fluid Mechanics and Multidisciplinary Design*. Springer International Publishing, Cham, 2021. doi: 10.1007/978-3-030-53847-7.
- [69] T. Poinsot and S. K. Lele. Boundary Conditions for Direct Simulation of Compressible Viscous Flows. *Journal of Computational Physics*, 101(1):104–129, 1992. doi: 10.1016/0021-9991(92)90046-2.
- [70] K. Förner and W. Polifke. Aero-Acoustic Characterization of Helmholtz Resonators in the Linear Regime with System Identification. In *22nd International Congress on Sound and Vibration (ICSV22)*, Florence, Italy, 2015.
- [71] A. Scotti and U. Piomelli. Numerical Simulation of Pulsating Turbulent Channel Flow. *Physics of Fluids*, 13(5):1367–1367, 2001. doi: 10.1063/1.1359766.
- [72] A. Scotti and U. Piomelli. Turbulence Models in Pulsating Flows. *AIAA Journal*, 40(3): 537–544, 2002. doi: 10.2514/2.1679.
- [73] S. van Buren, A. Cárdenas Miranda, and W. Polifke. Large Eddy Simulation of Enhanced Heat Transfer in Pulsatile Turbulent Channel Flow. *Int. J. of Heat and Mass Transfer*, 144: 118585, 2019. doi: 10.1016/j.ijheatmasstransfer.2019.118585.
- [74] L. Wang and X.-Y. Lu. An Investigation of Turbulent Oscillatory Heat Transfer in Channel Flows by Large Eddy Simulation. *Int. J. of Heat and Mass Transfer*, 47:2161–2172, 2004. doi: 10.1016/j.ijheatmasstransfer.2003.11.010.
- [75] K. Förner, J. Tournadre, P. Martínez-Lera, and W. Polifke. Scattering to Higher Harmonics for Quarter Wave and Helmholtz Resonators. *AIAA Journal*, 55(4):1194–1204, 2017. doi: 10.2514/1.J055295.
- [76] J. Ottinger. *Numerical Simulation of Enhanced Heat Conduction in Oscillating Laminar Parallel-Plate Flow under an Axial Temperature Gradient*. Bachelor Thesis, TU Munich, Munich, Germany, 2018. URL <https://mediatum.ub.tum.de/doc/1538023/1538023.pdf>.
- [77] D. Kollmeier. *Instationäre Wärmeleitung in dickwandigen Komponenten konventioneller Kraftwerke*. Bachelor Thesis, TU Munich, Munich, Germany, 2018. URL <https://mediatum.ub.tum.de/doc/1442264/1442264.pdf>.

- [78] Y. Lian. *Analytical and Numerical Investigation of the Damping Behavior of a Quarter Wave Resonator Using an Incompressible Approach*. Bachelor Thesis, TU Munich, Munich, Germany, 2018. URL <https://mediatum.ub.tum.de/doc/1452924/1452924.pdf>.
- [79] U. Hartmann. *Validation of Acoustic Boundary Conditions in OpenFOAM*. Bachelor Thesis, TU Munich, Munich, Germany, 2018. URL <https://mediatum.ub.tum.de/doc/1462849/1462849.pdf>.
- [80] M. Maurer. *Numerische Stabilitätsuntersuchung der akustischen Kopplung von Resonator und Flammenmodell*. Bachelor Thesis, TU Munich, Munich, Germany, 2018. URL <https://mediatum.ub.tum.de/doc/1462439/1462439.pdf>.
- [81] S. van Buren, K. Förner, and W. Polifke. Analytical and Numerical Investigation of the Damping Behavior of a Quarter-Wave Resonator with Temperature Inhomogeneity. In C. Stemmer, N. A. Adams, O. J. Haidn, R. Radespiel, T. Sattelmayer, W. Schröder, and B. Weigand, editors, *Annual Report*, pages 35–47. Sonderforschungsbereich/Transregio 40, 2017.
- [82] S. van Buren and W. Polifke. Enhanced Heat Transfer in Turbulent Channel Flow Exposed to High Amplitude Pulsations. In C. Stemmer, N. A. Adams, O. J. Haidn, R. Radespiel, T. Sattelmayer, W. Schröder, B. Weigand, and B. Weigand, editors, *Annual Report*, pages 39–56. Sonderforschungsbereich/Transregio 40, 2018.
- [83] S. van Buren and W. Polifke. Enhanced Longitudinal Heat Transfer in Turbulent Oscillatory Channel Flow. In C. Stemmer, N. A. Adams, O. J. Haidn, R. Radespiel, T. Sattelmayer, W. Schröder, and B. Weigand, editors, *Annual Report*, pages 35–48. Sonderforschungsbereich/Transregio 40, 2019.

Bibliography

List of Figures

1.1	Damages of a combustor face plate due to thermoacoustic instability.	2
1.2	L-shaped quarter-wave resonator in a Vulcain 2 engine.	2
2.1	Geometry and boundary conditions of a quarter-wave channel.	16
2.2	First eigenfrequency ω for different temperatures T_1 and channel widths r_h	23
2.3	Second eigenfrequency ω for different temperatures T_1 and channel widths r_h	24
2.4	Third eigenfrequency ω for different temperatures T_1 and channel widths r_h	25
2.5	Absolute pressure amplitude $ p_1 $ (—) and velocity amplitude $ U_1/A $ (- - -, factor $\rho_2 c_2$) for the first eigenfrequency at different temperatures T_1 and channel widths r_h	27
2.6	Phase of pressure p_1 (—) and velocity U_1/A (- - -) for the first eigenfrequency at different temperatures T_1 and channel widths r_h	28
2.7	Absolute pressure amplitude $ p_1 $ (—) and velocity amplitude $ U_1/A $ (- - -, factor $\rho_2 c_2$) for the second eigenfrequency at different temperatures T_1 and channel widths r_h	32
2.8	Phase of pressure p_1 (—) and velocity U_1/A (- - -) for the second eigenfrequency at different temperatures T_1 and channel widths r_h	33
2.9	Absolute pressure amplitude $ p_1 $ (—) and velocity amplitude $ U_1/A $ (- - -, factor $\rho_2 c_2$) for the third eigenfrequency at different temperatures T_1 and channel widths r_h	34
2.10	Phase of pressure p_1 (—) and velocity U_1/A (- - -) for the third eigenfrequency at different temperatures T_1 and channel widths r_h	35
3.1	Sketch of a Helmholtz resonator (left) and a quarter-wave resonator (right). . .	38
3.2	Geometry and boundary conditions of a quarter-wave resonator with geometrical length L , end correction δ_0 , and effective length L_e . Laudien et al. [8] proposed the fictive neck length L_r as a fitting parameter.	39

3.3 Validation of the magnitude of the reflection coefficient R vs. the frequency f . Analytical results (—) by Laudien et al. [8], numerical results (●) by van Buren et al. [12], and the present model: end correction and adiabatic walls (—), end correction and isothermal walls (---), and no end correction and adiabatic walls (....).	42
3.4 Model of the present study: Reflection coefficient $ R $ (first row), specific resistance $\text{Re}(z)$ (second row), and specific reactance $\text{Im}(z)$ (third row) vs. the frequency ω and hydraulic radius r_h . From left to right, three different area ratios $\beta = 1, 10$, and 100 are shown. The blue dots (●) indicate the parametric set-ups of the latter discussion of the acoustic profiles (see Sec. 3.4.3). Furthermore, the central blue dots indicate the parametric set-ups of optimal damping ($ R = 0$).	44
3.5 Model of the present study without thermal boundary layer: Reflection coefficient $ R $ (first row), specific resistance $\text{Re}(z)$ (second row) and specific reactance $\text{Im}(z)$ (third row) vs. the frequency ω and hydraulic radius r_h . From left to right, three different area ratios $\beta = 1, 10$, and 100 are shown.	45
3.6 Model by Laudien et al. [8]: Reflection coefficient $ R $ (first row), specific resistance $\text{Re}(z)$ (second row) and specific reactance $\text{Im}(z)$ (third row) vs. the frequency ω and hydraulic radius r_h . From left to right, three different area ratios $\beta = 1, 10$, and 100 are shown.	46
3.7 Magnitude of normalized pressure $ p_1 /(\rho c)$ (—) and velocity $ U_1 /A$ (---) for $\beta = 1$	48
3.8 Phase of pressure $\angle p_1$ (—) and velocity $\angle U_1$ (---) for $\beta = 1$	49
3.9 Magnitude of the characteristic waves $ f $ (—) and $ g $ (---) for $\beta = 1$	50
3.10 Phase of the characteristic waves $\angle f$ (—) and $\angle g$ (---) for $\beta = 1$	51
3.11 Magnitude of normalized pressure $ p_1 /(\rho c)$ (— and —) and velocity $ U_1 /A$ (---) for $\beta = 10$. The velocity (---) and pressure (—) are normalized by the area ratio $\beta = 10$ within the resonator ($x < 4\text{ m}$).	53
3.12 Phase of pressure $\angle p_1$ (—) and velocity $\angle U_1$ (---) for $\beta = 10$	54
3.13 Magnitude of the characteristic waves $ f $ (—) and $ g $ (---) for $\beta = 10$. Within the resonator ($x < 4\text{ m}$) the characteristic waves are normalized by the area ratio $\beta = 10$	55
3.14 Phase of the characteristic waves $\angle f$ (—) and $\angle g$ (---) for $\beta = 10$	56
4.1 Heat transfer in oscillating channel flow as studied by Kurzweg [27].	60
4.2 Effective normalized thermal diffusivity vs. Womersley and Prandtl numbers.	66
4.3 Effective (absolute) thermal diffusivity vs. Womersley and Prandtl numbers.	66

4.4	Individual components (term 2 (■) and term 3 (□)) of thermal diffusivity according to Rott at the pressure node ($x = L$)	67
4.5	Individual components (term 2 (■) and term 3 (□)) of thermal diffusivity according to Rott for increased oscillation amplitudes at the pressure node ($x = L$)	67
4.6	Individual components (term 1 (■), term 2 (■), and term 3 (□)) of thermal diffusivity according to Rott for increased oscillation amplitudes with pressure oscillations ($x = L/2$)	68
4.7	Tidal displacement vs. Womersley number and duct length.	68
5.1	Sketch of a combustion chamber with wall-normal (\dot{q}_\perp , see Sec. 5.3.1) and longitudinal (\dot{q}_\parallel , see Sec. 5.3.2) heat transfer.	71

List of Figures

Supervised Students

Associated with this Ph. D. thesis are several bachelor's theses supervised by the author of the present work. These were prepared at the Thermofluidynamics Group, Technical University of Munich (TUM) during the years 2017 through 2020 under the present author's close supervision. Parts of these supervised theses have been incorporated into the present thesis. The author would like to express his sincere gratitude to all formerly supervised students for their commitment and support of this research project and of the Ph. D. thesis at hand.

Student	Thesis
Daniel Kollmeier	Bachelor's Theses Instationäre Wärmeleitung in dickwandigen Komponenten konventioneller Kraftwerke [77] (in German, online available) May 7, 2018
Yujie Lian	Bachelor's Theses Analytical and Numerical Investigation of the Damping Behavior of a Quarter Wave Resonator using an Incompressible Approach [78] (online available) August 15, 2018
Joachim Ottinger	Bachelor's Theses Numerical Simulation of Enhanced Heat Conduction in Oscillating Laminar Parallel-Plate Flow under an Axial Temperature Gradient [76] (online available) September 14, 2018
Ulrich Hartmann	Bachelor's Theses Validation of Acoustic Boundary Conditions in OpenFOAM [79] (online available) September 28, 2018
Michaela Maurer	Bachelor's Theses Numerische Stabilitätsuntersuchung der akustischen Kopplung von Resonator und Flammenmodell [80] (in German, online available) October 29, 2018

Supervised Students

A Reproduction of Papers

The major publications related to the topic of the thesis are reproduced in the following appendices. Further annual project reports were published in book-form [81–83].

Heat Transfer in Pulsating Flow and Its Impact on Temperature Distribution and Damping Performance of Acoustic Resonators



Simon van Buren and Wolfgang Polifke

Abstract A numerical framework for the prediction of acoustic damping characteristics is developed and applied to a quarter-wave resonator with non-uniform temperature. The results demonstrate a significant impact of the temperature profile on the damping characteristics and hence the necessity of accurate modeling of heat transfer in oscillating flow. Large Eddy Simulations are applied to demonstrate and quantify enhancement in heat transfer induced by pulsations. The study covers wall-normal heat transfer in pulsating flow as well as longitudinal convective effects in oscillating flow. A discussion of hydrodynamic and thermal boundary layers provides insight into the flow physics of oscillatory convective heat transfer.

1 Introduction and Placement in SFB

Combustion instabilities jeopardize the structural integrity of rocket combustion chambers. One measure to ensure safe operating conditions is the application of acoustic resonators to suppress the thermo-acoustic feedback. Modern engines such as the Vulcain 2 combustion chamber include L-shaped quarter-wave resonators. Due to regenerative cooling, large temperature differences exist between the hot combustion gases and the cooled chamber walls. The transient heat-up process brings additional uncertainty.

S. van Buren (✉) · W. Polifke

Department of Mechanical Engineering, Technical University of Munich, 85748 Garching, Germany

e-mail: vanburen@tfd.mw.tum.de

W. Polifke

e-mail: polifke@tum.de

© The Author(s) 2021

N. A. Adams et al. (eds.), *Future Space-Transport-System Components under High Thermal and Mechanical Loads*, Notes on Numerical Fluid Mechanics and Multidisciplinary Design 146, https://doi.org/10.1007/978-3-030-53847-7_6

During the first funding period of SFB Transregio 40, A. Cardenas developed analytical correlations for the acoustic damping characteristics of a quarter-wave resonator, which indicate that the impact of temperature inhomogeneities is significant [20]. Thus accurate acoustic predictions require the detailed knowledge of the temperature distribution within a resonator. In this context, the turbulent pulsating nature of the flow in the resonator presents a crucial challenge for the modeling of heat transfer. Experimental results that reported significant enhancement of average heat transfer could not be reproduced in numerical simulations [20]. Low-order network models were developed to evaluate rocket engine combustion stability under the influence of acoustic resonators [11].

During the second funding period, K. Förner identified and quantified significant non-linear effects resulting from large oscillation amplitudes (e.g. vortex shedding) [12, 13]. This implies a high degree of uncertainty for the analytical correlations derived by Cardenas. On the contrary, high-resolution numerical studies are not prone to these inaccuracies.

In the final funding period, S. van Buren merged the two prior lines of study: A numerical framework to predict acoustic damping characteristics was developed and applied to quarter-wave resonators with local temperature inhomogeneities. Subsequently, heat transfer in turbulent pulsation flows was revisited and the range of investigations was extended to larger oscillation amplitudes. Indeed, significant wall-normal enhancement of heat transfer could be confirmed at increased amplitudes. To account for the geometry of a quarter-wave resonator tube, the investigations were extended to convective longitudinal effects in oscillating flows.

Based on the focus on heat transfer, the present project is assigned to the research area *Structural Cooling* (RA A). The integrated acoustic examination of the resonator in the *Combustion Chamber* reveals additional close connection to RA C.

2 Impact of Temperature Inhomogeneities on Damping Performance

A variety of analytical correlations to quantify the damping characteristic of acoustic resonators have been derived in analogy to mass-spring-damper systems (e.g. [15, 16, 21]). For the case of a Helmholtz resonator, the acoustically compact fluid in the neck section presents the oscillating mass (velocity fluctuation u' , compare Figs. 1 and 2). The compressible fluid in the cavity (volume V) acts as the restoring spring. Damping is induced by either viscous friction in the neck section (losses *linear* to the velocity perturbation u') or vortex shedding (*non-linear* losses of higher order). In particular the latter introduces a large degree of uncertainty.

Laudien et al. [19] extended prior studies to the geometry of a quarter-wave resonator (Fig. 3). The difficulty connected to this geometry is the increased axial length scale (quarter-wave length at eigenfrequency) that violates the assumption of acous-

Fig. 1 Sketch of a Helmholtz resonator, with highlighted oscillating fluid mass in the neck region.
Redrawn from [20]

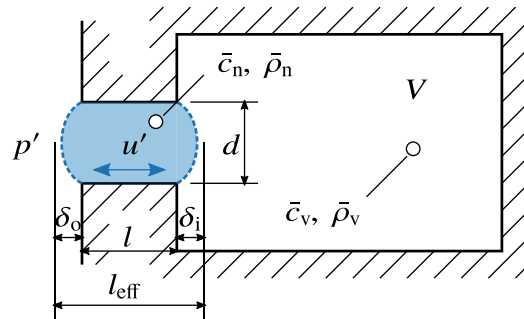


Fig. 2 Mass-spring-damper system, excited by pressure perturbation p' , responding in velocity fluctuation u' .
Redrawn from [20]

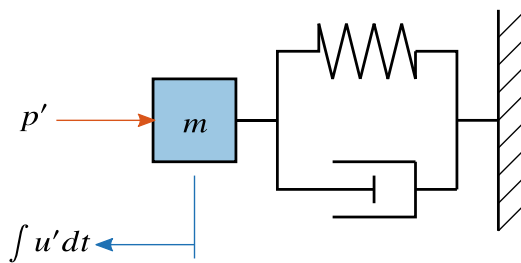


Fig. 3 Sketch of a quarter-wave resonator, with highlighted oscillating fluid mass derived by the representative length l_r .
Redrawn from [20]

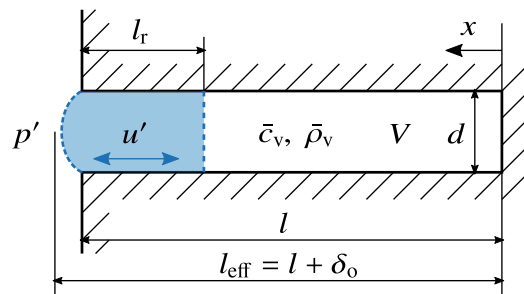
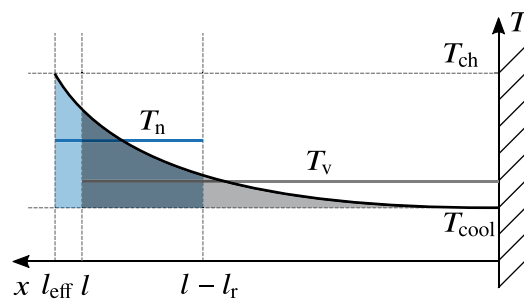


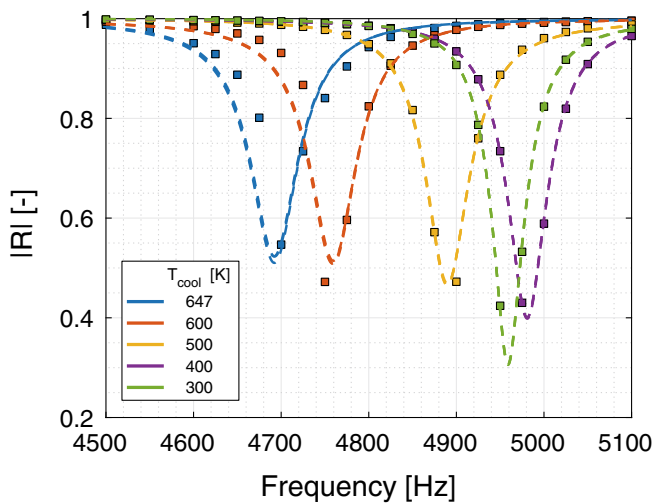
Fig. 4 Polynomial and average temperature profile in the neck and volume regions in a quarter-wave resonator



tic compactness. Laudien's model is restricted to a homogeneous fluid temperature, as it has a significant impact on the local density ρ and thus on the speed of sound c .

Resonators used in combustion chambers are generally exposed to significant temperature gradients. Figure 4 shows a schematic axial temperature distribution within a quarter-wave resonator: Hot combustion gas dominates at the front opening, whereas the backing of the cavity is exposed to regenerative cooling. During the first funding period of SFB Transregio 40 Cardenas [20] extended an approach by

Fig. 5 Gain of the reflection coefficient for harmonic excitation (squares) and results for three randomly generated broadband excitations obtained by CFD/SI (dashed lines)



Kumar and Sujith [17] and introduced temperature inhomogeneities to the model of Laudien et al. [19]. Based on the analytical solution by Kumar and Sujith, applicable temperature profiles $T(x)$ are mathematically restricted to a polynomial form:

$$T(x) = (ax + b)^n. \quad (1)$$

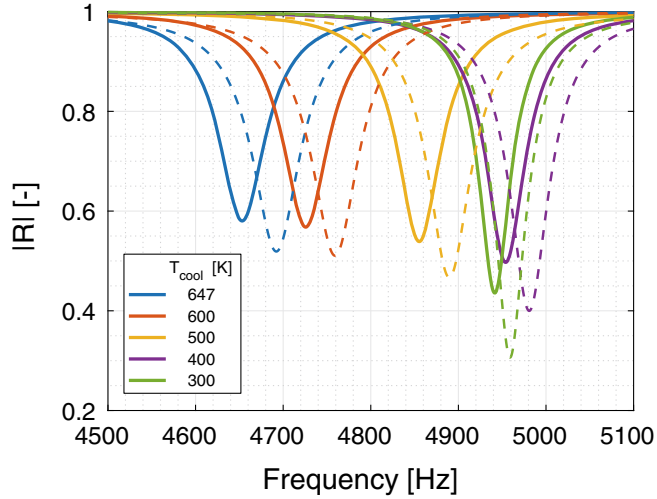
The analytical model of Cardenas [20] revealed that temperature inhomogeneities have a significant impact on the damping performance, i.e. they cause a shift in eigenfrequency, a reduction of the effective frequency range and the minimum reflection coefficient. The frequency-dependent reflection coefficient $R(\omega)$ quantifies the ratio of the reflected acoustic wave g to the incident wave f :

$$R(\omega) = \frac{g}{f}. \quad (2)$$

Subsequently, a numerical framework based on computational fluid dynamics (CFD) for the calculation of the reflection coefficient $R(\omega)$ was presented and applied to quarter-wave resonators with temperature inhomogeneities by van Buren [2, 3]. The resonator is modeled by two- or three-dimensional wedge geometries with an imposed temperature profile. Incident acoustic waves are imposed in the form of harmonic as well as broadband forcing. The time series data generated with the latter approach is post-processed by system identification (SI)—a form of supervised machine learning—and only requires one single simulation to determine results for a wide range of frequencies. Central advantages over the analytical model are the flexibility of arbitrary temperature distributions and the incorporation of non-linear effects. Details on the numerical framework and simulation setup are given in [2, 3].

Figure 5 compares numerical results of harmonic and broadband forcing (CFD/SI). Overall, the qualitative and quantitative agreement is very good. This generates confidence in both methods. The plot also illustrates the physical impact of tempera-

Fig. 6 Gain of the reflection coefficient of the analytical model (solid lines) and averaged results obtained by system identification of broadband excitation (dashed lines)



ture inhomogeneities: All five setups have identical mean temperatures ($T = 647$ K) along the resonator tube. As the gradient between cooled backing and hot front opening is increased a significant shift in eigenfrequency is introduced ($\omega \approx 4600$ Hz to 5000 Hz). Furthermore, the effective frequency range of damping narrows and the minimum reflection coefficient R decreases. Both effects reduce the effectiveness of the resonator as a damper of thermo-acoustic instabilities.

Figure 6 compares CFD/SI results with the analytical correlation. There is qualitative agreement but quantitative offset in both frequency and reflection coefficient.

3 Impact of Acoustic Oscillations on Heat Transfer

The accurate computation of the acoustic characteristics of the resonator requires precise knowledge of the local temperature distribution of the working fluid. Therefore, fundamental understanding of heat transfer in the presence of strong acoustic perturbations is indispensable. For the problem at hand, physical boundary conditions define two categories of heat transfer [20]: First, within the combustion chamber, wall normal heat transfer from the hot fluid to the cooled wall occurs in turbulent *pulsating flows*. The pulsations originate from the superposition of a mean-flow and acoustic velocity perturbations. Second, within the resonator tube, axial heat transfer from the hot front section to the cooled backing of the cavity exists. In contrast to the first category, mean-flow is absent here, one speaks of *oscillating flow*.

Figure 7 illustrates the modeling of an acoustically compact duct section at the position of a pressure node: In the small domain from $x = X$ to $x = X + dx$, pressure perturbation p_3 are not present, whereas acoustic velocity fluctuations u are maximum. The selection of this domain of interest is consistent with numerous previous studies, which report that enhancement in heat transfer coincides with velocity fluctuations rather than pressure oscillations [8–10, 14].

Fig. 7 One-dimensional mode shape of the second harmonic in a channel. Mean flow is driven by the pressure gradient of $P_0(x)$

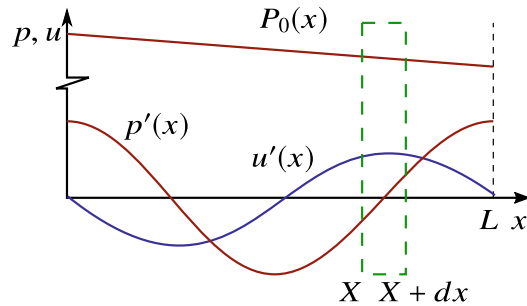


Fig. 8 Cyclic simulation domain of an acoustically compact channel section at a pressure node

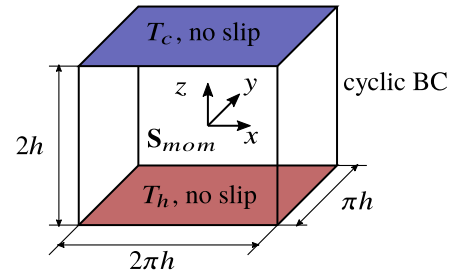


Figure 8 depicts the numerical domain at the location of a pressure node. The channel is confined by two walls of distance $2h$. For the investigation of wall-normal heat transfer, these walls are constrained to homogeneous but different temperatures (T_h and T_c as shown in the figure). In the second case of longitudinal heat transfer, constant axial temperature gradients are applied. Cyclic conditions apply to the remaining four boundary patches. One central advantage of this setup is the generation of fully developed turbulent flow without the requirement of turbulent inflow conditions. The flow is driven by a momentum source term S_{mom} that accounts for the acoustic oscillations via the spatial gradient of the pressure perturbation p' and for the mean-flow via the gradient of the overall pressure P_0 (compare Fig. 7).

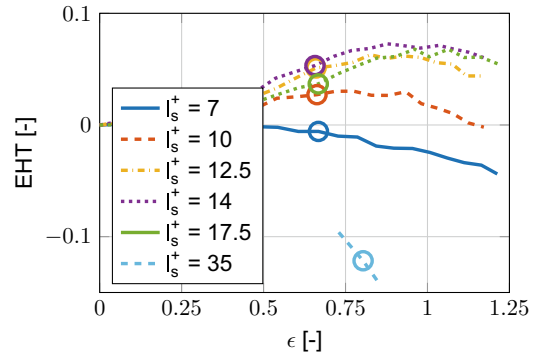
More detailed information of the incompressible Large Eddy Simulation is provided in [1, 4], including the selection of turbulence models, a mesh independence study and the validation against analytical, experimental and numerical results.

3.1 Wall Normal Heat Transfer

In this section, the core findings for wall-normal heat transfer in turbulent pulsating channel flows are presented and discussed. More detailed results are provided in [1, 4].

The figures in this section show the enhancement in heat transfer (EHT) versus non-dimensional pulsation amplitude ϵ for various Stokes' lengths l_s^+ . The EHT is defined as the enhancement in wall-normal heat flux of the turbulent pulsating flow $\dot{q}_{w,puls}$ over a turbulent but non-pulsation reference $\dot{q}_{w,ref}$:

Fig. 9 Temporal averaged EHT over amplitude ϵ for various Stokes' length l_s^+ corresponding to different frequencies



$$\text{EHT} = \frac{\dot{q}_{w,puls} - \dot{q}_{w,ref}}{\dot{q}_{w,ref}}. \quad (3)$$

The non-dimensional pulsation amplitude ϵ relates the pulsating velocity amplitude a_u at the channel center-plane (index c) to the mean velocity of the corresponding non-pulsating reference:

$$\epsilon = \left. \frac{a_u}{u_{ref}} \right|_c. \quad (4)$$

Lastly, the non-dimensional Stokes' length l_s^+ is introduced as a measure for the pulsation frequency:

$$l_s^+ = \frac{u_\tau}{v} \delta_s = \frac{\text{Re}_\tau}{h} \delta_s, \quad (5)$$

where Re_τ is the turbulent Reynolds number and $\delta_s = (2\omega/v)^{1/2}$ the classical Stokes length.

During the first funding period, numerical simulations by Cardenas [20] could not reproduce experimental results that report EHT of more than 100%. To resolve these discrepancies, the present study investigates flows at increased turbulent Reynolds number $\text{Re}_\tau = 350$ (instead of $\text{Re}_\tau \approx 180$). Furthermore, the numerical framework includes the dynamic calculation of locally resolved turbulent Prandtl numbers. Figure 9 depicts the temporal average of enhancement in heat transfer versus pulsation strength ϵ for various frequencies l_s^+ . EHT is most pronounced at frequencies around $l_s^+ \approx 14$ and velocity amplitudes close to flow reversal (i.e. $\epsilon \approx 1$). In the parameter range under investigation, only minor effects of EHT confirm the results by Cardenas [20]. A time-resolved investigation over one pulsation period reveals significant variation in EHT, ranging from strong reduction (larger than 50%) to clear enhancement (up to 45%, Fig. 10).

The local maximum in EHT at $\epsilon \approx 1$ led originally to the conclusion that LES does not capture pronounced EHT [20]. However, this conclusion was premature. Indeed, examination of the time-resolved heat transfer (Fig. 10) strongly indicates the relevance of large flow velocities. This suggested the extension of the parameter range under investigation and to increase the pulsation strength to values beyond

Fig. 10 Phase related EHT for various non-dimensional Stokes' length l_s^+ at exemplary $\epsilon \approx 0.65$ (depicted by circles in Fig. 9)

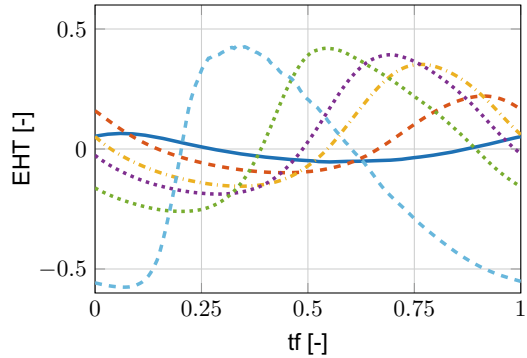


Fig. 11 Time averaged enhancement of heat transfer over the pulsation amplitude at $l_s^+ = 14$. Including results of Wang and Zhang [22]

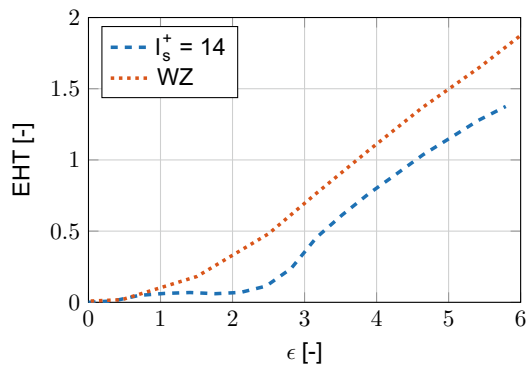
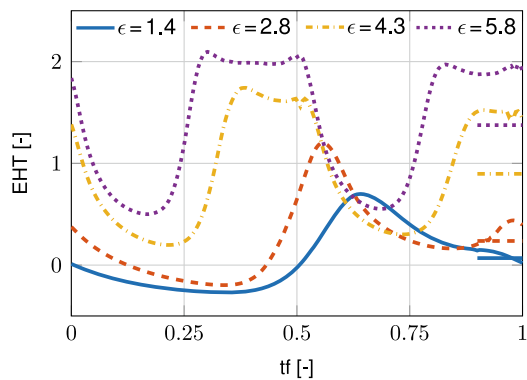


Fig. 12 Ensemble averaged enhancement of heat transfer for four high pulsation amplitudes at $l_s^+ = 14$



$\epsilon = 1.25$. The plateau in Fig. 11 (dashed blue line) shows that no significant enhancement in heat transfer develops below velocity amplitudes corresponding to $\epsilon < 2$, but for larger amplitudes ($\epsilon > 2$), a clear and significant increase in EHT develops. Despite numerous difference in physical modelling and numerical setup, the results qualitatively agree with the work of Wang and Zhang [22]. The significant enhancement in heat transfer is well explained by Fig. 12: At pulsation amplitudes close to flow reversal (e.g. $\epsilon = 1.4$), times of flow velocities close to rest hinder an overall (time-averaged) enhancement. In the case of significant flow reversal, these times of flow stagnation are quickly surpassed, providing longer intervals at large flow velocities.

3.2 Longitudinal Heat Transfer

The computational setup for the study of wall-normal heat transfer in pulsating turbulent flow is modified to account for a longitudinal convective mechanism first studied by Kurzweg [18]. Kurzweg derived a closed analytical expression for axial heat transfer in oscillatory laminar channel flows constrained by a constant axial temperature gradient. The velocity oscillations enhance the molecular thermal diffusivity by orders of magnitude: The fluid receives a wall heat flux at the hot reversal point, oscillates to the cold reversal point and returns its thermal energy to the walls. During the final funding period of SFB Transregio 40, van Buren applied LES to extend Kurzweg's investigations to turbulent flows. Details on the numerical setup, results and discussions are given in [5, 7]

Kurzweg [18] proposed an effective thermal diffusivity κ_e . In its non-dimensional form, this diffusivity is normalized by the angular frequency ω of the oscillation and the square of the tidal displacement Δx^2 : $\kappa_e/\omega\Delta x^2$. The red line in Fig. 13 shows Kurzweg's analytical results for effective thermal diffusivity over the Prandtl number Pr of the fluid. In agreement with the previous numerical study, $l_s^+ = 14$ was selected. This correlates with a Womersley number of $\text{Wo} \approx 35$ and indicates thin hydrodynamic boundary layers compared to the channel width. Numerical results are displayed by the blue, orange, yellow and purple line, which are ordered by increasing oscillation strength. The lower two amplitudes generate laminar flow conditions and show overall agreement with the analytical correlation. At larger amplitudes, deviations appear at high Prandtl numbers, exceeding the location of the peak at $\text{Wo}^2 \text{Pr} \approx \pi$. These differences induced by the onset of turbulence are more apparent in the semi-logarithmic presentation in Fig. 14. The turbulence-induced enhancement of longitudinal heat transfer ϵ_{turb} is defined as the effective thermal diffusivity κ_e in respect to its laminar reference. In the spectrum of technically relevant Prandtl numbers (e.g. $\text{Pr} \approx 0.7$ for air), an increase of 100% is expected. Future numerical investigations will extend the range of Prandtl numbers to these values.

Fig. 13 Double-logarithmic presentation of the non-dimensional effective thermal diffusivity κ_e

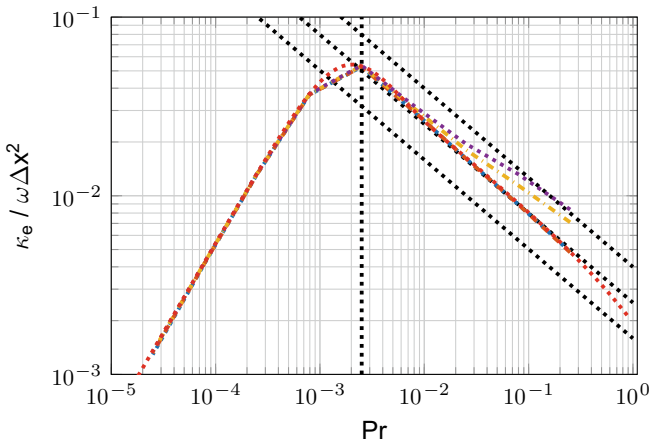


Fig. 14 Semi-logarithmic presentation of the enhancement of longitudinal heat transfer ϵ_{turb}

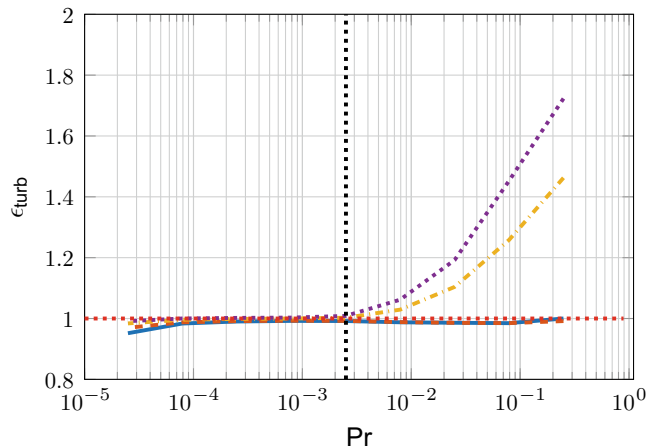


Figure 15 provides physical insight for the enhancement in effective thermal diffusivity at large Prandtl numbers approaching unity. To interpret the results, recall that the oscillating fluid is characterized by thin hydrodynamic boundary layers (i.e. $Wo \approx 35$). The left plot of Fig. 15 shows a fluid Prandtl number of $Pr = 0.0025$. This indicates a thermal boundary layer clearly exceeding its hydrodynamic counterpart. The plot reveals that the complete cross-sectional area of the channel ($\eta = z/h$) contributes to the longitudinal heat transfer. This is because disturbances in the temperature distribution propagate throughout the entire channel up to its center-plane. For increasing Prandtl numbers (center: $Pr = 0.025$, right $Pr = 0.25$), this wall-normal propagation is limited by the thermal conductivity. As a consequence, centered sections of the channel do not contribute to the convective transport anymore. In particular, the laminar setup is restricted to small wall-confined regions. The enhancement induced by turbulence is explained by an increase in wall normal heat flux, which increases the effective cross-sectional area.

van Buren and Polifke [1] also proposed a turbulence-related convective heat transfer coefficient h_{turb} . In the range of thin hydrodynamic boundary layers, this one-dimensional modeling approach—based on assumptions of bulk velocities and bulk temperatures outside of the boundary layer—predicts a scaling of ϵ_{turb} with the square-root of the Prandtl number Pr . A comprehensive discussion of interactions between hydrodynamic and thermal boundary layers is provided in [6].

Figure 16 shows qualitative agreement of the numerical results (colored lines) and the analytic prediction (black dotted lines). The turbulence-dependent coefficient h_{turb} is evaluated at $Pr = 0.25$. According to its definition (details are given in [1]), the coefficient is zero for laminar flows and increases with oscillation amplitude or turbulence intensity, respectively. This is denoted by the non-dimensional forcing amplitude λ .

The trend of the turbulent coefficient h_{turb} versus the forcing amplitude λ is depicted in Fig. 17. Up to the laminar-to-turbulent transition, h_{turb} is zero. At this threshold a significant increase is attributed to the initial onset of turbulence. With increasing amplitudes in the turbulent regime, the enhancement continuously decays.

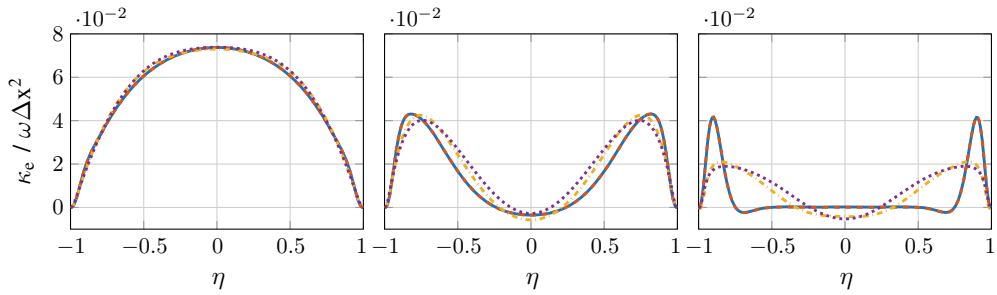


Fig. 15 Space-resolved effective thermal diffusivity over the channel width $2h$ at $\alpha^2 \text{Pr} = \pi$ (left), 10π (center) and 100π (right) for $\lambda = 100$ (blue), 150 (orange), 200 (yellow) and 250 (purple), $\alpha = 35.4$

Fig. 16 Detailed parametric study of enhancement in longitudinal heat transfer ϵ_{turb} for increasing, equi-spaced oscillation amplitudes ($\lambda = 162.5$ to 250, $\Delta\lambda = 12.5$). The black lines denote the model of van Buren and Polifke [1]

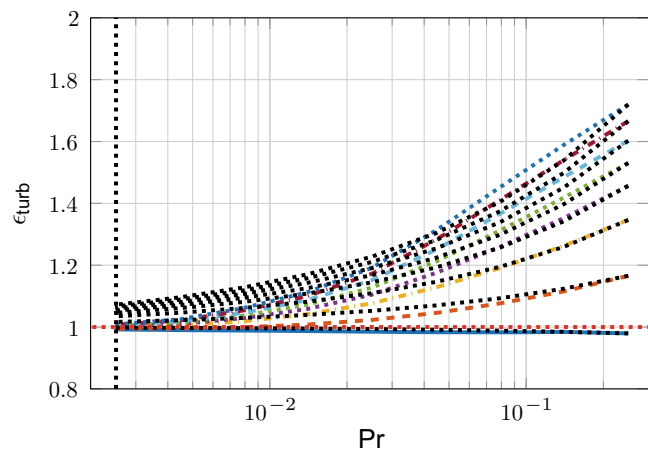
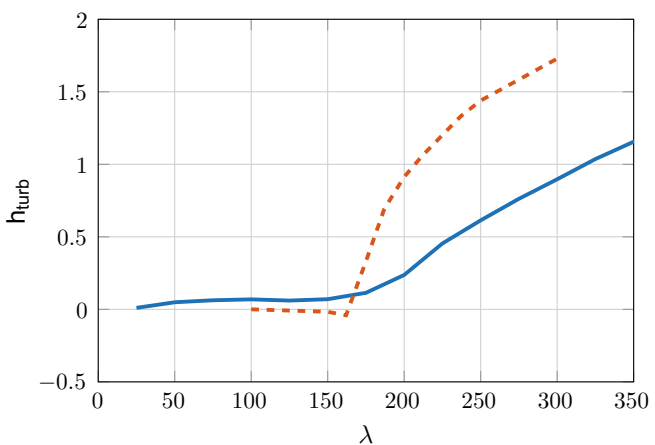


Fig. 17 Comparison of EHT (blue) [1] and the turbulence induced convective heat transfer coefficient h_{turb} (orange) plotted over the non-dimensional amplitude λ . Evaluated at $\text{Pr} = 0.25$



Although there are numerous physical deviations between the setup of wall-normal and longitudinal enhancement in heat transfer (e.g. pulsating vs. oscillating flow, wall-normal vs. longitudinal temperature gradient, ...), results of the wall-normal study are also included in Fig. 17. Note that some characteristic features compare qualitatively: For both flows, there is certain threshold in forcing amplitude (i.e. $\lambda \approx 160$) beyond which overall heat transfer clearly increases. For the longitudinal heat transfer, this is explained by the laminar-to-turbulent transition. Due to the mean-flow, the wall-normal setup is always turbulent. Interestingly—and in agreement with conclusions given in [1]—significant EHT does not develop below this threshold. Furthermore, both results show a declining growth with increasing amplitude in the turbulent regime.

4 Summary and Conclusions

A numerical framework for the quantitative prediction of acoustic damping characteristics was developed and applied to quarter-wave resonators with temperature inhomogeneities. The results confirm the analytical finding of the first funding period, i.e. that the temperature distribution within the resonator has a significant impact and cannot be represented adequately by only the mean temperature. Central advantages of the numerical approach are the flexibility of arbitrary temperature distributions and the resolved investigation of non-linear losses (e.g. vortex shedding). It is self-evident that accurate acoustic predictions require precise knowledge of the present temperature distribution.

First LES-based evidence for significantly enhanced wall-normal heat transfer in turbulent pulsating flow was given. This confirms experimental studies that report enhancement of more than 100%. The present work provides quantitative results that cover a wide range of forcing frequencies and pulsation amplitudes. Below velocity amplitudes of significant flow reversals, the time-averaged enhancement of heat transfer is marginal. First with significant flow reversal ($\epsilon \approx 2.5$), periods of flow stagnation quickly pass and allow for major enhancement of more than 100%. The present study demonstrates the risk-potential to the thermal integrity of rocket engine combustion chambers: Extreme thermal loads are opposed to restrictions in design and material properties, resulting in little safety margins. Unforeseen enhancement in fluid-to-wall heat transfer during the design process may result in a catastrophic destruction of the chamber.

Within the resonator tube, longitudinal convective effects in oscillating flows are evaluated. In the range of physically relevant Prandtl numbers (e.g. air with $Pr \approx 0.7$), the effective thermal diffusivity enhances significantly. Based on a comprehensive examination of hydrodynamic and thermal boundary layers, a simple model quantifies the impact of turbulence.

The present study sheds light on the complexity of a comprehensive design process of rocket combustion chambers. In particular, the close interdependence between acoustics and heat transfer requires a holistic treatment: The acoustic amplitude

has an impact on heat transfer and thus on the temperature distribution. The local temperature—in turn— influences the damping characteristic of the acoustic resonators. One possible consequence is the shift in effective damping frequency and thus an overall change in acoustic amplitude (closing the feedback-loop at hand). Furthermore, non-linear damping effects present a second direct coupling mechanism between acoustic amplitude and the damping characteristics of the resonator. To conclude, these interdependences do not allow for a decoupled analysis of acoustics and heat transfer. In regards to a numerically supported design process, this finding comes along with major challenges in the selection of length and time scales. On the one hand, highly resolved LES are required to capture effect of EHT and vortex shedding. On the other hand, the length scale of the combustion chamber has to be considered over the time scale of the transient heating process. In future studies, sophisticated approaches that make use of reduced-order models might overcome current restrictions imposed by computational resources. This may include an iterative procedure between the different orders in time scales or an evaluation of EHT by an imposed wall model. From an applied point of view, one is well advised to adhere to the established practice of placing the resonator openings adjacent to cool recirculation zones, where only minor changes in temperature are expected, in order to avoid the complications discussed.

Acknowledgements Financial support has been provided by the German Research Foundation (Deutsche Forschungsgemeinschaft – DFG) in the framework of the Sonderforschungsbereich Transregio 40. Computational resources have been provided by the Leibniz Supercomputing Center (LRZ).

References

1. van Buren, S., Miranda, A.C., Polifke, W.: Large eddy simulation of enhanced heat transfer in pulsatile turbulent channel flow. *Int. J. Heat Mass Transf.* **144**, 118585 (2019). <https://doi.org/10.1016/j.ijheatmasstransfer.2019.118585>
2. van Buren, S., Förner, K., Polifke, W.: Analytical and numerical investigation of the damping behavior of a quarter-wave resonator with temperature inhomogeneity. In: Stemmer, C., Adams, N.A., Haidn, O.J., Radespiel, R., Sattelmayer, T., Schröder, W., Weigand, B. (eds.) Annual Report, pp. 35–47, vol. 40. Sonderforschungsbereich/Transregio (2017)
3. van Buren, S., Förner, K., Polifke, W.: Acoustic impedance of a quarter-wave resonator with non-uniform temperature. In: Accepted for ICSV27, Prague, CZ (2021)
4. van Buren, S., Polifke, W.: Enhanced heat transfer in turbulent channel flow exposed to high amplitude pulsations. In: Stemmer, C., Adams, N.A., Haidn, O.J., Radespiel, R., Sattelmayer, T., Schröder, W., Weigand, B., Weigand, B. (eds.) Annual Report, pp. 39–56, vol. 40. Sonderforschungsbereich/Transregio (2018)
5. van Buren, S., Polifke, W.: Enhanced longitudinal heat transfer in turbulent oscillatory channel flow. In: Stemmer, C., Adams, N.A., Haidn, O.J., Radespiel, R., Sattelmayer, T., Schröder, W., Weigand, B. (eds.) Annual Report, pp. 35–48, vol. 40. Sonderforschungsbereich/Transregio (2019)
6. van Buren, S., Polifke, W.: Enhanced longitudinal heat transfer in oscillatory channel flow – a theoretical perspective. In: Accepted for ISROMAC18: J. Phys.: Conf. Series. Institute of Physics, (2020)

7. van Buren, S., Polifke, W.: Turbulence-induced enhancement of longitudinal heat transfer in oscillatory channel flow. Submitted to Int. J. Therm. Sci. (2020)
8. Dec, J.E., Keller, J.O., Arpacı, V.S.: Heat transfer enhancement in the oscillating turbulent flow of a pulse combustor tail pipe. Int. J. Heat Mass Transf. **35**(9), 2311–2325 (1992). [https://doi.org/10.1016/0017-9310\(92\)90074-3](https://doi.org/10.1016/0017-9310(92)90074-3)
9. Dec, J.E., Keller, J.O.: Time-resolved gas temperatures in the oscillating turbulent flow of a pulse combustor tail pipe. Combust. Flame **80**, 358–370 (1990). [https://doi.org/10.1016/0010-2180\(90\)90112-5](https://doi.org/10.1016/0010-2180(90)90112-5)
10. Dec, J.E., Keller, J.O.: Pulse combustor tail-pipe heat-transfer dependence on frequency, amplitude, and mean flow rate. Combust. Flame **77**(3–4), 359–374 (1989). [https://doi.org/10.1016/0010-2180\(89\)90141-7](https://doi.org/10.1016/0010-2180(89)90141-7)
11. Förner, K., Cárdenas Miranda, A., Polifke, W.: Mapping the influence of acoustic resonators on rocket engine combustion stability. J. Propuls. Power **31**(4), 1159–1166 (2015). <https://doi.org/10.2514/1.B35660>
12. Förner, K., Polifke, W.: Nonlinear aeroacoustic identification of Helmholtz resonators based on a local-linear neuro-fuzzy network model. J. Sound Vib. **407**, 170–190 (2017). <https://doi.org/10.1016/j.jsv.2017.07.002>
13. Förner, K., Tournadre, J., Martínez-Lera, P., Polifke, W.: Scattering to higher harmonics for quarter wave and Helmholtz resonators. AIAA J. **55**(4), 1194–1204 (2017). <https://doi.org/10.2514/1.J055295>
14. Harrje, D.T.: Heat transfer in oscillating flow. 3-g, Department of Aerospace and Mechanical Science, Princeton University (1967)
15. Ingard, U.: On the theory and design of acoustic resonators. J. Acoust. Soc. Am. **25**(6) (1953). <https://doi.org/10.1121/1.1907235>
16. Keller, J.J., Zauner, E.: On the use of Helmholtz resonators as sound attenuators. Z. Angew. Math. Phys. **46**, 297–327 (1995). <https://doi.org/10.1007/BF01003552>
17. Kumar, M.B., Sujith, R.I.: Exact solution for one-dimensional acoustic fields in ducts with polynomial mean temperature profiles. J. Vib. Acoust. **120**(4), 965–969 (1998). <https://doi.org/10.1115/1.2893927>
18. Kurzweg, U.H.: Enhanced heat conduction in oscillating viscous flows within parallel-plate channels. J. Fluid Mech. **156**, 291–300 (1985). <https://doi.org/10.1017/S0022112085002105>
19. Laudien, E., Pongratz, R., Piero, R., Preclik, D.: Fundamental mechanisms of combustion instabilities: experimental procedures aiding the design of acoustic cavities. Liquid Rocket Engine Combustion Instability, pp. 377–399 (1995). <https://doi.org/10.2514/5.9781600866371.0377.0399>
20. Miranda, A.C.: Influence of enhanced heat transfer in pulsating flow on the damping characteristics of resonator rings. Ph.D. thesis, TU München (2014)
21. Rayleigh, L.: The Theory of Sound. Macmillan, London (1896)
22. Wang, X., Zhang, N.: Numerical analysis of heat transfer in pulsating turbulent flow in a pipe. Int. J. Heat Mass Transf. **48**(19–20), 3957–3970 (2005). <https://doi.org/10.1016/j.ijheatmasstransfer.2005.04.011>

Open Access This chapter is licensed under the terms of the Creative Commons Attribution 4.0 International License (<http://creativecommons.org/licenses/by/4.0/>), which permits use, sharing, adaptation, distribution and reproduction in any medium or format, as long as you give appropriate credit to the original author(s) and the source, provide a link to the Creative Commons license and indicate if changes were made.

The images or other third party material in this chapter are included in the chapter's Creative Commons license, unless indicated otherwise in a credit line to the material. If material is not included in the chapter's Creative Commons license and your intended use is not permitted by statutory regulation or exceeds the permitted use, you will need to obtain permission directly from the copyright holder.



27th INTERNATIONAL CONGRESS ON SOUND AND VIBRATION
12 – 16 July 2020, Prague



Annual Congress of the International Institute of Acoustics and Vibration (IIAV)

ACOUSTIC IMPEDANCE OF A QUARTER-WAVE RESONATOR WITH NON-UNIFORM TEMPERATURE

Simon van Buren, Kilian Förner and Wolfgang Polifke

Technical University of Munich, Garching, Germany

e-mail: vanburen@tfd.mw.tum.de

This study proposes a semi-analytical approach to predict the acoustic impedance of a quarter-wave resonator with non-uniform temperature. In analogy to well-known models for Helmholtz resonators, the quarter-wave resonator is represented as a mass-spring-damper system. The treatment is limited to polynomial temperature profiles, but does take into account that the resonator cavity is not acoustically compact.

In order to assess the validity and accuracy of the semi-analytical results, computational fluid dynamics (CFD) simulations are carried out for a variety of temperature profiles in a quarter-wave resonator cavity. The acoustic reflection offered by the resonator opening to imposed incoming acoustic waves is evaluated, either by spectral analysis of time series generated by repeated, monofrequent excitation, or by system identification of acoustic signals generated with broad-band excitation. System identification – a variant of supervised machine learning – requires only a single simulation run to characterize the resonator over the frequency range of interest. The validation study shows good quantitative agreement between the mono-frequent and broadband excitation cases, as well as qualitative consistency with the analytical predictions.

The present study demonstrates that resonator eigenfrequencies as well as maximum effectiveness and bandwidth of acoustic damping are quite sensitive to temperature inhomogeneities. In the context of thermo-acoustic combustion instability, where resonators are frequently employed as a means of passive control. The results suggest that the acoustic characteristics of a resonator with hot combustion products at the inlet and a cooled backing cannot be computed simply with a representative average of the temperature distribution. These findings underline the necessity of a comprehensive design process, which includes thermal analysis in order to assure optimum resonator effectiveness.

Keywords: acoustic resonator, temperature inhomogeneity, CFD

1. Introduction

Combustion instabilities jeopardize the structural integrity of combustion chambers. One measure to ensure safe operating conditions is the installation of acoustic resonators to increase overall acoustic dissipation and to suppress the thermo-acoustic feedback. For optimal performance, resonators need to be tuned to eigenfrequencies of instabilities. Large temperature gradients exist between the hot combustion gases and the cooled chamber walls. Furthermore, acoustic pulsations in the turbulent flow enhance the

heat transfer [1]. In consequence, the local variations in the speed of sound affect the frequency range of damping. In coupled analysis of combustion chamber and resonator elements, Chemnitz et al. [2] showed the high sensitivity of global stability toward the damping characteristics of the resonator. Already minor changes in the damping eigenfrequency may cause fatal destruction of the chamber. Thus, a reliable quantification of the effects of temperature inhomogeneities on the resonator eigenfrequency is crucial for the design of safe operating.

In 1896, Rayleigh [3] modeled the Helmholtz resonator as a mass-spring-damper system. Since then, many authors (see e.g. [4, 5, 6]) used this analogy to describe the behavior of acoustic resonators in a semi-analytical way. Cárdenas [7] adapted the model for quarter-wave resonators and accounts also for temperature inhomogeneities inside the resonator. This formulation is reviewed in the following and extended to the specific needs of the present study. The semi-analytical model serves as reference for the validation of the CFD setup presented in Section 4.

2. Acoustic Quantities

The *reflection coefficient* $R(\omega)$ characterizes the acoustic damping of a resonator in frequency domain ($\hat{\cdot}$ -operator):

$$R(\omega) = \frac{\hat{g}(\omega)}{\hat{f}(\omega)}, \quad (1)$$

where ω is the *angular frequency*. It evaluates the ratio of the one-dimensional characteristic waves, traveling up- and downstream (f and g -wave, compare Figs. 1 and 2)

$$f = \frac{1}{2} \left(\frac{p'}{\bar{\rho}\bar{c}} + u' \right) \quad \text{and} \quad g = \frac{1}{2} \left(\frac{p'}{\bar{\rho}\bar{c}} - u' \right). \quad (2)$$

where p' is the *pressure fluctuation*, u' the *velocity fluctuation*, $\bar{\rho}$ the *mean density* and \bar{c} the *mean speed of sound*. The reflection coefficient R and the *acoustic impedance* $Z \equiv \hat{p}/\hat{u} = \Phi + i\Psi$ are linked via:

$$R(\omega) = \frac{Z(\omega) - \bar{\rho}\bar{c}}{Z(\omega) + \bar{\rho}\bar{c}}, \quad (3)$$

where Φ is the *resistance*, while Ψ is the *reactance*.

3. Analytical Model

The presented analytical model for the acoustic impedance Z combines two independent approaches. The mass-spring-damper analogy allows to determine the resistance. First introduced by Rayleigh [3] in 1896, the analogy has often been applied and refined. For example, Ingard [4] as well as Keller and Zauner [5] extended the model semi-analytically to describe the damping behavior of Helmholtz resonators, as shown in Fig. 1. Laudien et al. [6] investigated a way of transferring the concept to quarter-wave resonators. In the present work, this approach is extended to account for temperature inhomogeneities. The reactance of the resonator is modeled in accordance with Cárdenas [7].

3.1 Resistance of a Quarter-Wave Resonator with Temperature Inhomogeneities

The differential equation that describes the mass-spring-damper system consists of four fundamental components: the inertia of the mass (fluid in the neck), the restoring force of the spring (gas in the backing cavity of length l), the damping (viscous friction and non-linear effects) and the excitation by an external

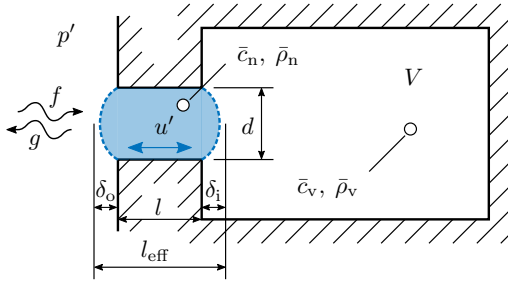


Figure 1: Sketch of a Helmholtz resonator, with highlighted oscillating fluid mass in the neck region. Redrawn from [7].

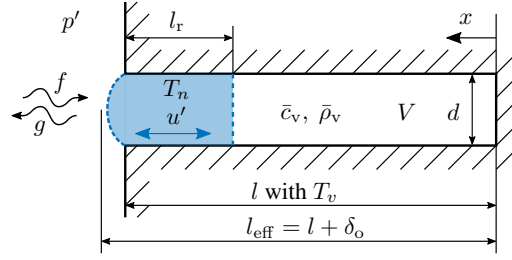


Figure 2: Sketch of a quarter-wave resonator, with highlighted oscillating fluid mass derived by the representative length l_r . Redrawn from [7].

force (acoustic pressure fluctuation) [5]. In order to obtain the frequency-based damping characteristics for an excitation p' and assumed linear response u' , the Fourier transformed ($q' = \hat{q}e^{i\omega t}$) system reads:

$$(1+s)(l_r + \delta l_o)\bar{\rho}_n\omega i\hat{u} - [s\bar{\rho}_n(l+d)\omega + \xi\bar{\rho}_n\hat{u}] \hat{u} + \frac{A_n\bar{\rho}_v\bar{c}_v^2}{V\omega} i\hat{u} = \hat{p}. \quad (4)$$

The *representative neck length* l_r (compare Fig.2) corresponds to the length at which the eigenfrequency of the mass-spring-damper system corresponds to the geometric eigenfrequency of the quarter-wave resonator [6]. This approach, accounting for temperature inhomogeneities, is presented in Section 3.3.

An additional portion of mass located at the tube directly outside of the resonator (index $_o$) is taken into account by the end correction δl_o . For small neck diameters ($d/D \ll 1$) a semi-analytical approximation for the length $\delta l_o \approx 4d/(3\pi)$ is given by Munjal [8]. The *effective neck length* l_{eff} is defined as the length from the back of the tube to the mouth, including the correction δl_o :

$$l_{eff} = l + \delta l_o. \quad (5)$$

In cylindrical ducts the *boundary-layer parameter* s , accounting for viscous effect within a small *Stokes boundary layer* $\delta_s/d \ll 1$, is defined as:

$$s = \frac{1}{d} \left(1 + \frac{\gamma - 1}{\sqrt{Pr}} \right) \delta_s \quad \text{with} \quad \delta_s = \sqrt{\frac{2\mu}{\rho\omega}}, \quad (6)$$

where Pr denotes the *Prandtl number*, μ the *dynamic viscosity* and γ the *ratio of specific heats*.

To eliminate the non-linearity in the dissipation term of Eq. (4), Keller and Zauner [5] introduced a factor ϵ_{nl} : $\xi\bar{\rho}_n\hat{u}^2 \approx \epsilon_{nl}s\bar{\rho}_n d\omega\hat{u}$. In this study, the non-linear influence is negligible ($\epsilon_{nl} = 0$) [9].

The resistance of the quarter-wave resonator is obtained as the real part of the impedance, which is derived by the rearrangement of Eq. (4):

$$\Phi = \left(1 + \frac{\gamma - 1}{\sqrt{Pr}} \right) \left(1 + \epsilon_{nl} + \frac{l_r}{d} \right) \sqrt{2\bar{\rho}_n\mu\omega}. \quad (7)$$

3.2 Reactance of a Quarter-Wave Resonator with Temperature Inhomogeneities

Since the backing cavity of a quarter-wave resonator cannot be assumed to be acoustically compact, Cárdenas [7] developed a general correlation for the acoustic reactance. Based on an approach by Kumar

and Sujith [10], the closed-form expression for the reactance of a resonator with a polynomial temperature profile,

$$T(x) = (ax + b)^n, \quad (8)$$

reads:

$$\begin{aligned} \Psi = & - \left[i\bar{\rho}_{\text{ch}}\omega((a + \nu\sigma)P_{-\nu}(\beta T_1^\sigma)P_\nu(bT_2^\sigma) + \beta\sigma P_{-1-\nu}(bT_1^\sigma)P_\nu(bT_2^\sigma)T_1^\sigma \right. \\ & \left. - P_{-\nu}(\beta T_2^\sigma)((\alpha - \nu\sigma)P_\nu(\beta T_1^\sigma) + \beta\sigma P_{-1+\nu}(\beta T_1^\sigma)T_1^\sigma))T_2^{1/N} \right] / \\ & [an(((\alpha - \nu\sigma)P_\nu(bT_1^\sigma) + \beta\sigma P_{-1+\nu}(\beta T_1^\sigma)T_1^\sigma)((\alpha + \nu\sigma)P_{-\nu}(\beta T_2^\sigma) + \beta\sigma P_{-1-\nu}(\beta T_2^\sigma)T_2^\sigma) \\ & - ((\alpha + \nu\sigma)P_{-\nu}(\beta T_1^\sigma) + \beta\sigma P_{-1-\nu}(\beta T_1^\sigma)T_1^\sigma)((\alpha - \nu\sigma)P_\nu(\beta T_2^\sigma) + \beta\sigma P_{-1+\nu}(\beta T_2^\sigma)T_2^\sigma))] , \end{aligned} \quad (9)$$

where P_n denotes the Bessel function of first kind with order n . The parameter α , β , σ and ν read:

$$\alpha = \frac{1}{2} \left(\frac{1}{n} - 1 \right), \quad \beta = \frac{\omega}{an\sqrt{\gamma R_s}\sigma}, \quad \sigma = \left(\frac{1}{n} - \frac{1}{2} \right) \text{ and } \nu = \frac{1-n}{2-n}. \quad (10)$$

For a given resonator geometry and temperature profile, the reactance Ψ is a function of the angular frequency ω .

3.3 Calculation of the Representative Neck Length

The temperature profile $T(x)$ (compare Fig. 4) anchors at the cooled wall at the back of the resonator at $T = T_{\text{cool}}$, and the temperature increases to $T = T_{\text{ch}}$ just outside the resonator opening. Two overlapping fluid regions are defined in the resonator: the backing volume at an average temperature of T_v , and the neck region at T_n (compare Fig. 2).

Following Laudien et al. [6], the eigenfrequency of the mass-spring-damper system selected that the representative length l_r agrees with the quarter-wave frequency of the resonator. The latter is defined by the angular frequency ω_{eig} for which the reactance Ψ (Eq. (9)) of the quarter-wave resonator equals zero.

The undamped angular eigenfrequency of the mass-spring-damper system is given as the square-root of the ratio of the spring-constant to the mass. Applying this to the analogy obtained in Eq. (4) yields the eigenfrequency f_{eig} (with $f = \omega/(2\pi)$):

$$f_{\text{eig}} = \frac{\bar{c}_v}{2\pi} \sqrt{\frac{A_n}{V(1+s)(l_r + \delta l_o)} \frac{\bar{\rho}_v}{\bar{\rho}_n}}. \quad (11)$$

In Eq. (11), the average density for the neck and the backing volume region are calculated by utilizing the perfect-gas equation of state to describe the correlation between the local density and the temperature profile:

$$\begin{aligned} \bar{\rho}_n &= \frac{\int_{l-l_r}^{l_{\text{eff}}} \bar{\rho}(x)dx}{l_{\text{eff}} - (l - l_r)} = \frac{\int_{l-l_r}^{l_{\text{eff}}} \frac{p}{R_s T(x)} dx}{l_r + \delta l_o}, \\ \bar{\rho}_v &= \frac{\int_0^l \bar{\rho}(x)dx}{l} = \frac{\int_0^l \frac{p}{R_s T(x)} dx}{l}. \end{aligned} \quad (12)$$

Using Eqs. (11) to (12), the representative neck length l_r can be calculated as a function of the temperature profile and serves as input parameter for the resistance, defined in Eq. (7).

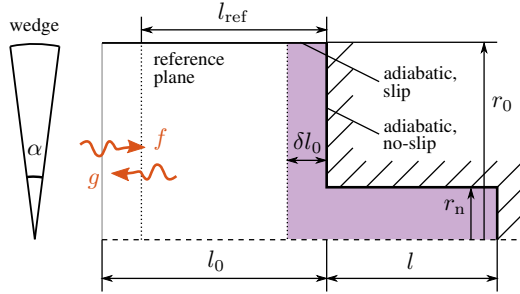


Figure 3: Sketch of a quarter-wave resonator attached to a channel of the length l_0 as implemented for simulation.

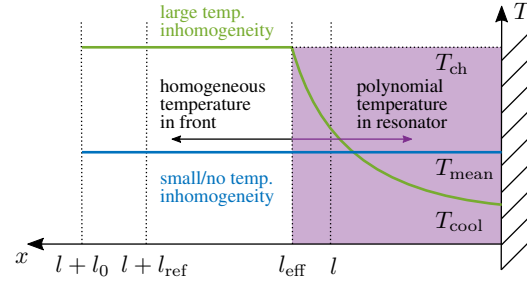


Figure 4: Initial constant and polynomial temperature profile along the x -direction in a quarter-wave resonator.

4. Numerical Implementation

In the present study, the authors present a numerical framework to quantify the damping behavior of a quarter-wave resonator with non-uniform temperature. As an advantage over the analytical model, this approach allows for arbitrary temperature distributions. Furthermore, the numerical method does not require for empirical parameters (e.g. the non-linear coefficient).

This section describes the numerical case setup, including the geometrical domain, initial and boundary conditions and solver settings. The evaluation via System-Identification follows.

The axis-symmetric wedge domain consists of the quarter-wave resonator (length l and neck radius r_n) attached to a flow channel (length l_0 and radius r_0 , compare Fig. 3). At the left inlet boundary interface, the planar inward-traveling f -wave is applied via a Navier-Stokes Characteristic Boundary Condition (NSCBC) [11]. The reflected outward-traveling g -wave is evaluated at a reference plane, located at a distance l_{ref} from opening of the resonator. The length l_{ref} is chosen to be sufficiently large for reflected g -waves to develop planar characteristics. All boundary conditions, besides the inlet, are adiabatic. At the physical walls of the resonator and the channel face plate, no-slip conditions are applied for the fluid flow, while the circumference boundary of the channel shows slip characteristics.

Considering the axial symmetry of the geometry, a structured graded mesh is generated as a two-dimensional grid with a wedge angle $\alpha = 4^\circ$. The Stokes boundary layer at the walls is resolved with 9 cells, yielding a minimum cell size of $d_{\text{cell,min}} \approx 8.0 \cdot 10^{-6}$ m at frequencies of $f \approx 4700$ Hz.

In agreement with the temperature profile of the analytical approach, the geometry is divided at the effective resonator length (see the purple area in Fig. 3). Figure 4 shows the temperature within the resonator from the backing wall (T_{cool}) to the effective length l_{eff} (T_{ch}). Inside the channel volume, the homogeneous temperature T_{ch} is applied. Further initial condition is a constant pressure p of the resting fluid ($u = 0$). The parameters for the numerical setup are summarized in Table 1.

An extended version of the compressible solver `rhoPimpleFoam` of the software OpenFOAM 2.3.1 is used [12]. For this study, both harmonic and broadband excitation are applied. The evaluation of the CFD results excited by a broadband input-signal is realized by System-Identification (CFD/SI). Based on the studies by Förner and Polifke [13], the identification process utilizes the output-error model:

$$g[k] = \frac{B}{F} f[k] + e[k]. \quad (13)$$

Considering discrete-time signals, $f[k]$ is the input (f -wave) at time-step k , $g[k]$ is the output (g -wave) and $e[k]$ is Gaussian white noise. B and F denote polynomials in the time shift operator. Appropriate orders of these polynomials are 3 for B and 2 for F [13].

Table 1: Parameters used for the numerical simulation.

initial conditions	T_{cool}	[K]	647	600	500	400	300
	T_{ch}	[K]	647	698	844	1075	1498
	n	[–]	–1.5				
	T_{mean}	[K]	647				
	p	[Pa]	$1.0 \cdot 10^8$				
geometry	l	[mm]	40.75				
	l_0	[mm]	100				
	l_{ref}	[mm]	90				
	r_n	[mm]	3.4				
	r_0	[mm]	34				
thermo-physical properties	M	[g/mol]	13.7				molar mass
	c_p	[J/(kg K)]	1500				specific heat capacity
	μ	[Pa s]	$5.5 \cdot 10^{-5}$				dynamic viscosity
	Pr	[–]	0.71				Prandtl number
numerical properties	$d_{\text{cell,min}}$	[m]	$8.0 \cdot 10^{-6}$				min. cell size
	n_{cell}	[–]	$2.2 \cdot 10^4$				number of cells
	d_{cell}/δ_s	[–]	9				cells in Stokes layer
	Δt	[s]	$5.0 \cdot 10^{-8}$				time step

5. Results

For the presentation of the results, five polynomial temperature profiles are selected. The mean temperature is set to be constant at $T_{\text{mean}} = 647$ K, while the temperature at the cooled resonator back is varied. Thereby, the hot channel temperature results as a dependent quantity.

5.1 Analytical Results

The results of the analytical correlation (Eq. (9)) are presented in Fig. 5. The colormap shows the gain of the reflection coefficient vs. frequency and temperature ratio. First, an increase of the temperature gradient leads to an increase of the eigenfrequency up to a maximum at $f_{\text{eig,max}} \approx 4980$ Hz. Afterwards, a decline of the eigenfrequency is observed.

The evaluation of discrete temperature ratios is shown in Fig. 6. In addition to the shift of eigenfrequencies, this plot clearly reveals an increase of the maximum damping performance for higher temperature ratios: for a constant temperature profile $T_{\text{ch}} = T_{\text{cool}} = T_{\text{mean}} = 647$ K, a gain of $|R| \approx 0.58$ is predicted, while the maximum temperature ratio of $T_{\text{ch}}/T_{\text{cool}} = 4.99$ yields a gain of $|R| \approx 0.33$.

5.2 Numerical Results

Figure 7 shows the numerical results of this study. Considering harmonic excitation, simulations are run for sinusoidal incoming f -waves with frequency intervals of 25 Hz. The resulting resonator performance of this discrete excitation pattern is given by the colored squares. For the system-identification, three randomly generated broadband simulations are run for each temperature ratio. The results of the identified system are given by the dashed lines. At an identification time-length of 0.04 s, the very good agreement of the results for the three random broadband signals indicates the expected independence of the generated f -wave.

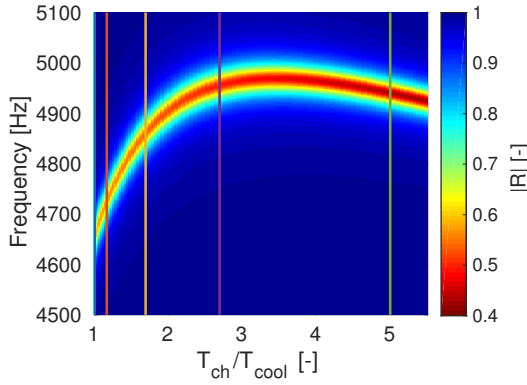


Figure 5: Analytical results for gain of the reflection coefficient vs. frequency and temperature ratio T_{ch}/T_{cool} .

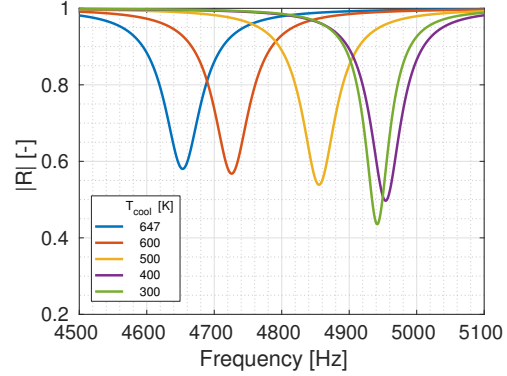


Figure 6: Analytical results for gain of the reflection coefficient vs. frequency for various of temperature ratios T_{ch}/T_{cool} .

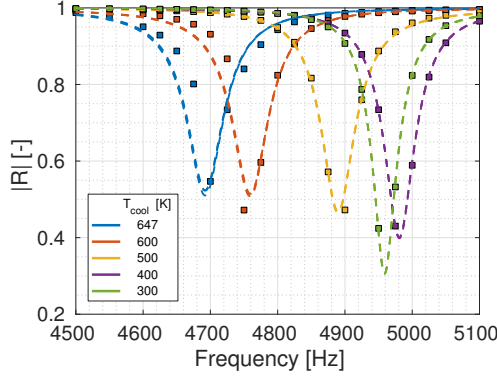


Figure 7: Gain of the reflection coefficient for harmonic excitation (squares) and results for three randomly generated broadband excitations obtained by CFD/SI (dashed lines).

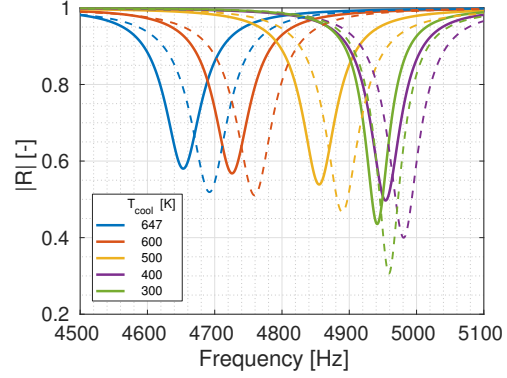


Figure 8: Gain of the reflection coefficient of the analytical model (solid lines) and averaged results obtained by system identification of broadband excitation (dashed lines).

The comparison of the results derived from harmonic and broadband excitation shows very good agreement for all temperature ratios. Thus, in further studies the method of system identification may be used to save computational costs.

Finally, analytical and numerical (broadband excitation) results are compared in Fig. 8. Both trends driven by increasing temperature ratios - the shift of eigenfrequency and the maximum damping behavior - correspond for the analytical and the numerical approach. However, the gain of the reflection coefficient of the numerical results are slightly lower then those of the analytical formulation. Furthermore, the eigenfrequencies predicted by the numerical approach is slightly higher.

6. Summary and Conclusions

In this study, the damping behavior of quarter-wave resonators is investigated analytically and numerically. The focus lies on the consideration of temperature inhomogeneities, as they can be expected to occur in combustion chambers due to high temperature gradients between hot combustion gas and cooled

chamber walls.

For the analytical approach, the resistance is modeled based on the work by Laudien et al. [6]. The reactance is given from a closed-form expression [7]. Overall, an extended analytical model is presented accounting for axial temperature inhomogeneities within the resonator. A numerical framework is presented as a more flexible design tool without the requirement for semi-empirical correlations. The combined CFD/SI procedure is successfully validated against simulation results from harmonically excited simulations for several temperature profiles.

The results of the analytical and the CFD/SI approach show good agreement. Both reveal a comparable increase in the maximum damping performance for rising temperature ratios as well as a shift in eigenfrequency. The results clearly underline that the mean temperature is not a sufficient measure for the description of the damping characteristics. Instead, a more detailed knowledge of the temperature profile is required for an accurate prediction of the acoustic behavior. For an a-priori known temperature profile, the presented CFD/SI tool-chain can be used to generate highly accurate models with low numerical cost.

Acknowledgments

Financial support has been provided by the German Research Foundation (Deutsche Forschungsgemeinschaft – DFG) in the framework of the Collaborative Research Center SFB/TRR40. Computational resources have been provided by the Leibniz Supercomputing Center (LRZ).

REFERENCES

1. van Buren, S., Cárdenas Miranda, A. and Polifke, W. Large Eddy Simulation of Enhanced Heat Transfer in Pulsatile Turbulent Channel Flow, *Int. J. of Heat and Mass Transfer*, **144**, 118585, (2019).
2. Chemnitz, A., Kings, N. and Sattelmayer, T. Modification of Eigenmodes in a Cold-Flow Rocket Combustion Chamber by Acoustic Resonators, *Journal of Propulsion and Power*, **35** (4), 765–779, (2019).
3. Rayleigh, L., *The Theory of Sound*, Macmillan, London (1896).
4. Ingard, U. On the Theory and Design of Acoustic Resonators, *Journal of Acoustical Society of America*, **25** (6), (1953).
5. Keller, J. J. and Zauner, E. On the Use of Helmholtz Resonators as Sound Attenuators, *Zeitschrift für angewandte Mathematik und Physik*, **46**, 297–327, (1995).
6. Laudien, E., Pongratz, R., Piero, R. and Preclick, D. Fundamental Mechanisms of Combustion Instabilities: Experimental Procedures Aiding the Design of Acoustic Cavities, *Liquid Rocket Engine Combustion Instability*, pp. 377–399, (1995).
7. Cárdenas Miranda, A., *Influence of Enhanced Heat Transfer in Pulsating Flow on the Damping Characteristics of Resonator Rings*, PhD Thesis, TU München, (2014).
8. Munjal, M. L., *Acoustics of Ducts and Mufflers*, Wiley, Chichester, West Sussex, United Kingdom, 2nd edn. (2014).
9. Förner, K. and Polifke, W. Nonlinear Aeroacoustic Identification of Helmholtz Resonators Based on a Local-Linear Neuro-Fuzzy Network Model, *J. Sound Vibration*, **407**, 170–190, (2017).
10. Kumar, M. B. and Sujith, R. I. Exact Solution for One-Dimensional Acoustic Fields in Ducts With Polynomial Mean Temperature Profiles, *Journal of Vibration and Acoustics*, **120** (4), 965–969, (1998).
11. Poinsot, T. and Lele, S. K. Boundary Conditions for Direct Simulation of Compressible Viscous Flows, *Journal of Computational Physics*, **101** (1), 104–129, (1992).
12. The OpenFOAM Foundation, (2017), *OpenFOAM 2.3.1*. <https://openfoam.org/>.
13. Förner, K. and Polifke, W. Aero-Acoustic Characterization of Helmholtz Resonators in the Linear Regime with System Identification, *22nd International Congress on Sound and Vibration (ICSV22)*, Florence, Italy, Jul., (2015).

Enhanced longitudinal heat transfer in oscillatory channel flow – a theoretical perspective

Simon H. van Buren and Wolfgang Polifke

Department of Mechanical Engineering
Technical University of Munich
85748 Garching b. München, Germany
Email: vanburen@tfd.mw.tum.de

ABSTRACT

*Enhanced longitudinal heat transfer in viscous, laminar, single-phase, oscillatory channel flow is investigated in the present paper. Kurzweg (J. Heat Transf. **107**, 1985) analysed this case theoretically and derived a correlation for a non-dimensionalized effective thermal conductivity in terms of Prandtl and Womersley numbers. The present investigation contributes analysis of limiting cases and physical interpretation to the results of Kurzweg. A simplified model with isothermal walls is proposed, applicable if working fluid and channel wall material exhibit sufficiently large differences in thermal inertia. Examined over a wide range of Womersley numbers, this model reveals six distinct regimes characterized by the Prandtl number of the fluid. The respective thickness of hydrodynamic and thermal boundary layers relative to the channel width is relevant in this context. Maximum effective thermal conductivity is attained when the thermal boundary layer expands over the full channel width. The influence of Womersley number is discussed and explained in terms of the interplay of hydrodynamic and thermal flow characteristics. These patterns reveal either quasi-steady parabolic or oscillating bulk characteristics. The importance of the thermal boundary layer thickness motivates the introduction of a new non-dimensional group, making it easier to classify the various regimes of enhanced longitudinal heat transfer.*

INTRODUCTION

Several authors report enhanced axial transport of passive scalars, such as contaminants, induced by oscillations in capillary tubes [1–4]. The reported enhanced transport exceeds purely molecular diffusion by orders of magnitude. The enhancement is attributed to the interaction between oscillating radial velocity profiles and local variations in concentration. Thus, an effective axial diffusion rate is formulated.

Kurzweg and coworkers [5, 6] exploited the similarity between molecular diffusion and heat transfer when investigating heat transfer between two water reservoirs at different temperatures, connected by a bundle of capillary tubes. Inducing high-frequency velocity oscillations to the fluid, heat transfer between the reservoirs increased by four orders of magnitude over the non-oscillating reference case, where heat conduction was the only mechanism of heat transfer. In a final step, Kurzweg [7] developed a comprehensive analytical model for the effective thermal diffusivity. Choosing a non-dimensional formulation, Kurzweg [7] identified the *Womersley number* α , defined as the ratio of transient inertial and viscous forces, as a key parameter and highlighted that effective diffusivity is reduced at large as well as small Womersley numbers. Maximum longitudinal heat transfer is reported to occur when the *Prandtl number* Pr satisfies the relation $\alpha^2 \text{Pr} \approx \pi$. Later studies evaluated theoretically and experimentally the so-called “dream pipe” – a capillary heat transfer tube bundle (e.g. Kaviany [8–10] and Nishio et al. [11]). In contrast to the original work by Kurzweg [7], circular ducts instead of two-dimensional channels were considered. Inaba et al. [12] contributed to the understanding of the influence of the properties of the channel wall (i.e. its thermal conductivity and thickness). Puvaneswari and Shailendra [13] provided an extended mathematical investigation that includes viscoelastic fluids employed as the oscillating heat carriers.

The challenging acoustic design of passive damping devices in rocket engines motivates the present work. Commonly used quarter-wave resonators are designed as capillary tubes and prevent catastrophic thermoacoustic instabilities. However, extreme thermal flow conditions inside the combustion chamber complicate the design process. For example, turbulent pulsations trigger enhanced heat transfer between the hot combustion gas and regeneratively cooled walls [14, 15].

Enhanced longitudinal heat transfer in oscillatory channel flow – a theoretical perspective

The resulting temperature gradients within the resonator strongly influence its acoustic properties [14, 16] and thus jeopardize the sensitive acoustic stability of the engine [17, 18].

This theoretical investigation assumes an incompressible flow to focus only on diffusive effects contributing to enhanced heat transfer. Heat pump effects induced by thermoacoustic density fluctuations are neglected. Furthermore, evaporation of propellant is not considered. The reader should keep in mind the potential relevance of latent heat and liquid-vapor two-phase flow (e.g. Miura et al. [19, 20]).

The present study contributes to the understanding of the physical mechanisms of heat transfer enhancement in oscillating channel flow: As a starting point, the next section outlines the model by Kurzweg [7] and simplifications proposed by van Buren and Polifke [21, 22]. Then the present paper provides insight into three related problems:

Firstly, the (mathematical) influence of Womersley and Prandtl number. Based on the simplified analytical model [21, 22], six distinct characteristic regimes are identified. These regimes are connected to the limiting constellations of hydrodynamic and thermal boundary layers.

Secondly, the (physical) interplay of hydrodynamic and thermal boundary layers. Based on the characteristics of the limiting thermal and hydrodynamic profiles (bulk vs. quasi-steady parabolic profiles), physical explanations for the quantitative scaling of the effective thermal diffusivity are derived for each regime. The wall-normal thermal penetration depth is revealed as a significant key driver of the problem at hand.

Thirdly, focusing on the interplay of boundary layers and the importance of thermal penetration depth, a corresponding non-dimensional group is introduced, which is defined as the ratio of transient thermal inertia and wall-normal conductive heat flux. This novel non-dimensional group, which we name the “Kurzweg number” in acknowledgement of Kurzweg’s seminal analysis, underlines the importance of the thermal boundary layer: In five out of six constellations of boundary layers, the Kurzweg number suffices to quantify the effective thermal conductivity (alongside with the Womersley number), which serves as a measure of enhanced longitudinal heat transfer (ELHT).

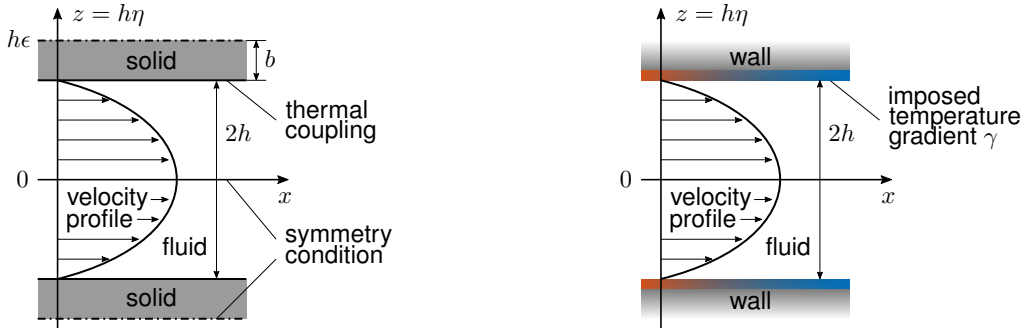


Fig. 1. Geometry of oscillating fluid flow between parallel channel walls. Left: Kurzweg [7], right: van Buren and Polifke [21, 22].

REVISITING THE LITERATURE

Model by Kurzweg

In 1985, Kurzweg [7] presented a closed-form analytical expression for the effective longitudinal thermal diffusivity κ_e in oscillatory channel flow. The two-dimensional fluid channel (width $2h$) is confined by solid walls (thickness $2b$) in span-wise z -direction (see Fig. 1, left). In the wall-normal direction, symmetry condition is applied at the center-line of the channel and at the center-line of each wall, considering a stack of parallel channels. In non-dimensional notation $\eta = z/h$, these symmetries are at $\eta = 0$ and $\eta = \pm\epsilon$, respectively, where the geometric wall-to-channel characteristic is defined as $\epsilon \equiv (b + h)/h$.

In stream-wise x -direction, the harmonically oscillating fluid (e.g. forced by an oscillating pressure gradient) exhibits a velocity profile $U(\eta, t)$ described by:

$$U(\eta, t) = U_0 f(\eta) e^{i\omega t} = U_0 \frac{i\lambda}{\alpha^2} \left[1 - \frac{\cosh(\sqrt{i}\alpha\eta)}{\cosh(\sqrt{i}\alpha)} \right] e^{i\omega t}, \quad (1)$$

where U_0 is a representative velocity, λ the non-dimensional pressure gradient, t the time, and ω the angular frequency. The Womersley number α is defined as the ratio of transient inertial and viscous forces:

$$\alpha^2 \equiv \frac{\rho\omega U}{\mu U h^2} = \frac{\omega h^2}{\mu\rho^{-1}} = \frac{\omega h^2}{\nu}, \quad (2)$$

Enhanced longitudinal heat transfer in oscillatory channel flow – a theoretical perspective

where μ denotes the dynamic viscosity, ν the kinematic viscosity, and ρ the density of the fluid. Under the assumption of temporal and stream-wise periodicity, Eqn. (1) is an exact solution of the Navier-Stokes equations (*Stokes problem*). The channel-averaged tidal replacement Δx follows by the integration of Eqn. (1):

$$\Delta x = \frac{2U_0\lambda}{\omega\alpha^2} \left| 1 - \frac{\tanh(\sqrt{i}\alpha)}{\sqrt{i}\alpha} \right|. \quad (3)$$

Kurzweg [7] accounts for conjugate heat transfer between the channel walls and the oscillating fluid. Within the walls, heat conduction is the only transport mechanism, whereas additional convective transport is considered within the fluid. The *effective thermal diffusivity* κ_e is then defined such that its product with the average stream-wise temperature gradient γ equals the time-averaged convective thermal flux across the channel cross-sectional dimension with width $\eta = 1$ [1]:

$$\kappa_e\gamma = \frac{\omega}{2\pi} \int_0^{2\pi/\omega} \int_0^1 \Re[T(x, \eta, t)] \Re[U_0 f(\eta) e^{i\omega t}] d\eta dt, \quad (4)$$

Kurzweg [7] provides a solution of Eqn. (4) to quantify enhanced longitudinal heat transfer (ELHT) in non-dimensional form:

$$\frac{\kappa_e}{\omega\Delta x^2} = \frac{\text{Pr}[(1-H)\bar{h} + (1-\bar{H})h] + (\bar{h} - \bar{j}\bar{H}) + (h - jH)}{16\alpha^2(\text{Pr}^2 - 1) \left| 1 - \frac{\tanh(\sqrt{i}\alpha)}{\sqrt{i}\alpha} \right|^2}, \quad (5)$$

where

$$h(\alpha) = \sqrt{i}\alpha \tanh(\sqrt{i}\alpha), \quad j(\text{Pr}, \alpha) = \sqrt{i\text{Pr}}\alpha \tanh(\sqrt{i\text{Pr}}\alpha) \quad (6)$$

and

$$H(\text{Pr}, \xi, \sigma, \alpha, \epsilon) = \frac{1}{\text{Pr}} \frac{\xi \sqrt{\text{Pr}} \tanh(\sqrt{i}\alpha) + \sqrt{\sigma} \tanh(\sqrt{i\sigma \text{Pr}}\alpha(\epsilon - 1))}{\xi \tanh(\sqrt{i \text{Pr}}\alpha) + \sqrt{\sigma} \tanh(\sqrt{i\sigma \text{Pr}}\alpha(\epsilon - 1))}. \quad (7)$$

$\text{Pr} = \nu/\kappa_f$ denotes the fluid Prandtl number and the bar $\bar{\cdot}$ the complex conjugate of the functions h , j , and H . Non-dimensional characteristics describing the material properties (fluid vs. solid) are the ratio of thermal conductivities $\xi = k_f/k_s$ and the ratio of thermal diffusivities $\sigma = \kappa_f/\kappa_s$, respectively.

Simplifications by van Buren and Polifke

In a follow-up study, van Buren and Polifke [21, 22] introduced a simplification that is valid for many technical applications: For configurations with thick walls compared to the channel width ($b \gg h$), the geometric characteristic ϵ simplifies:

$$b \gg h \Rightarrow \epsilon \gg 1. \quad (8)$$

Furthermore, if the thermal conductivity of the fluid k_f (e.g. air) is much smaller than the thermal conductivity of the solid k_s (e.g. metal), $k_f \ll k_s$, the thermal material characteristic ξ approaches zero:

$$k_f \ll k_s \Rightarrow \xi \approx 0. \quad (9)$$

Physically speaking, these assumptions imply time-invariant temperatures at the fluid-solid interface. Thereby, the applied assumptions coincide with parametric set-up of maximum heat transfer concluded by Inaba et al. [12]. As depicted in Fig. 1 (right) and shown in [21, 22], the stream-wise temperature gradient γ is maintained spatially and temporally constant. Exploiting

Enhanced longitudinal heat transfer in oscillatory channel flow – a theoretical perspective

the simplifications which these assumptions allow (i.e. $H \rightarrow 1/\text{Pr}$), Eqn. (5) is rewritten as:

$$\frac{\kappa_e^*}{\omega \Delta x^2} = \frac{2 \text{Pr} \Re(h) - \frac{2}{\text{Pr}} \Re(j)}{16\alpha^2(\text{Pr}^2 - 1) \left| 1 - \frac{\tanh(\sqrt{i}\alpha)}{\sqrt{i}\alpha} \right|^2}. \quad (10)$$

In the present study, this simplified expression serves as the starting point for a comprehensive discussion of the interplay between hydrodynamic and thermal boundary layers. In this process, findings by Kurzweg [7] are confirmed, expanded, and interpreted in a physical context.

DISCUSSION OF THE SIMPLIFIED MODEL

Influence of Womersley and Prandtl number

In this section, observations of the influence of Womersley and Prandtl number on the effective thermal diffusivity are categorized and discussed. In this context, three central findings of Kurzweg [7] regarding the non-dimensional effective thermal diffusivity $\kappa_e^*/(\omega \Delta x^2)$ are confirmed, namely: (i) For large Womersley numbers α , thermal diffusivity is proportional to $1/\alpha$. (ii) For small α , thermal diffusivity is proportional to α^2 . (iii) There is a maximum in thermal diffusivity close to $\alpha^2 \text{Pr} = \pi$.

In the following, these findings are expanded and discussed in a physical context. First, Eqn. (10) is rearranged and rewritten as follows:

$$\frac{\kappa_e^*}{\omega \Delta x^2} = \overbrace{\frac{\text{Pr}}{8\sqrt{2}\alpha(\text{Pr}^2 - 1) \left| 1 - \frac{\tanh(\sqrt{i}\alpha)}{\sqrt{i}\alpha} \right|^2}}^{\Psi} \left[\underbrace{g(\alpha) - \text{Pr}^{-3/2} g(\alpha\sqrt{\text{Pr}})}_{\Phi - \Theta} \right], \quad (11)$$

where

$$g(\zeta) = \frac{e^{2\sqrt{2}\zeta} - 2e^{\sqrt{2}\zeta} \sin(\sqrt{2}\zeta) - 1}{e^{2\sqrt{2}\zeta} + 2e^{\sqrt{2}\zeta} \cos(\sqrt{2}\zeta) + 1}. \quad (12)$$

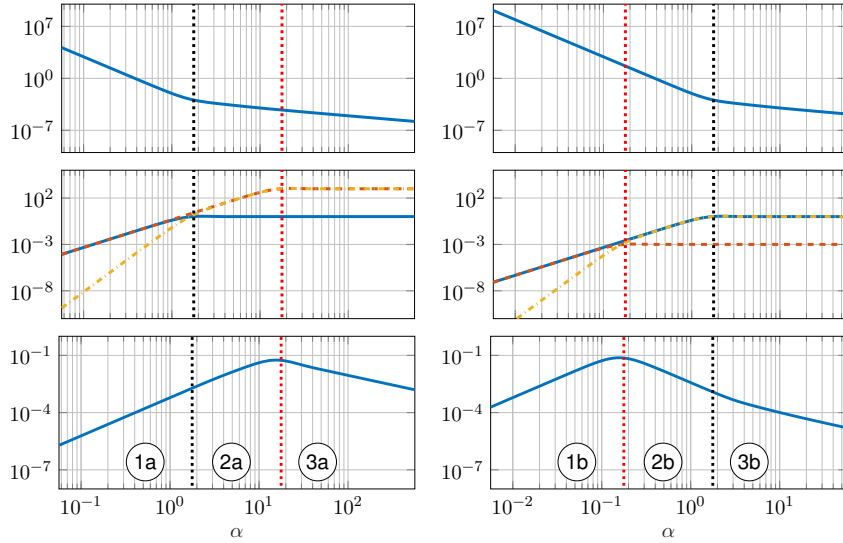


Fig. 2. Separate display of individual terms of equation. Left: $\text{Pr} = 0.01$, right: $\text{Pr} = 100$. Top: $|\Psi|$, middle: Φ (—), Θ (---), $|\Phi - \Theta|$ (----), bottom: ELHT $\kappa_e^*/(\omega\Delta x^2)$. Dotted lines: $\alpha = \sqrt{\pi}$ (.....), $\alpha = \sqrt{\pi/\text{Pr}}$ (....).

The purely real-valued denominator is factored out and rearranged (Ψ). The difference between Φ and Θ remains. To drop the imaginary part attributed to the functions of $h(\alpha)$ and $j(\text{Pr}, \alpha)$, rewriting leads to a generalized function $g(\zeta)$. The argument of the function g is either the Womersley number (see Φ) or a combination of Womersley and Prandtl number (see Θ).

Figure 2 displays the individual terms of Eqn. (11) vs. the Womersley number α for a small (left side, $\text{Pr} = 0.01$) and a large Prandtl number (right side, $\text{Pr} = 100$), fluid characteristics that are representative of liquid metal and viscous oils, respectively. At ambient condition, the Prandtl numbers of fluids such as water ($\text{Pr} \approx 10$) or air ($\text{Pr} \approx 0.7$) lie well inside this range. The red dotted vertical line marks the maximum of ELHT at $\alpha = \sqrt{\pi/\text{Pr}}$, already observed by Kurzweg. The black dotted line denotes $\alpha = \sqrt{\pi}$. At this value of α , hydrodynamic boundary layer thickness δ (also known as Stokes boundary layer) and channel width h are of the same order of magnitude because:

$$\delta = \sqrt{2\nu/\omega} \Rightarrow \frac{\delta}{h} = \frac{\sqrt{2}}{\alpha}. \quad (13)$$

Enhanced longitudinal heat transfer in oscillatory channel flow – a theoretical perspective

Table 1. Distinct regimes of longitudinal heat transfer in dependence of Womersley number α and Prandtl number Pr .

$\alpha \rightarrow 0$	$\text{Pr} < 1$	$\text{Pr} > 1$	$\alpha \rightarrow \infty$
(1)	$\sqrt{\pi} < \alpha < \sqrt{\pi/\text{Pr}}$ (2a)	$\sqrt{\pi/\text{Pr}} < \alpha < \sqrt{\pi}$ (2b)	(3)
$ \Psi $	$1/\alpha^5$	$1/\alpha$	$1/\alpha^5$
$ \Phi - \Theta $	α^7	α^3	α^3
$\kappa_e^*/(\omega \Delta x^2)$	α^2	α^2	$1/\alpha^2$

In the range $\alpha < \sqrt{\pi}$, indicative of capillary flow with $\delta > h$, the double-logarithmic presentation of Fig. 2 reveals a power-law scaling with $1/\alpha^5$ for $|\Psi|$ (1) and (2b). Conversely, for $\alpha > \sqrt{\pi}$ (e.g. acoustic quarter-wave resonators), the pre-factor $|\Psi|$ scales with $1/\alpha$ (2a) and (3). Thus, these slopes are attributed to the hydrodynamic boundary layer either extending over the full channel width or being confined to the close vicinity of the wall (black dotted line). At $\alpha = \sqrt{\pi/\text{Pr}}$ (red dotted line), no change in slopes occurs.

The second row of Fig. 2 shows Φ and Θ . Originating from the function $g(\zeta)$, the scaling of both terms changes from α^3 to α^0 as the argument ζ approaches $\zeta \approx \sqrt{\pi}$. For Φ , the argument of $g(\zeta)$ is the Womersley number α , thus being related to the hydrodynamic boundary layer thickness. On the other hand, Θ relates $\zeta = \alpha\sqrt{\text{Pr}}$. In this context, the thermal boundary layer thickness δ_{th} is the thermal analog of the Stokes boundary layer thickness and reads:

$$\delta_{th} = \sqrt{2\kappa/\omega} \Rightarrow \frac{\delta_{th}}{h} = \frac{\sqrt{2}}{\alpha\sqrt{\text{Pr}}}. \quad (14)$$

It directly shows that Θ is connected to the spatial extent of thermal penetration (red dotted line). In addition to the findings of Kurzweg [7], the difference between Φ and Θ reveals a third regime (2) of Womersley numbers with constant scaling. The placement of this range depends on the Prandtl number Pr being smaller or larger than unity. Physically speaking, this indicates that the thermal boundary layer δ_{th} already extends over the full channel width, while the hydrodynamic boundary layer δ is wall-confined (2a, $\text{Pr} < 1$), or vice versa (2b).

The bottom row of Fig. 2 shows the effective thermal diffusivity $\kappa_e^*/(\omega\Delta x^2)$ as calculated by the three individual terms of Eqn. (11). As reported by Kurzweg [7], the maximum lies at $\alpha \approx \sqrt{\pi/\text{Pr}}$. Interestingly, the reported third regime (2a) vanishes for $\text{Pr} < 1$ (i.e. it shows the same characteristics as regime (1)). However, for $\text{Pr} > 1$, this additional regime (2b) persists and scales with the inverse square of the Womersley number $1/\alpha^2$. Table 1 summarizes the results.

Interplay of hydrodynamic and thermal boundary layers

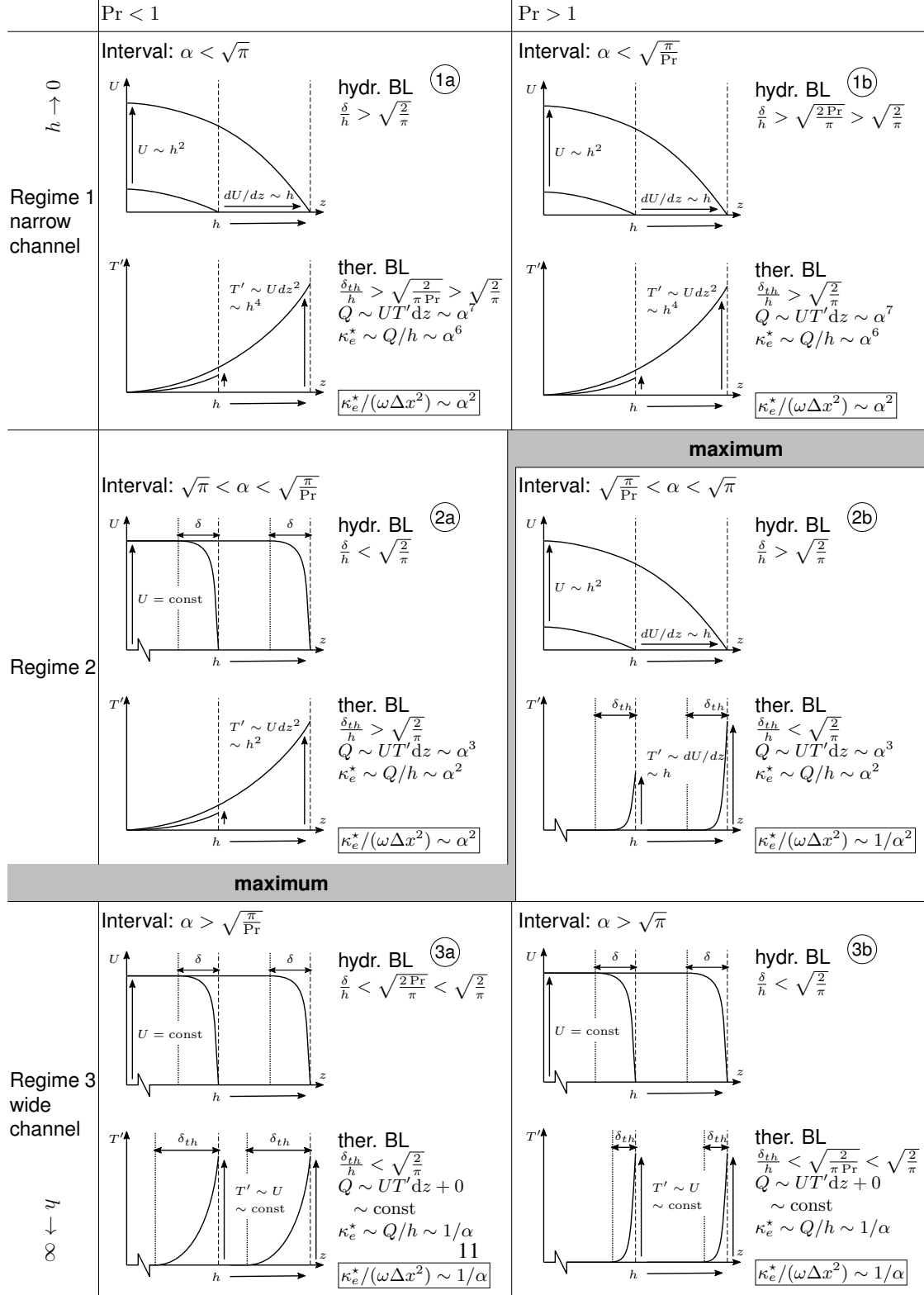
In this section, the physical interplay of velocity and temperature profile is discussed and interpreted in terms of the resulting effective thermal conductivity $\kappa_e^*/(\omega\Delta x^2)$. As presented in the previous section, each of the six possible combinations of Womersley and Prandtl number (1) – (3) and (a) – (b) are categorized in Tab. 2. In favor of a comprehensible presentation, the variation of the Womersley number α is illustrated by adjusting the channel width. In all plots of Tab. 2, this approach is depicted by two channel realizations of increasing width h in the z -direction, where the vertical dashed lines denote the shifting confining wall. Meanwhile, the angular frequency ω and the fluid viscosity ν are constant.

Firstly and referring to Tab. 2, the reader is reminded of the two distinct profile characteristics that an oscillating channel flow exhibits in its limiting cases: At small channel width h (1), a quasi-steady parabolic velocity profile $U(z)$ exists across the flow channel. Thus, the magnitude of velocity fluctuations scales with the square of the channel width h . For the opposite case of large channel width h (3), hydrodynamic boundary layers are confined to the close vicinity of the wall. In this case, the channel width does not affect the magnitude of velocity fluctuations. Figure 3 sketches the parabolic (blue line) and bulk limit (orange line), respectively.

In a second step, the temperature fluctuations $T'(z)$ are quantified. In analogy to the velocity profile, the channel width h distinguishes between quasi-steady parabolic and bulk characteristics. However, the thermal threshold lies at $\delta_{th}/h \approx \sqrt{2}/(\pi \text{Pr})$. As elaborated in the previous section, the Prandtl number classifies constellations of only one boundary layer (hydrodynamic or thermal) expanding into the center of the channel (2). Furthermore, the temperature profile is directly linked to the velocity profile: the driving wall-normal temperature disturbances are induced by the stream-wise tidal fluid displacement.

Enhanced longitudinal heat transfer in oscillatory channel flow – a theoretical perspective

Table 2. Physical interpretation of slopes in dependence of channel width h (representing the Womersley number α) and Prandtl number Pr ($\text{Pr} < 1$ indicates that the thermal boundary layer (BL) is wider than the hydrodynamic BL and vice versa).



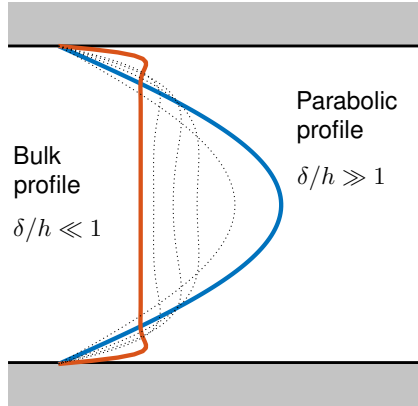


Fig. 3. Characteristic limiting velocity profiles of an oscillating channel flow: parabolic (—) and bulk profile (—).

Alongside each temperature plot in Tab. 2, the corresponding value of thermal diffusivity is given. The convective heat flux Q yields the integral spatial product of velocity and temperature fluctuations over the channel cross-section. The effective thermal diffusivity κ_e^* corresponds to Eqn. (4). In its non-dimensional form $\kappa_e^*/(\omega\Delta x^2)$, the tidal displacement Δx is incorporated.

In the present paper, the procedure is exemplarily presented for the regimes ①a) and ③b):

Regime ①a) is defined by $\alpha^2 \ll \pi$ and thus develops a parabolic velocity profile. This implies a velocity difference U between the walls and the center of the channel, scaling proportionally with the square of the channel width h : $U \sim h^2$. The above velocity difference now acts as the triggering temperature disturbance: The fluid at the wall is at rest, whereas, in the center of the channel, the adjoining hot/cold fluid flows in at the velocity U . Furthermore, the thermal penetration is much larger than the channel width in regime ①a) ($\alpha^2 \text{Pr} \ll \pi$). In consequence, also a parabolic temperature profile develops throughout the channel. The wall-induced temperature disturbance T' scales with the triggering velocity disturbance over the channel width: $T' \sim Udz^2 \sim h^4$. In the next step, the heat flux Q follows from the temperature disturbances T' convected by the velocity U over the channel width: $Q \sim UT'dz \sim h^7 \sim \alpha^7$ (with $\alpha \sim h$, only the channel width h is changed in this set-up). The effective thermal diffusivity κ_e^* follows as the averaged heat flux Q over the channel width h : $\kappa_e^* \sim Q/h \sim \alpha^6$. Finally, the tidal displacement Δx is proportional to the square of the channel width h^2 (compare Eqn. (3)), and thus the non-dimensional scaling for the effective thermal diffusivity $\kappa_e^*/(\omega\Delta x^2)$ reads $\kappa_e^*/(\omega\Delta x^2) \sim \alpha^2$.

Enhanced longitudinal heat transfer in oscillatory channel flow – a theoretical perspective

Regime ③b) is defined by $\alpha^2 \gg \pi$ and thus develops a bulk velocity profile. In this case, the velocity U in the center of the channel does not depend on the channel width h but is constant. Derivations from this velocity U are restricted to the very thin hydrodynamic boundary layer close to the wall, and temperature disturbances are limited to the even smaller thermal boundary layer ($\text{Pr} \gg 1$). As temperature disturbances T' are triggered by the constant velocity fluctuation, they are also constant and do not change with the channel width h . Analog to the previous example, the heat flux Q results from the convective transport of temperature disturbances over the channel width. However, this effect is restricted to the constant boundary layer thickness in the present regime: $Q \sim UT' dz \sim \text{const}$. The effective thermal diffusivity κ_e^* follows as the averaged heat flux Q over the channel width h : $\kappa_e^* \sim Q/h \sim 1/\alpha$. Finally, the tidal displacement Δx does not depend on the channel width h^2 (compare Eqn. (3)), and thus the non-dimensional scaling for the effective thermal diffusivity $\kappa_e^*/(\omega \Delta x^2)$ reads $\kappa_e^*/(\omega \Delta x^2) \sim \alpha^2$.

For all six regimes, results match previous findings and underline the importance of interplay between hydrodynamic and thermal boundary layers. A more comprehensible picture is provided by the evaluation of effective thermal diffusivity vs. both Womersley and Prandtl number in Fig. 4. The three coloured solid lines on the surface-plot (orange: $\alpha = \sqrt{\pi}$, black: $\text{Pr} = 1$, and blue $\alpha^2 \text{Pr} = \pi$) represent the three thresholds and define the six regimes. The colored bottom of the plot further clarifies the parabolic or bulk characteristics of the hydrodynamic and thermal profile: Blue indicates regions of parabolic profiles (i.e. large boundary layers), whereas orange indicates bulk profiles (i.e. small boundary layers). The hatched area corresponds to $\text{Pr} < 1$ and describes larger thermal boundary layers compared to its hydrodynamic counterpart. The six green lines indicate each parameter range evaluated in Fig. 2 and Tabs. 1 and 2. Again, the maximum appears for parameter combinations that yield $\alpha^2 \text{Pr} = \pi$ (e.g. compare with the blue line in Fig. 4). As derived above (e.g. in Eq. 14), such conditions correspond to channel flows where the thermal penetration depth approaches the center of the channel. Thus, transient temperature fluctuations (driven by wall-normal fluid-to-wall heat exchange) occur within the complete cross-sectional area of the channel. In particular in the center of the channel, where velocity oscillations are large, the interplay of thermal and hydrodynamic oscillations drives the maximum convective

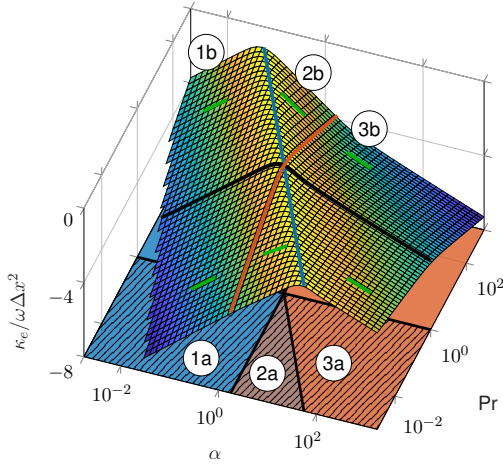


Fig. 4. Effective thermal diffusivity vs. Womersley and Prandtl number.

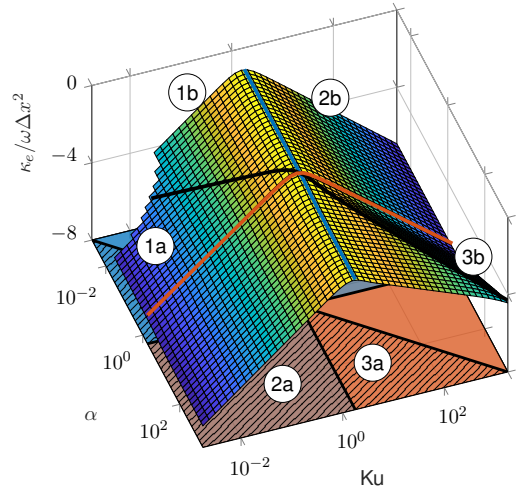


Fig. 5. Effective thermal diffusivity vs. Womersley and Kurzweg number.

heat transfer in the longitudinal direction.

The next section builds on this physically explanation and motivates the introduction of the Kurzweg number.

INTRODUCTION OF THE KURZWEG NUMBER

The Womersley number α yields the ratio of transient inertial and viscous force. The present paper proposes an analogous definition of a non-dimensional *Kurzweg number* Ku as the ratio of thermal inertia and conductive heat flux:

$$Ku^2 \equiv \frac{\rho c \omega T}{k_f Th^2} = \frac{\omega h}{\kappa_f} = \frac{\omega h}{\nu} Pr = \alpha^2 Pr, \quad (15)$$

where ρ is the density and c the specific heat capacity of the fluid. This definition allows to estimate the thermal penetration depth δ_{th} solely in terms of the Kurzweg number as:

$$\frac{\delta_{th}}{h} = \frac{\sqrt{2}}{Ku}. \quad (16)$$

Enhanced longitudinal heat transfer in oscillatory channel flow – a theoretical perspective

Rearranging Eqn. (10) with the Kurzweg instead of the Prandtl number, the thermal diffusivity reads:

$$\frac{\kappa_e^*}{\omega \Delta x^2} = \overbrace{\frac{\Psi^*}{Ku^2}}^{8\sqrt{2}\left(\frac{Ku^4}{\alpha^4}-1\right)\left|1-\frac{\tanh(\sqrt{i}\alpha)}{\sqrt{i}\alpha}\right|^2} \left[\underbrace{\frac{\Phi^*}{\alpha^3 g(\alpha)}} - \underbrace{\frac{\Theta^*}{Ku^3 g(Ku)}} \right]. \quad (17)$$

Notice Φ^* and Θ^* , which are of identical form, only depending on the profile of hydrodynamic and thermal boundary layer thickness, respectively.

Figure 5 reveals that the presentation in terms of Womersley and Kurzweg (instead of Prandtl) numbers simplifies the physical interpretation: In five out of six regimes, the effective thermal diffusivity is governed solely by the Kurzweg number, which represents the thermal boundary layer thickness. The exception is regime (3b), which is characterized by bulk velocity profiles in combination with thermal boundary layers confined to the very close vicinity of the wall ($\delta_{th} < \delta$). In this case, the Womersley number α also has an influence on the longitudinal heat transfer.

CONCLUSIONS

The present study provides a comprehensive discussion of effective longitudinal heat transfer in oscillatory channel flow. The analysis is based on the framework by Kurzweg [7] and simplifications proposed in [21,22]. Qualitative evaluation of limiting cases reported by Kurzweg is confirmed and discussed in the context of hydrodynamic and thermal boundary layer characteristics. Combinations of boundary layer configurations reveal six possible setups of either disturbance extending throughout the complete channel cross-section or not.

The maximum in effective thermal diffusivity is physically attributed to the thermal boundary layer thickness approaching the center of the channel when large temperature fluctuations prevail over the majority of the cross-section. This empathizes the importance of the thermal penetration depth, which is directly incorporated in the proposed definition of a Kurzweg number Ku . The adjusted formulation expands on the physical interpretability as it provides a decoupled treatment

Reproduction of Papers

Enhanced longitudinal heat transfer in oscillatory channel flow – a theoretical perspective

of hydrodynamic and thermal boundary layers. The novel representation shows that in five out of six regimes, the Womersley number has no impact on the effective thermal conductivity. However, only the thermal penetration (presented by the Kurzweg number) affects the problem at hand.

ACKNOWLEDGEMENTS

Financial support has been provided by the German Research Foundation (Deutsche Forschungsgemeinschaft – DFG) in the framework of the Sonderforschungsbereich Transregio 40.

NOMENCLATURE

Symbols

Δx	channel-averaged tidal replacement
δ	hydrodynamic boundary layer thickness
δ_{th}	thermal boundary layer thickness
κ	thermal diffusivity
μ	dynamic viscosity
ν	kinematic viscosity
ω	angular frequency
ρ	density
b	half wall thickness
c	specific heat capacity
h	half channel width
Q	convective heat flux
T	temperature
t	time
U	velocity
x, y, z	spatial dimensions

Dimensionless Quantities

α	Womersley number
ϵ	geometric wall-to-channel characteristic
η	spatial dimension
λ	pressure gradient
Ku	Kurzweg number
Pr	Prandtl number
Ψ, Φ, Θ	terms of simplified model
σ	ratio of thermal diffusivities
ξ	ratio of thermal conductivities
h, j, H, g	functions
Superscripts	
$\bar{\cdot}$	complex conjugate
$*$	simplified/adjusted model
$'$	fluctuation
Subscripts	
0	representative
e	effective

REFERENCES

- [1] Chatwin, P. C., 1975. "On the Longitudinal Dispersion of a Passive Contaminant in Oscillatory Flows in Tubes". *J. of Fluid Mechanics*, **71**, pp. 513–527.
- [2] Jaeger, M. J., and Kurzweg, U. H., 1983. "Determination of the Longitudinal Dispersion

Enhanced longitudinal heat transfer in oscillatory channel flow – a theoretical perspective

- Coefficient in Flows Subjected to High-Frequency Oscillations". *Physics of Fluids*, **26**(6), p. 1380.
- [3] Watson, E. J., 1983. "Diffusion in Oscillatory Pipe Flow". *J. of Fluid Mechanics*, **133**, Aug., pp. 233–244.
- [4] Joshi, C. H., Kamm, R. D., Drazen, J. M., and Slutsky, A. S., 1983. "An Experimental Study of Gas Exchange in Laminar Oscillatory Flow". *J. of Fluid Mechanics*, **133**, Aug., pp. 245–254.
- [5] Kurzweg, U. H., 1985. "Enhanced Heat Conduction in Fluids Subjected to Sinusoidal Oscillations". *Int. J. of Heat Transfer*, **107**(2), p. 459.
- [6] Kurzweg, U., and de Zhao, L., 1984. "Heat Transfer by High-Frequency Oscillations: A New Hydrodynamic Technique for Achieving Large Effective Thermal Conductivities". *Physics of Fluids*, **27**(11), pp. 2624–2627.
- [7] Kurzweg, U. H., 1985. "Enhanced Heat Conduction in Oscillating Viscous Flows within Parallel-Plate Channels". *J. of Fluid Mechanics*, **156**, pp. 291–300.
- [8] Kaviany, M., 1986. "Some Aspects of Enhanced Heat Diffusion in Fluids by Oscillation". *Int. J. of Heat and Mass Transfer*, **29**(12), pp. 2002–2006.
- [9] Kaviany, M., 1990. "Performance of a Heat Exchanger Based on Enhanced Heat Diffusion in Fluids by Oscillation: Analysis". *J. of Heat Transfer*, **112**(1), pp. 49–55.
- [10] Kaviany, M., and Reckker, M., 1990. "Performance of a Heat Exchanger Based on Enhanced Heat Diffusion in Fluids by Oscillation: Experiment". *J. of Heat Transfer*, **112**(1), Feb., pp. 56–63.
- [11] Nishio, S., Shi, X.-H., and Zhang, W.-M., 1995. "Oscillation-Induced Heat Transport: Heat Transport Characteristics Along Liquid-Columns of Oscillation-Controlled Heat Transport Tubes". *Int. J. of Heat and Mass Transfer*, **38**(13), Sept., pp. 2457–2470.
- [12] Inaba, T., Morita, G., and Saitoh, K.-i., 2004. "Longitudinal heat transfer enhanced by fluid oscillation in a circular pipe with conductive wall". *Heat Transfer?Asian Research*, **33**(2), Mar., pp. 129–139.
- [13] Puvaneswari, P., and Shailendhra, K., 2018. "A Dramatic Enhancement of Heat Transfer in Dream Pipe with Viscoelastic Fluids". *Journal of Applied Fluid Mechanics*, **11**(3), May,

Enhanced longitudinal heat transfer in oscillatory channel flow – a theoretical perspective

- pp. 621–635.
- [14] van Buren, S., and Polifke, W., 2021. “Heat Transfer in Pulsating Flow and its Impact on Temperature Distribution and Damping Performance of Resonators”. In *Future Space-Transport-System Components under High Thermal and Mechanical Loads*, W. Schröder, N. A. Adams, O. J. Haidn, R. Radespiel, T. Sattelmayer, W. Schröder, and B. Weigand, eds., no. 146 in Notes on Numerical Fluid Mechanics and Multidisciplinary Design. Springer International Publishing, pp. 97–111.
- [15] van Buren, S., Cárdenas Miranda, A., and Polifke, W., 2019. “Large Eddy Simulation of Enhanced Heat Transfer in Pulsatile Turbulent Channel Flow”. *Int. J. of Heat and Mass Transfer*, **144**, Dec., p. 118585.
- [16] van Buren, S., Förner, K., and Polifke, W., 2017. “Analytical and Numerical Investigation of the Damping Behavior of a Quarter-Wave Resonator with Temperature Inhomogeneity”. In *Annual Report*, C. Stemmer, N. A. Adams, O. J. Haidn, R. Radespiel, T. Sattelmayer, W. Schröder, and B. Weigand, eds. Sonderforschungsbereich/Transregio 40, Oct., pp. 35–47.
- [17] Cárdenas Miranda, A., and Polifke, W., 2014. “Combustion Stability Analysis of Rocket Engines with Resonators Based on Nyquist Plots”. *Journal of Propulsion and Power*, **30**(4), pp. 962–977.
- [18] Förner, K., Cárdenas Miranda, A., and Polifke, W., 2015. “Mapping the Influence of Acoustic Resonators on Rocket Engine Combustion Stability”. *Journal of Propulsion and Power*, **31**(4), Apr., pp. 1159–1166.
- [19] Miura, M., Nagasaki, T., and Ito, Y., 2017. “Experimental investigation of heat transport with oscillating liquid column in pulsating heat pipe using forced oscillation system”. *Int. J. of Heat and Mass Transfer*, **106**, Mar., pp. 997–1004.
- [20] Miura, M., Nagasaki, T., and Ito, Y., 2019. “Experimental study on heat transport induced by phase changes associated with liquid column oscillation in pulsating heat pipes”. *Int. J. of Heat and Mass Transfer*, **133**, Apr., pp. 652–661.
- [21] van Buren, S., and Polifke, W., 2019. “Enhanced Longitudinal Heat Transfer in Turbulent Oscillatory Channel Flow”. In *Annual Report*, C. Stemmer, N. A. Adams, O. J. Haidn, R. Radespiel,

Enhanced longitudinal heat transfer in oscillatory channel flow – a theoretical perspective

- T. Sattelmayer, W. Schröder, and B. Weigand, eds. Sonderforschungsbereich/Transregio 40, Nov., pp. 35–48.
- [22] van Buren, S., and Polifke, W., 2021. “Turbulence-Induced Enhancement of Longitudinal Heat Transfer in Oscillatory Channel Flow”. *submitted to Int. J. Heat Fluid Flow.*



Large eddy simulation of enhanced heat transfer in pulsatile turbulent channel flow



S. van Buren ^{*}, A. Cárdenas Miranda, W. Polifke

Technical University of Munich, Department of Mechanical Engineering, 85748 Garching b. München, Germany

ARTICLE INFO

Article history:

Received 29 April 2019

Received in revised form 19 July 2019

Accepted 14 August 2019

Keywords:

Enhanced convective heat transfer
Turbulent channel flow
High amplitude pulsation
Large eddy simulation (LES)

ABSTRACT

Heat transfer in pulsatile turbulent channel flow is investigated by means of Large Eddy Simulation. Incompressible flow within a periodic computational domain is driven by a pulsating axial pressure gradient at a turbulent Reynolds number of $Re_t = 350$. A localized dynamic sub-grid scale approach is chosen to model unclosed stress terms. A layer-averaged sub-grid model determines turbulent Prandtl numbers that depend on wall distance. Compared to the existing literature, a much wider range of oscillation parameters is studied. In particular, forcing frequencies correspond to Womersley numbers from $Wo = 14$ to 70 , while forcing amplitudes reach values that result in strongly pronounced flow reversal, i.e. reverse flow velocities up to five times larger than the mean flow velocity.

At moderate pulsation amplitudes, i.e. in the range of emerging flow reversal, strong deviations of instantaneous heat transfer rates from the temporal mean are observed. Particularly at times of flow reversal, an increase in heat transfer up to 60% above non-pulsatile values is observed. However, when averaging over a complete cycle, any enhancement in mean heat transfer is only minor.

On the other hand, simulations at larger pulsations amplitudes that result in strongly pronounced flow reversal, show an enhancement of mean heat transfer in excess of 100%. Note that such significant enhancement of heat transfer has not been reported previously in Large Eddy Simulation of turbulent pulsatile flow. The paper offers a physical interpretation of the results and concludes that an overall increase in turbulent transport is responsible for the observed significant enhancement of convective heat transfer.

© 2019 Elsevier Ltd. All rights reserved.

1. Introduction and motivation

In the literature, strong enhancement of convective heat transfer in pulsating flows driven by acoustic fields has been reported repeatedly. In extreme cases, the reported enhancement reached levels that compromise the thermal integrity of devices suffering from thermoacoustic instabilities. One specific example for such devices is a rocket engine combustion chamber. Exceeding the designed wall heat flux may obviously endanger a secure operation with possibly catastrophic consequences. Therefore, the reliable prediction of heat transfer in turbulent pulsating flows is crucial for a comprehensive design process of combustion chambers.

For the case of rocket motors, Harrie et al. [1,2] give an overview of observed incidents and report that under representative conditions, unstable operation does not permit reliable measurements, such that eventually only a severe hardware damage can be attested. Harrje cautions that due to the aggressive conditions in

the chambers, most of the experimental information is limited and of rather qualitative nature. Nevertheless, in a final report [3], Harrie concludes that the heat transfer under periodic unsteady conditions can exceed its steady state value by more than 100% and that flow reversal, prevalent in the vicinity of a velocity anti-node, plays a decisive role.

Due to the wide range of perturbation frequencies and mean flow Reynolds numbers used in the various investigations, apparently contradictory arguments can be found in the literature, with both enhancement and decrease of heat transfer being reported.

In a laboratory scale, Perry and Culick [4] studied the average heat transfer in a solid propellant T-burner that exhibited combustion instabilities. In the presence of combustion-driven oscillation, enhanced heat transfer (EHT) proportional to the square root of the oscillation amplitudes and the fourth root of the frequency was found.

Dec and co-workers studied the phenomenon in a pulse combustor, which was operated in limit cycle over a range of frequencies and amplitudes that included flow reversal. In a series of papers [5–8], local heat transfer enhancement by up to 300% was

* Corresponding author.

E-mail address: vanburen@tfd.mw.tum.de (S. van Buren).

Nomenclature	
Symbols	
Δ	filter width
δ_s	Stokes length
ϵ	pulsation strength
ϵ_{dis}	dissipation rate
η	enhancement of heat transfer
λ	wave number
ν	kinematic viscosity
ω	angular frequency
ϕ	phase lag
ρ	density
τ_w	wall friction
τ_{ij}	subgrid scale stress tensor
φ	phase angle
\vec{S}_{mom}	momentum source term
A, a	amplitudes
A_{ij}	Reynolds stress (amplitude)
c	speed of sound
c_v, c_e	dynamic coefficients
E	turbulent kinetic energy spectrum
f	frequency
h	half channel height
k	kinetic energy
L	acoustic wave length
L_x, L_y	stream-/span-wise domain size
N_t	number of cycles
p	pressure
q	heat flux
q_j	unresolved heat flux
R_{ij}	Reynolds stress (time-averaged)
T	temperature
t	time
u	velocity
u_τ	friction velocity
x, y, z	spatial dimensions
Dimensionless Quantities	
He	Helmholtz number
Ma	Mach number
Nu	Nusselt number
Pr	Prandtl number
Re_τ	turbulent Reynolds number
Wo	Womersley number
l_s^+	non-dimensional Stokes length
Superscripts	
$\bar{\cdot}$	resolved grid scale
\cdot	temporal average
$\langle \cdot \rangle$	temporal and spatial averaging
$\langle \cdot \rangle_p$	ensemble average
$+$	non-dimensional
$'$	acoustic fluctuation
$''$	turbulent fluctuation
Subscripts	
0	constant, initial condition
b	bulk
c	center-plane
l	lower wall
u	upper wall
w	wall-plane
ha	higher harmonics
ref	non-pulsating reference case
sgs	unresolved subgrid scale
tot	total

reported. The novelty compared to previous investigations was that detailed measurements of velocity, temperature, and heat flux rates were performed. The investigations put forward the hypothesis that a combination of increased turbulence in the shear layer and strong convection, driven by transverse flows at times of flow reversal, is responsible for enhanced heat transfer. However, it was not possible to elucidate the mechanism that leads to said transverse flows.

Habib et al. [9], when studying heat transfer at various pulsation frequencies in laminar pulsating pipe flow, encountered increased as well as reduced Nusselt numbers, and established that the effects are primarily present in the thermally developing region. However, the magnitude of the enhancement was far smaller than in the above mentioned turbulent cases.

Hemida et al. [10] attempted to clarify these issues with a theoretical analysis of heat transfer in laminar pulsating flow in a tube with constant wall heat flux. They found that the local Nusselt number exhibits a spatial modulation along the tube with values both higher and lower than in the stationary case. The perturbations are most pronounced in the thermally developing region and are damped out further downstream. However, the amplitudes imposed in the studies of Hemida et al. [10] are restricted to pulsating flow without center-line flow reversal.

In an analytical study, Lundgren et al. [11] resolved flow and heat transfer in laminar, pulsating flows in channel configurations, including pipe flow. The consideration of an oscillating axial temperature is the most important novelty of their study. Furthermore, they considered large amplitudes with center-line flow reversal. A

fully developed flow field was assumed, pressure and velocity gradients in the axial direction that oscillated harmonically in time were imposed. Qualitatively, their results match the behavior of the experiments performed by Dec et al. [5–8] well, displaying second harmonics in the channel bulk temperature modulation. However, the results cannot be compared quantitatively, because of the absence of turbulent scales. Nevertheless, the study also demonstrates the possibility of both enhanced and decreased heat transfer, depending on the relative phase between temperature and velocity fluctuations.

Numerical studies based on computational fluid dynamics (CFD) give detailed insight into transient phenomena, also for the pertinent case of turbulent pulsating flows. Thyageswaran [12] simulated the turbulent flow in a pulse combustor tail pipe and reproduced the high heat transfer rates reported by Dec et al. [5–8]. In order to resolve the tail pipe domain in its entirety, Thyageswaran's simulations employed unsteady Reynolds-averaged Navier-Stokes (RANS) turbulence models and wall models. Well established wall models failed to reproduce correctly the transient behavior of the heat transfer, thus a modified model was proposed, which reproduced the higher heat transfer rates at least qualitatively. Unfortunately, this formulation does not give insight into the mechanisms leading to the enhancement.

Scotti and Piomelli [13,14] studied momentum transfer, in particular wall shear stress, in pulsating channel flow by means of Direct Numerical Simulations (DNS), Large Eddy Simulation (LES) and RANS. It was demonstrated that conventional RANS models fail to properly predict the flow dynamics in this case [13]. The validity

and advantages of the LES approach (trade-off between resolution and computational costs) to study unsteady problems such as turbulent pulsating flows were confirmed for a wide range of frequencies [13]. Furthermore, it was shown that dynamic sub-grid scale models, which can be considered as state of the art in LES modelling, are capable of modeling accurately the unclosed terms also in transient cases. In this context, it is important that the near wall region is fully resolved, making the necessity of dynamically adapted coefficients evident. The studies of Scotti and Piomelli were restricted to incompressible flow without heat transfer and focused on near wall momentum transfer. It was observed that the fluctuations in the near wall region generated by the pulsating pressure gradient do not propagate beyond a characteristic distance. The so-called turbulent Stokes length was estimated using the sum of the molecular and turbulent diffusivities.

Wang and Lu [15] employed LES based on the dynamic Smagorinsky sub-grid scale model to study turbulent structures and passive heat transfer in turbulent pulsating flow between parallel plates. The influence of the Prandtl number at a turbulent Reynolds number of $Re_t = 350$ on the thermal response of the flow was investigated. The results confirmed that for high Prandtl numbers the temperature fluctuations and the mechanisms involved in the heat transfer process are confined to a very thin region close to the wall. Furthermore, the influence of the organized pulsations on the time average quantities (in particular heat transfer) was found to be marginal for the conditions investigated, which did not exhibit center-line flow reversal.

Wang and Zhang [16] examined heat transfer in a two-dimensional duct, applying unsteady RANS equations. In distinction to the prior studies, instead of cyclic boundary conditions a long inlet region was applied. The investigation of Wang and Zhang [16] extends to large pulsation amplitudes with strongly pronounced flow reversal. Amplitudes reached up to six times the mean flow velocity and large pulsation amplitudes greatly promoted the time-averaged heat transfer. An optimum Womersley number was connected to the enhancement. Note that this approach conflicts with the conclusions of Scotti and Piomelli [13,14] who argue that RANS simulations are not adequate for the problem at hand.

Cardenas [17] performed a computational study with focus on the effect of enhancement of heat transfer in turbulent acoustic channel flows. Lower Reynolds numbers ($Re_t = 180$) than in the works of Scotti and Piomelli [13] and Wang and Lu [15] were investigated. For pulsation amplitudes approaching flow reversal, a slight enhancement of heat transfer was found at pressure nodes (less than 10%). Effects of acoustic impedance, i.e. the relative amplitude and phase of pressure and velocity fluctuations, were investigated as possible causes for the discrepancies from experimental studies. Thus, the study extends to a weakly compressible formulation to account for positions away from the pressure node.

In summarizing the literature review on heat transfer in pulsating flows (compare Table 1), it is noted that, with the exception of

for Wang and Zhang [16], all studies that report significant enhancement of heat transfer are of experimental nature, with pulsations driven by acoustic waves. The experimentally observed magnitudes of heat transfer enhancement were not consistently reproduced or convincingly explained by the numerical and theoretical studies. In other words, although strong evidence of enhanced heat transfer in pulsating flow has been presented, a fully satisfactory explanation of the responsible mechanisms remains as elusive as quantitative predictions. Thus additional fundamental research in this area is necessary.

The present paper aims to offer physical interpretation for significant heat transfer enhancement in pulsatile turbulent channel flow. Note that such significant enhancement of heat transfer has not been reported previously in Large Eddy Simulation. Compared to the existing literature, a considerably wider range of parameters is studied. In particular, forcing frequencies correspond to Womersley numbers from 14 to 70, while forcing amplitudes reach values that result in strongly pronounced flow reversal, i.e. reverse flow velocities up to five times larger than the mean flow velocity. Based on highly resolved LES, the investigation of pulsating flow fields is carried out at Reynolds number $Re_t = 350$. Fully developed intrinsic turbulence spectra are generated by the imposed mean axial pressure gradient combined with cyclic boundary conditions. For the closure of unresolved terms, dynamic localized approaches, accounting for partly unsteady flow characteristics, are carefully selected. Data-reduction, obtained by a variety of runtime averaging operations, allows for meaningful interpretation of the results. The turbulent kinetic energy is identified as an important characteristic. In current dominated flows without flow reversal, relaminarization and its effect on EHT are discussed. The extensive physical interpretation of prevailing flow characteristics provides novel insight in the interaction of turbulence and heat transfer. Arguments are given why significant EHT was not reported in prior numerical LES studies, but only in experimental investigations. To close this gap, the range of pulsation amplitudes is extended to values significantly larger than those of previous numerical and theoretical studies. Cases of strong flow reversal with pulsation amplitudes up to five times the mean flow velocity are investigated.

The present study is structured as follows: Section 2.1 describes the set-up of the cyclic simulation domain which is then linked to the acoustically compact region of a pressure node in Section 2.2. The governing equations of the LES are stated in Section 2.3 and closed by the turbulence model (Section 2.4). Details on the methods of data reduction for the evaluation of the numerical experiments (Section 2.7) are presented in Section 2.5. Non-dimensional characteristics are introduced in Section 2.6.

The results of the numerical study are presented as follows: First, a validation case is studied in Section 3. A more detailed investigation of relaminarization of pulsating flows in the range of emerging flow reversal follows (Section 4). At these moderate pulsation amplitudes, the influences of both forcing frequency

Table 1
Summary of the literature review on heat transfer in pulsating flows.

	Numerical method	Significant EHT	Flow regime	Significant flow reversal
Harrje et al. [1–3]	Experimental	✓	Turbulent	✓
Perry et al. [4]	Experimental	✓	Turbulent	✓
Dec et al. [5–8]	Experimental	✓	Turbulent	✓
Habib et al. [9]	Experimental	✗	Laminar	✗
Hemida et al. [10]	Theoretical	✗	Laminar	✗
Lundgren et al. [11]	Theoretical	✗	Laminar	✗
Thyageswaran [12]	Numerical	RANS	✗/✓	Turbulent
Wang et al. [15]	Numerical	LES	✗	Turbulent
Wang et al. [16]	Numerical	RANS	✓	Turbulent
Cardenas [17]	Numerical	LES	✗	Turbulent

and pulsation amplitude on heat transfer are studied (Section 5.1 and 5.2, respectively). In Section 6, the study is extended to flows with high pulsation amplitudes, which significantly exceed flow reversal.

Finally, Section 7 summarizes and offers conclusions of the study. All symbols are specified in the appended nomenclature.

2. Computational setup for turbulent, pulsating channel flow with heat transfer

2.1. Simulation domain setup

To provide a fundamental analysis of heat and momentum transfer in turbulent, pulsating flow driven by an acoustic field, a channel flow configuration as shown in Fig. 1 with cyclic boundary conditions in the stream-wise and span-wise directions has been chosen.

The flow is driven by an imposed momentum source term \vec{S}_{mom} , which overcomes viscous losses at the walls and emulates the pulsating acoustic pressure gradients that drive the pulsations. The major advantage of this configuration is that it affords high resolution of the turbulent flow without the requirement of an inflow turbulence model. Once the flow is fully developed, the turbulent structures do not depend on initial or boundary conditions, but are inherently driven by the near wall turbulence production, resulting in a realistic turbulence spectrum. Note that the present setup is not suitable for hydrodynamically or thermally developing flows, cf. the studies of Habib et al. [9] and Hemida et al. [10].

The channel half height h is the characteristic geometry length scale. Non-slip conditions are imposed at the top and bottom walls. In order to capture large turbulent structures, the domain extends $L_x = 2\pi h$ in the stream-wise and $L_y = \pi h$ in the span-wise direction. Furthermore, to induce heat transfer, the top and bottom walls are kept at different temperatures T_l and T_u , respectively. Conjugate heat transfer is not considered in the analysis and thus, Dirichlet boundary conditions are employed. This approach is justified by the results of Emmert et al. [18], who argued that a wall of finite thickness does not contribute to EHT. Fluid properties are assumed to be constant for low differences in temperature.

It is pointed out that the presented setup of the simulation domain is well documented in the literature which thus allows comprehensive validation (e.g. [13,15,17]). Most of the earlier studies focus on incompressible pulsating flows and do not link to acoustics as the driving mechanism. However, as will be shown in the next section, regions of acoustic pressure nodes physically coincide with such pulsating flows. In the context of EHT, the localized investigation in the vicinity of pressure nodes agrees with numerous experimental studies ([1,2,4–8]) that identify the large velocity fluctuations as a main driving mechanism.

In the following section, the link to an acoustically driven, turbulent, pulsating channel flow is given by the derivation of the imposed momentum source term \vec{S}_{mom} .

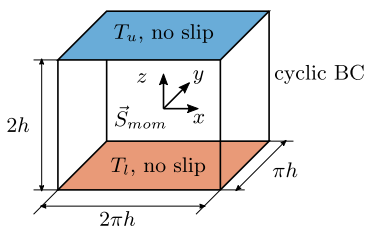


Fig. 1. Cyclic simulation domain of an acoustically compact channel section at a pressure node.

2.2. Acoustically compact properties derived from duct acoustics

Consider a one-dimensional acoustic field in an closed channel of length L and small transverse dimensions. From linear theory, the mode shape of the second harmonic reads [19]:

$$\frac{p'}{\rho_0 c_0}(x, t) = 2A \cos(2\pi x/L) \cos(\omega t) = a_p(x) \cos(\omega t), \quad (1)$$

$$u'(x, t) = -2A \sin(2\pi x/L) \sin(\omega t) = a_u(x) \sin(\omega t), \quad (2)$$

where A is a constant defining the magnitude of the sound pressure level. Small Mach numbers $Ma \ll 1$ are assumed such that the influence of mean flow on the acoustic wave propagation can be neglected. Fig. 2 shows schematically the amplitudes p' and u' of the velocity and pressure waves along the channel. The alternation between pressure and velocity nodes in periods of $L/4$ is evident. If the location $X + \pi h$ is placed on a pressure node, the velocity fluctuates with maximum amplitude, while the pressure remains constant.

If acoustic waves are present in turbulent channel flow, one distinguishes between several contributions to the mean and fluctuating flow variables, which are characterized by respective velocity and length scales of considerably different magnitudes: acoustic perturbations u' and p' propagate at the speed of sound; at low frequencies only plane waves can propagate along the channel length L , with wave lengths much larger than the channel height h . Turbulent perturbations u'' and p'' are transported through the domain at velocities similar to the reference flow velocity, their length scales are a fraction of the channel half height h . Underlying these contributions is a constant, uniform mean pressure gradient $dp_0/dx = const.$, which drives the mean flow. A triple-decomposition can be formulated, which for pressure reads

$$p = p_0(x) + p'(x, t) + p''(\vec{x}, t). \quad (3)$$

As indicated in Eq. (3) and Fig. 2, which shows the axial distribution of mean pressure p_0 and acoustic pressure p' at an instant time t , the oscillating acoustic component $p'(\vec{x}, t)$ is non-uniform in space. However, if the computational domain – denoted by the dashed box in Fig. 2 – is acoustically compact, i.e. if its length $2\pi h$ is much less than the acoustic wavelength L , the acoustic pressure gradient may be treated as approximately uniform in space. The characteristic dimensionless group in this context is the Helmholtz number $He \equiv \omega 2\pi h/c_0$, based on the frequency ω , speed of sound c_0 and domain length $L_x = 2\pi h$ [20]. A compact domain implies that $He \ll 1$.

In the limit of acoustic compactness, the flow forcing by the mean and acoustic pressure gradients can be represented by a momentum source term that is uniform within the computational domain,

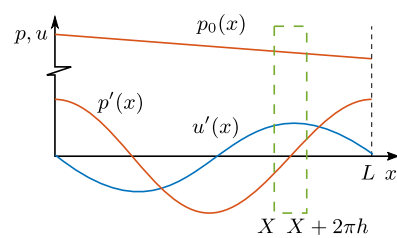


Fig. 2. Instantaneous mode shape of the second harmonic in a channel. Mean flow is driven by the pressure gradient of $p_0(x)$.

$$\begin{aligned}\vec{S}_{mom}(t) &= \left(\frac{dp_0}{dx} + \frac{\partial p'(x,t)}{\partial x} \Big|_{x=x} \right) \vec{e}_x = (p_{0,x} + a_{p,x} \cos(\omega t)) \vec{e}_x \\ &= p_{0,x} (1 + a_{p,x}^+ \cos(\omega t)) \vec{e}_x,\end{aligned}\quad (4)$$

where the subscript x indicates derivative with respect to the independent variable x .

2.3. LES governing equations

The Large Eddy Simulation (LES) approach has proven its capability to simulate turbulent pulsating flows in several studies [13], especially if so-called *dynamic models* (see Section 2.4) are used. The spatial filtering of the discrete mesh can be expressed as the convolution of the primitive variable ψ with a grid dependent *filter function* $G(\vec{x})$. Several filter or kernel functions G in both spectral or physical space exist [21], which depend on the grid scale filter $\bar{\Delta}$. Applying the filter function, the primitive variables are decomposed into a resolved or *grid scale*, and an unresolved or *subgrid scale* (SGS) contribution, respectively:

$$\psi = \bar{\psi} + \psi_{sgs}. \quad (5)$$

For low Mach numbers and small temperature differences, the incompressible Navier–Stokes equations with constant properties – in particular constant density ρ_0 – are appropriate. For this case, the filtered balance equations for mass, momentum and energy can be written as:

$$\frac{\partial \bar{u}_i}{\partial x_i} = 0, \quad (6)$$

$$\frac{\partial \bar{u}_i}{\partial t} + \frac{\partial}{\partial x_j} (\bar{u}_i \bar{u}_j) = -\frac{1}{\rho_0} \frac{\partial \bar{p}}{\partial x_i} + v \frac{\partial^2 \bar{u}_i}{\partial x_j \partial x_j} - \frac{\partial \tau_{ij}}{\partial x_j} + \frac{1}{\rho_0} \vec{S}_{mom}, \quad (7)$$

$$\frac{\partial \bar{T}}{\partial t} + \frac{\partial}{\partial x_j} (\bar{u}_j \bar{T}) = \Pr \frac{\partial^2 \bar{T}}{\partial x_j \partial x_j} - \frac{\partial q_j}{\partial x_j}, \quad (8)$$

where v denotes the kinematic viscosity and \Pr the Prandtl number.

The subgrid scale stress tensor τ_{ij} is defined as $\tau_{ij} = \bar{u}_i \bar{u}_j - \bar{u}_i \bar{u}_j$ [22]. The temperature is considered as a passive scalar and the filtered diffusion flux is closed by a gradient diffusion model. Analogously to τ_{ij} , the unresolved heat flux q_j of the scalar temperature T reads $q_j = \bar{u}_j \bar{T} - \bar{u}_j \bar{T}$.

Closure of the unresolved terms, which result from the sub-grid scales, is archived with two localized methods. The momentum equation is closed by a method proposed by Kim and Menon [23]. For the energy equation, a gradient approach suggested by Moin et al. [24] is applied in a layer-averaged form to increase numerical stability. These two dynamic methods are described in the following.

2.4. LES turbulence model

A localized one-equation model describes the unresolved kinetic energy k_{sgs} by the transport equation

$$\frac{\partial k_{sgs}}{\partial t} + \bar{u}_i \frac{\partial k_{sgs}}{\partial x_i} = -\tau_{ij} \frac{\partial \bar{u}_i}{\partial x_j} - \epsilon_{dis} + \frac{\partial}{\partial x_i} \left(v_{sgs} \frac{\partial k_{sgs}}{\partial x_i} \right), \quad (9)$$

where v_{sgs} denotes the turbulent eddy viscosity at sub-grid scale. The terms that describe the change rate of the subgrid kinetic energy k_{sgs} are convection, production, dissipation and diffusion [23]. The unresolved stress tensor τ_{ij} is modeled via the subgrid scale eddy viscosity v_{sgs} :

$$\tau_{ij} = -2v_{sgs} + \frac{2}{3} \delta_{ij} k_{sgs}, \quad (10)$$

where

$$v_{sgs} = c_v \bar{\Delta} \sqrt{k_{sgs}}. \quad (11)$$

Finally, the model is closed by scaling the dissipation rate ϵ_{dis} :

$$\epsilon_{dis} = c_\epsilon \frac{\sqrt{k_{sgs}}}{\bar{\Delta}}. \quad (12)$$

The coefficients c_v and c_ϵ are determined following a dynamic approach supposed by Kim and Menon [23]. It is based on scale similarity assumptions and the application of a least square method leads to a significant reduction of computational costs [25]. The *simplefilter* implementation of OpenFOAM is used where the test filter width is twice the grid filter. For a detailed description of the numerical implementation, please consult [23].

The unresolved heat flux q_j is modeled as

$$q_j = \frac{v_{sgs}}{\Pr_{sgs}} \frac{\partial \bar{T}}{\partial x_j} \quad (13)$$

where \Pr_{sgs} denotes the turbulent Prandtl number. The dynamic determination of the turbulent Prandtl number follows the approach suggested by Germano et al. [26]. Subsequently, the least square method was applied by Lilly [27]. Detailed information of the layer-based, spatially averaged numerical implementation are provided by Moin et al. [24], Wang and Lu [15] as well as by Morar [25].

At this point, it is emphasized that Scotti and Piomelli [13] as well as Wang and Lu [15] applied the dynamic Smagorinsky model, which assumes local equilibrium at all times. In accordance with Cardenas [17], the present study judiciously applies the kinetic energy equation model to consider partly unsteady characteristics induced by pulsations.

2.5. Data reduction through averaging operators

For the meaningful characterization of turbulent pulsating flows, data reduction through averaging is required. Due to the mesh resolution under consideration and in order to reduce storage requirements, the reduction takes place during simulation runtime.

The *temporal averaging* of a quantity $\psi(\vec{x}, t)$ over a total time t_{tot} will be denoted by the hat operator (\cdot) and is defined as:

$$\hat{\psi}(\vec{x}) = \frac{1}{t_{tot}} \int_0^{t_{tot}} \psi(\vec{x}, t) dt. \quad (14)$$

Exploiting the geometrical invariance in stream-wise and span-wise direction of the simulation domain, an additional spatial averaging of planes parallel to the top and bottom walls is introduced for further reduction and the increase of statistical validity. This combination of *temporal* and *spatial averaging* operations will be denoted by angle brackets:

$$\langle \psi \rangle(z) = \frac{1}{t_{tot} L_x L_y} \int_0^{L_x} \int_0^{L_y} \int_0^{t_{tot}} \psi(\vec{x}, t) dt dy dx. \quad (15)$$

When dealing with pulsating flows driven at a single frequency $f = 2\pi\omega$, *phase* or *ensemble averaging* can help in the identification of coherent structures. As argued by Scotti and Piomelli [13], this assumes that the major contribution of the system response occurs at the forcing frequency. This kind of operation will be denoted by subscripted angle brackets $\langle \cdot \rangle_p$ and is defined as:

$$\langle \psi \rangle_p(z, \varphi) = \frac{1}{N_t L_x L_y} \sum_{j=1}^{N_t} \int_0^{L_x} \int_0^{L_y} \psi\left(\vec{x}, \frac{\varphi}{\omega} + 2\pi \frac{(j-1)}{\omega}\right) dy dx, \quad (16)$$

where N_t denotes the number of cycles under consideration and $\varphi \in [0, 2\pi]$ is the phase angle. The phase averaged quantities can be further decomposed into a mean, a harmonic and a non-linear component as proposed in [13]:

$$\langle \psi \rangle_p(z, \varphi) = \langle \psi \rangle(z) + a_\psi(z) \cos(\varphi + \phi_\psi(z)) + \psi_{ha}(z, \varphi). \quad (17)$$

Of course, the stationary component corresponds to the temporal and spatial average of the original quantity. The harmonic component can be seen as a real valued amplitude, and thus may exhibit a phase lag ϕ_ψ towards a reference value. Note that both amplitude and phase lag are in general functions of the wall distance. Usually, the phase lag is defined using the axial velocity pulsations at the channel center-line as reference. From the phase averaging definition, the oscillating component accounts only for the contribution of the forcing frequency. The contributions at higher harmonics are all added up in the term ψ_{ha} which is of course a function of the phase φ and the wall normal location z .

For the pulsating channel flow, a *triple decomposition* into average, acoustic and turbulent contributions widely used in the literature can be written in terms of the average operators just introduced as:

$$\psi(\vec{x}, t) = \langle \psi \rangle + a_\psi(z) \cos(\omega t + \phi_\psi(z)) + \psi''(\vec{x}, t), \quad (18)$$

where ψ'' denotes the turbulent fluctuations and higher harmonics ψ_{ha} are omitted for simplicity.

2.6. Non-dimensional characterization of turbulent pulsating flows

For steady turbulent channel flows, the stream-wise pressure gradient $p_{0,x}$ is in equilibrium with the wall friction $\tau_w = v \partial u / \partial z|_{z=w}$, where the index w denotes the wall-plane. Defining the friction velocity as $u_\tau = \sqrt{\tau_w / \rho} = \sqrt{h p_{0,x} / \rho}$ and the non-dimensional wall distance $z^+ = z u_\tau / v$, the turbulent Reynolds number yields:

$$Re_\tau = \frac{h u_\tau}{v} = \frac{h}{v} \sqrt{\frac{h p_{0,x}}{\rho}}. \quad (19)$$

The *Womersley number* Wo is a dimensionless expression of the pulsatile flow frequency in relation to viscous effects:

$$Wo = \sqrt{\frac{\omega h^2}{v}}. \quad (20)$$

The *Nusselt number* characterizes heat transfer and can be interpreted as the non-dimensional temperature gradient at the wall:

$$Nu = \frac{q_w}{\Delta T_b} \frac{h \Pr}{v \rho c_p} = \frac{h}{\Delta T_b} \left. \frac{\partial T}{\partial z} \right|_w, \quad (21)$$

where q_w is the heat flux at the wall and ΔT_b the temperature difference of bulk and wall temperature. Due to symmetry of the problem at hand, $\Delta T_b = (T_l - T_u)/2$ holds.

To account for unsteadiness, Ramaprian and Tu [28] found the Stokes number to be insufficient in turbulent pulsating flows: Comparing time scales of diffusion driven penetrations, they found that effective diffusion may be significantly enhanced by turbulence. Thus, a *non-dimensional frequency* ω^+ is commonly used to characterize turbulent pulsating flows (e.g. [29]):

$$\omega^+ = \frac{\omega v}{u_\tau^2}. \quad (22)$$

Using the non-dimensional frequency, Scotti and Piomelli [13] formulated an adapted non-dimensional Stokes length I_s^+ that can be directly related to the classical Stokes length δ_s :

$$I_s^+ = \sqrt{\frac{2}{\omega^+}} = \frac{u_\tau}{v} \delta_s \quad \text{where} \quad \delta_s = \sqrt{\frac{2v}{\omega}}. \quad (23)$$

It directly follows that the Womersley number Wo may also be interpreted in terms of the Stokes boundary layer thickness:

$$Wo \sim \frac{h}{\delta_s}. \quad (24)$$

A common method to quantify the strength of pulsations is to relate the velocity amplitude to the mean flow velocity in the center-plane (index c):

$$\epsilon = \left. \frac{a_u}{\langle u_{ref} \rangle} \right|_c. \quad (25)$$

Thus, $\epsilon < 1$ describes *current dominated* flows, which are mainly controlled by the forcing frequency [13,29]. Values of $\epsilon > 1$ (*pulsation dominated* flows) indicate the presence of flow reversal. In the present study, flows in the range of emerging flow reversal $\epsilon \lesssim 1.2$ are referred to as flows with *moderate amplitudes*. *Large amplitudes* include strongly pronounced effects of flow reversal ($\epsilon \gtrsim 2$).

The enhancement of heat transfer η is defined as the normalized increase of the wall heat transfer of the pulsating flow compared to a non-pulsating reference case:

$$\eta = \frac{q_w - q_{w,ref}}{q_{w,ref}} = \frac{Nu - Nu_{ref}}{Nu_{ref}}. \quad (26)$$

Positive values of η indicate an enhancement in heat transfer, while negative values quantify a reduction.

2.7. CFD solver setup

The numerical implementation is carried out with the finite volume software OpenFOAM (Version v1706+) [30]. The PISO algorithm is used to iteratively solve the system of discretized partial differential equations derived from conservation of mass, momentum and energy. The flexibility of the open source code allows for required adjustments, including source terms, LES models and averaged outputs for post-processing.

The chosen simulation parameters with constant properties are displayed in Table 2. The mesh applied consists of $66 \times 66 \times 102$ cells on a structured grid. In periodic stream-wise and span-wise direction, the cells are arranged in an equidistant manner. In the direction perpendicular to the channel walls, hyperbolic spacing is applied to properly resolve the wall interaction. For a steady turbulent flow without acoustic pulsation, the first cell center lies at $z^+ \approx 0.5$. In the literature, these mesh properties are found to be sufficient for a mesh-independent LES of the problem at hand [13,15]. In addition to the provided references, the benchmark case provided by Scotti and Piomelli [13] was reevaluated: Mesh resolutions with first cell center down to $z^+ \approx 0.1$ were considered. It was found that the velocity at the wall and at the channel center as well as wall heat flux deviate by less than 1.5%. Thus the mesh-independence reported in the literature is confirmed [13,15].

To assure an adequate consideration of large stream-wise flow structures [31], an extended periodic simulation domain of $L_x = 6\pi h$ was studied. Only very small differences between the two domains were observed in first-order statistics (velocity and wall heat flux) and second order statistics (Reynolds shear stresses). Thus it is concluded that the domain size of $L_x = 2\pi h$ is sufficient to capture dominant eddy structures of the problem under investigation.

Table 2
Simulation parameters.

Re_τ	l_s^+	T_u^+	T_l^+	Pr	Δx^+	Δy^+	L_x	L_y	Mesh
350	7 to 35	0	1	0.71	33.3	16.7	$2\pi h$	πh	$66 \times 66 \times 102$

3. Validation

Three exemplary operation points with acoustic forcing are described and compared to some of the data available in the literature to serve as a validation for the turbulent pulsating case. The cases correspond to the ones studied experimentally by Tardu et al. [29], which were subsequently also used in the numerical studies of Scotti and Piomelli [14], Wang and Lu [15] and Cardenas [17]. Table 3 lists the key parameters of the three different computed cases in the present study compared against the ones used by the investigations mentioned. All cases lie in the current dominated regime with a normalized velocity center-line amplitude of approximately $\epsilon \approx 0.7$.

The different cases are simulated using the numerical setup presented in the previous section and run for several periods to obtain robust temporal and phase averaged statistics. Fig. 3 shows the axial velocity components after performing the triple decomposition given by Eq. (17) and plotted in wall units. The profiles of the present LES simulations are compared against the results of the investigations listed in Table 3. The first row in the figure shows the time averaged part of the non-dimensional axial velocity $\langle u^+ \rangle$ with $\langle u^+ \rangle = u/u_\tau$, which clearly follows the classical law of the wall. In all frequency regimes, the profiles collapse to the classical law of the wall $\langle u^+ \rangle = 2.5 \ln(z^+) + 5$ and $\langle u^+ \rangle = z^+$, respectively, denoted by the dashed lines and the agreement between the different investigations is very good. Especially close to the wall, velocity variations are smaller than 2%. Considering the more central log law region, deviations to previous numerical studies remain below 10%. In the low frequency regime, it seems that the logarithmic region is shifted slightly to a position closer to the wall. For the other frequencies, the average profiles lie close to the ones of the stationary case without pulsations. The middle row shows the ensemble averaged velocity amplitude a_u^+ normalized by its center-line value a_{uc}^+ . As expected, the thickness of the turbulent Stokes layer is inversely proportional to the square-root of the forcing frequency ranging from 10 in the high to 500 in the low frequency regime (compare Eq. (23)). Again, the concordance between the three investigations is remarkably good.

Finally, the third row in the figure gives the phase difference $\Delta\phi_u = \phi_u(z) - \phi_u(h)$ between the wall and channel center-line velocity fluctuations. Unfortunately, the wall normal profiles of this quantity are not given in the publication of Scotti and Piomelli, only the values for the skin friction phase are provided, such that only one value per frequency case is plotted in the third row of Fig. 3. For high frequencies, the behavior is almost identical to the one of laminar pulsating channel flow. Due to the lower momentum of the fluid close to the wall, it reacts faster to the pressure gradient pulsations, leading to a phase advance of $\pi/4$ as predicted by Lighthill [32]. For lower frequencies this phase advance reduces. It is interesting that in the low frequency case, the phase of the near wall region decreases further, even takes on negative values. The magnitude of this phase lag is of the order of $\pi/40$ in the case studied here. Concerning the phase, the degree of conformity between the three investigations is very good.

It is important that the comparison between the three investigations is valid even though different turbulent Reynolds numbers are used in each of them, ranging from $Re_\tau = 432$ in the experimental study to $Re_\tau = 180$ in the study by Cardenas [17]. The forcing frequencies are chosen such that the resulting turbulent Stokes numbers l_s^+ are comparable, representing the low, medium and high frequency regimes, respectively. This preliminary comparison confirms that, concerning the momentum transfer, the proper similarity parameters are the non-dimensional frequency ω^+ or Stokes length l_s^+ and the velocity amplitude ratio at the channel center-line, as proposed by Scotti and Piomelli [13].

Concerning the thermal response of the flow to the harmonic unsteadiness, the situation only has limited similarity with the hydrodynamic response. This is easily explained by the different fundamental driving mechanisms: The velocity field is driven by the imposed pressure gradient whereas the temperature field results from the potential of a heated upper channel wall and a cooled lower channel wall. As already shown by Wang and Lu [15], for the three cases investigated, the time independent part of the non-dimensionalized temperature plotted in wall normal direction follows also the logarithmic law of the wall with a near wall buffer layer and a logarithmic bulk region. The Reynolds

Table 3
Parametric setup of reviewed studies, used for the validation of the pulsating channel flow at three levels of frequency (high, medium and low) indicated by the Stokes length l_s^+ , the pulsation amplitude ϵ with the corresponding forcing pressure amplitude a_{px}^+ and the turbulent Reynolds number Re_τ .

	High	l_s^+	Medium	Low	ϵ	a_{px}^+	Re_τ	Wo
BCP (Present Study)	7		14		0.67 0.66 0.80	200 50 8	350	70.7 35.4 14.1
TBB [29]	8.1		16		- 0.64 -		432	
SP [13]	7		14		0.66 0.70 0.79	200 50 8	350	
WL [15]	7		14		≈ 0.70 ≈ 0.70 ≈ 0.70	200 50 8	350	
CA [17]	7.1		15.3		0.7 0.78 0.70		180	

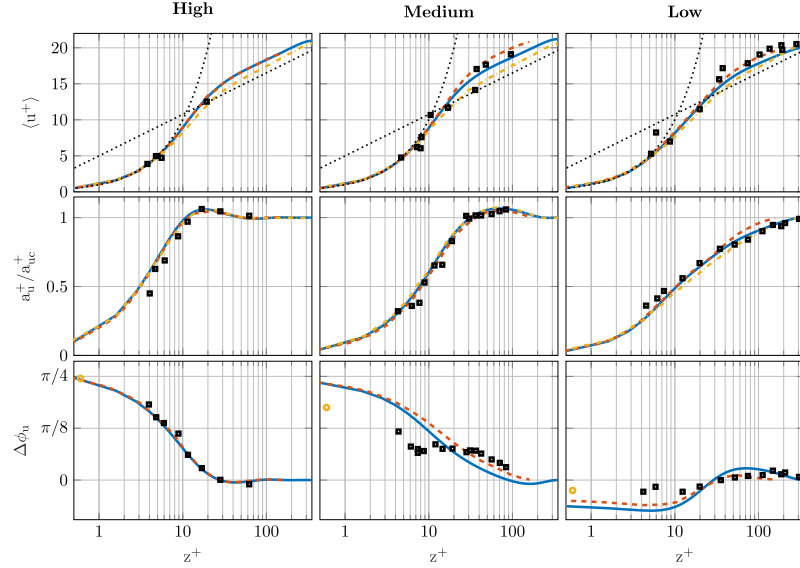


Fig. 3. Triple decomposition of wall distance dependent dimensionless velocity ($\langle u^+ \rangle_p = \langle u^+ \rangle + a_{u+} \cos(\omega t + \phi_u)$): local mean velocity, amplitude and phase difference. Results of the present study (—) are compared to CP [17] (---), SP [13] (----, ●) and TBB [29] (■) for high ($I_s^+ = 7$), medium ($I_s^+ = 14$) and low ($I_s^+ = 35$) frequency.

analogy with the Prandtl number dependency still holds and the temperature profiles can be predicted accurately by classical steady flow correlations. Wang and Lu showed that the thermal penetration length is strongly dependent on the fluid properties as described by the Prandtl number. They studied the response of a turbulent flow of $\text{Nu} \approx 28$ and a series of Prandtl numbers $\text{Pr} = 0.1, 1, 10, 50$, and 100 to harmonic velocity fluctuations. Unfortunately, Wang and Lu do not provide the data in a way that is easy to reproduce and comparisons can only be performed qualitatively. The results of Cardenas [17] are obtained at a lower turbulent Reynolds number and thus the range of the non-dimensional wall distance differs. As a consequence, this also limits the validation to qualitative conclusions.

Fig. 4 shows the triple decomposition components computed from the present LES plotted in wall normal direction. The plot on the left shows the time independent component for the three frequency regimes. It is evident that this component is relatively insensitive to the harmonic forcing of the flow, in agreement with the results of Wang and Lu and Cardenas. Concerning the organized pulsations given by the temperature amplitude a_T^+ and marked on the right side of the figure, the penetration length of

the perturbations is also inversely proportional to the forcing frequency. However, the magnitude of the temperature oscillations strongly depends on the forcing frequency and the reference Nusselt number. At high frequencies, the oscillations are marginal. For the small Prandtl and Nusselt numbers used in the present investigation, the temperature oscillations become relevant only at lower frequencies. This is in agreement with the observations of Wang and Lu [15] and Cardenas [17].

Beside the first-order flow statistics presented above, second-order Reynolds shear stresses are validated against the benchmark case ($I_s^+ = 7$) by Scotti and Piomelli [13] in Fig. 5. The time-averaged Reynolds stress is defined as $R_{ij}^+ = \overline{u_i^+ u_j^+}$, where the velocity u is made dimensionless by u_τ . The harmonic pulsation amplitude is denoted by A_{ij}^+ . Again, the shear stresses of the LES capture the DNS-benchmark quite well. Largest deviations show at wall-normal direction (R_{33}^+ and A_{33}^+). This corresponds well to the findings of Scotti and Piomelli [13].

In Fig. 6, the turbulent kinetic energy spectrum E^+ is presented as another important second-order benchmark. The two-dimensional spectrum is calculated as the integral over a circle in

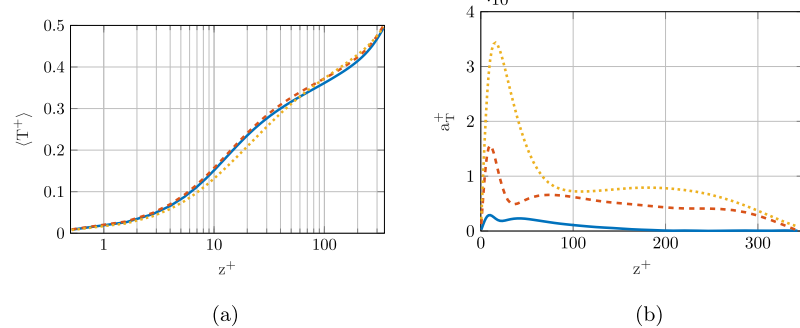


Fig. 4. Local temperature distribution over the channel height at high (—), medium (---) and low (----) frequency. (a) Mean temperature $\langle T^+ \rangle$, (b) Temperature amplitude a_T^+ .

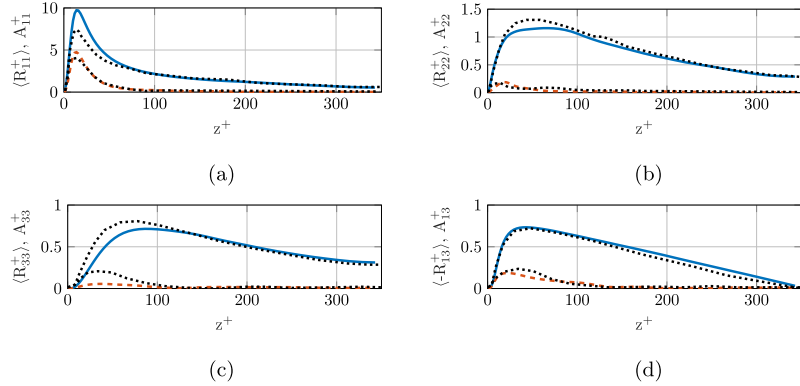


Fig. 5. Time-averaged Reynolds shear stress R_{ij}^+ (—) and its harmonic amplitude A_{ij}^+ (---) against DNS-data (· · · · ·) by [13], $I_s^+ = 7$. (a) R_{11}^+ and A_{11}^+ , (b) R_{22}^+ and A_{22}^+ , (c) R_{33}^+ and A_{33}^+ , (d) R_{13}^+ and A_{13}^+ .

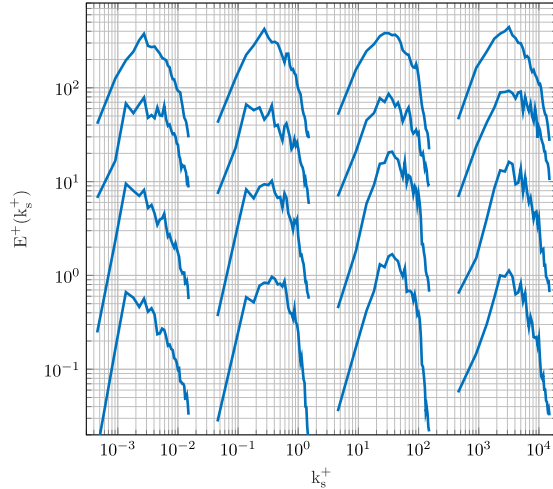


Fig. 6. Two-dimensional turbulent kinetic energy spectra during one cycle, $I_s^+ = 7$. Left to right: phase angles $\varphi = 0, \pi/2, \pi$ and $3\pi/2$ with an offset by a factor of 100. Bottom to top: xy -planes at $z^+ = 8, 13, 32$ and 108 with an offset by a factor of 10.

the xy -plane such that $\lambda_s^+ = \lambda_x^+ + \lambda_y^+$, where λ^+ is the non-dimensional wave number. Results are presented at four equi-spaced times of a cycle ($\varphi = \omega t - 2\pi n$, no specification of phase lag is given in [13]) at for different heights z^+ . Unfortunately, no qualitative comparison to the results of Scotti and Piomelli [13] is possible, as they do not specify dimensional values of the wavelength. However, a qualitative comparison shows good agreement. In particular, the cutoff lies outside the inertia range which justifies the dynamic LES approach. Likewise, the wavy characteristics of the magnitude in the energy spectrum E^+ is reproduced. This holds especially in regions close to the wall.

Based on the good agreement with the data of previous investigations, it can be stated with confidence that the test case setup and LES solver used in the present study reproduce the hydrodynamic and thermal behavior of turbulent pulsating flows with good accuracy.

4. Intermediate relaminarization of current dominated flow

A closer examination of the ensemble averaged flow velocities for three frequencies $I_s^+ = 7, 14$ and 35 is given in Fig. 7. For the center-plane velocity u_c^+ (Fig. 7a) it is apparent that the profiles

of high and medium frequencies almost match, while the pulsating velocity amplitude is slightly larger at the lower frequency level. Regarding the velocity in the cell closest to the wall ($z^+ = 0.5$, Fig. 7b) a sine pulsation is again found for high and medium frequency, showing a phase lag of $\Delta\phi_u \approx \pi/4$ to the center flow. However, at low frequency $I_s^+ = 7$, the periodic velocity clearly deviates from a sine wave in the wall region, with a steep velocity increase around the assumed position of the sine oscillation maximum.

Searching for an explanation of this effect, in Fig. 8 the prevailing flow regime is evaluated by the wall distance resolved ensemble average of the velocity turbulent energy k^+ in span-wise y -direction. At high frequency $I_s^+ = 7$ (left) only marginal changes of the flow structure are evident, as k_y^+ remains almost constant in all characteristic flow regions (viscous sublayer, buffer layer, log-law region and outer layer). In the case of medium frequency $I_s^+ = 14$, increasing temporal changes of k_y^+ begin to develop within the buffer layer at $z^+ = 10.1$ and the log-law region at $z^+ = 35.9$ and 100.4 . Lastly, at low frequencies $I_s^+ = 35$, a strongly transient behavior of the turbulent energy is displayed: As the flow velocity decreases, the turbulent energy decreases to values close to $k_y^+ = 0$. This behavior is indicative of a gradual relaminarization of the flow, which is made possible by intervals of low flow velocities due to the low frequency [14,33–37]. Once the momentum driven flow velocity increases, a sudden increase in the span-wise kinetic energy k_y^+ occurs, predominately in the log-law region. This behavior is interpreted as a transition from a laminar to a turbulent flow regime.

We are aware that neither the ensemble averaged span-wise turbulent energy $\langle k_y^+ \rangle_p$, nor the sub-grid scale energy $\langle k_{sgs}^+ \rangle_p$ as it is used in Section 5, describe the turbulent flow properties in an extensive manner [38]. However, they provide a meaningful reference for a first interpretation of flow regimes and turbulence intensity as it is intended in the present study. Comparison of the two values shows good qualitatively agreement, particularly phase angles of characteristic points as minima am maxima match well. For future studies, a more detailed investigation of contributing turbulence scales is of interest.

Fig. 9 further substantiates this argument, showing instantaneous span-wise flow velocities at four instances of time: At the first instance, corresponding to $\varphi = 1/4\pi$, only minor fluctuations are present throughout the channel. Especially within the outer layer, where wall effects are smallest, almost no span-wise flow occurs, indicating an almost laminar flow. Within the short period of time between $\varphi = 1/4\pi$ and $1/2\pi$ a distinct flow transition

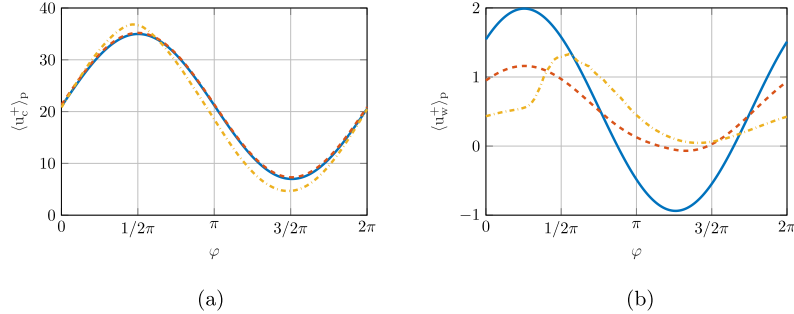


Fig. 7. Ensemble average of velocity u^+ for high (—), medium (---) and low (---) forcing frequency at $l_s^+ = 7, 14$ and 35 respectively. Pulsation amplitude $\epsilon \approx 0.7$. (a) Center-plane, (b) Near-wall region at $z^+ = 0.5$.

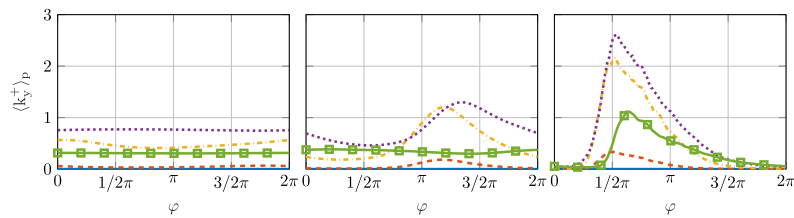


Fig. 8. Ensemble averaged turbulent energy k^+ in span-wise y -direction at high (left), medium (center) and low (right) frequency in various layers of the flow (viscous sublayer ($z^+ = 0.5$, —)), buffer layer ($z^+ = 10.1$, ---), log-law region ($z^+ = 35.9$, - - -) and outer layer ($z^+ = 100.4$, ·····) and outer layer ($z^+ = 342.9$, - - - -).

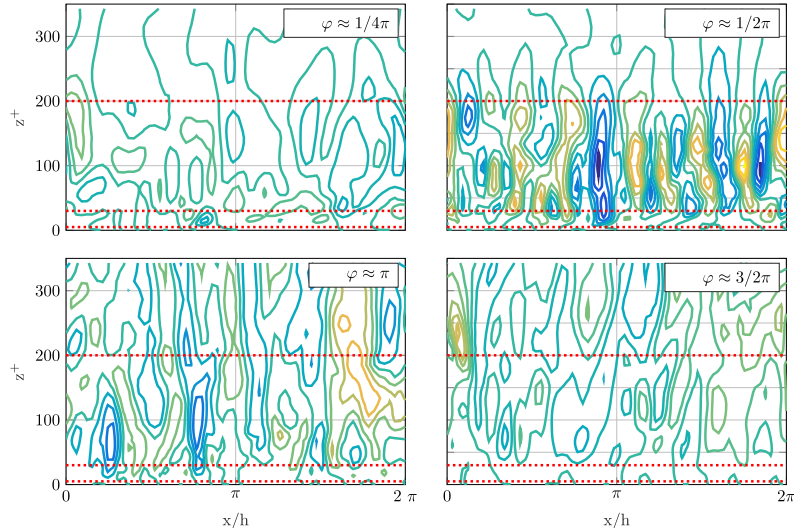


Fig. 9. Contours of instantaneous span-wise velocity fluctuations a_{xy}^+ at phase angles $\varphi = 1/4\pi, 1/2\pi, \pi$ and $3/2\pi$ for the low frequency case. Dotted lines indicate the regions of outer layer ($z^+ > 200$), log-law region ($30 < z^+ < 200$) and buffer layer ($z^+ < 30$).

occurs in the log-law region and the adjoining buffer layer. Meanwhile the outer layer remains mostly untouched by the transition. At $\varphi = \pi$ span-wise velocity fluctuations begin to extend into the outer layer. With decreasing flow velocities, the dissipation of turbulent fluctuations throughout the channel is initialized and clearly visible at $\varphi = 3/2\pi$. No distinct transition from high turbulence to a laminar-like flow is apparent. Instead, the relaminarization appears as a gradual process over the remaining 87.5% of the period from $\varphi = 1/2\pi$ to $1/4\pi$.

Regarding the velocity close to the wall shown in Fig. 7b, the effect of the sudden increase of stream-wise velocity coincides with the flow transition observed in Fig. 8 and 9: the transition from laminar to turbulent occurs quickly in the buffer layer and the log-law region between $\varphi = 1/4\pi$ and $1/2\pi$. Driven by the transition, turbulent momentum transport is enabled from higher flow velocity regions of the inner channel. Likewise, the higher velocity amplitude in Fig. 7a is explained by lower frictional resistance during the prevalence of laminar flow characteristics [39].

Based on the examination of changes in flow regimes, the following sections evaluate the influence of forcing frequency and pulsation amplitude on EHT.

5. Enhanced heat transfer at moderate pulsation amplitudes

5.1. Influence of forcing frequency

The temporal average of the EHT $\hat{\eta}$, as it is defined in Eq. (26), is depicted in Fig. 10a. For high and low frequencies $I_s^+ = 7$ and $I_s^+ = 35$, respectively, an overall negative EHT and thus a reduction of heat transfer in the pulsating flow occurs. Furthermore, EHT decreases monotonously with increasing pulsation amplitudes. Within a range of medium forcing frequencies, a slight enhancement of the overall heat transfer up to $\hat{\eta}_{max} \approx 7.5\%$ is observed. For a more detailed understanding of the influence of frequency, additional medium level frequencies besides $I_s^+ = 14$ are evaluated, as proposed by Scotti and Piomelli [13]. All curves in the medium frequency range share the characteristics of an initial increase in EHT. A maximum is shown at pulsation amplitudes close to center-plane flow reversal ($\epsilon = 1$), before further increase in pulsation amplitude leads to a reduction of EHT $\hat{\eta}$.

The circles in Fig. 10a denote simulations with a dimensionless momentum amplitude $a_{px}^+ = 5000\omega^+$, corresponding to the value proposed and investigated by Scotti and Piomelli [13]. In Fig. 10b, the EHT of these cases is evaluated as the ensemble average over several pulsation period to display phase dependent characteristics: At high frequencies ($I_s^+ = 7$), the ensemble averaged EHT $\langle \eta \rangle_p$ remains almost constant over the complete period, describing a shallow harmonic sine oscillation. With a decrease in frequency, the amplitude of the oscillation shifts into the positive EHT domain, leading to a temporal averaged positive EHT as shown in Fig. 10a. The moment of the local maximum moves to an earlier phase angle, while the clear characteristics of a sine wave slightly regresses up to a Stokes layer of $I_s^+ = 14$. The examination of the timing of maximum heat transfer indicates the period of temporal flow velocity minimums (compare Fig. 7a and b).

The observation of maximum heat transfer at periods close to flow reversal with maximum turbulence agrees well with experimental investigations: Dec and co-workers [5–8] also identified turbulence in the shear layer to be responsible for the enhanced heat transfer during times of flow reversal. In addition, they emphasize the effect of strong transverse convection. The mechanism that generates the convection could neither be elucidated by Dec and co-workers (secondary flows or coherent vortex structures), nor it is observed in the numerical setup of this study. Comparison to studies of Habib et al. [9] and Hemida et al. [10] are limited, as the setups under investigation differ (e.g. spatial developing laminar flow vs. transient turbulent flow).

At the lowest frequency ($I_s^+ = 35$), clear differences to the other cases are apparent: A pronounced shift to negative values of EHT $\langle \eta \rangle_p$ is accompanied by a distortion of the sine characteristics. Recalling the evaluation of flow regimes in Section 4, the steep positive incline in EHT corresponds to the period of flow transition from laminar to turbulent characteristics. This conforms well with the assumption of increased convective heat transfer in turbulent flows. The subsequent strong decline with large negative EHT values far below those discussed at higher frequencies is reasoned by the decreased heat transfer connected to laminar flows.

5.2. Influence of pulsation amplitude

While Section 5.1 mainly focused on the impact of frequency on EHT, this section studies the impact of pulsation amplitudes in a more detailed manner. Therefore, the medium forcing frequency of $I_s^+ = 14$ ($Wo \approx 35.4$), which shows maximum EHT performance among the cases considered in the present study (see Fig. 10a), is selected. This observation coincides well with the results of Wang and Zhang [16], who found identified an optimum Womersley number $Wo_{WZ} \approx 40$ at which heat transfer is maximally enhanced. Recall the importance of flow regime and turbulence intensity as remarked in Section 4.

Five distinct velocity amplitudes ($\epsilon = 0.5, 0.7, 0.8, 1.0$ and 1.2) are compared, where the case of $\epsilon = 0.7$ corresponds to the pulsation amplitudes studied by Scotti and Piomelli [13] and which was already presented in the validation study in Section 3. In Fig. 11a and b the ensemble averaged velocity at the center-plane and in the wall-closest cell ($z^+ = 0.5$) are shown. Compared to abrupt changes as observed at low frequencies (Fig. 7), a sine wave behavior prevails, indicating no sudden transition from laminar to turbulent flow characteristics. This assessment is also supported by the turbulent kinetic sub-grid scale energy k_{sgs}^+ within the buffer layer, given in Fig. 11c: no abrupt increase of turbulent energy is evident. However, pulsation amplitude has clear effect on sub-grid scale energy, and thus the intensity of turbulence: After times of above average flow velocity, the turbulent energy between the buffer layer and the log-law region increases to its peak, while periods of below average flow velocity coincide with a decrease in turbulent energy. An increase in pulsation amplitude is associated with higher peaks as well as lower minima in turbulent energy. Considering temporal average, the changes in turbulent energy are only marginal, as it is indicated by the markers on the right side of Fig. 11c.

Finally, the ensemble averaged EHT $\langle \eta \rangle_p$ is illustrated in Fig. 11d. In a qualitative evaluation, periods of high turbulence are almost immediately followed by a positive EHT and vice versa, indicating a slight time lag between the turbulent kinetic energy k_{sgs}^+ and the enhancement in heat transfer η . The degree of turbu-

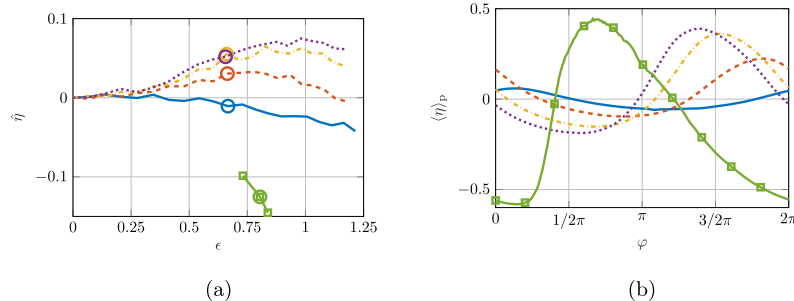


Fig. 10. Enhancement of heat transfer η for forcing frequencies corresponding to $I_s^+ = 7$ (—), $I_s^+ = 10$ (---), $I_s^+ = 12.5$ (—·—), $I_s^+ = 14$ (···) and $I_s^+ = 35$ (■—■). (a) Temporal average, (b) Phase related at $\epsilon \approx 0.7$.

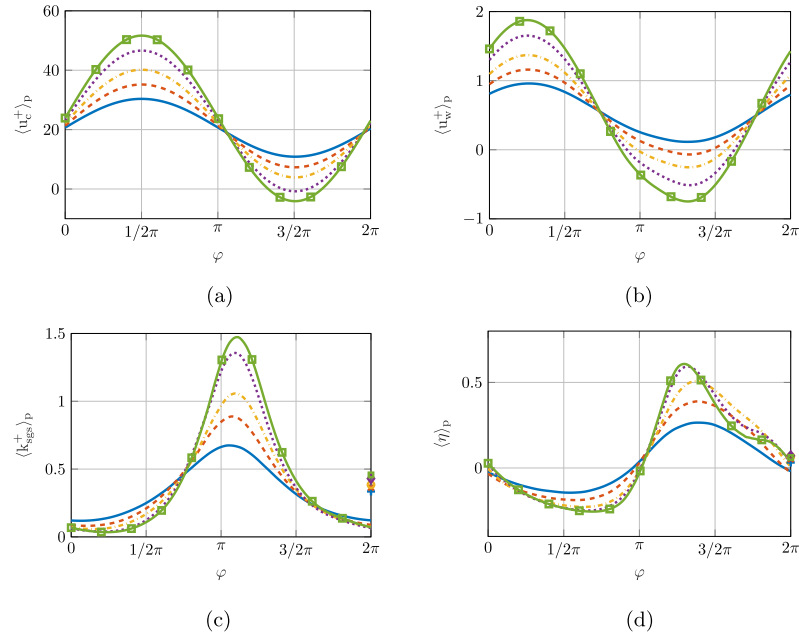


Fig. 11. Phase related characteristics at medium frequency of $l_s^+ = 14$ for various pulsation amplitudes: $\epsilon = 0.5$ (solid blue line, solid blue circle), $\epsilon = 0.7$ (dashed red line, open red star), $\epsilon = 0.8$ (dash-dot yellow line, open yellow circle), $\epsilon = 1.0$ (dotted purple line, solid purple diamond) and $\epsilon = 1.2$ (solid green line, solid green square). (a) Center-plane velocity, (b) Near-wall velocity at $z^+ = 0.5$, (c) Turbulent kinetic sub-grid scale energy k_{sgs}^+ in the buffer layer at $z^+ = 35.9$, (d) Enhanced heat transfer $\langle \eta \rangle_p$.

lence between the buffer layer and the log-law region shows qualitative accordance with the EHT.

For a more quantitative evaluation, the ratio of maximum and minimum EHT amplitudes to the corresponding sub-grid kinetic energy k_{sgs}^+ in the log-law region at $z^+ = 35.9$ is shown in Fig. 12. The plot underlines the direct influence of turbulence on the enhancement of convective heat transfer. Overall, a close to linear relation is found between the unresolved turbulent energy and the heat transfer, indicated by the approximately constant ratios. This correlation does not only hold for the maximum and minimum values as already qualitatively reported, but is also valid for the overall temporal averaged heat transfer, which is the key parameter of interest in the present study. Since the variation of time-averaged turbulence as a consequence of increasing pulsation amplitude is only marginal, an almost constant overall EHT $\hat{\eta}$ presents a plausible result, recalling that enhancement in heat transfer is strongly connected to intensity of turbulence. The absence of generation

of turbulence and its gradual dissipation during periods of low flow velocity, that are predominately present at times close to flow reversal, leads to almost no increase in time-averaged turbulence for increasing pulsation amplitudes ϵ .

As a consequence, the present study is extended to larger pulsation amplitudes to diminish the effect of slow flow velocities by increasing negative flow velocities. In the following section, the accompanying higher degree of turbulence and its correlation to the EHT are presented.

6. Extension to large pulsation amplitudes

As outlined in the previous section, there are strong indications that the effect of large EHT is connected to high pulsation amplitudes with significant flow reversal: Previous studies mainly focused on flows approaching flow reversal. However, the previous findings of this study show that periods of low flow velocities, as they primarily exist in flows close to flow reversal, introduce time-spans of absence of turbulence generation. Thus, one novelty this study has shown is that flows close to flow reversal are characterized by a net dissipation of turbulent energy. It follows that the time-averaged turbulence intensity stays almost constant for a range of increasing pulsation amplitudes. Recalling the coupling of turbulence and enhancement in heat transfer (see Section 5.2), an extension of this study to higher pulsation amplitudes is proposed. The presence of large reversed flow velocities shortens the periods of low flow velocities and thus prolongates periods of turbulence generation. Wang and Zhang [16] followed a similar approach and studied comparable large pulsation amplitudes in a tube. However, they applied a RANS approach which was judged to be insufficient for the problem at hand [14]. In this section, results for flows with strongly pronounced flow reversal ($\epsilon > 1.2$ up to $\epsilon \approx 6$) are presented at $l_s^+ = 14$.

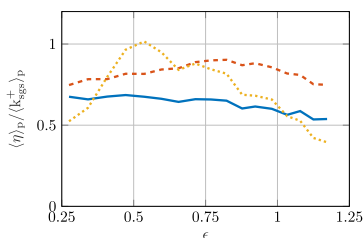


Fig. 12. Ratio of maximum (solid blue line), minimum (dashed red line) and mean (dash-dot yellow line) EHT η and corresponding maximum, minimum and mean sub-grid scale kinetic energy k_{sgs}^+ in the log-law region ($z^+ = 35.9$) for a range of pulsation amplitudes, $l_s^+ = 14$ (e.g. $\max(\langle \eta \rangle_p) / \max(\langle k_{sgs}^+ \rangle_p)$).

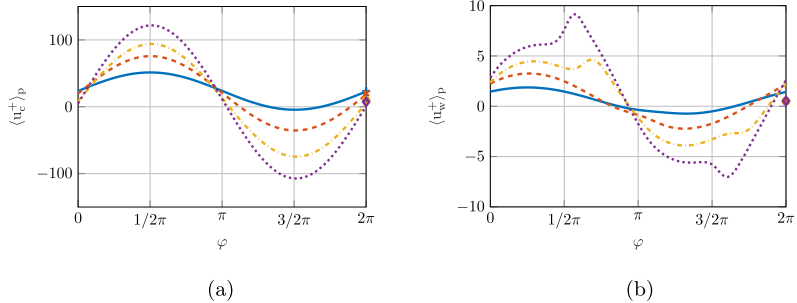


Fig. 13. Ensemble averaged flow velocity u^+ at $l_s^+ = 14$ for pulsation amplitudes: $\epsilon = 1.4$ (—, +), $\epsilon = 2.8$ (—, *, ■), $\epsilon = 4.3$ (—, ○), and $\epsilon = 5.8$ (—, ♦). (a) Center-Plane, (b) Near-wall region at $z^+ = 0.5$.

In Fig. 13 the ensemble averaged velocity at the center-plane and close to the wall at $z^+ = 0.5$ are plotted. Four different pulsation amplitudes are selected, starting at $\epsilon = 1.4$ (slight effects of flow reversal) and ranging up to $\epsilon = 5.7$ (mainly pulsation dominated flows). At the center-plane, a regular sine-wave shape of the velocity is present. On the other hand, close to the wall, the ensemble averaged velocity fluctuations are of more irregular shape for high pulsation amplitudes. As described in Section 4, flow transitions and altered momentum transfer from the inner channel to the wall region result from this behavior.

Furthermore, with increasing pulsation amplitudes the mean flow velocity at the center-plane decreases significantly from approximately 20 to 8 (compare temporal average markers on the right side of Fig. 13a). This results from the periodic computational setup, where the time-averaged pressure gradient maintains the mean flow inspite of the wall shear stress. With the specified turbulent Reynolds number $Re_t = 350$ this pressure gradient is constant. Expressing the skin friction as the gradient of the averaged wall velocity (markers on the right side of Fig. 13b), it is found that this value meets the requirement of being constant over the full range of pulsation amplitudes. Therefore, higher wall shear stress induced by an increase in average turbulence causes the decrease of mean flow velocity. The corresponding degree of turbulence is indicated by the kinetic energy in y -direction as show in Fig. 14. For the cases studied before ($0 < \epsilon < 1.2$), only a negligible change of the mean center-plane flow velocity was observed, as also the overall degree of turbulence was only marginally affected (compare case of $\epsilon = 1.4$ in Fig. 14 where span-wise velocity perturbations are still small). Note that different boundary conditions were used by Wang and Zhang [16] where they modeled the entire tube geometry instead of a periodic section. Thus, they applied a fixed volume flow rate instead of the local pressure gradient.

For a frequency corresponding to $l_s^+ = 14$, the amplitude-dependent enhancement in heat transfer is shown in Fig. 15. Up to a pulsations of $\epsilon \approx 2$, only minor EHT exists. This range coincides with the previous investigations at medium amplitudes up to slight flow reversal. As expected previously, a local minimum

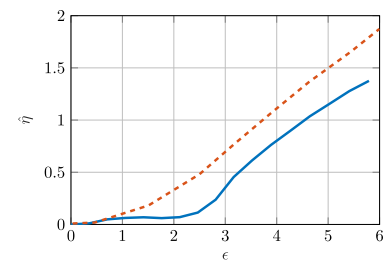


Fig. 15. Time averaged enhancement of heat transfer η over the pulsation amplitude at $l_s^+ = 14$ (—). For reference, results of Wang and Zhang [16] are displayed (—).

exists ($\epsilon \approx 2$). For larger pulsation amplitudes with $\epsilon > 2$ a significant increase in EHT occurs. A doubling of heat transfer compared to the turbulent reference case without pulsation is reached at $\epsilon \approx 4.5$.

The results by Wang and Zhang [16] are also included in Fig. 15. The reader is reminded of the different scenarios under investigation: Wang and Zhang studied a spatially developing pipe flow. On the contrary, the objective of the present study is to investigate the enhanced heat transfer in a fully developed pulsatile turbulent channel flow. Effects of relaminarization and subsequent transition to turbulence may be connected to characteristics of developing flows. Further discrepancies between the configurations are the two-dimensional RANS approach with a fixed flow velocity at the inlet (vs. a pressure gradient driven flow). Thus a 1:1 correspondence should not be expected. Nevertheless, in terms of non-dimensional characteristics, the two cases compare remarkably well: Wang and Zhang apply a different definition of the Reynolds number, yielding a value of $Re_{WZ} = 25000$ whereas the problem under investigation corresponds to $Re_{WZ} = 24845$. The frequency is connected to the Womersley number, which is $Wo_{WZ} = 40$ in the work of Wang and Zhang, while $Wo = 35.4$ for the present case at $l_s^+ = 14$. Qualitatively, the results of both studies agree: At high

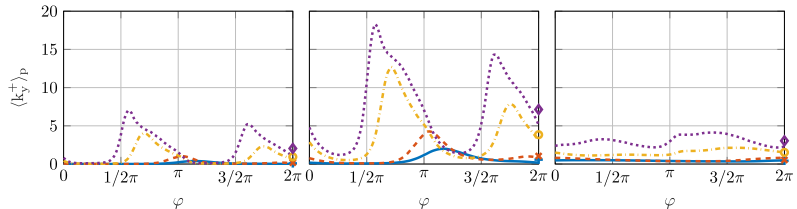


Fig. 14. Ensemble averaged turbulent kinetic energy k^+ in span-wise direction y at $l_s^+ = 14$ in buffer layer ($z^+ = 10.1$, left), log-law region ($z^+ = 35.9$, center) and outer layer ($z^+ = 342.9$, right) for four high pulsation amplitudes: $\epsilon = 1.4$ (—, +), $\epsilon = 2.8$ (—, *, ■), $\epsilon = 4.3$ (—, ○), and $\epsilon = 5.8$ (—, ♦).

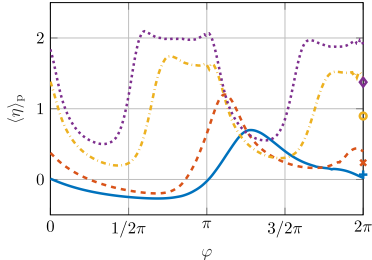


Fig. 16. Ensemble averaged enhancement of heat transfer η at high pulsation amplitudes: $\epsilon = 1.4$ (solid line, \diamond), $\epsilon = 2.8$ (dashed line, $*$), $\epsilon = 4.3$ (dash-dot line, \circ) and $\epsilon = 5.8$ (dotted line, \blacklozenge), $t_c^+ = 14$.

pulsation amplitudes, a significant increase in convective heat transfer is predicted, while small pulsation amplitudes only lead to marginal enhancement up to 6%. However, the overall enhancement of the present study is smaller than that reported by Wang and Zhang [16]. In addition, between $\epsilon \approx 1$ and 2, the small local decrease in EHT η is not found by Wang and Zhang [16]. In laboratory scale, Perry and Culick [4] reported EHT proportional to the oscillation amplitude. This characteristic also shows in the results of the present study for pulsation amplitudes $\epsilon > 2.5$.

A more precise view of the period at which the enhancement occurs is provided in the ensemble averaged depiction in Fig. 16: Over the pulsation period the enhancement is not uniform, but there are sections of significant increase and times of minor increase (or even decline) for the four exemplary amplitudes under investigation. Again, a strong link between turbulence and EHT is observed. Especially accounting for the log-law region at $z^+ = 35.9$ (Fig. 14, center), periods of high EHT relate to periods of high turbulence and vice versa. For lower amplitudes ($\epsilon = 1.4$), only one peak in EHT exists. This is explained by low turbulence at periods close to flow reversal when velocity fluctuations recede while the fluid is close to rest. With increasing pulsation amplitudes, these periods of rest are quickly passed and instead, times of high reverse flow velocity establish. Thus a second peak in turbulent energy as well as EHT develops at times of maximum flow reversal.

Summarizing, at high pulsation amplitudes the causes of EHT are twofold: firstly, increased flow velocity and correlating turbulence enhances the convective heat transfer and secondly, long periods of flow velocities close to rest are replaced by times of large (negative) flow velocities.

7. Conclusions

This study investigates by Large Eddy Simulation (LES) the impact of standing acoustic waves on convective heat transfer mechanisms in turbulent channel flows. In accordance with the literature, where the largest enhancement of heat transfer is reported to occur at locations of maximum velocity fluctuations, the domain of investigation is set at a pressure node. Assuming large acoustic wave lengths compared to the size of the simulation domain, an incompressible simulation approach is justified. The use of cyclic boundary conditions and a momentum driven flow allows for a fully developed turbulent flow profile.

The LES approach employed is validated successfully against the DNS data of Scotti and Piomelli [13]. Compared to the work of Cardenas [17], flows with larger turbulent Reynolds numbers are included in the present study. Besides the dynamic determination of the localized turbulent viscosity v_{sgs} , a layer-averaged calculation of the turbulent Prandtl number Pr_{sgs} is applied. Simu-

lations with constant Prandtl number $\text{Pr}_{\text{sgs}} = 0.9$, which where performed for reference, show that this procedure affects the predicted heat transfer only marginally. Thus the choice of a constant turbulent Prandtl number is justified in further investigations. Overall the flow field characteristics show very good agreement with the literature.

The maximum temporal averaged enhancement of heat transfer (EHT) reported in the first part of the present study reaches values of up to 7.5% and occurs at medium pulsation frequencies and amplitudes close to flow reversal. The enhancement remains far below the increase of more than 100% reported in experiments (e.g. [3]). Evaluation of the phase dependent heat transfer shows momentary enhancement of more than 60%.

A detailed investigation reveals a strong correlation between EHT and the respective momentary flow regime, in particular its degree of turbulence: At times of high turbulence, especially in the log-law region of the flow, heat transfer is enhanced, while the prolonged absence of large velocity gradients during periods of flow stagnation close to flow reversal induces a decline in heat transfer. This observation presents an important novelty and suggests further study. It also aligns with the hypothesis of Dec and co-workers [5–8] that increased turbulence in the shear layer is responsible for enhanced heat transfer. The reported transverse flows at times of flow reversal were not reproduced in the current study.

Reassessing the problem at hand with these findings, the examination of larger pulsation amplitudes presents the logical extension and a central novelty of the present study: In the second part, flows with forcing resulting in relative pulsation amplitudes $\epsilon \gg 1$ are investigated to account for increased turbulence. Turbulence activity is enhanced because on the one hand flow velocity amplitudes are higher, while on the other hand periods during which the fluid is nearly at rest are shorter. The simulations at high amplitudes confirm the correlation between turbulence and EHT. Starting at $\epsilon \approx 2$, a continuous and significant enhancement of heat transfer η is found. At $\epsilon \approx 4.5$, the enhancement exceeds an increase of 100%. Thereby, conclusions from the literature, which report enhanced heat transfer as a highly relevant mechanism in turbulent pulsating flows, are reproduced for the first time in an LES based computational study.

In future studies, the contribution of the resolved turbulent fluctuations to the enhancement of heat transfer is of great interest. In particular, the impact of participating turbulence scales and the relevance of flow regions defined by the wall normal distance z^+ may contribute to a coherent understanding of the phenomena. Furthermore, the non-dimensional results presented in this study are to be transferred and evaluated under the physical conditions of a rocket combustion chamber.

Declaration of Competing Interest

The authors declared that there is no conflict of interest.

Acknowledgments

Financial support has been provided by the German Research Foundation (Deutsche Forschungsgemeinschaft – DFG) in the framework of the Sonderforschungsbereich Transregio 40. Computational resources have been provided by the Leibniz Supercomputing Center (LRZ).

References

- [1] D.T. Harrje, F.H. Reardon, Liquid Propellant Rocket Combustion Instability, Technical Report NASA-SP-194, Scientific and Technical Information Office, National Aeronautics and Space Administration, Washington, DC, U.S.A, 1972.

- [2] P.K. Tang, D.T. Harrje, W.A. Sirignano, Experimental verification of the energy dissipation mechanism in acoustic dampers, *J. Sound Vib.* 26 (2) (1973) 263–276.
- [3] D.T. Harrje, *Heat Transfer In Oscillating Flow*, 3-g, Departement of Aerospace and Mechanical Science, Princeton University, 1967.
- [4] E.H. Perry, F.E.C. Culick, Measurements of wall heat transfer in the presence of large-amplitude combustion-driven oscillations, *Combust. Sci. Technol.* 9 (1–2) (1974) 49–53, <https://doi.org/10.1080/00102207408960336>.
- [5] J.E. Dec, J.O. Keller, Pulse combustor tail-pipe heat-transfer dependence on frequency, amplitude, and mean flow rate, *Combust. Flame* 77 (3–4) (1989) 359–374, [https://doi.org/10.1016/0010-2180\(89\)90141-7](https://doi.org/10.1016/0010-2180(89)90141-7).
- [6] J.E. Dec, J.O. Keller, Time-resolved gas temperatures in the oscillating turbulent flow of a pulse combustor tail pipe, *Combust. Flame* 80 (1990) 358–370.
- [7] J.E. Dec, J.O. Keller, V.S. Arpacı, Heat transfer enhancement in the oscillating turbulent flow of a pulse combustor tail pipe, *Int. J. Heat Mass Transf.* 35 (9) (1992) 2311–2325, [https://doi.org/10.1016/0017-9310\(92\)90074-3](https://doi.org/10.1016/0017-9310(92)90074-3).
- [8] V.S. Arpacı, J.E. Dec, J.O. Keller, Heat transfer in pulse combustor tailpipes, *Combust. Sci. Technol.* 94 (1993) 131–146.
- [9] M.A. Habib, A.M. Attya, A.I. Eid, A.Z. Aly, Convective heat transfer characteristics of laminar pulsating pipe air flow, *Heat Mass Transf.* 38 (3) (2002) 221–232, <https://doi.org/10.1007/s002310100206>.
- [10] H.N. Hemida, M.N. Sabry, A. Abdel-Rahim, H. Mansour, Theoretical analysis of heat transfer in laminar pulsating flow, *Int. J. Heat Mass Transf.* 45 (8) (2002) 1767–1780, [https://doi.org/10.1016/S0017-9310\(01\)00274-5](https://doi.org/10.1016/S0017-9310(01)00274-5).
- [11] E. Lundgren, U. Markstein, A. Holst, 2003. Enhanced heat transfer in an oscillating pipe flow, in: 6th ASME-JSME Thermal Engineering Joint Conference TED-AJ03-1.
- [12] S. Thyageswaran, Numerical modeling of pulse combustor tail pipe heat transfer, *Int. J. Heat Mass Transf.* 47 (12–13) (2004) 2637–2651.
- [13] A. Scotti, U. Piomelli, Numerical simulation of pulsating turbulent channel flow, *Phys. Fluids* 13 (5) (2001) 1367.
- [14] A. Scotti, U. Piomelli, Turbulence models in pulsating flows, *AIAA J.* 40 (3) (2002) 537–544.
- [15] L. Wang, X.-Y. Lu, An investigation of turbulent oscillatory heat transfer in channel flows by large eddy simulation, *Int. J. Heat Mass Transf.* 47 (10–11) (2004) 2161–2172.
- [16] X. Wang, N. Zhang, Numerical analysis of heat transfer in pulsating turbulent flow in a pipe, *Int. J. Heat Mass Transf.* 48 (19–20) (2005) 3957–3970, <https://doi.org/10.1016/j.ijheatmasstransfer.2005.04.011>.
- [17] A. Cárdenas Miranda, Influence of Enhanced Heat Transfer in Pulsating Flow on the Damping Characteristics of Resonator Rings PhD Thesis, TU München, 2014.
- [18] T. Emmert, A. Cárdenas, W. Polifke, Low-order analysis of conjugate heat transfer in pulsating flow with fluctuating temperature, *J. Phys.: Conf. Ser.* 395 (2012), <https://doi.org/10.1088/1742-6596/395/1/012040>.
- [19] M.L. Munjal, *Acoustics of Ducts and Mufflers*, John Wiley & Sons, 1987.
- [20] S.W. Rienstra, A. Hirschberg, An Introduction to Acoustics, Tech. Rep. IWDE 92-06, Eindhoven University of Technology, 2018.
- [21] T. Poinsot, D. Veynante, *Theoretical and Numerical Combustion*, RT Edwards, Inc., 2005.
- [22] A. Leonard, Energy cascade in large eddy simulations of turbulent fluid flows, *Adv. Geophys.* 18A (1974) 237–248.
- [23] W.-W. Kim, S. Menon, A new dynamic one-equation subgrid-scale model for large eddy simulations, in: 33rd Aerospace Sciences Meeting and Exhibit, American Institute of Aeronautics and Astronautics, Reno, NV, USA, 1995, 1–9, <https://doi.org/10.2514/6.1995-356>.
- [24] P. Moin, K. Squires, W. Cabot, S. Lee, A dynamic subgrid-scale model for compressible turbulence and scalar transport, *Phys. Fluids A* 3 (11) (1991) 2746–2757, <https://doi.org/10.1063/1.858164>.
- [25] D. Morar, Subgrid-scale heat flux modeling for large eddy simulation of turbulent mixed convection Ph.D. thesis, Karlsruher Institut of Technology, Karlsruhe, Germany, 2014.
- [26] M. Germano, U. Piomelli, P. Moin, W.H. Cabot, A dynamic subgrid-scale eddy viscosity model, *Phys. Fluids A* 3 (7) (1991) 1760, <https://doi.org/10.1063/1.857955>.
- [27] D.K. Lilly, A proposed modification of the Germano subgrid-scale closure method, *Phys. Fluids* 3 (A 4) (1992) 633–635.
- [28] B.R. Ramaprian, S.W. Tu, Fully developed periodic turbulent pipe flow. Part 2. The detailed structure of the flow, *J. Fluid Mech.* 137 (-1) (1983) 59, <https://doi.org/10.1017/S0022112083002293>.
- [29] S.F. Tardu, G. Binder, R.F. Blackwelder, *Turbulent channel flow with large-amplitude velocity oscillations*, *J. Fluid Mech.* 267 (1994) 109–151.
- [30] OpenFoam, OpenFoam v1706+, 2017.
- [31] J. Jiménez, Near-wall turbulence, *Phys. Fluids* 25 (10) (2013) 101302, <https://doi.org/10.1063/1.4824988>.
- [32] M.J. Lighthill, The response of laminar skin friction and heat transfer to fluctuations in the stream velocity, *Proc. Roy. Soc. London A* 224 (1954) 1–23, <https://doi.org/10.1098/rspa.1954.0137>.
- [33] D.C. Winter, R.M. Nerem, Turbulence in pulsatile flows, *Ann. Biomed. Eng.* 12 (4) (1984) 357–369, <https://doi.org/10.1007/BF02407780>.
- [34] L. Shemer, Laminar-turbulent transition in a slowly pulsating pipe flow, *Phys. Fluids* 28 (12) (1985) 3506, <https://doi.org/10.1063/1.865303>.
- [35] D. Greenblatt, E.A. Moss, Pipe-flow relaminarization by temporal acceleration, *Phys. Fluids* 11 (11) (1999) 3478–3481, <https://doi.org/10.1063/1.870205>.
- [36] B. Ünsal, F. Durst, Pulsating flows: experimental equipment and its application, *JSME Int. J. Ser. B* 49 (4) (2006) 980–987, <https://doi.org/10.1299/jsmeb.49.980>.
- [37] R. Trip, D.J. Kuik, J. Westerweel, C. Poelma, An experimental study of transitional pulsatile pipe flow, *Phys. Fluids* 24 (1) (2012) 014103, <https://doi.org/10.1063/1.3673611>.
- [38] I. Marusic, G.J. Kunkel, Streamwise turbulence intensity formulation for flat-plate boundary layers, *Phys. Fluids* 15 (8) (2003) 2461–2464, <https://doi.org/10.1063/1.1589014>.
- [39] S. Dhawan, R. Narasimha, Some properties of boundary layer flow during the transition from laminar to turbulent motion, *J. Fluid Mech.* 3 (04) (1958) 418, <https://doi.org/10.1017/S0022112058000094>.

Turbulence-induced enhancement of longitudinal heat transfer in oscillatory channel flow

S. van Buren and W. Polifke*

*Technical University of Munich, Department of Mechanical Engineering
85748 Garching b. München, Germany*

Abstract

An analytical correlation for longitudinal heat transfer in oscillatory flow was proposed by Kurzweg (1985). However, the treatment was limited to laminar flows, which motivates the extension of the analysis to the turbulent regime. In the present paper, turbulence-induced enhancement of longitudinal heat transfer in oscillatory channel flow is investigated by means of Large Eddy Simulation (LES) and supplemented with analytical considerations. Incompressible flow within a periodic computational domain is driven by an oscillating longitudinal pressure gradient, generating both laminar and turbulent flow characteristics. A wide range of oscillation amplitudes is considered, while a constant axial temperature gradient is maintained at the upper and lower channel walls. Kurzweg's analytical correlation for effective longitudinal thermal diffusivity is simplified to match the numerical setup.

The numerical results of laminar flows show excellent agreement with the analytical solution. In the turbulent case, enhanced longitudinal heat transfer emerges for flows characterized by the product of squared Womersley number α and Prandtl number Pr fulfilling $\alpha^2 \text{Pr} > \pi$. In order to explain this observation, the interaction of wall-confined thermal and hydrodynamics Stokes boundary layers is scrutinized, a simple correlation for the effective thermal diffusivity in laminar oscillatory flow is deduced from the analysis. This model

*Corresponding author
Tel.: +49-89-289-16195
E-mail address: vanburen@tfd.mw.tum.de

consolidates the two phenomena of wall-normal heat transfer and the longitudinal convective transport. Finally, the correlation is expanded to account for the impact of turbulence intensity on heat transfer. This quantification compares favorably against the wall-normal heat transfer, which reveals similar characteristic features.

Keywords: Enhanced longitudinal heat transfer; Turbulent channel flow; Large eddy simulation (LES)

1. Introduction

The performance of acoustic resonators is strongly influenced by the temperature of the working fluid. Large differences in temperature along the length of quarter-wave resonators further intensify the variation in performance [1]. Such physical conditions of extreme variation in local temperature are common attributes of rocket engine combustion chambers, where resonators are used as passive damping devices. Regenerative cooling of the chamber walls induces low temperatures in the backing of the cavity, opposing the hot combustion gas at the mouth of the resonator. The risk potential is obvious: Changes in damping characteristics induced by changes in local temperature (e.g. during the transient heating after ignition) jeopardize the acoustic stability and thus the integrity of the system. Therefore, the prediction and reliable understanding of heat transfer within the oscillating flow within the resonator tube is crucial for a comprehensive design process. Topical research activities by the industrial field of combustion dynamics illustrate the practical relevance of the problem at hand: Bothien and Wassmer [2] discussed the key importance of the prevailing temperature in the tube of a Helmholtz resonator to accurately predict its resonance frequency. Using a seeding particle method on a resonator with a cooling purging flow, Ćosić et al. [3] captured the time-averaged axial concentration gradient in the tube section. The analogy between molecular diffusion and heat transfer indicates a similar temperature gradient between the hot grazing flow in the combustion chamber and the cooled backing of the cavity.

Strong physical similarity exists between the tube section of an acoustic resonator and oscillatory flows through capillary tubes, which have been widely studied in the literature. In contrast to pulsating flows, oscillating flows show no time-averaged mean-flow. Numerous authors report enhanced axial dispersion of passive scalars – such as contaminations – induced by oscillations [4, 5, 6, 7]. The reported enhancement in transport of contaminations exceeds the pure molecular diffusion by orders of magnitude. The enhancement is attributed to the interaction between oscillating radial velocity profiles and local variation in concentration. Thus, an effective axial diffusion rate is formulated. All these studies are restricted to laminar flows.

Kurzweg [8] elaborated on the similarity between molecular diffusion and heat transfer. The only significant difference arises from a more complex definition of thermal boundary conditions. Indeed, Kurzweg and Zhao [9] experimentally confirm this hypothesis. They investigated heat transfer between two water reservoirs at different temperatures, connected by a bundle of capillary tubes. Inducing high frequency velocity oscillations to the fluid, heat transfer between the reservoirs increased by four orders of magnitude over the non-oscillating reference where conductivity was the only heat transfer mechanism. The axial velocity is defined by the unsteady harmonic solution of the Navier-Stokes-equations, known as Stokes problem. In a final step, Kurzweg [10] developed a comprehensive analytical model for the effective thermal diffusivity. Conjugate heat transfer from the oscillating fluid to the channel walls yields a generalized formulation with multiple input parameters. In its non-dimensional form, Kurzweg [10] identifies the *Womersley number* α as a key parameter, highlighting the diffusivity-reducing impact of both large and small Womersley numbers, respectively. Maximum longitudinal heat transfer is reported in dependence of the *Prandtl number* Pr at $\alpha^2 \text{Pr} \approx \pi$. Further researchers elaborated on the theoretical and experimental evaluation of the so-called “dream pipe” – a capillary heat transfer tube bundle (e.g. Kaviany [11, 12, 13] and Nishio et al. [14]).

In his concluding remarks, Kurzweg [10] emphasizes that his study is restricted to laminar flows and that ”the role of turbulence in such oscillating

flows with high ω (*angular oscillation frequency*) and Δx (*tidal displacement*) should receive special attention”.

The present study directly follows Kurzweg’s suggestion and expands on ”the role of turbulence”. Accounting for material properties of metal (channel wall) and air (fluid), the analytical correlation of Kurzweg [10] (Section 2.1) is simplified to match the setup under investigation (Section 2.2). This allows to impose Dirichlet boundary conditions at the wall/fluid interface. The investigation assumes an incompressible flow to focus only on diffusive effects contributing to enhanced heat transfer. Heat pump effects induced by thermoacoustic density fluctuations are neglected. Furthermore, evaporation of propellant is not considered. The reader is reminded of the potential relevance of latent heat and liquid-vapor two-phase flow (e.g. Miura et al. [15, 16]).

A validated Large Eddy Simulation (LES) approach is applied on a periodic channel domain [17] (Section 3.1). After additional validated against the analytical results for the laminar case (Section 3.2), the results (Section 4) are interpreted in the physical context of boundary layer interaction (Section 4.1). Special attention is given to the case of thin hydrodynamic boundary layers at high frequencies ($\alpha = 35.4$). The importance of the thermal penetration depth is elucidated. To quantify the effect of turbulence intensity on the effective thermal diffusivity, a definition of *enhancement of longitudinal heat transfer* $\varepsilon_{\text{turb}}$ (ELHT) is proposed. Based on considerations of a laminar case (Section 4.3.1), a *convective heat transfer coefficient* h_{turb} is carefully defined, such that it only depends on the oscillation amplitude (Section 4.3.2). The evaluation of this coefficient is discussed in the context of prior studies [17]. Finally, Section 5 summarizes the findings and offers conclusions of the study. All symbols used are specified in the appended nomenclature.

2. Analytical model definition

The numerical configuration applied in this study is designed in close analogy to the analytical approach presented by Kurzweg [10]. This choice combines

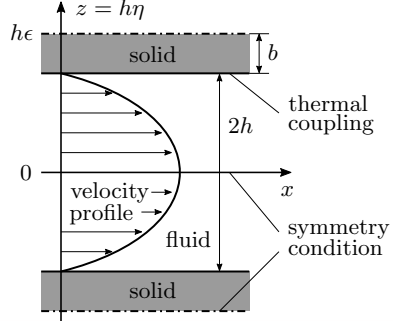


Figure 1: Geometry of fluid flow in between parallel channel walls as investigated by Kurzweg [10].

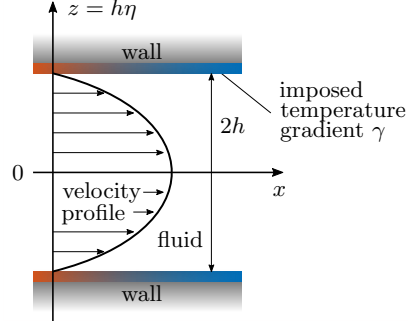


Figure 2: Simplified geometry with imposed wall temperature gradient, matching the computational setup.

two major advantages: First, the simulation results may be validated against the analytical solution for laminar flow. Second, the use of computational fluid dynamics (CFD) lifts the limitation of the analytical results to purely laminar flow characteristics. Closing this gap already reported by Kurzweg is the main objective of this study. Furthermore, there is close correspondence to the previous study by van Buren et al. [17], allowing to utilize an established and validated numerical setup.

This section summarizes the theoretical analysis by Kurzweg [10]. Based on the problem at hand, simplifications are suggested and exploited to map the boundary conditions of the three-dimensional simulation domain. In the last subsection, an overview of the numeric solver and its validation is given.

2.1. Laminar model of Kurzweg with conjugate heat transfer

In his paper from 1985, Kurzweg [10] presents a closed analytical formulation for the effective longitudinal thermal diffusivity κ_e in oscillating channel flow. The two-dimensional setup under investigation is sketched in Fig. 1: Two parallel solid walls confine a fluid channel of width $2h$ in z -direction. The non-dimensional position normal to the wall reads $\eta = z/h$ with the symmetry-line of the channel located at $z = \eta = 0$. Both walls are of thickness $2b$ and pe-

riodically adjoin neighboring fluid channels, yielding the indicated symmetry condition. The wall-to-channel ratio ϵ is an important geometrical parameter of the configuration:

$$\epsilon \equiv \frac{b+h}{h}. \quad (1)$$

The unsteady but harmonically oscillating stream-wise (x -direction) velocity profile $u_x(\eta, t)$ follows from the exact solution of the Navier-Stokes-equations. Known as "Stokes problem", neither initial nor axial boundary conditions are required due to temporal and stream-wise periodicity. This limits the approach to steady state oscillations (e.g. the system has overcome transient behavior from initial condition) and to locations x far away from changes geometry (e.g. from the inlet/outlet of the channel). Assuming a laminar flow, the axial velocity u_x is given by the real part of the harmonic oscillation

$$u_x(\eta, t) = u_0 f(\eta) e^{i\omega t} = u_0 \frac{i\lambda}{\alpha^2} \left[1 - \frac{\cosh(\sqrt{i}\alpha\eta)}{\cosh(\sqrt{i}\alpha)} \right] e^{i\omega t}, \quad (2)$$

where u_0 is a representative velocity, t the time, ω the angular frequency, $\alpha = h\sqrt{\omega/\nu}$ the Womersley number, ν the kinematic viscosity and ρ the density of the fluid. The non-dimensional pressure gradient is defined as $\lambda = |\partial p/\partial x| h^2 / (\rho u_0 \nu)$. For further non-dimensional interpretation, the tidal displacement averaged over the channel width reads [10]

$$\Delta x = \frac{2u_0\lambda}{\omega\alpha^2} \left| 1 - \frac{\tanh(\sqrt{i}\alpha)}{\sqrt{i}\alpha} \right|. \quad (3)$$

To determine the local, time-dependent temperature $T(x, \eta, t)$, differential equations for the solid and the fluid domain are formulated. Within the solid wall, heat conduction is the only transfer mechanism, whereas the fluid domain also accounts for convective transport induced by the oscillating flow. The ratio of thermal conductivities k_f in fluid and k_s solid is denoted by

$$\mu \equiv k_f/k_s. \quad (4)$$

Effects of viscous heating are not considered, as they are typically of negligible magnitude. Adiabatic Neumann boundary conditions apply at the planes of

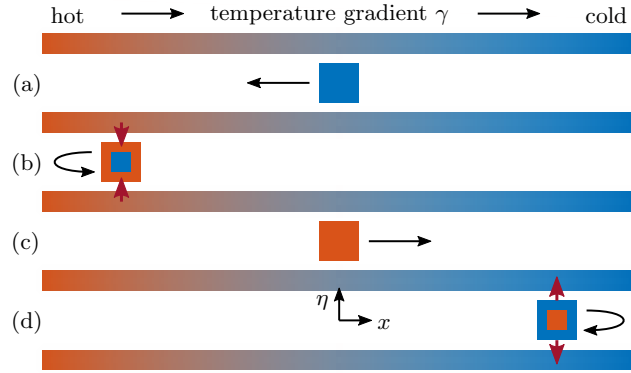


Figure 3: Schematic of oscillation-induced convective heat transfer described by Kurzweg [10].

symmetry ($z = 0$ and $h\epsilon$) depicted in Fig. 1 and thermal coupling (continuous temperature and heat flux) applies at the fluid-solid interface ($z = h$). Solutions for the temperature profile are found in the literature and explicitly stated by Kurzweg [10].

Having found closed expressions for velocity and temperature, an effective thermal diffusivity κ_e is formulated as the convective transport averaged over the channel width within one period of oscillation:

$$-\kappa_e \gamma = \frac{\omega}{2\pi} \int_0^{2\pi/\omega} \int_0^1 \Re[T(x, \eta, t)] \Re[u_0 f(\eta) e^{i\omega t}] d\eta dt. \quad (5)$$

Fig. 3 illustrates the heat transfer mechanism expressed by Eq. (5): (a) Cold fluid oscillates from a cold channel section (right side) to a hot channel section (left side). (b) During the residence time close to the left turning point, the fluid is heated by the hot walls, indicated by the red arrows. (c) Oscillating back to the right section of the channel, the fluid convectively transfers sensible enthalpy, which is then (d) transferred to the cold walls close to the right turning point, closing the loop to state (a). In summary and time-averaged over one oscillation period (compare to Eq. (5)), this yields a positive heat flux resulting from the velocity oscillation. This mechanism was already described by Kurzweg [10]. Although the title of that paper speaks of “Enhanced Heat Conduction...”, it is clear that the mechanism of heat transfer enhancement is essentially

convective.

The ratio of effective longitudinal thermal diffusivity κ_e (convective transport mechanism) and purely molecular thermal diffusivity κ_f defines the *Péclet number* Pe of the problem at hand. Furthermore, Kurzweg [10] showed that this characteristic scales with his definition of the Péclet number $\text{Pe}_K = u_0 h / \kappa_f$:

$$\frac{\kappa_e}{\kappa_f} = \text{Pe} \sim \text{Pe}_K. \quad (6)$$

The correlation clearly underlines the predominant convective transport mechanism that drives the strong longitudinal enhancement in heat transfer, attributed to large velocity amplitudes u_0 and small thermal diffusivity of the fluid κ_f .

In its non-dimensional presentation, Kurzweg [10] formulates the solution of Eq. (5) as:

$$\frac{\kappa_e}{\omega \Delta x^2} = \frac{\text{Pr} [(1 - H)\bar{h} + (1 - \bar{H})h] + (\bar{h} - \bar{j}\bar{H}) + (h - jH)}{16\alpha^2(\text{Pr}^2 - 1) \left| 1 - \frac{\tanh(\sqrt{i}\alpha)}{\sqrt{i}\alpha} \right|^2}, \quad (7)$$

where

$$h(\alpha) = \sqrt{i}\alpha \tanh(\sqrt{i}\alpha), \quad (8)$$

$$j(\text{Pr}, \alpha) = \sqrt{i}\text{Pr}\alpha \tanh(\sqrt{i}\text{Pr}\alpha), \quad (9)$$

and

$$H(\text{Pr}, \mu, \sigma, \alpha, \epsilon) = \frac{1}{\text{Pr}} \frac{\mu \sqrt{\text{Pr}} \tanh(\sqrt{i}\alpha) + \sqrt{\sigma} \tanh(\sqrt{i\sigma}\text{Pr}\alpha(\epsilon - 1))}{\mu \tanh(\sqrt{i}\text{Pr}\alpha) + \sqrt{\sigma} \tanh(\sqrt{i\sigma}\text{Pr}\alpha(\epsilon - 1))}, \quad (10)$$

where $\text{Pr} = \nu / \kappa_f$ is the fluid Prandtl number,

$$\sigma \equiv \kappa_f / \kappa_s \quad (11)$$

the ratio of thermal diffusivity $\kappa = k / (\rho c)$ and c the specific heat capacity. The bar-operator $\bar{\cdot}$ denotes the complex conjugate of the functions h , j and H . Surprisingly, the non-dimensional presentation in Eq. (7) is solely a function of material properties (Pr , μ and σ), geometry (ϵ) and Womersley number α . It is independent of the representative velocity u_0 and the prevailing uniform axial temperature gradient (compare [4]).

2.2. Assumption of fixed wall temperature

As outlined in Section 2.1, the analytical derivations of Kurzweg [10] consider conjugate heat transfer in a coupled system of fluid and wall interaction. However, many setups of physical interest are characterized by a solid of high specific heat capacity c , density ρ and thermal conductivity k compared to the fluid. In particular, this holds for metallic walls, confining a channel filled with air. This allows for the following assumptions:

$$k_f \ll k_s \rightarrow \mu \approx 0 \quad (12)$$

and

$$\rho_f c_f \ll \rho_s c_s. \quad (13)$$

For the ratio of thermal diffusivity σ , no definite limit exists, due to the opposing effects of thermal conductivity and heat capacity.

Regarding the geometry, the diameter of quarter-wave resonators in combustion chambers is typically much smaller than the wall thickness, yielding:

$$h \ll b \rightarrow \epsilon \approx \infty. \quad (14)$$

Physical interpretation of the proposed assumptions yields a Dirichlet boundary condition at the fluid-solid interface ($z = h$). In agreement with the previous modeling, the local wall temperature is defined by its gradient $\gamma = \partial T / \partial x$ and is depicted in Fig. 2. The simplified expression (denoted by the star *) of Kurzweg's solution (7) reads:

$$\frac{\kappa_e^*}{\omega \Delta x^2} = \frac{2 \text{Pr} \Re(h) - \frac{2}{\text{Pr}} \Re(j)}{16\alpha^2(\text{Pr}^2 - 1) \left| 1 - \frac{\tanh(\sqrt{i}\alpha)}{\sqrt{i}\alpha} \right|^2}. \quad (15)$$

This derivation exploits that $H^* = 1/\text{Pr}$ is purely real-valued. As a direct consequence, the expansion of the complex conjugate terms in the numerator of Eq. (7) simplify such that all imaginary parts cancel out.

The assumptions introduced in this section were validated by comparing results of the original model (7) and the simplified result (15). For material

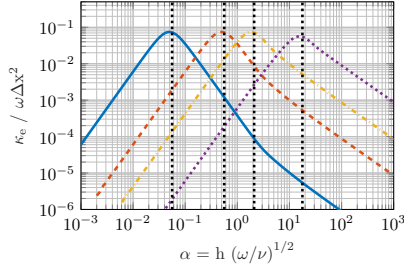


Figure 4: Simplified Kurzweg model for different Prandtl numbers: $\text{Pr} = 1000$ (—), 10 (---), 0.71 (—·—), 0.01 (···). Dotted lines denote $\alpha^2 \text{Pr} = \pi$.

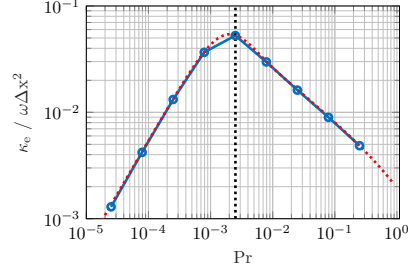


Figure 5: Results for effective thermal diffusivity vs. Prandtl number Pr for low amplitude oscillation at $\alpha = 35.4$: Simulation (●—●), simplified Kurzweg (···).

properties of metal and air, differences between the effective thermal diffusivities κ_e and κ_e^* , respectively, are marginal over the parameter range ($\alpha = 35.4$ and $\text{Pr} = [2.5 \times 10^{-5}, 0.25]$) under investigation. An exemplary plot at four distinct Prandtl numbers ($\text{Pr} = 0.01, 0.71, 10, 1000$) is shown in Fig. 4 and perfectly reproduces the results of Kurzweg [10], including the maximum thermal diffusivity close to $\alpha^2 \text{Pr} = \pi$. The vanishing thermal diffusivity for both limiting cases $\alpha \rightarrow 0$ and $\alpha \rightarrow \infty$, respectively, is also well explained by the mechanism outlined in Fig. 3: On the one hand, low oscillation frequencies (corresponding to $\alpha \rightarrow 0$) demonstrate a quasi-steady state. Energy is no longer convected due to the immediate thermal equilibrium. On the other hand, high frequencies (corresponding to $\alpha \rightarrow \infty$) result in negligible time spans of the fluid close to either reversal point. Thus, there is a limit on the amount of energy that is initially induced and extracted afterward. The original model (7) and the simplified result (15) both reproduce the expected time-invariant temperatures at the wall surface. In conclusion, the choice of the computational domain presented in the next section is justified.

3. Definition and validation of the numerical model

In this section, the numerical framework is presented. The phenomena under investigation in the present work (longitudinal heat transfer in a turbulent oscillating channel flow) fundamentally differs from our previous study ‘Large Eddy Simulation of Enhanced Heat Transfer in Pulsatile Turbulent Channel Flow’ [17]. The former study focused on wall-normal heat transfer (i.e. between a cold bottom wall and a hot top wall). The effect of turbulence, induced by increasing pulsation amplitudes, revealed a significant enhancement in heat transfer over the non-pulsating reference. In contrary, the present study investigates the overall transport in stream-wise direction. Thus, the wall-normal transport only presents one part of a more complex mechanism when the fluid inside the channel receives or rejects energy from/to the wall (compare Phases (b) and (d) in Fig. 3). In addition, the complete mechanism also involves convective stream-wise transport (Phases (a) and (c)) and more hidden interdependencies (e.g. a saturation of the ‘thermal loading’ (Phase (b)): the fluid can only receive heat until it reaches the temperature of the adjacent wall).

Despite all physical deviations between the present study and the previous work [17], many numerical considerations can be reapplied. Section 3.1 outlines the adapted simulation domain. This is followed by the governing equations and solver setup (Section 3.2. The validation (Section 3.3) is based on comparison with experimental data and a DNS benchmark [17]. In addition, laminar flows are validated against the analytical correlation and the threshold of laminar-to-turbulent transition is compared against experimental results.

3.1. *Simulation domain setup*

The computational domain (Fig. 6) is designed to study the effect of enhanced longitudinal heat transfer in both laminar and turbulent oscillating channel flow. The lower and upper walls confine the channel of width $2h$ in wall-normal z -direction. No-slip velocity boundary condition and a constant temperature gradient γ in stream-wise x -direction are imposed. The span-wise

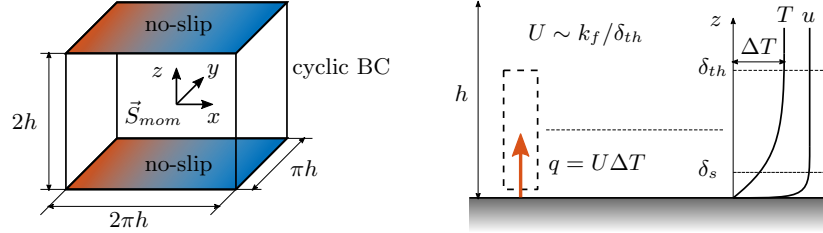


Figure 6: Cyclic simulation domain of a channel section with an oscillating momentum source term \vec{S}_{mom} and axial gradients in wall temperature.

Figure 7: Bulk temperature approach to model convective heat transfer. The hydrodynamic BL is smaller than the thermal BL which is smaller than the channel width.

(y -direction) and stream-wise boundary patches are cyclic, allowing the fluid to periodically circulate though the domain of length $L_x = 2\pi h$ and width $L_y = \pi h$. A key advantage of this approach is the self-generation of turbulent flows, independent of the need for long inlet regions or turbulence inlet models (e.g. [17, 18, 19]).

The simulation domain models a short stream-wise section of a long channel. The upper and lower walls of this long channel are imposed with constant stream-wise temperature gradient γ . Regarding the short simulation domain, this yields a periodic temperature symmetry: Fluid leaving the 'cold' (right) side of the domain, re-enters on the 'hot' (left) side with a temperature jump of $\Delta T = \gamma 2\pi h = \gamma L_x$ and vice versa. This approach allows to model a constant temperature gradient in a cyclic domain. Based on studies by Chatwin [4], Kurzweg [10] used the same method for analytical derivations of capillary flows between two fluid reservoirs at different temperatures. The method is applicable to wide technical field of channel flows confined by a constant time-averaged temperature gradient (e.g. resonator tubes).

The fluid oscillation is driven by a harmonic momentum source term \vec{S}_{mom}

Re_τ	$\lambda = a_{p,x}^+$	$l_s^+ \rightarrow \alpha$	Pr	$\Delta T/(\gamma h)$	L_x/h	L_y/h
350	100 to 300	14 → 35.4	2.5×10^{-5} to 0.25	2π	2π	π

Table 1: Physical simulation parameters.

which can be expressed in terms of a non-dimensional pressure gradient λ :

$$\begin{aligned}
\vec{S}_{\text{mom}} &= \frac{\partial p}{\partial x} \cos(\omega t) \vec{e}_x \\
&= \lambda \frac{\rho u_0 \nu}{h^2} \cos(\omega t) \vec{e}_x \\
&= a_{p,x}^+ p_{0,x} \cos(\omega t) \vec{e}_x \\
&= a_{p,x}^+ \frac{\text{Re}_\tau \nu^2 \rho}{h^3} \cos(\omega t) \vec{e}_x.
\end{aligned} \tag{16}$$

In addition, Eq. (16) states the momentum source in terms of the turbulent Reynolds number Re_τ and the non-dimensional amplitude $a_{p,x}^+$ as introduced in [17], where pulsating flows with non-zero time-averaged mean-flow are studied. Although the present study does not include mean-flow – and thus the definition of the turbulent Reynolds number has no physical relevance to the problem at hand – there is good reason to define $\lambda = a_{p,x}^+$ and $u_0 = (\text{Re}_\tau \nu)/h$ to facilitate comparison between the two studies. A second dimensional parameter of relevance is the forcing frequency: In the present study, the Womersley number α is selected as its non-dimensional counterpart for direct correlation with Kurzweg [10]. On the other hand van Buren et al. [17] choose the non-dimensional Stokes length $l_s^+ = u_\tau \sqrt{2/(\omega \nu)}$, where $u_\tau = \text{Re}_\tau \nu/h$ is the friction velocity. Rearrangement of (non-dimensional) *Pi groups* yields $\alpha = \sqrt{2}\text{Re}_\tau/l_s^+$.

One technical application of the problem at hand is the oscillating flow in quarter-wave resonators. Located in the cold recirculation zone close to the injector face-plate (Hydrogen, temperature ≈ 180K, pressure ≈ 80bar), typical defining properties are angular frequencies $\omega = 1000$ to 10000s^{-1} , tube-diameters of 1.5mm and a kinematic viscosity of $\nu \approx 7 \times 10^{-7}\text{m}^2/\text{s}$. This yields Womersley numbers in an order of magnitude ranging from $\alpha = 10$ to 100. Note the direct correlation to the Stokes boundary layer thickness $\delta_s = \sqrt{2\nu/\omega}$ given by $\alpha = \sqrt{2}h/\delta_s$. Hence, the present study is characterized by flows of small

hydrodynamic boundary layers δ_s compared to the half channel width h .

To match the non-dimensional Stokes length $l_s^+ = 14$ of our earlier study [17], a Womersley number of $\alpha = 35.4$ is carefully chosen to lie well inside the range of technical interest. Table 1 summarizes the physical parameters of the present study.

Yet another important aspect of the modeling approach is its applicability to compact regions of acoustic pressure nodes and justifies the cross-reference to the front section of an acoustic quarter wave resonator. For a more detailed presentation, the reader may consult [17].

3.2. Governing equations, CFD solver setup and Evaluation

The numerical model was implemented in the finite volume software OpenFOAM (Version v1706+) [20]. Using the PISO algorithm, the LES-filtered system of incompressible conservation equations for mass and momentum is solved. The temperature field is calculated as a passive scalar, neglecting effects of viscous heating. A dynamic one-equation kinetic energy model is used to evaluate fully localized subgrid-scale viscosity and wall-distance dependent subgrid-scale Prandtl numbers. Run-time averaging of selected flow characteristics is implemented for significant reduction of storage consumption. A detailed description of the LES governing equations, the turbulence model applied and the CFD solver setup is provided in [17].

The calculation of the effective thermal diffusivity in Eqn. 5 only holds for the case of laminar flows described by Kurzweg [10]. For the extended numerical evaluation of the present study, the locally resolved temperature $T(x, y, z, t)$ and velocity $u_x(x, y, z, t)$ (in stream-wise x -direction) applies to the fluid with turbulent fluctuations. In consequence, the spatial integration extends from the one-dimensional channel width to the complete and three-dimensional simulation/channel domain. Thereby, the two additional spatial dimensions (x and y -direction) serve - beside the evaluation over n oscillation cycles - as an aver-

aging operator:

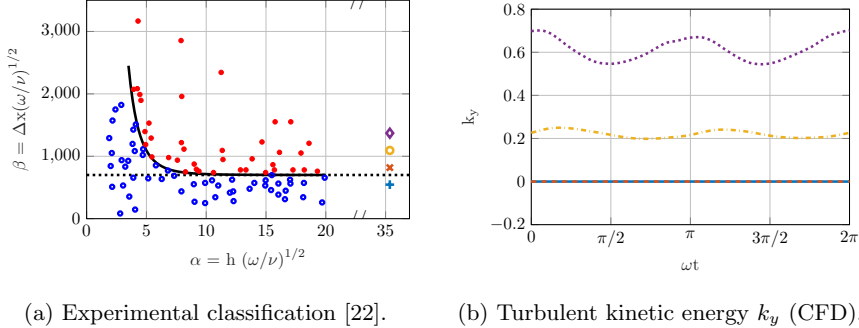
$$-\kappa_{e,\text{turb}}\gamma = \frac{\omega}{2\pi n} \frac{1}{2hL_xL_y} \int_0^{2\pi n/\omega} \int_{-h}^h \int_{-L_y/2}^{L_y/2} \int_{-L_x/2}^{L_x/2} T(x, y, z, t) u_x(x, y, z, t) dx dy dz dt. \quad (17)$$

3.3. Validation

In our prior investigation ([17]), the numerical framework for simulation of heat transfer in turbulent pulsating channel flow was carefully validated against experimental and DNS data. This previous study serves as the basis of validation for the turbulent oscillating flow under investigation in the present work. Since the present work also considers laminar flows, additional analytical and experimental validation for the laminar flow regime is provided.

The numerical set-up and the parameter range under investigation in the present work largely coincides with [17]. In particular, the solvers, turbulence models and meshes are identical. Furthermore, fluid properties as well as forcing frequencies and velocity amplitudes match. Thus, we are confident that the validation for turbulent flows given in [17], also applies to the present work. The following paragraph summarize the scope and results of the validation study. For further details, the reader should consult our prior publication [17].

The first-order statistics of velocity amplitude and phase across the channel width showed good agreement to experimental data by Tardu et al. [21]. Furthermore, the first-order statistics compared remarkably well to a DNS benchmark provided by Scotti and Piomelli [18]. The DNS data also permitted validation of second-order statistics, namely the Reynolds shear stress, the harmonic amplitude and the turbulent kinetic energy spectra. Good agreement was found also for these quantities. The evaluation of the turbulent kinetic energy spectra confirmed that LES cutoff lies well outside the inertia. range. The stream-wise domain length L_x was found to be adequate to capture large flow-structures. The selected mesh size of 66x66x102 cells on a structured grid (equidistant spacing in stream- and span-wise direction, hyperbolic spacing in wall-normal



(a) Experimental classification [22]. (b) Turbulent kinetic energy k_y (CFD).

Figure 8: Validation of laminar (●) to turbulent (●) transition in dependence of the non-dimensional pressure gradient $\lambda = 100$ (—, +), 150 (---, *), 200 (----, ○) and 250 (……, ♦) at $\alpha = 35.4$.

direction) showed grid-independent flow characteristics. In summary, we are confident that the numerical setup is well capable to accurately model the turbulent flow regime for the problem at hand.

For laminar flows, simulation results are compared against the simplified Kurzweg model at the Womersley number under investigation ($\alpha = 35.4$). It is emphasized that the analytical results are based on an exact solution of convective and conductive heat transfer based on an exact velocity solution of the Navier-Stokes equations. Neither simplifying assumptions nor (semi-)empirical (tuning-)parameters were introduced by Kurzweg, strengthening our confidence in the validity of the analytical results. Fig. 5 shows perfect agreement between analytical and simulation results over the entire range of Prandtl numbers investigated.

As this study aims to explore the impact of turbulence in comparison to a laminar flow, validation of threshold for the onset of turbulence is given in a second step. In an experimental study, Kurzweg et al. [22] classified laminar and turbulent flows based on the non-dimensional oscillation amplitude $\beta = \Delta x \sqrt{\omega/\nu}$ (compare Fig. 8a). This parameter reveals close correspondence to the Reynolds number as the ratio of inertial forces to viscous forces. For large Womersley numbers, as they are considered in this study, Kurzweg ob-

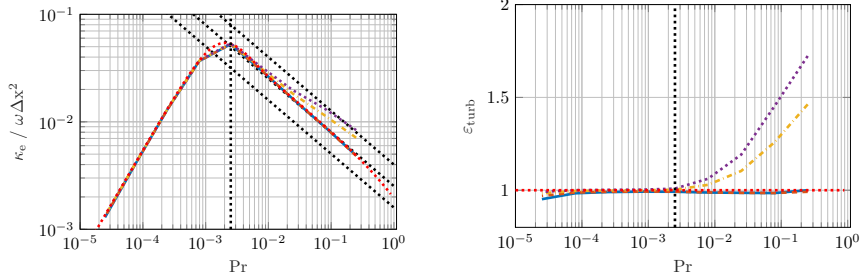
served laminar-turbulent transition at $\beta \approx 700$. In the present numerical study, simulations were performed at four oscillation amplitudes of increasing strength, namely at $\lambda = 100, 150, 200$ and 250 , which are included in Fig. 8a and indicate $\lambda = 100$ to be laminar, only.

Fig. 8b shows the non-dimensional turbulent kinetic energy k_y as it evolves over one period of oscillation (layer-averaged, measured in span-wise y -direction at the center-plain $z = 0$). This parameter, in contrast to Kurzweg et al. [22], suggests that the two lower oscillation amplitudes ($\lambda = 100$ and 150) result in laminar flows, whereas the two higher oscillation amplitudes ($\lambda = 200$ and 250) trigger turbulence. In respect to the experimental prediction, a reasonable agreement is established, with only $\lambda = 150$ deviating from the expected characteristics. One explanation are the perfectly smooth wall-surfaces and ideal (cyclic) inflow conditions in the CFD suppressing the laminar-to-turbulent transition, whereas natural imperfections of the experiment trigger the development of turbulence.

4. Results: Effective heat transfer enhanced by turbulence

The present section presents numerical results on the impact of turbulence on the longitudinal effective heat transfer. A deeper analysis and discussion is dedicated to two questions that arise in connection with the results: First (Section 4.1), what regions of the channel contribute to the heat transfer enhancement? How does turbulence affect the boundary layers and how deep do thermal disturbances penetrate into the channel? Second (Section 4.2), how does turbulence enhances the longitudinal advection? Or is the overall enhancement of longitudinal heat transfer merely related to wall-normal effects?

Fig. 9a shows numerical results for the effective thermal diffusivity at a constant Womersley number $\alpha = 35.4$. Four oscillation amplitudes (two laminar, two turbulent, compare validation in Section 3.2) are depicted vs. the Prandtl number. In addition, Fig. 9b provides a normalized and semi-logarithmic presentation of those results, which shows the enhancement attributed to the effects



(a) Absolute double-logarithmic presentation of the non-dimensional effective thermal diffusivity κ_e .
 (b) Relative semi-logarithmic presentation of the enhancement of longitudinal heat transfer $\varepsilon_{\text{turb}}$ due to turbulence.

Figure 9: Effective thermal diffusivity for laminar and turbulent flows at $\lambda = 100$ (—), 150 (---), 200 (—·—) and 250 (····) vs. simplified Kurzweg model (····). The vertical dotted line denotes $\alpha^2 \text{Pr} = \pi$, the inclined dotted lines scale with $1/\sqrt{\text{Pr}}$ (····), $\alpha = 35.4$.

of turbulence in a more explicit manner. This plot suggests to define the turbulent enhancement of longitudinal heat transfer (ELHT) as the increase in thermal diffusivity relative to the analytical results for the reference case of laminar oscillating flow:

$$\varepsilon_{\text{turb}} \equiv \frac{\kappa_{e,\text{turb}}}{\kappa_e}. \quad (18)$$

Thus, an turbulence-induced enhancement in heat transfer is characterized by values of $\varepsilon_{\text{turb}} > 1$. Note our nomenclature that evaluates effective thermal diffusivity as the increase in heat transfer of a laminar oscillation over a non-oscillating case. ELHT is purely associated to the turbulence-induced contribution over the laminar (but oscillating) reference.

Comparing the absolute (left) and relative (right) evaluation of heat transfer in Fig. 9, physical relevance of the maximum in non-dimensional effective thermal diffusivity κ_e (left) is limited. This is reasoned by the extremely small and unrealistic values of Prandtl number ($\text{Pr} \approx 0.0025$) in the vicinity of the peak. However, when quantifying the impact of turbulence over the laminar reference (right), ELHT develops and enhances with increasing Prandtl number. In particular in the range of physical relevance (e.g. air with $\text{Pr} \approx 0.7$),

a significant impact of turbulence is expected with a factor of about 0.5. Of course, the (absolute) non-dimensional effective thermal diffusivity κ_e has already decreased by about one to two orders of magnitude for these values of Prandtl number. Nevertheless, it still exceeds the pure thermal diffusivity at large oscillation amplitudes and high frequencies. As a consequence, both effective thermal diffusivity and ELHT contribute to the physical application at hand.

The findings of the numerical study are categorized as follows:

1. There is no ELHT in laminar flows. Supporting prior analytical theory, this coincides with our definition of ELHT and the amplitude invariant results in Fig. 9b ($\varepsilon_{\text{turb}} \approx 1$ for $\lambda = 100$ and 150).
2. At low Prandtl numbers (in particular $\alpha^2 \text{Pr} < \pi$), there is also no effect of turbulence on the effective thermal diffusivity.
3. At large Prandtl numbers (in particular $\alpha^2 \text{Pr} > \pi$), an increase in the Prandtl number Pr results in an increase in ELHT $\varepsilon_{\text{turb}}$.
4. At large Prandtl numbers (in particular $\alpha^2 \text{Pr} > \pi$), an increase in oscillation amplitude (or pressure gradient λ , respectively) results in an increase in ELHT $\varepsilon_{\text{turb}}$.
5. Overall, the effect of ELHT is modest for the parameter range under investigation and remains below 75%. However, the two previous statements indicate further enhancement at larger Womersley and Prandtl numbers (point 3.) as well as at larger oscillation amplitudes (point 4.).

These observations coincide perfectly with the suggestion of Kurzweg [10], concluding that at high Womersley numbers α (corresponding to the right branch of $\alpha^2 \text{Pr} > \pi$) and large tidal displacements Δx (corresponding to large oscillation amplitudes induced by the non-dimensional pressure gradient λ) need further investigation.

4.1. Physical interpretation of thermal penetration depth

This section aims to physically interpret the observations on ELHT $\varepsilon_{\text{turb}}$ provided in the previous Section 4 (in particular at $\alpha^2 \text{Pr} \geq \pi$, see [23] for an

extended analysis of this non-dimensional II-group). For this, a more meaningful presentation of the boundary layers and their hydrodynamic and thermal interactions is given.

Recall that the non-dimensional Womersley number $\alpha = \sqrt{2}h/\delta_s$ can be rewritten in terms of the Stokes boundary layer thickness (Section 3.1). It follows that – given $\alpha = 35.4$ – the results of this study are confined hydrodynamic boundary layers much smaller than the channel width:

$$\frac{\delta_s}{h} = \frac{\sqrt{2}}{\alpha} \approx 0.04. \quad (19)$$

Thus, the channel flow under investigation is predominantly characterized by an oscillating bulk velocity, with only relatively thin wall regions deviating from this pattern.

Concerning the thermal boundary layer, an analogy may be developed: The local change in temperature generates the driving potential of the development of a boundary layer. Thus, as argued above, the small hydrodynamic boundary layer generates a wall-normal temperature potential confined to the immediate vicinity of the wall. The thermal boundary layer thickness δ_{th} is given by $\delta_{th} = \sqrt{2\kappa/\omega} = \sqrt{2\nu/(\omega \text{Pr})} = \delta_s/\sqrt{\text{Pr}}$, which can be expressed in terms of the Prandtl number Pr . The ratio of thermal boundary layer to channel width reads

$$\frac{\delta_{th}}{h} = \frac{\sqrt{2}}{\alpha\sqrt{\text{Pr}}} \approx \frac{0.04}{\sqrt{\text{Pr}}}. \quad (20)$$

In the present study, Prandtl numbers $\text{Pr} < 1$ are considered, which correspond to a thermal boundary layer thickness larger than its hydrodynamic counterpart. The parameter range characterized by first emergence of ELHT ($\alpha^2 \text{Pr} > \pi$) is specified by a thermal boundary layer thickness just extending into the channel center ($\delta_{th}/h = \sqrt{2/\pi} = 0.8 \approx 1$).

Finally, the effective thermal diffusivity is interpreted as a result of the interaction of hydrodynamic and thermal boundary layers: Recall Eq. (5), which states that the effective thermal diffusivity results from the convective transport of temperature fluctuations by an oscillating flow. As a direct consequence, two competing mechanisms are induced by the two boundary layers: On the one

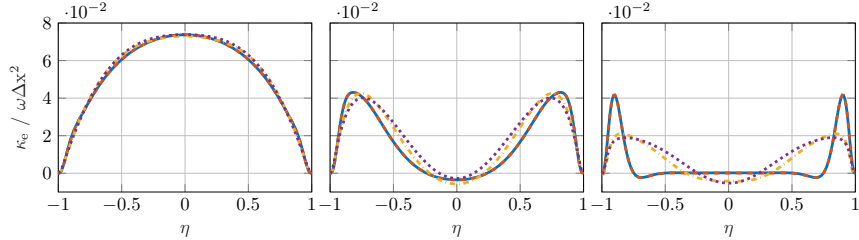


Figure 10: Spatial profile of effective thermal diffusivity across the channel width $2h$ ($-1 \leq \eta \leq 1$) at $\alpha^2 \text{Pr} = \pi$ (left), 10π (center) and 100π (right) for $\lambda = 100$ (—), 150 (---), 200 (—·—) and 250 (····), $\alpha = 35.4$.

hand, velocities are largest outside the hydrodynamic boundary layer, thus one might expect an increase in diffusivity towards the center of the channel. On the other hand, temperature fluctuations diminish outside the thermal boundary layer, thus near wall regions within the thermal boundary layer should contribute dominantly to thermal diffusivity. Returning to the parameters under investigation, we note first that a thin hydrodynamic boundary layer permits large bulk velocities across the channel width. Second, the thermal boundary layer width is varied by the Prandtl number Pr . Observing maximum thermal diffusivity at thermal boundary layers extending just into the channel center agrees perfectly with these considerations.

This physical interpretation if boundary layer interplay is evident in the spatial profiles of the effective thermal diffusivity presented in Fig. 10. From left to right, simulation results for increasing Prandtl numbers are presented, starting at $\text{Pr} = 0.0025$, which corresponds to $\alpha^2 \text{Pr} = \pi$. In this configuration the thermal boundary layer extends into the center of the channel, such that the entire cross-section contributes to the convective heat transfer. Additional wall-normal turbulent transport does not improve performance. In a mathematical sense, this shows by the equal areas underneath the curves, which coincide for the laminar and turbulent cases. A further decrease of the Prandtl number yields corresponding findings and is not included in Fig. 10.

Turning our attention to the center and right plots of Fig. 10, the Prandtl

numbers are increased to $\text{Pr} = 0.025$ and 0.25 , respectively ($\delta_{th}/h = 0.25$ and 0.08). For laminar cases, it is evident that the contribution of the channel center declines, as it lies clearly outside the thermal boundary layer. Consequently, the temperature in the channel center is not fluctuating. For such conditions, there is a noticeable effect of turbulence on effective longitudinal heat transfer: The turbulence-induced increase in wall-normal convective heat transfer (compare [17]) widens the thermal boundary layer thickness such that a larger cross-section area contributes to the enhanced longitudinal heat transfer. As the intensity in turbulence increases, the thermal penetration depth expands further into the channel. This, in turn, increases the ELHT $\varepsilon_{\text{turb}}$.

For large Prandtl numbers Pr (center and right plot in Fig. 10) a small but not negligible reverse in heat transfer reveals inside the channel. This phenomena is explained by the time lag that occurs when the thermal disturbances propagate from the originating walls into the center of the channel. By the time the temperature disturbance reaches the center, the fluid motion may have reversed and thus carry the thermal energy in the corresponding opposing direction. Similar, supposedly unexpected behaviors show for example in the velocity over-shoot of Stokes problem.

4.2. On the longitudinal effect of turbulence

This section elaborates on the longitudinal convective effect of turbulence. In particular, we address the question if the enhancement of longitudinal heat transfer is attributed to an increased longitudinal transport, or rather to wall-normal exchange in the boundary layers.

Figure 11 summarizes selected thermal characteristics for over the complete range of parameters (top row, Section 4.1) and over the range of particular physical interest (bottom row, Section 4.3). The plots (a) and (d) on the left side denote the effective thermal diffusivity κ_e defined by Eqn. (17). They clearly reveal the expected enhanced heat transfer around $\text{Pr} = 0.0025$, which corresponds to Kurzweg's finding: $\alpha^2 \text{Pr} \approx \pi$. Increasing oscillation strengths drive the enhancement.

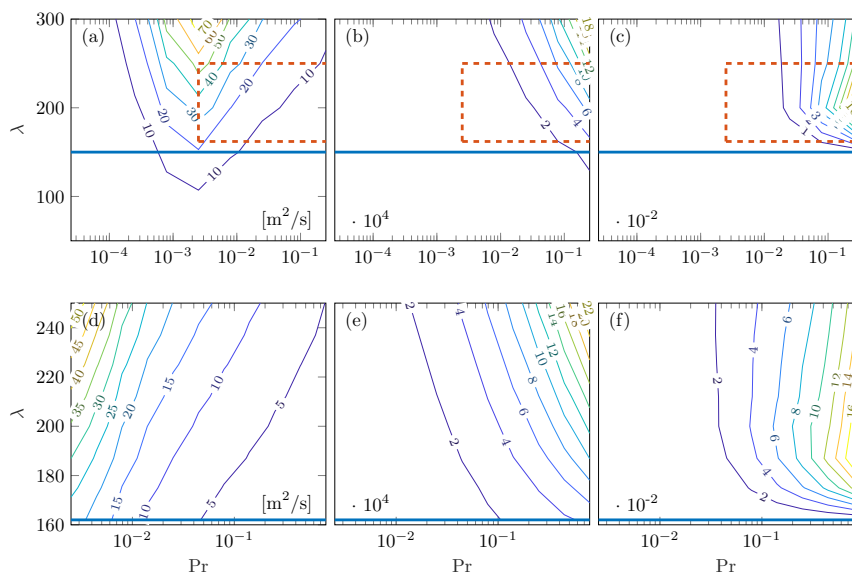


Figure 11: Effective thermal diffusivity κ_e (left), Péclet number Pe (center) and turbulent enhancement of longitudinal convection ξ_{turb} (right) over the full parameter range (top row) and over the range of deeper interest (bottom row, denoted by the dashed box (—·—) in the top row). Laminar/turbulent transition: —.

The centered plots (b) and (e) relate the ratio of effective longitudinal thermal diffusivity to the molecular fluid diffusivity: κ_e/κ_f . This definition of the Péclet number Pe (compare Eqn. (6)) reveals increasing values with an increase in the oscillation amplitude λ and in the Prandtl number Pr. Thereby, the Péclet number underlines the crucial importance of the convective transport mechanism. However, this observation directly leads to the following question: Does the turbulence significantly increase the longitudinal convective transport? Or is it merely attributed to the underlying oscillatory motion?

To quantify the longitudinal turbulent transport over a laminar reference, the laminar effective thermal diffusivity is defined as

$$-\kappa_{e,\text{lam}}\gamma = \frac{\omega}{2\pi n} \frac{1}{2h} \int_0^{2\pi n/\omega} \int_{-h}^h \left(\frac{1}{L_x L_y} \int_{-L_y/2}^{L_y/2} \int_{-L_x/2}^{L_x/2} T(x, y, z, t) dx dy \right. \\ \left. \frac{1}{L_x L_y} \int_{-L_y/2}^{L_y/2} \int_{-L_x/2}^{L_x/2} u_x(x, y, z, t) dx dy \right) dz dt, \quad (21)$$

where a spatial layer-wise averaging of the temperature T and velocity u_x is performed before the respective multiplication, suppressing the consideration of turbulent fluctuations.

The plots (c) and (f) on the right side of Fig. 11 show the relative impact of turbulent effects on the longitudinal convective transport:

$$\xi_{\text{turb}} = \frac{\kappa_{e,\text{turb}} - \kappa_{e,\text{lam}}}{\kappa_{e,\text{lam}}}. \quad (22)$$

In the laminar regime below the horizontal blue line that denotes the threshold of the limiting numerical set-up, turbulent effects do not impact the longitudinal transport: $\xi_{\text{turb}} = 0$. In the turbulent regime, relevant longitudinal convection shows for large Prandtl numbers (i.e. low molecular thermal conductivity of the fluid). This effect slightly diminishes with increasing oscillation strength λ . However and in comparison with the enhancement in longitudinal heat transfer $\varepsilon_{\text{turb}}$ (e.g. Fig. 12), the contribution of enhancement in longitudinal convection ξ_{turb} is relatively small: At the bounding parameter range with $\text{Pr} = 0.79$,

the longitudinal convection fulfills $\xi_{\text{turb}} < 18\%$ whereas overall enhancement in longitudinal heat transfer easily exceeds 50% or even 100% (in particular at large oscillation amplitudes). In conclusion, the additional turbulence-driven longitudinal convection is of minor importance for the overall enhancement in longitudinal heat transfer. Instead, the wall-normal turbulent enhancement in heat transfer (compare also [17]) promotes the thermal ‘loading’ and ‘unloading’ of the oscillating fluid. Most of the convective transfer in longitudinal direction is attributed to the regular underlying oscillation without turbulent fluctuations.

4.3. Modeling

This section provides a simple qualitative model for longitudinal heat transfer. Throughout the derivation, a confined hydrodynamic boundary layer (Womersley number $\alpha = 35.4$) and a thermal boundary layer smaller than the channel width ($\alpha^2 \text{Pr} > \pi$) but wider than its hydrodynamic counterpart ($\text{Pr} < 1$) is assumed. In a first step, the model is qualitatively validated against the laminar flow and then extended to quantify the effect of turbulence.

4.3.1. Modeling without turbulence

The assumptions introduced in Section 4.3 suggest a bulk temperature approach, meaning that the temperature in the center is not disturbed. On the other hand, at values of Prandtl number $\text{Pr} < 1$, temperature disturbances occur mainly within the bulk velocity region (compare Fig. 7). Referring to the calculation of the effective thermal diffusivity in Eq. (5), the majority of the channel cross-section shows constant bulk velocity ($\delta_s/h \ll 1$), whereas temperature fluctuations are present throughout the thermal boundary layer. Considering these constraints, a qualitative interpretation of effective thermal diffusivity κ_e questions what wall-normal heat flux q is transferred to the fluid at the hot reversal point and then released back to the wall at the cold reversal point. In general, such heat flux $q = U\Delta T$ is expressed by the product of thermal transmittance U and the temperature potential ΔT . As depicted in Fig. 7, the imposed temperature potential is solely induced by the local velocity

fluctuation close to the wall. Accounting for pure wall-normal heat conduction in the laminar case, the expression for the thermal transmittance U reads $U \sim k_f/\delta_{th} \sim 1/\sqrt{\text{Pr}}$. In conclusion, the qualitative evaluation of Eq. (5) yields

$$\frac{\kappa_e}{\omega \Delta x^2} \sim q \sim \Delta T U \sim \frac{k_f}{\delta_{th}} \sim \frac{1}{\sqrt{\text{Pr}}}, \quad (23)$$

suggesting inverse scaling effect of the square-root of the Prandtl number Pr .

Fig. 9a includes the predicted quality of Eq. (23) (dotted lines). Very good agreement is obtained within the range of constraints for the laminar case. The agreement holds best in the range of $\text{Pr} = 0.025$ to 0.25 . Approaching the limits, inaccuracies result from the violation of following assumptions:

- Small Prandtl numbers (e.g. $\text{Pr} < 0.025$) violate the assumption of bulk temperature in the center of the channel.
- Large Prandtl numbers (e.g. $\text{Pr} > 0.25$) violate the assumption of constant velocities throughout the thermal boundary layer.

4.3.2. Modeling with addition of turbulence

Building upon the laminar considerations given in Section 4.3.1, the impact of turbulence is included in this section. The additional wall-normal convective heat transfer induced by turbulence is denoted by the coefficient h_{turb} . Thus, h_{turb} is defined to be zero for laminar flow and to increase with increasing turbulence. Considering laminar heat conduction and turbulent convective heat transfer to act in parallel the extended form of Eq. (23) reads:

$$\frac{\kappa_e^*}{\omega \Delta x^2} \sim q^* \sim \Delta T U^* \sim \Delta T(U + h_{\text{turb}}). \quad (24)$$

Applying the definition of ELHT $\varepsilon_{\text{turb}}$ to be the normalized effective thermal diffusivity in respect to the laminar case (see Section 4), it follows:

$$\varepsilon_{\text{turb}} \sim \frac{U^*}{U} \sim 1 + \frac{h_{\text{turb}} \delta_{th}}{k_f} \sim 1 + \text{Nu} \sim 1 + h_{\text{turb}} \sqrt{\text{Pr}}. \quad (25)$$

In this notation the Nusselt number Nu describes the ratio of resistance based on laminar heat conduction and turbulent convection. Proportionality to the

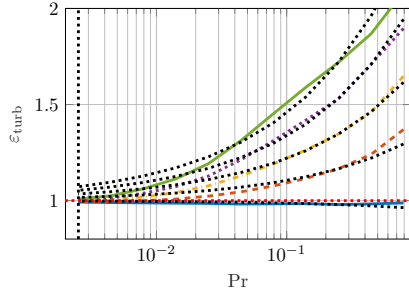


Figure 12: Parametric study of enhancement in longitudinal heat transfer $\varepsilon_{\text{turb}}$ for increasing oscillation amplitudes $\lambda = 162.5$ (—), 175 (---), 187.5 (—·—), 212.5 (····) and 250 (—). The black dotted lines denote the model from Eq. (25).

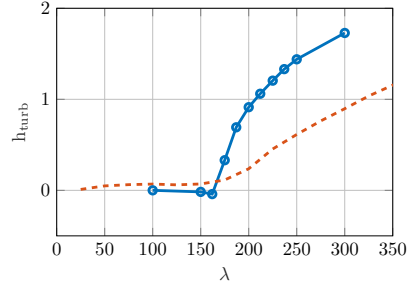


Figure 13: Comparison of turbulence-induced convective heat transfer coefficient h_{turb} (●—●) and EHT (---) [17] plotted vs. non-dimensional amplitude λ .

square root of the Prandtl number $\sqrt{\text{Pr}}$ is found, weighted with the convective heat transfer coefficient h_{turb} .

Fig. 12 shows results of ELHT $\varepsilon_{\text{turb}}$ in a more extensive parametric study for the parameter range of interest (turbulent flows, $\alpha^2 \text{Pr} > \pi$). The extended range of Prandtl numbers accounts for thermophysical properties of air ($\text{Pr} \approx 0.7$). Furthermore, the correlation of Eq. (25) is evaluated at $\text{Pr} = 0.25$ for each oscillation amplitude (dotted lines). In a first assessment, the qualitative prediction of a scaling proportional to the square-root of the Prandtl number ($\sim \sqrt{\text{Pr}}$) holds well. Nevertheless, a more detailed discussion of limitations of validity and its physical interpretation is given at this point:

- Confirming findings of limitations for laminar flows (Section 4.3.1), small Prandtl numbers (e.g. $\text{Pr} < 0.025$) violate the assumption of bulk temperature in the center of the channel. This error increases with additional heat transfer induced by turbulent convection, thus explaining the over-prediction of ELHT when approaching $\alpha^2 \text{Pr} = \pi$. In more physical terms, the entire channel cross-section already contributes to the effective thermal diffusivity (compare Fig. 10, left plot), such that turbulence has no

further contribution.

- Turning to large Prandtl numbers (e.g. $\text{Pr} \approx 0.25$), a slightly regressive behavior is revealed for large oscillation amplitudes. This observation has not been clarified, yet.

The convective heat transfer coefficient h_{turb} for each forcing amplitude is derived by fitting Eq. (25) at $\text{Pr} = 0.25$. The result is given in Fig. 13 vs. non-dimensional pressure gradient λ . In the laminar regime, i.e. for $\lambda \leq 162.5$, the expected behavior of $h_{\text{turb}} = 0$ is obtained. At the onset of turbulence $\lambda > 162.5$, the convective heat transfer coefficient h_{turb} increases monotonously with the oscillation amplitude. The initially large enhancement at laminar to turbulent transition is followed by a continuous decline in slope, indicating a decreasing influence of turbulence at high amplitudes.

Finally, a qualitative comparison to wall-normal enhanced heat transfer is included in Fig. 13. Recall the differences between the two studies: van Buren et al. [17] investigated enhancement of cross-stream heat transfer between two parallel plates of different temperature, whereas this study is concerned with axial temperature variation. Furthermore van Buren et al. [17] considered a developed pulsating flow, where critical Reynolds numbers for the onset of turbulence are already exceeded by the mean flow velocity rather than by high oscillation amplitudes. Despite these deviations, similar characteristics exist: First, significant increase in EHT [17] does not show before the laminar/turbulent transition of the present study is reached. This coincides well with the conclusions given by van Buren et al. [17], i.e. significant EHT only occurs at considerable turbulent intensities. This, in turn, only occurs for flows with pronounced flow reversal. Second, both studies reveal an initially large enhancement at amplitudes leading to increased turbulence. This is followed by a notable decline for the two setups under investigation.

5. Conclusions

Axial heat transfer in oscillating turbulent channel flow is investigated by means of Large Eddy Simulation (LES). Incompressible flow within a periodic computational domain is driven by a wide range of oscillating axial pressure gradients, generating both laminar and turbulent flows. The analytical solution to a laminar flow given by Kurzweg [10] is simplified to consider imposed temperature boundary conditions rather than investigating a problem of conjugate heat transfer within fluid and solid domain. This conforms well with setups of metallic walls confining an air-filled fluid channel. The applied numerical methods were carefully validated in a prior study [17].

The present numerical study provides first qualitative proof and evaluation of ELHT. For thin hydrodynamic boundary layers, a significant turbulence-induced increase in heat transfer may exist over the laminar counterpart. In particular in the range of physically meaningful Prandtl numbers (e.g. $\text{Pr} \approx 0.7$ for air), an enhancement of more than 100% shows. This coincides well with the conclusion given by Kurzweg [10], who identified the regime of $\alpha^2 \text{Pr} > \pi$ to be of interest for further studies related to the impact of turbulence. The numerical results identify the crucial importance of turbulence-increased wall-normal heat transfer as a drive of the enhancement. In contrast, longitudinal turbulent convective exchange contributes little contribution on the overall mechanism.

An analytical model consolidates the turbulence-induced enhanced wall-normal heat transfer with the oscillation-induced longitudinal convective transport to qualitatively explain the influence of the Prandtl number and the oscillation amplitude. Seen by themselves, neither of these mechanisms propose a novelty (e.g. wall-normal enhancement by van Buren et al. [17] and longitudinal enhancement by Kurzweg [10]. However in aggregation, they generate insight to the physical boundary layer interaction for wall-confined Stokes boundary layers ($\alpha = 35.4$).

First restricted to laminar flows, high convective velocity prevails outside of the hydrodynamic boundary layer. Thus, most effective convective heat transfer

exists, if this region of maximum velocity overlaps with the presence of temperature disturbance. This thermal disturbance, in turn, is found within the thermal boundary layer. In consequence, maximum effective thermal diffusivity is attributed to thermal boundary layer thicknesses approaching the channel width, or – as recognized by Kurzweg [10] – $\alpha^2 \text{Pr} \approx \pi$. Furthermore, the presented model gives physical interpretation for the scaling of effective thermal diffusivity with $1/\sqrt{\text{Pr}}$.

Based on the laminar model, the correlation is expanded to quantify the impact of turbulence on heat transfer. In this process, a turbulence intensity correlated scaling of the enhanced longitudinal heat transfer $\varepsilon_{\text{turb}} \sim \sqrt{\text{Pr}}$ is derived and well supported by the numerical results. In a final step, the results are compared against a setup of sole wall-normal heat transfer that reveal similar characteristic features. Thereby, conclusions given by van Buren et al. [17] substantiate the physical interpretation of the present study.

Declaration of Competing Interest

The authors declared that there is no conflict of interest.

Acknowledgments

Financial support has been provided by the German Research Foundation (Deutsche Forschungsgemeinschaft – DFG) in the framework of the Sonderforschungsbereich Transregio 40. Computational resources have been provided by the Leibniz Supercomputing Center (LRZ).

Nomenclature

Symbols		
Δx	averaged tidal displacement	ω angular frequency
δ_s	Stokes boundary layer thickness	ρ density
δ_{th}	thermal boundary layer thickness	\tilde{S}_{mom} momentum source term
γ	temperature gradient	b wall thickness
κ	thermal diffusivity	c specific heat capacity
ν	kinematic viscosity	h half channel width
		k thermal conductivity
		k_y span-wise turbulent kinetic energy
		L_x, L_y stream- and span-wise domain size

p	pressure	Pr	Prandtl number
q	wall-normal heat flux	σ	ratio of thermal diffusivity
T	temperature	$\varepsilon_{\text{turb}}$	enhancement of long. heat transfer
t	time	ξ_{turb}	enhancement of long. convection
U	thermal transmittance	h_{turb}	convective heat transfer coefficient
u	velocity	l_s^+	Stokes length
u_τ	friction velocity	n	number of periods
x, y, z	spatial coordinates	Superscripts	
Dimensionless Quantities		$\bar{\cdot}$	complex conjugate
α	Womersley number	$*$	adjusted
β	oscillation amplitude	Subscripts	
ϵ	ratio of wall to fluid thickness	lam	laminar
η	wall-normal coordinate	turb	turbulent
λ	non-dimensional pressure gradient	e	effective
Pe	Péclet number	f	fluid
Re_τ	turbulent Reynolds number	o	reference condition
μ	ratio of thermal conductivity	s	solid

References

- [1] S. van Buren, K. Förner, W. Polifke, Acoustic impedance of a quarter-wave resonator with non-uniform temperature, in: Accepted for 27th Int. Conf. Sound Vibration (ICSV27), Prague, CZ, 2021.
- [2] M. R. Bothien, D. Wassmer, Impact of Density Discontinuities on the Resonance Frequency of Helmholtz Resonators, AIAA Journal 53 (4) (2015) 877–887. doi:10.2514/1.J053227.
- [3] B. Čosić, D. Wassmer, S. Terhaar, C. O. Paschereit, Acoustic Response of Helmholtz Dampers in the Presence of Hot Grazing Flow, J. of Sound and Vibration 335 (2015) 1–18. doi:10.1016/j.jsv.2014.08.025.
- [4] P. C. Chatwin, On the longitudinal dispersion of a passive contaminant in oscillatory flows in tubes, J. of Fluid Mechanics 71 (1975) 513–527. doi:10.1017/S0022112075002716.
- [5] M. J. Jaeger, U. H. Kurzweg, Determination of the longitudinal dispersion coefficient in flows subjected to high-frequency oscillations, Physics of Fluids 26 (6) (1983) 1380. doi:10.1063/1.864323.

- [6] E. J. Watson, Diffusion in oscillatory pipe flow, *J. of Fluid Mechanics* 133 (1983) 233–244. doi:[10.1017/S0022112083001883](https://doi.org/10.1017/S0022112083001883).
- [7] C. H. Joshi, R. D. Kamm, J. M. Drazen, A. S. Slutsky, An experimental study of gas exchange in laminar oscillatory flow, *Journal of Fluid Mechanics* 133 (1983) 245–254. doi:[10.1017/S0022112083001895](https://doi.org/10.1017/S0022112083001895).
- [8] U. H. Kurzweg, Enhanced Heat Conduction in Fluids Subjected to Sinusoidal Oscillations, *Int. J. of Heat Transfer* 107 (2) (1985) 459. doi:[10.1115/1.3247437](https://doi.org/10.1115/1.3247437).
- [9] U. Kurzweg, L. de Zhao, Heat transfer by high-frequency oscillations: A new hydrodynamic technique for achieving large effective thermal conductivities, *Physics of Fluids* 27 (11) (1984) 2624–2627. doi:[10.1063/1.864563](https://doi.org/10.1063/1.864563).
- [10] U. H. Kurzweg, Enhanced Heat Conduction in Oscillating Viscous Flows within Parallel-Plate Channels, *J. of Fluid Mechanics* 156 (1985) 291–300. doi:[10.1017/S0022112085002105](https://doi.org/10.1017/S0022112085002105).
- [11] M. Kaviany, Some aspects of enhanced heat diffusion in fluids by oscillation, *Int. J. of Heat and Mass Transfer* 29 (12) (1986) 2002–2006. doi:[10.1016/0017-9310\(86\)90022-0](https://doi.org/10.1016/0017-9310(86)90022-0).
- [12] M. Kaviany, Performance of a heat exchanger based on enhanced heat diffusion in fluids by oscillation: Analysis, *J. of Heat Transfer* 112 (1) (1990) 49–55. doi:[10.1115/1.2910363](https://doi.org/10.1115/1.2910363).
- [13] M. Kaviany, M. Reckker, Performance of a Heat Exchanger Based on Enhanced Heat Diffusion in Fluids by Oscillation: Experiment, *J. of Heat Transfer* 112 (1) (1990) 56–63. doi:[10.1115/1.2910364](https://doi.org/10.1115/1.2910364).
- [14] S. Nishio, X.-H. Shi, W.-M. Zhang, Oscillation-induced heat transport: Heat transport characteristics along liquid-columns of oscillation-controlled heat transport tubes, *Int. J. of Heat and Mass Transfer* 38 (13) (1995) 2457–2470. doi:[10.1016/0017-9310\(94\)00372-3](https://doi.org/10.1016/0017-9310(94)00372-3).

- [15] M. Miura, T. Nagasaki, Y. Ito, Experimental investigation of heat transport with oscillating liquid column in pulsating heat pipe using forced oscillation system, *Int. J. of Heat and Mass Transfer* 106 (2017) 997–1004. doi:[10.1016/j.ijheatmasstransfer.2016.10.069](https://doi.org/10.1016/j.ijheatmasstransfer.2016.10.069).
- [16] M. Miura, T. Nagasaki, Y. Ito, Experimental study on heat transport induced by phase changes associated with liquid column oscillation in pulsating heat pipes, *Int. J. of Heat and Mass Transfer* 133 (2019) 652–661. doi:[10.1016/j.ijheatmasstransfer.2018.12.081](https://doi.org/10.1016/j.ijheatmasstransfer.2018.12.081).
- [17] S. van Buren, A. Cárdenas Miranda, W. Polifke, Large Eddy Simulation of Enhanced Heat Transfer in Pulsatile Turbulent Channel Flow, *Int. J. of Heat and Mass Transfer* 144 (2019) 118585. doi:[10.1016/j.ijheatmasstransfer.2019.118585](https://doi.org/10.1016/j.ijheatmasstransfer.2019.118585).
- [18] A. Scotti, U. Piomelli, Numerical simulation of pulsating turbulent channel flow, *Physics of Fluids* 13 (5) (2001) 1367–1367. doi:[10.1063/1.1359766](https://doi.org/10.1063/1.1359766).
- [19] L. Wang, X.-Y. Lu, An investigation of turbulent oscillatory heat transfer in channel flows by large eddy simulation, *Int. J. of Heat and Mass Transfer* 47 (2004) 2161–2172. doi:[10.1016/j.ijheatmasstransfer.2003.11.010](https://doi.org/10.1016/j.ijheatmasstransfer.2003.11.010).
- [20] OpenFoam, OpenFoam v1706+ (2017).
- [21] S. F. Tardu, G. Binder, R. F. Blackwelder, Turbulent channel flow with large-amplitude velocity oscillations, *J. of Fluid Mechanics* 267 (1994) 109–151. doi:[10.1017/S0022112094001138](https://doi.org/10.1017/S0022112094001138).
- [22] U. H. Kurzweg, E. R. Lindgren, B. Lothrop, Onset of turbulence in oscillating flow at low Womersley number, *Physics of Fluids* 1 (12) (1989) 1972–1975. doi:[10.1063/1.857469](https://doi.org/10.1063/1.857469).
- [23] S. van Buren, W. Polifke, Enhanced Longitudinal Heat Transfer in Oscillatory Channel Flow – a Theoretical Perspective, in: Accepted for ISROMAC: Journal of Physics: Conference Series, Institute of Physics, 2020.